SANDIA REPORT

SAND2003-3453
Unlimited Release
Printed September 2003

Remote Sensing Data Exploitation for Geologic Characterization of Difficult Targets

Laboratory Directed Research and Development Project 38703

Final Report

Mary M. Moya and Charles L. Walker, Signal and Image Processing Systems
Bridget Ford and Jody Smith, Remote Sensing and Exploitations
Laurence S. Costin and Allen Lappin, Geomechanics

Sandia National Laboratories
PO Box 5800
Albuquerque NM 87185-2356

John Stormont
University of New Mexico, Dept. of Civil Engineering
MSC01 1070
Albuquerque, NM 87131-0001

Jeffrey A Mercier
University of Arizona, Electrical and Computer Engineering Dept
1230 E. Speedway
Tucson AZ 85721

Majeed M. Hayat, and Biliana Paskaleva
University of New Mexico, ECE Department
MSC01 1100
Albuquerque, NM 87131-0001

Prepared by
Sandia National Laboratories
Albuquerque, New Mexico 87185

Sandia is a multiprogram laboratory operated by Sandia Corporation,
a Lockheed Martin Company, for the United States Department of Energy's
National Nuclear Security Administration under Contract DE-AC04-94AL85000.

Approved for public release; further dissemination unlimited

Sandia National Laboratories

Issued by Sandia National Laboratories, operated for the United States Department of Energy by Sandia Corporation.

NOTICE: This report was prepared as an account of work sponsored by an agency of the United States Government. Neither the United States Government, nor any agency thereof, nor any of their employees, nor any of their contractors, subcontractors, or their employees, make any warranty, express or implied, or assume any legal liability or responsibility for the accuracy, completeness, or usefulness of any information, apparatus, product, or process disclosed, or represent that its use would not infringe privately owned rights. Reference herein to any specific commercial product, process, or service by trade name, trademark, manufacturer, or otherwise, does not necessarily constitute or imply its endorsement, recommendation, or favoring by the United States Government, any agency thereof, or any of their contractors or subcontractors. The views and opinions expressed herein do not necessarily state or reflect those of the United States Government, any agency thereof, or any of their contractors.

Printed in the United States of America. This report has been reproduced directly from the best available copy.

Available to DOE and DOE contractors from
U.S. Department of Energy
Office of Scientific and Technical Information
P.O. Box 62
Oak Ridge, TN 37831

Telephone: (865)576-8401
Facsimile: (865)576-5728
E-Mail: reports@adonis.osti.gov
Online ordering: http://www.doe.gov/bridge

Available to the public from
U.S. Department of Commerce
National Technical Information Service
5285 Port Royal Rd
Springfield, VA 22161

Telephone: (800)553-6847
Facsimile: (703)605-6900
E-Mail: orders@ntis.fedworld.gov
Online order: http://www.ntis.gov/help/ordermethods.asp?loc=7-4-0#online

SAND 2003-3453
Unlimited Release
Printed September 2003

Remote Sensing Data Exploitation for Geologic Characterization of Difficult Targets

Laboratory Directed Research and Development Project 38703

Final Report

Mary M. Moya and Charles Walker
Signal and Image Processing Systems

Bridget Ford and Jody Smith
Remote Sensing and Exploitations

Laurence S. Costin and Allen Lappin
Geomechanics

Sandia National Laboratories
PO Box 5800
Albuquerque NM 87185-0751

John Stormont
University of New Mexico, Dept. of Civil Engineering, MSC01 1070
Albuquerque, NM 87131-0001

Jeffrey A Mercier
University of Arizona, Electrical and Computer Engineering Dept
1230 E. Speedway
Tucson AZ 85721

Majeed M. Hayat, and Biliana Paskaleva
University of New Mexico, ECE Department, MSC01 1100
Albuquerque, NM 87131-0001

ABSTRACT

Characterizing the geology, geotechnical aspects, and rock properties of deep underground facility sites can enhance targeting strategies for both nuclear and conventional weapons. This report describes the results of a study to investigate the utility of remote spectral sensing for augmenting the geological and geotechnical information provided by traditional methods. The project primarily considered novel exploitation methods for space-based sensors, which allow clandestine collection of data from denied sites. The investigation focused on developing and applying novel data analysis methods to estimate geologic and geotechnical characteristics in the vicinity of deep underground facilities. Two such methods, one for measuring thermal rock properties and one for classifying rock types, were explored in detail. Several other data exploitation techniques, developed under other projects, were also examined for their potential utility in geologic characterization.

This Page Left Intentionally Blank

Executive Summary

Characterizing the geology, geotechnical characteristics, and rock properties of deep underground facility sites that are located more than 20 m below the surface can enhance targeting strategy for both nuclear and conventional weapons. The inaccessibility of facility sites of interest complicates development of complete and robust geological and geotechnical characterizations. Without direct access to site areas to investigate geological structure and stratigraphy and test rock samples in order to develop site-specific data, investigators depend on alternative data sources. Traditional data sets (maps, literature, mining records, etc.) often produce conflicting information (sometimes a result of intentional deception) or no direct information in regions of interest. High-resolution panchromatic imagery can provide information about drainage patterns and fault lines, but fails to provide other important information such as thermal properties.

This report describes the results of a study to investigate the utility of remote spectral sensing for augmenting the geological and geotechnical information provided by traditional methods. The work was performed under a Laboratory Directed Research and Development project, referred to as the RemoteGeo LDRD. The project (and this report) primarily considered novel exploitation methods for space-based sensors, which allow clandestine collection of data from denied sites. The investigation focused on developing and applying novel data analysis methods to estimate geologic and geotechnical characteristics in the vicinity of deep underground facilities. The first step in the investigation was to identify geologic features and geotechnical data that are not generally available from other sources and that add value to the analysts' interpretation. This exercise resulted in identification of several features of interest, such as:

- Specific rock types;
- Contacts between bedrock/parent material and unconsolidated or younger materials;
- Locations of significant secondary phases *within* geologically young materials; and
- Detailed location of various types of lithologic and/or structural contacts.

It also led to the following information needs:

- Drainage and ridgeline analyses of areas of interest;
- Slope and aspect analyses of areas of interest; and
- Determination of a limited set of physical characteristics of the rock mass such as fracture spacing and porosity.

To develop and assess new data exploitation methods for geological characterization in denied areas, we considered a selection of the available space-based spectral sensor systems to represent currently available data-gathering systems. The systems considered are:

- LANDSAT Thematic Mapper (ETM+);
- Multi-spectral Thermal Imager (MTI);
- Advanced Spaceborne Thermal Emission and Reflection Radiometer (ASTER); and
- HYPERION.

In reviewing the many geologic information needs and the capabilities of the space-based remote spectral sensors, we identified two areas on which to focus our development efforts. In addition,

we investigated various methods developed under other projects at SNL that have the potential to enhance interpretation of remotely sensed data to aid a geologist's characterization of a remote site.

We focused our first effort on developing a method to estimate rock mass thermal property data from a single thermal image. The proposed method calculates temperature differences near sun/shade boundaries to predict the thermal parameters of the surrounding rock. We developed analytical methods to estimate thermal inertia and other rock properties from the measured temperature differences resulting from different sun exposure histories. In addition, we conducted field measurements to evaluate the concept of extracting information from sun-shade temperature differences. The measurements were conducted at an existing field-test facility that was previously well characterized and instrumented. These experiments focused on the near-surface processes and material properties that give rise to the measured temperature differences. The results provided in this report are encouraging but do not provide a complete solution. Many complicating factors such as the presence of moisture, vegetation, self-shaded regions, and variable wind speeds have yet to be dealt with in a comprehensive way.

We focused our second effort on investigating the feasibility of using multi-spectral data, which captures broadband spectral features and general spectral shape, to discriminate general categories of rock type. Previous investigators had successfully demonstrated the ability to exploit hyperspectral image data to identify minerals. Additionally, the ASTER sensor has demonstrated an ability to detect some specific rock types from ratios of spectral features. For our effort, we identified seven general categories of rock type and selected representative laboratory spectrometer spectra from the ASTER hyperspectral database. We filtered the laboratory data to emulate MTI spectra and investigated the spectral separability of the classes using separability metrics. We tested a number of approaches to classify the data and measured the generalizability of the classification. Finally, we searched ratios of spectral bands to find those that yielded the best features for classification. This latter technique proved to be quite accurate in classifying rock types. A preliminary conclusion drawn from this effort is that rock types can be mathematically separated based on their multi-spectral signatures, as sampled by the bands of the MTI. Such separability was investigated in the presence of adverse factors such as the presence of additive soil, vegetation, water, and other minerals as well as variations in grain size.

In addition, we examined several other techniques for potential application to geological investigations. The most promising techniques include:

- Spatial and Spectral Derivative Filtering: For MTI images, this technique may enhance specific features of interest such as disturbed soil areas, muck piles, and underground facility vents at a sub-pixel resolution.
- Supersampling: The method employs micro scanning, which takes advantage of the MTI satellite's flexible pointing capability and its over designed optical system. The result is a four-fold increase in resolution, which can improve the detectability in the long wave infrared (LWIR) bands of sedimentary rock layering and other features that would ordinarily be smaller than the LWIR ground resolution.
- Robust Spectral Segmentation: A new spectral segmentation algorithm is available that can identify spectrally similar regions, or segments, within a spectral image without the

difficulties encountered by other segmentation algorithms. Ideally, the segments would correspond to objects in the field of view comprised of similar materials. The segmentation algorithm is designed to include spectra that have the same general shape characteristics in the same segment. Thus, this algorithm could be used to achieve a rough identification of how many different rock types occur in the scene.

- Synthetic Aperture Radar (SAR): Interferometric SAR data can be used to construct high-resolution Digital Elevation Models (DEMs). DEMs with 3-meter post spacings are typical.

In the process of developing new techniques for estimating thermal inertia and spectral identification of rock types, several useful by-products resulted that can generally be applied to other work. These are:

- Software to calculate exact sun exposure of each pixel in a scene, given a DEM, time of day, and time of year.
- Software to calculate a DEM from multi-look MTI (or other satellite) images. The advantage of this method is that the DEM will be registered automatically with the image spectral bands.
- Enhanced thermal modeling software and analytical tools that could be applied to a wide variety of remote sensing analysis problems, such as monitoring the condition of roads and bridges, monitoring vegetative growth, and searching for disturbed soil regions (as indicators of past construction work).

In conclusion, this study has developed a method to estimate rock thermal properties from MTI thermal measurements and a preliminary method for classifying generic rock types from multi-spectral image data. The study demonstrated an initial proof-of-concept for both these methods and shows the potential benefit to augment geologic and geotechnical interpretation of denied sites. We recommend further analysis and development of these methods to mitigate potential sources of error identified herein. The recommended follow-on development should produce predictable methods for extracting information from remote multi-spectral imagery to aid an analyst in characterizing the geology and understanding the geotechnical characteristics of remote sites.

Contents

Executive Summary **3**
1 Introduction **17**
  1.1 Geologic and Geotechnical Characterization Needs 17
  1.2 Space-based Remote Spectral Sensing Technology 19
    Primary Purpose 19
  1.3 Data Exploitation Methods Developed and Tested in this Study 21
  1.4 Report Outline 22
2 Thermal Inertia Estimation from Sun/Shade Temperature Differences **23**
  2.1 Introduction and Approach 23
    2.1.1 Definition of Thermal Inertia (TI) and Apparent Thermal Inertia (ATI) . 23
    2.1.2 Rock Properties vs. Thermal Inertia 24
    2.1.3 Traditional Remote Sensing Estimation of ATI 24
    2.1.4 Model Estimation of Rock Thermal Properties 24
  2.2 Digital Elevation Extraction from Multiple MTI Data Sets 27
    2.2.1 Introduction 27
    2.2.2 MTI Geometric Correction 28
    2.2.3 Stereo Point Matching 32
    2.2.4 Elevation Extraction 35
    2.2.5 Conclusions and Future Work 37
  2.3 IR Response Model for Simulating Ground Temperature 37
    2.3.1 Description of Original IR Response Code Model 37
    2.3.2 Modifications to IR Response Code 41
    2.3.3 Summary of Model Limitations and Modifications 48
  2.4 Sun/Shade Times from DEM 49
    2.4.1 Ridge Simulation 49
    2.4.2 DEM Sunrise/Sunset Calculations 50
  2.5 Optimization to Estimate Thermal Parameters of Rock 51
    2.5.1 A Method to Estimate Thermal Parameters 51
    2.5.2 Optimization Procedures 52
  2.6 Simulation 53
    2.6.1 Forward Model 53
    2.6.2 Noiseless Optimization Methods 55
    2.6.3 Sensitivity 61
  2.7 Application to MTI Imagery 81
    2.7.1 Description of MTI 81
    2.7.2 Experimental Sites 81
    2.7.3 Experimental Procedures 85
    2.7.4 Rectification to DEM 85
    2.7.5 Atmospheric Correction 85
    2.7.6 Results 87
  2.8 Analytical Models for Surface Temperature Differences in Sun and Shade 90
    2.8.1 Introduction 90
    2.8.2 Model 1 - Model Without Soil Moisture 90
    2.8.3 Model 2 - Inclusion of Soil Moisture 95
    2.8.4 Model 3 - Inclusion of Vegetation 99

2.8.5 Conclusions 106
2.9 Field Measurements 106
2.9.1 Introduction 106
2.9.2 Measurement Methods 107
2.9.3 Results 108
2.9.4 Discussion 116
2.10 Evaluation of Analytical Models with Field Data 118
2.10.1 Introduction 118
2.10.2 Evaluation of Data from Bare Soil Surface 119
2.10.3 Evaluation of Data from Stone–Covered Surface 121
2.10.4 Evaluation of Albedo from Dry Soil 122
2.10.5 Evaluation of Vegetation Temperature Differences 123
2.10.6 Discussion 124
2.11 A Method for Estimating Bare Soil Temperature from Radiometric Temperatures that Include Vegetation 124
2.11.1 Introduction 124
2.11.2 Vegetation Indices (VIs) 125
2.11.3 Vegetation Index Applied to Sun–Shade Exposure 125
2.11.4 Comparison of Theoretical and Calculated VI – Tr Response 128
2.11.5 Application Approach 130
2.12 Atmospheric Correction for Thermal Infrared Satellite Imagery 131
2.12.1 Introduction 131
2.12.2 Atmospheric Correction 132
2.13 References 137
3 Spectral Separation and Classification of Rock Types 142
3.1 Introduction 142
3.2 Prior Work on Rock Classification 142
3.3 Theory and Background 144
3.3.1 Bayes Theory 144
3.3.2 Discriminant Function 144
3.3.3 Error Bounds 145
3.3.4 Minimum Distance Classifier 147
3.4 Rock-Type Class Definitions 148
3.5 Original Multi-Spectral Training Data and a Methodology for Training Set Enlargement 150
3.5.1 Inadequacy of Classification Using the Euclidian Distance as a Metric for Separability 151
3.5.2 Mean and Covariance-Matrix Estimation from a Limited Size Training Data 152
3.5.3 Augmentation of the Training Set 152
3.5.4 Preliminary Feature-Space Reduction 159
3.6 Definition of the Data Sets Used in the Separability and Classification Analysis 159
3.6.1 Overview 159
3.6.2 Testing Data Sets 160
3.6.3 Separability Study Outline 162
3.6.4 Classification Study Outline 163

3.7 Results Using Uncompressed Features ... 163
3.7.1 Separability According to Using Inter-Class Metrics ... 163
3.7.2 Separability According to Average Classification Error ... 167
3.7.3 Classification of the Testing Data ... 167
3.8 Results Using Compressed Features ... 173
3.8.1 Feature Extraction Using Canonical Analysis ... 173
3.8.2 The Use of Spectral Indices ... 178
3.8.3 Discussion of Results ... 182
3.9 Conclusions ... 187
3.10 Future Work ... 189
3.11 References ... 189
4 Other Tools ... 191
4.1 Spatial and Spectral Derivatives ... 191
4.2 Supersampling ... 192
4.3 Segmentation Using VNIR/SWIR for Rock Classes ... 193
4.4 High-Resolution Interferometric SAR Imagery and Rivertools ... 196
5 Summary and Recommendations ... 197
5.1 Summary and Conclusions ... 197
5.2 Recommendations ... 200
Appendix A ... 202

Figures

Figure 2.1 MTI Visible and Near IR image (false color IR) of Manzano Base area, Kirtland AFB ... 25
Figure 2.2 MTI Longwave IR (band N) of Manzano Base area ... 26
Figure 2.3 Geometric correction model ... 29
Figure 2.4 MTI focal plane detail ... 30
Figure 2.5 MTI telescope distortion plot ... 31
Figure 2.6 Resolution pyramid ... 33
Figure 2.7 Shifting window point matching ... 33
Figure 2.8 Parallel image correlation ... 34
Figure 2.9 Initial correlation results versus DTED surface plot ... 35
Figure 2.10 Ground–Up space intersection ... 36
Figure 2.11 Simulated temperatures for full sun and full shade: granite and soil ... 55
Figure 2.12 Error Surface: Thermal Conductivity vs. heat capacity. ... 57
Figure 2.13 Error surface: thermal inertia vs. diffusivity; granite ... 58
Figure 2.14 Error surface: thermal inertia vs. diffusivity; granite (expanded view) ... 59
Figure 2.15 Error surface: emissivity vs. thermal inertia; granite ... 60
Figure 2.16 Temperature bias: Objective functions for different rock types (linear scales) .. 64
Figure 2.17 Temperature bias: Objective function ... 65
Figure 2.18 Temperature bias: Relative errors and Objective function for 3epa ... 65
Figure 2.19 Temperature bias: Objective function (log-log plot) ... 66
Figure 2.20 Errors vs Temperature bias (optimizing emissivity, thermal inertia and diffusivity: 3epa) ... 66

Figure 2.21 Temperature bias: Objective functions for 4erpa (emissivity, reflectance, thermal inertia and diffusivity) 67
Figure 2.22 Temperature bias: all errors and Objective functions 4erpa 67
Figure 2.23 Temperature bias: Relative errors and Objective functions: Soil (4erpa) 68
Figure 2.24 Temperature bias: Relative errors and Objective funtions: Soil (4erpa). Note scale difference from preceding figure. 68
Figure 2.25 Temperature bias: Absolute relative errors (duplicate lines are for positive or negative errors) 69
Figure 2.26 Temperature bias Comparison of Objective functions for 3epa and 4erpa 69
Figure 2.27 Temperature bias Comparison of Objective functions for 3epa and 4erpa (semi-log plot) 70
Figure 2.28 Temperature bias Comparison of Objective functions for 3epa and 4erpa (log-log plot) 70
Figure 2.29 Temperature bias: Comparison of Optimizations 3epa and 4erpa for Soil 71
Figure 2.30 Temperature bias: Comparison of Optimizations 3epa and 4erpa for Granite 71
Figure 2.31 Temperature bias: Comparison of Optimizations 3epa and 4erpa for Limestone 72
Figure 2.32 Temperature bias: Comparison of Optimizations 3epa and 4erpa for Sandstone 72
Figure 2.33 Parameter errors vs. Objective function: Temperature bias 73
Figure 2.34 Irradiance noise sensitivity: Absolute parameter errors for emissivity and thermal inertia (3epa) 74
Figure 2.35 Irradiance noise sensitivity: Equivalent Temperature noise: vs. Relative errors (each point is mean of 10 instances) 75
Figure 2.36 Irradiance noise sensitivity: Errors vs. Irradiance standard deviation 75
Figure 2.37 Horizontal positional sensitivity by direct simulation 77
Figure 2.38 Rock type separability in presence of irradiance noise: emissivity vs. thermal inertia 78
Figure 2.39 Rock type separability in presence of irradiance noise; emissivity vs. thermal inertia (maximum std_dev=10: expanded scale) 78
Figure 2.40 Rock type separability in presence of radiance noise (0.1 to 50.0): thermal inertia vs. diffusivity 79
Figure 2.41 Rock properties: thermal inertia vs. diffusivity 79
Figure 2.42 MTI Band Response 81
Figure 2.43 Coyote Canyon test sites (MTI false color IR) 82
Figure 2.44 Coyote Canyon test site (MTI: RGB=NML) 82
Figure 2.45 Red Wing Mine test site (Shaded relief from DEM) 83
Figure 2.46 Temperature: Albuquerque Feb 2001 84
Figure 2.47 Wind Speed: Albuquerque, Feb 2001 84
Figure 2.48 Transmittance: MODTRAN China Lake 86
Figure 2.49 Up-welling path radiance: MODTRAN China Lake 87
Figure 2.50 Effect of path radiance offset Coyote Canyon (high resolution) 88
Figure 2.51 Effect of path radiance offset: Coyote Canyon (medium resolution) 88
Figure 2.52 Path radiance Coyote (low resolution) 89
Figure 2.53 Effect of Path Radiance Offset: Red Wing Mine ROI 1 89
Figure 2.54 Predicted temperature difference in sun and shade for granite and dirt properties from model described here and results of Walker (2002) 95

Figure 2.55 Surface temperature differences between sunlit and shaded regions as a function of saturation for three soil textures 99
Figure 2.56 Soil, vegetation and radiometric temperatures as function of fractional vegetation coverage for a partially dry soil and fully transpiring 104
Figure 2.57 Radiometric temperature as a function of fractional vegetation coverage for three different surface soil moisture values. The vegetation transpires at its maximum rate. 105
Figure 2.58 Radiometric temperature as a function of fractional vegetation coverage for three different root zone moisture amounts. The soil surface is completely dry so there is no evaporation. 105
Figure 2.59 Thermal image and photograph showing sun-shade boundary........ 109
Figure 2.60 Summary of sun-shade temperature difference vs. sunlit temperature........ 110
Figure 2.61 Thermal image and photograph of grama grass at ALCD test site........ 112
Figure 2.62 Thermal image of cobble pile 112
Figure 2.63 Lysimeter and air temperatures 113
Figure 2.64 Soil transfer coefficient, h, for dry and wet soil, and theoretical maximum from P–T approximation........ 114
Figure 2.65 Thermal conductivity as a function of soil saturation........ 115
Figure 2.66 Potential as a function of depth below surface 116
Figure 2.67 Comparison of temperature differences measured on March 12, 2003 for four different surface materials........ 117
Figure 2.68 Predicted temperature difference as a function of the moisture factor for three different wind speeds. Recorded wind speed was 1.7 m/s within about 1 minute of measurement. Measured surface temperature difference and moisture factor values are for bare soil at ALCD site on March 10, 2003. 120
Figure 2.69 Solid line is predicted temperature difference as a function of wind speed for bare soil with moisture factor of 0.3. Symbols denote measured temperatures at estimated wind speed on March 12, 2003 at ALCD site with bare soil........ 121
Figure 2.70 Model prediction of sun-shade temperature difference as a function of thermal inertia for two different values of albedo, corresponding to light and dark colored stone. Field measured temperature differences and interpreted thermal inertia are also given. 122
Figure 2.71 Interpreted albedos for April 11 and May 19 measured temperatures by matching to model simulations for these dates with variable albedos (solid lines)........ 123
Figure 2.72 Soil and vegetation temperatures with sunlit and shaded conditions 126
Figure 2.73 Radiometric temperature in sunlit and shaded conditions........ 127
Figure 2.74 Radiometric, soil and vegetation sun-shade temperature differences 127
Figure 2.75 Temperature differences from example calculations using simple model........ 128
Figure 2.76 Predicted temperatures from simple model 130
Figure 2.77 Example of data interpretation method using radiometric sun-shade temperature difference to estimate soil temperature difference 131
Figure 2.78 (a) Contributions to at sensor radiance within solar reflective regime (b) Contributions to at-sensor radiance from atmospheric and ground surface emissions........ 133
Figure 2.79 Screen capture image of MODTRAN GUI in IDL interface generated to allow users a more intuitive interaction with the radiative transfer code. [Interactive

Data Language, Research Systems, Inc.] The “read geometry” button located in the left column allows for the selection of an MTI image file, from which solar, sensor, and target geometry are read. In plotting MODTRAN outputs, the user has the option of applying MTI filter functions to all data outputs. Finally, the GUI provides the user with a means of generating LUT, which correlate atmospheric transmission and radiance values to a range of atmospheric parameters such as column water vapor........ 135
Figure 3.1 Hyperspectral signature of coarse hornfels, member of original training data for group 1 154
Figure 3.2 Hyperspectral signature of green grass, used to perturb the original training data 154
Figure 3.3 Hyperspectral signature of andradite mineral, used to perturb the original training data 155
Figure 3.4 Hyperspectral signature of distilled water, used to perturb the original training data........ 155
Figure 3.5 Hyper spectral signature of brown silty loam, used to perturb the original training data........ 156
Figure 3.6 Hyper spectral signature of Cellulose, used to perturb the original training data........ 156
Figure 3.7 Multi-spectral signatures of the original training data for group 1........ 157
Figure 3.8 Multi-spectral signatures of original training data for group1, perturbed with the mineral 157
Figure 3.9 Multi-spectral signatures of the original training data for group 1, perturbed with soil........ 157
Figure 3.10 Multi-spectral signatures of original training data for group 1, perturbed with green vegetation........ 158
Figure 3.11 Multi-spectral signatures of original training data for group 1, perturbed with water 158
Figure 3.12 Average separability and classification errors for 2 to 11 features selected........ 176
Figure 3.13 Multi-spectral signatures, representing three different rock types........ 181
Figure 3.14 Comparison between the three optimization techniques, for selecting the best pair of indices........ 182
Figure 3.15 Comparison between the three optimization techniques for selecting the best triplet of indices 183
Figure 4.1(a) MTI true-color image (Ivanpah, NV) 191
Figure 4.1(b) MTI VNIR Multi-spectral bi-directional derivative image 191
Figure 4.2 (a) MTI color infrared image (Delaware); (b) Derivative filteredVNIR Image; (c) Thermal texture Filtered TIR Image; (d) Spectral DerivativeVNIR Image 192
Figure 4.3 Microscanning and Yaw for Two-dimensional Supersampling 193
Figure 4.4(a) MTI thermal image of New Orleans Pontchartrain Center with 5 m effective GSD........ 193
Figure 4.4(b) Airborne panchromatic image of New Orleans Pontchartrain Center with 3 m GSD†........ 193
Figure 4.5 Color Infrared Composite Images of Primm Valley Golf Course taken from six perspective views of MTI Imagery........ 195

Figure 4.6 RSS-produced Segmentations from visible and near-infrared MTI bands of Primm Valley Golf Course 195
Figure 4.7(a) SNL 3m IFSAR DEM of Coyote Canyon on Manzano Base, Albuquerque, NM 196
Figure 4.7(b) Rivertools Output Derived from USGS 10 m DEMManzano Base, Albuquerque, NM 196
Figure A1 Temperature of radiating surface 203
Figure A2 Theorectical error relation between Temperature and Irradiance with no emissivity error 203
Figure A3 Relative errors Temperature as function of Irradiance and emissivity errors..... 204
Figure A4 Temperature and Irradiance errors from multiple start simulations (no noise or bias) 205
Figure A5 Sources of simulation errors 206
Figure A6 Sources of simulations error (Temperature vs. Irradiance) for small values of Temperature error 207
Figure A7 Temperature errors vs. Irradiance errors from Irradiance noise sensitivity data 208

Tables

Table 1.1 Spectral Band Characteristics of Landsat ETM+ 19
Table 1.2 Spectral Band Characteristics of MTI 20
Table 1.3 Spectral Band Characteristics of ASTER 21
Table 2.1 Solar Coefficients for IR Response Code* 39
Table 2.2 Material Properties of Selected Rocks* 54
Table 2.3 MTI Images Used at Test Sites 85
Table 2.4 Input Parameters 94
Table 2.5 Input parameters 98
Table 2.6 Input Parameters 103
Table 2.7 Summary of sun-shade temperature measurements on soils and vegetation 111
Table 3.1 Members of the original training data of groups 1-4. Letter “C” denotes the coarse-grain rocks and the letter “F” denotes the fine size rocks 149
Table 3.2 Continuation of Table 3.1. This table lists members of the original training data for groups 5 -7. The letter “C” denotes the coarse-grain rocks and the letter “F” denotes the fine size rocks. 150
Table 3.3 The numbering system for MTI- bands (red letters denote the bands that we initially avoided) 151
Table 3.4 Bands used in the preliminary analysis (Bands C and L visually identified to have low variance) 151
Table 3.5 Bands used in the separability and classification analysis 151
Table 3.6 Results of the separation of the original training data (Tables 3.1 and 3.2) among all seven groups, according to the Euclidean minimum-distance criterion 152
Table 3.7 Elements used to perturb the original training data and to create the enlarged training data set (training set 1). The odd number columns contain the perturbation’s identification number (ID), according to the database and to the

corresponding library and the even number columns contain the sample's name. 153

Table 3.8 Elements used to perturb the original training data for creation of testing data sets 1-2. The odd number columns (labelled in red color) contain the perturbation's identification number (ID), according to the database and the even number columns contain the sample's name. 161

Table 3.9. Samples outside of the original training set which are used to create testing set 3. The letter "f" denotes fine size rocks and letter "c" denotes coarse size rocks. 162

Table 3.10 Normalized Euclidian (relative to the maximal Euclidian distance) distances between members of any two groups when training set 1 is used as a training set for the classifier. The red color denotes the maximal value and the blue denotes the minimal value. The Euclidean distance measures only a relative distance from the mean point in the group. It does not take into account the distribution of the points in the group. The best separability, according to Euclidian distance, is achieved between groups 2 and 3 and between groups 2 and 7. The worst is between groups 1 and 7. Clearly, the Euclidean distance does not take into account the variability of the values in all dimensions and is, therefore, not an optimum discriminant analysis algorithm for this case. 164

Table 3.11 Normalized Mahalanobis (relative to the maximal Mahalanobis distance) distances between any two groups when training set 1 is used as a training set for the classifier. The red color denotes the maximal value and the blue color denotes the minimal values. Mahalanobis distances look at not only variations (variance) between the responses at the same wavelengths, but also at the inter-wavelength variations (co-variance). However, when the Mahalanobis distance is employed, only the separability between groups 1 and 4 is improved, compare to the case when Euclidian distance is used. The worst cases are between groups 5 and 6 and between groups 5 and 7. 165

Table 3.12 Normalized Bhattacharya (relative to the maximal Bhattacharya distance) distances between any two groups when training set 1 is used as training data for the classifier. The red colors denote the maximal value and the blue color denotes the minimal value. The best separability, according to Bhattacharya distance, was achieved between groups 1 and 4 and between groups 1 and 7. The worst are between groups 2 and 5 and between groups 5 and 6. We deem these groups to be *problematic*. 165

Table 3.13 Normalized (relative to the maximal values) Euclidian, Mahalanobis and Bhattacharya distances between any two groups when training set 2 is used as training data for the classifier. 166

Table 3.14 Normalized (relative to the maximal values) Euclidian, Mahalanobis and Bhattacharya distances between any two groups when training set 3 is used as training data for the classifier. 166

Table 3.15 Normalized (relative to the maximal value) Euclidian, Mahalanobis and Bhattacharya distances between any two groups, when training set 4 is used as training data for the classifier. 166

Table 3.16 Separability performance of the Bayesian classifier, when uncompressed data (all eleven bands) are used. Training sets 2-4 are created by adding testing sets from 1 to 3 (described in Section 3.5) consecutively to the training set 1. For each case,

the average separability error is calculated, according to Bayesian classifier. It is clear from the results, that best separability between all of the seven groups is achieved for training set 1. Separability error increases from 0.2% (training set 1) to 5% for the training data set 4, containing members outside of the original training data set (see Table 3.9). 167
Table 3.17 Classification performance of the Bayesian classifier when uncompressed data (all eleven bands) are used. We applied the Bayesian classifier (trained with the training set 1) to testing sets 1-3 and compared the average classification error for each set. Comparing the results for testing set 1, 2 and 3, the average classification error increased from 4% to 70%. For the third test, the classifier is not able to correctly classify neither one of the members of tested data for groups 1 and 3. Similar is the situation with group 4 and 6 (only few members are correctly classified). The best performance is seen for group 5, without any misclassified members. However, most of the misclassified members for the rest of the groups were classified as members of group 5. 170
Table 3.18 Classification performance of the Bayesian classifier for tests 1-3, when the size of group 5 is reduced by random selection of eight members of the original fifteen bands. The individual classification errors for groups 2, 4 and 6 are reduced but still the members of testing set 3 for group 1 and group 3 are all incorrectly classified. 170
Table 3.19 Classification performance of the Bayesian classifier for all tests 1-3, when the size of group five is reduced by “deterministic” selection of eight members of the original fifteen. The classification error for groups 2 and 6 is reduced compare to the case were the members are randomly selected. Still, the members of testing set 3 for group 1 and group 2 were entirely incorrectly classified. Note that a high misclassification error for group 5 appears. Most of the incorrect classified members are now confused as members of group 6, instead of group 5. 171
Table 3.20 Separability performance of the Bayesian classifier, when groups are created according to their geological properties and their grain size. The newly defined 8th group contains all fine elements of the original training data. With this data organization we achieve almost perfect separability. 171
Table 3.21 Classification performance of the Bayesian classifier at tests 1-3, applied over the eight groups. The higher error is again for testing set 3 and the performance is very close to the performance of the original data structure, where the rock’s samplers were distributed among seven groups. Most of the misclassified members are confused with group 8, since it now has the highest population... 172
Table 3.22 Separability performance of the Bayesian classifier for training data sets 1-4, when the original seven groups contain only coarse size elements. 172
Table 3.23 Classification performance of the Bayesian classifier for testing data sets 1-3, when the original seven groups contain only coarse size elements. Again, the classification performance for testing sets 1 and 2 is almost optimal, but the error for testing set 3 is still very high. Most of the misclassified members are confused as a members of group 5 and group 6. 173
Table 3.24 Separability performance of the Bayesian classifier for the five selected features using the canonical transformation. 176

Table 3.25 Classification performance of the Bayesian classifier for tests 1-3 using the canonical transformation. 177
Table 3.26 Separability performance of the Bayesian classifier for seven features using the canonical transformation. The average separability error for each one of the four training sets is lower compare to the case when five features were selected. 177
Table 3.27 Classification performance of the Bayesian classifier at tests 1-3 using the canonical transformation. Compared to the case for which five features were selected, the average classification error for testing set 1 in this case decreases, but for testing sets 2 and 3, the performances are very close. Most of the misclassified members at test 3 are labelled as members of groups 2, 5 and 6. . 177
Table 3.28a Pairs of ratios, corresponding to the maximum Bhattacharya distance between designated pairs of groups. Indices 34, 35 and 43 reoccurred in almost all pairs. Index 34 corresponds to the ratio between bands 4 (D) and 5 (E), index 35 is ratio between bands 4 (D) and 6 (G) and index 43 is ratio between bands 5 (E) and 6 (G). 179
Table 3.28b Maximum Bhattacharya distance values for pairs of ratios listed in Table 3.28a. Red color denotes the maximum Bhattacharya distance value and blue color denotes the minimum Bhattacharya distance value. When combination of two ratios is chosen according to Bhattacharya distance, maximal separability is achieved between groups 1 and 4 and the worst separability is between groups 3 and 5. 179
Table 3.29a Triplet of ratios, corresponding to the maximum Bhattacharya distances between designated pairs of groups. A unique triplet yields the best separability between all pairs of groups. This triplet contains the three ratios that most frequently occur in the two-ratios case (see Table 3.28a). Index 34 corresponds to the ratio between bands 4 (D) and 5 (E), index 35 is the ratio between bands 4 (D) and 6 (G) and index 43 is the ratio between bands 5 (E) and 6 (G). 180
Table 3.29b Maximum Bhattacharya distance values for triplets of ratios listed in Table 3.29a. Red color denotes the maximum Bhattacharya distance value and blue color denotes the minimum Bhattacharya distance value. The best separability is achieved between groups 1 and 4. The worst separability is also again between groups 3 and 5. 180
Table 3.30 Bayesian classification performance for tests 1-3 when two ratios are selected according to intersection optimization strategy. Index 1 corresponds to the ratio between bands 1(A) and 2(B); index 34 corresponds to the ratio between bands 4(D) and 5(E). 184
Table 3.31 Bayesian classification performance for tests 1-3, when two ratios are selected according to max-min optimization strategy. Index 16 corresponds to the ratio between bands 2(B) and 6(G) and index 50 corresponds to the ratio between bands 5(E) and 13(N). 184
Table 3.32 Bayesian classification performance for testing sets 1-3 when two ratios are selected according to minimal average error optimization strategy. Index 68 corresponds to the ratios between bands 8 (O) and 13 (N) and index 76 corresponds to the ratio between bands 11 (L) and 12 (M). 185
Table 3.33 Bayesian classification performance for testing sets 1-3 when three ratios are selected according to the maximal Bhattacharya distance between any two groups.

Index 34 corresponds to the ratio between bands 4 (D) and 5 (E), index 35 is the ratio between 4 (D) and 6 (G) and 43 is the ratio between bands 5 (E) and 6 (G). 185
Table 3.34 Bayesian classification performance for testing sets 1-3, when three ratios are selected according to max-min optimization strategy. Index 13 corresponds to the ratio between bands 2 (B) and 3 (C), index 16 is the ratio between bands 2 (B) and 6 (G) and index 50 is the ratio between bands 5 (E) and 13 (N). 186
Table 3.35 Bayesian classification performance for testing sets 1-3 when two 2-band ratios are selected according to minimal average error optimization strategy and one 3-band ratio is selected again according to the minimal average error optimization strategy.. Index 68 corresponds to the ratio between bands 8 (O) and 13 (N). Index 76 corresponds to the ratio between bands 11 (L) and 12 (M). 186
Table 3.36 Bayesian classification performance for testing sets 1-3 when three ratios are selected according to the minimal average error optimization strategy. Index 18 corresponds to the ratio between bands 2 (B) and 8 (O), index 72 corresponds to the ratio between bands 9 (J) and 13 (N), and index 76 corresponds to the ratio between bands 11 (L) and 12 (M). 187
Table A1 Pixel Properties for Granite 209

1 Introduction

Characterizing the geology, geotechnical characteristics, and rock properties of deep underground facility sites that are located more than 20 m below the surface can enhance targeting strategy for both nuclear and conventional weapons. For nuclear weapons targets, geologic (e.g., stratigraphy, structure, history, hydrology, and surface conditions) and geotechnical (e.g., rock and rock mass properties, ground support, construction methods, and opening sizes and shapes) data facilitate the estimation of surface penetration potential, ground shock propagation characteristics, and facility hardness. For conventional weapons targets, this geologic and geotechnical data can provide information regarding surface conditions for penetrating weapons and vulnerable surface features such as adits (entries).

The inaccessibility of facility sites of interest complicates development of complete and robust geological and geotechnical characterizations. Without direct access to site areas to investigate geological structure and stratigraphy and test rock samples in order to develop site-specific data, investigators depend on alternative data sources. Traditional data sets (maps, literature, mining records, etc.) often produce conflicting information (sometimes a result of intentional deception) or no direct information in regions of interest. High-resolution panchromatic imagery can provide information about drainage patterns and fault lines, but can not provide other important information such as thermal rock properties.

This report describes the results of a study to investigate the utility of remote spectral sensing for augmenting the geological and geotechnical information provided by traditional methods. The work was performed under a Laboratory Directed Research and Development project, referred to as the RemoteGeo LDRD. The project (and this report) primarily considered exploitation methods for space-based sensors, which allow clandestine collection of data from denied sites. The investigation focused on developing and applying novel data analysis methods to augment an analyst's interpretation of geologic and geotechnical characteristics in the vicinity of deep underground facilities. The first step in the investigation identified geologic features and geotechnical data that are not generally available from other sources and that add value to the analysts' interpretation. The results of this exercise are summarized in the following section and provide the motivation for the remainder of the study. Rather than explore advances in panchromatic imagery, we focused on exploiting available space-based spectral sensors and investigating properties of the associated data related to geological features and physical properties of the exposed rock mass. The sensor systems we considered are described below in Section 1.2. The Multi-spectral Thermal Imager (MTI) served as a test bed for many of the exploitation techniques described in this report. Section 1.3 introduces the novel approaches developed and tested under this study that will be described in detail in subsequent sections. Finally, Section 1.4 outlines the contents of the remainder of the report.

1.1 Geologic and Geotechnical Characterization Needs

Before attacking the problem of data exploitation for geologic characterization, we narrowed the scope of the project to address the most significant geological and geotechnical issues that are not well satisfied by current data sets. The geologic assessment team joined the investigators responsible for image analysis and processing to develop a complete list of specific geologic features that, if identified at a site, would provide information about the geologic conditions, rock properties, or geotechnical constraints on construction of the facility. In general, a geologic investigation of a site focused on developing the following types of information:

- **General geologic setting and history**
  The large-scale regional and local geologic processes that have influenced the formation of and subsequent changes to the rock mass are important in developing an understanding of the regional setting and estimating the effects of long-term tectonic forces on rock conditions. Seasonal effects like freezing depth and duration are also important relative to surface conditions and weathering.
- **Stratigraphy and Structure**
  Site-specific information on rock composition, degree of consolidation, secondary alterations or weathering, layer thickness, and variability and continuity are of key importance. In addition, the effects of any deformational event such as jointing, faulting, and layer tilting are of interest.
- **Hydrology**
  Because of the importance both to ground shock and to constructability, hydrologic information such as depth to water table and the saturation levels in the unsaturated zone are essential.
- **Rock properties**
  Identifying of specific rock types as well as both intrinsic and in-situ rock properties is important. Rock properties include physical properties such a density, porosity, and void fraction; mechanical properties such as compressive and tensile strength, friction angle, and elastic moduli; and geotechnical properties of the rock mass such as joint spacing, orientation and condition, rock mass quality and rating, and deformation modulus.
- **Surface conditions**
  Other types of information that are not specifically geologic in nature, but are important to estimates of penetration success, include topography, vegetation, and the presence of cultural remnants (foundations, roads, etc).

The results of our more focused effort revealed that there are several areas for which current information is usually sparse and exploiting remote spectral data could have a significant impact and add value to the characterization process. This resulted in a desire to apply spectral analysis in several specific areas, including:

- Detailed location of the contact between bedrock/parent material and unconsolidated or younger materials. Potential methods for locating these contacts include mapping rock characteristics such as thermal inertia or tracking mineralogical differences between parent material and soil/colluvium/alluvium.
- Location of significant secondary phases *within* geologically young materials, such as basin or valley fills, especially in arid or semi-arid areas. In these areas, caliches, gypsiferous horizons, and salt-bearing horizons are often developed and can significantly affect excavation stability, although they are not normally included in regional-scale mapping studies.
- Detailed location of various types of lithologic and/or structural contacts, both within and among mapped geologic units, for example, variations in bedding thicknesses and lithologies *within* a mapped stratigraphic unit at the scale of an individual portal or adit.

This level of information is typically included only in the largest-scale geologic maps and is not normally available internationally.

- Drainage and ridgeline analyses of areas of interest, conducted to define bedrock/material domains within the region of interest.
- Slope and aspect analyses of areas of interest, which are particularly needed for analyses of potential soil thicknesses and evaluation of the potential affects of topographic or structural features on the water table.
- Identifying specific rock types by their characteristic proportions of mineralogical content.
- Determination of a limited set of physical characteristics of the rock mass such as fracture spacing and porosity. Given some confirmation of the basic physical characteristic of a rock unit (such as porosity), it is usually possible to reduce considerably the uncertainty in key modeling parameters that correlate well with these basic physical properties (i.e. rock strength and modulus).

1.2 Space-based Remote Spectral Sensing Technology

To develop and assess new data exploitation methods for geological characterization in denied areas, we considered a selection of the available space-based spectral sensor systems to represent currently available data-collection systems. The characteristics of these systems are briefly described below.

LANDSAT Thematic Mapper (ETM+)

Landsat ETM+ applies whisk-broom scanning to collect 7-band multi-spectral image data. Three visible (VIS), one near infrared (NIR), and two mid-wave infrared (MWIR) bands have 30-meter ground sample distance (GSD). The long-wave infrared (LWIR) band has 120-meter GSD. Table 1.1 summarizes the ETM+ bands. The ETM+ swath width is 185 km. The ETM+ focal plane array includes a 16-pixel linear array for each of the lower wavelength bands, VIS through MWIR, and a 4-pixel linear array for the LWIR band. Bands 5 and 7 have been used for rock type discrimination.

Table 1.1 Spectral Band Characteristics of Landsat ETM+

Band	Wavelength (µm)	Description	GSD (meters)	Primary Purpose
1	0.45 - 0.52	Blue	30	Water penetration
2	0.53 - 0.61	Green	30	Vegetation reflectance
3	0.63 - 0.69	Red	30	Chlorophyll absorption
4	0.78 - 0.9	NIR	30	Vegetation discrimination and vigor
5	1.55 - 1.75	MWIR	30	Vegetation and soil moisture
6	10.4 - 12.5	LWIR	60	Thermal mapping
7	2.09 - 2.35	MWIR	30	Mineral and rock type discrimination
8	0.52 - 0.90	NIR	15	

Multi-spectral Thermal Imager (MTI)

MTI, sponsored by the Department of Energy, applies push-broom scanning to collect 15-band multi-spectral image data. Three VIS and NIR band have 5-meter GSD and the remaining NIR, short-wave infrared (SWIR), MWIR, and LWIR bands have 20-meter GSD. Table 1.2 summarizes the MTI bands. The MTI swath width is 14 km. The MTI focal plane includes three sensor chip arrays (SCAs). Each SCA contains a 828-pixel linear photovoltaic silicon diode detector array for each of bands A-D, a 207-pixel linear photovoltaic indium antimonide detector array for each of bands E-K and O, and a 207-pixel linear photovoltaic mercury cadmium telluride detector array for each of LWIR bands L-N. The MTI thermal bands can be used to help estimate thermal rock parameters. MTI has flexible pointing capability allowing the generation of digital elevation data from multiple perspective views of the same scene.

Table 1.2 Spectral Band Characteristics of MTI

Band	Wavelength (µm)	Description	GSD (meters)	Primary Purpose
A	0.45 - 0.52	Blue	5	Water penetration
B	0.52 - 0.6	Green	5	Vegetation reflectance
C	0.62 - 0.68	Red	5	Chlorophyll absorption
D	0.76 - 0.86	NIR	5	Vegetation discrimination and vigor
E	0.86 - 0.89	SWIR	20	Water vapor reference
F	0.91 - 0.97	SWIR	20	Water vapor
G	0.99 - 1.04	SWIR	20	Water vapor reference
H	1.36 - 1.39	SWIR	20	Cirrus clouds
I	1.55 - 1.75	SWIR	20	Vegetation and soil moisture
0	2.08 - 2.35	SWIR	20	Mineral and rock type discrimination
J	3.5 - 4.1	MWIR	20	Surface temperature estimates
K	4.87 - 5.07	MWIR	20	Surface temperature estimates
L	8.0 - 8.4	LWIR	20	Water vapor
M	8.4 - 8.85	LWIR	20	Surface temperature estimates
N	10.2 - 107	LWIR	20	Surface temperature estimates

Advanced Spaceborne Thermal Emission and Reflection Radiometer (ASTER)

ASTER, a cooperative effort between NASA and Japan's Ministry of Economy Trade and Industry (METI), incorporates three scanners to provide image data in 14 spectral bands identified in Table 1.3. ASTER has a 60-km swath width. ASTER’s LWIR bands can be used to estimate thermal rock parameters, albeit at lower spatial resolutions than those provided by MTI. ASTER’s ability to collect both nadir-looking and backward-looking images in band 3 of the same location on the same satellite pass facilitates the creation of digital elevation data directly from the spectral data. ASTER also has SWIR bands that were designed specifically to provide some rock and mineral discrimination capability.

Table 1.3 Spectral Band Characteristics of ASTER

Band	Wavelength (µm)	Description	GSD (meters)	Primary Purpose
1	0.52 - 0.6	Green	15	Vegetation reflectance
2	0.63 - 0.69	Red	15	Chlorophyll absorption
3	0.76 - 0.86	NIR	15	Nadir-looking; vegetation discrimination and vigor
3	0.76 - 0.86	NIR	15	Backward-looking; vegetation discrimination and vigor
4	1.6 - 1.7	SWIR	30	Vegetation and soil moisture
5	2.145 - 2.185	SWIR	30	Mineral and rock type discrimination
6	2.185 - 2.225	SWIR	30	Mineral and rock type discrimination
7	2.235 - 2.285	SWIR	30	Mineral and rock type discrimination
8	2.295 - 2.365	SWIR	30	Mineral and rock type discrimination
9	2.36 - 2.43	SWIR	30	Mineral and rock type discrimination
10	8.125 - 8.475	LWIR	90	Thermal
11	8.475 - 8.825	LWIR	90	Thermal
12	8.925 - 9.275	LWIR	90	Thermal
13	10.25 - 10.95	LWIR	90	Thermal
14	10.95 - 11.65	LWIR	90	Thermal

HYPERION

The Hyperion sensor collects image data over 220 bands with 30-meter GSD in the spectral range from 0.4 to 2.4 µm. It has a 7.6 km swath width. The sensor's spectral sampling of 10 nm allows for very detailed land cover classifications. Initial analysis from the EO-1 Science Validation Team indicates good results with mineral maps using the SWIR band data.

1.3 Data Exploitation Methods Developed and Tested in this Study

In reviewing the many needs identified in Section 1.1 and the capabilities of the space-based remote spectral sensors outlined in Section 1.2, we identified the following two areas on which to focus our development efforts. In addition, we report on other methods developed under other projects at SNL that have the potential to enhance the interpretation of remotely sensed data to aid a geologist's characterization of a remote site.

While other investigators have demonstrated the feasibility of estimating the apparent thermal inertia from day/night pairs of thermal imagery, we focused our attention on extracting thermal property data from a single image. The method requires the measurement of temperature differences near sun/shade boundaries to predict the thermal parameters of the surrounding rock. Toward this end, MTI provides 20-meter spatial resolution and incorporates design features to facilitate accurate surface temperature measurements. A region of the MTI imagery can thus be reasonably chosen within which a single rock type is present and a sun/shade boundary exists. A thermal model is then applied to predict the thermal response of the isolated rock type. Assuming a known set of rock parameters (thermal inertia, broadband emissivity, and diffusivity) and a known solar exposure history (based on the location, time of day, time of year, atmosphere, terrain), this theoretical model provides an estimate of the emitted surface radiance or corresponding surface temperature. Conversely, the rock parameters may be estimated from combined knowledge of the solar heating history and MTI-measured radiance. Specifically, we apply an optimization routine to estimate the rock parameters that minimize the mean-square difference between the MTI-measured temperature/radiance and the model-predicted temperature/radiance.

Previous investigators have successfully demonstrated the ability to exploit hyperspectral image data to identify minerals. The ASTER sensor has demonstrated an ability to detect some specific rock types from ratios of spectral features. We decided to investigate the feasibility of using multi-spectral data, which captures broadband spectral features and general spectral shape, to discriminate general categories of rock type. We identified seven general categories of rock type and selected representative laboratory spectrometer spectra from the ASTER hyperspectral database. We filtered the laboratory data to emulate MTI spectra and investigated the spectral separability of the classes using separability metrics. We tested a number of approaches to classify the data and measure the generalizability of the classification. We also investigated methods of feature selection to reduce the dimensionality of the classifier. Finally, we searched ratios of spectral bands to find those that yielded the best features for classification.

1.4 Report Outline

The remainder of this report describes the development and testing of the aforementioned methods. Section 2 describes our proposed method of remotely estimating thermal inertia using sun/shade radiance differences measured from multi-spectral data. Section 3 describes results of the rock type classification study, which examined the separability and classifiability of generic rock types based on their multi-spectral spectra. Section 4 describes a new robust spectral segmentation algorithm that identifies segments of spectrally similar pixels within a multi-spectral image. Section 4 also summarizes other remote-sensing tools useful in aiding the geologist in identifying geologic features such as drainage patterns and faults. Section 5 summarizes the results of the study as well as the methods developed and tested and provides recommendations for further investigations.

2 Thermal Inertia Estimation from Sun/Shade Temperature Differences

2.1 Introduction and Approach

The RemoteGeo LDRD team investigated a novel method to estimate thermal rock properties using MTI thermal imagery by exploiting the differential heating histories of pixels in the vicinity of shadows. Simulations using a one-dimensional heat transfer model with time varying boundary conditions (heat flux at surface) predict surface rock temperatures with significant differences (5-15 °C) as functions of local sunrise/sunset times and thermal rock parameters. The pixel-by-pixel sunrise/sunset times within a thermal image depend on the date of collection and the site's location and topography, which can be obtained from a digital elevation model (DEM). Estimating the thermal rock parameters (e.g., emissivity, reflectance, thermal conductivity and thermal capacity or equivalently thermal inertia and diffusivity) from the model requires an optimization code that searches the space of rock parameters to minimize the sum-of-squares difference between model-predicted temperatures and temperatures estimated from the MTI thermal bands over a number of spatial pixels. We have demonstrated feasibility of the optimization approach through simulation. Sensitivity analyses indicate that the method can produce reasonable rock parameter estimates even in the presence of measurement errors. The basic heat transfer model neglects the effects of moisture and vegetation. We applied the basic method to MTI thermal imagery collected from desert test sites where vegetation and moisture are minimized. The test results yielded limited success, probably because of the unmodeled factors. Field tests demonstrated the significant impact of even small amounts of moisture and vegetation. We developed some simple models for soil moisture and vegetation. While preliminary tests of these simple models show some promise, we recommend comprehensive evaluation and testing as follow-on to this study.

2.1.1 Definition of Thermal Inertia (TI) and Apparent Thermal Inertia (ATI)

The two basic physical properties governing the flow of heat in materials are: 1) heat capacity (c), which is the amount of heat energy required to raise the temperature of a substance by a unit temperature interval; and 2) thermal conductivity (k), which is the rate at which heat passes through a given thickness of material with a given temperature gradient. The governing equation for a one-dimensional heat flow is thus shown in Equation 2.1 in Section 2.3.1.

An additional thermal property that has been proved important, especially in thermal remote sensing, is thermal inertia (p), (Price [1977], Carlson [1986], Short and Stuart [1982]). This property is itself derived from the fundamental quantities of heat capacity, thermal conductivity and material density. It is typically written in the form $p = \sqrt{k\rho C}$, where the material's specific heat (C) is related to the density (ρ) and heat capacity(c) of the material by $c = \rho C$.

In general, thermal inertia defines the resistance of a material to a change in temperature for a given addition of heat energy. For example, surface materials with a high thermal inertia heated throughout a diurnal cycle will experience a smaller temperature change than will materials with lower thermal inertia. Due to the difficulty associated with remote determination of thermal inertia, the solution to Equation 2.1 is typically simplified by observing only the maximum temperature difference (ΔT) over a given diurnal cycle. Using this simplification, the temperature difference is related to an approximate form of thermal inertia referred to as the material's apparent thermal inertia or ATI. Specifically, ATI is given by:

$$\Delta T = K \frac{S(1-A_0)}{ATI},$$

where S is the solar flux incident at the surface, A_0 is the apparent albedo, and K is a scaling factor often set to one.

2.1.2 Rock Properties vs. Thermal Inertia

Apparent thermal inertia is affected by, among other factors, the mineralogy, porosity, and water content of the exposed surface of the rock mass. The rock mass porosity depends greatly on the natural porosity of the intact rock and the degree of fracturing of the rock mass. Thermal inertia has been demonstrated to be very useful in discrimination of geologic units (Pohn, et al. [1974]) and recent work by Podwysocki and Shellum (2003) has demonstrated that, for a given rock type, ATI can be correlated with variations of other physical rock properties such as density and porosity. A primary determinant of rock strength is the porosity of the rock. For a given rock type, therefore, it can be anticipated that an empirical relationship exists between rock strength, porosity, and ATI. Thus, the remote estimation of thermal inertia provides an important method of estimating key parameters for the determination of surface penetrability and weapons effects.

2.1.3 Traditional Remote Sensing Estimation of ATI

To date, most remote sensing measurements of thermal rock properties (in particular thermal inertia) have relied on measuring temperatures at a number of times during the diurnal cycle. It can be shown that ATI is related to the actual thermal inertia of a surface (Price [1977] and Carlson [1986]) through a Fourier expansion of the solar heating cycle. For purposes of simplification, only the first one or two terms are retained for calculations. This method has the advantage of simplicity; however it also neglects significant details regarding the heating and cooling history of the ground. Some authors have reported improvements in ATI using more detailed models (Sobrino, et al. [1998]); however, these techniques require both day and night images to estimate ATI. When using a sun-synchronous satellite such as MTI, the dates that these images are made are often necessarily separated by multiple days. Additionally, registration of such day/night image pairs may prove challenging. A simple method of obtaining the temperature difference of pixels in the same image, one fully illuminated all day and the other fully shaded all day, is presented in Section 2.8.2.

2.1.4 Model Estimation of Rock Thermal Properties

The DOE Multi-spectral Thermal Imager (MTI), with a 5-meter GSD in the visible and near-infrared (VNIR) and 20-meter GSD in the short-, mid-, and long-wave infrared (SWIR, MWIR, LWIR, respectively), has the potential to provide improved estimates of rock thermal properties. This depends on the exploitation of different heating histories of various pixels in a scene. Shading caused by adjacent rough topography gives rise to differential solar illumination heating of scene pixels.

Figures 2.1 and 2.2 show examples of the differential heating of a surface due to shading. Figure 2.1 is an MTI VNIR (false color IR) image taken over Manzano Base (the mountain peaks in the north center) close to Sandia National Laboratories at Kirtland AFB in New Mexico. The topography of the area is evident from the shadows in the image. Figure 2.2 shows the LWIR image (10.425 µm band N) of the same collection. Assuming a constant emissivity across the region, the darker LWIR pixels will correspond to regions with a lower temperature. For this image, these pixels also correspond to the shadowed ground samples made apparent in the false color VNIR image. The VNIR bands measure reflected solar radiance. The LWIR bands measure emitted thermal radiance of the ground surface. (The sun radiates negligible energy to be reflected in LWIR wavelengths.) Shaded pixels in the VNIR image correlate with colder pixels in the LWIR image because shaded regions have not warmed up as much as nearby pixels that are illuminated by the sun. In addition, the thermal profile in Figure 2.2 shows that the pixels to the immediate west of the shadow exhibit a temperature gradient consistent with the length of time since local sunrise. This observation suggests that we can use temperatures of the pixels near the shadow to estimate the heating rate of the corresponding rock. These estimates require calculation of the terrain-modulated solar illumination as a function of time for the relevant ground pixels.

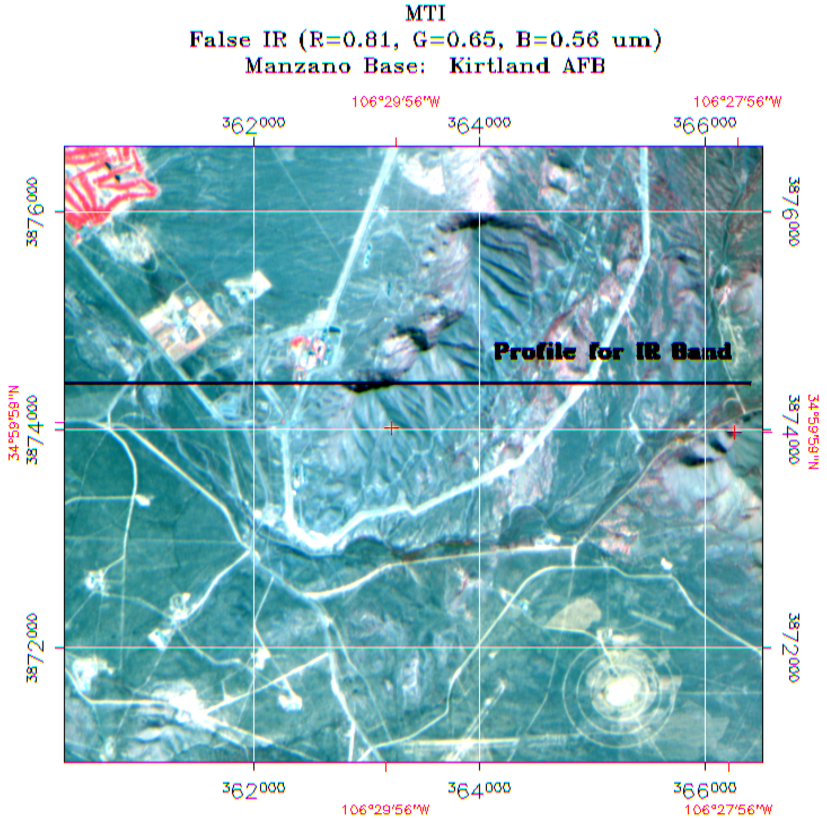

Figure 2.1 MTI Visible and Near IR image (false color IR) of Manzano Base area, Kirtland AFB

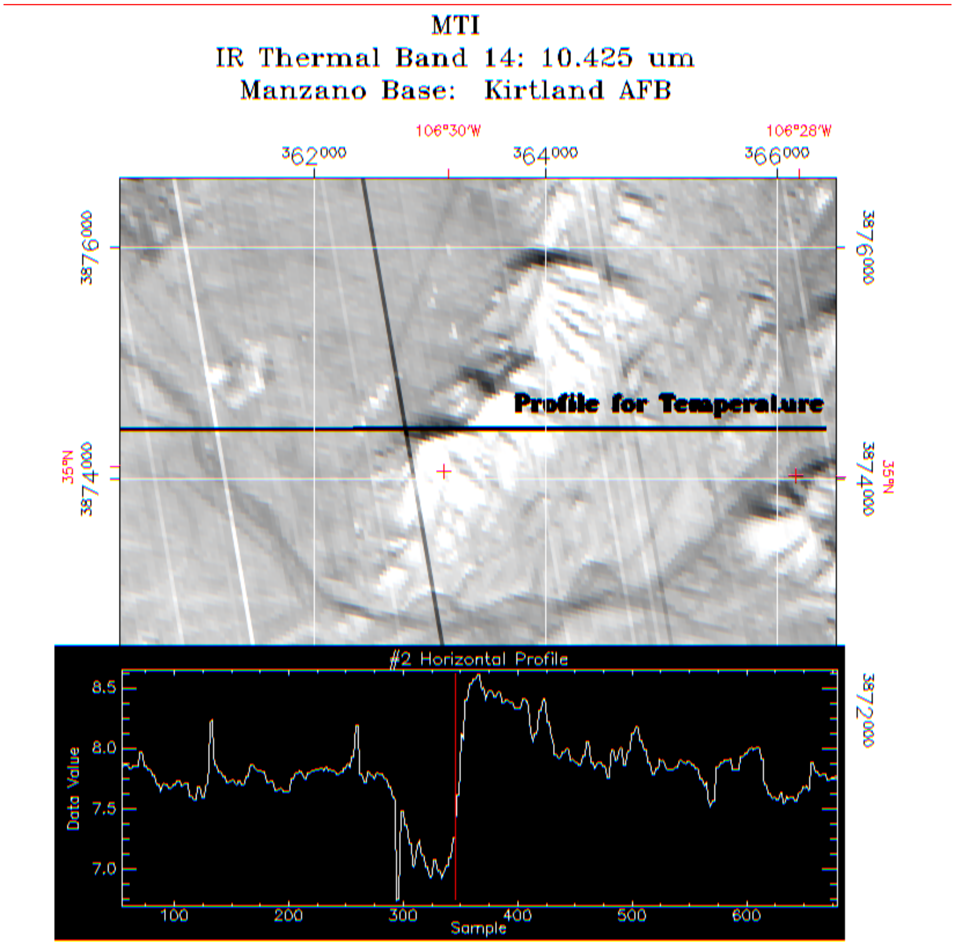

Figure 2.2 MTI Longwave IR (band N) of Manzano Base area

We apply a one-dimensional heat transfer model to estimate the thermal properties of the ground surface. The heat transfer model estimates temperatures of the ground given rock thermal parameters and time-dependent boundary conditions, primarily solar illumination, air temperature and wind speed. We calculate the solar illumination using a digital elevation model (DEM), which represents the local topography, and the solar ephemeris for the known location and date of the image. Finally, we apply optimization methods to search for the rock parameters that produce the smallest difference between the modeled temperature and the temperature measured from the thermal image for each pixel near the selected shadow.

Requirements:

- Single thermal image (with shadows) – high spatial resolution of MTI permits exploitation of shadows.
- Simulation of surface temperature as a function of rock properties (e.g., thermal inertia, heat capacity, thermal conductivity, porosity, reflectivity, and emissivity), solar illumination history, and weather (i.e., the IR Response code).
- DEM to provide times of sunrise and sunset for solar illumination history and surface normal of selected image pixels. (Implies a requirement that image be ortho-rectified to

match image and DEM points. Actually the requirement is that we can determine geographic coordinates in the image so we know which DEM points to use.)

- Atmospheric correction of image to provide surface radiance. In addition, we can use a “good” atmosphere as a better model than the climatology in the current code.
- Optimization of rock properties to match simulated and measured pixel temperatures or radiances.

Advantages:

- Needs only single day image (eliminating problem of matching day/night pixels for comparison and time lag between day/night collections).
- Emissivity can be estimated as part of optimization.
- Determination of actual thermal inertia, a physical rock property.

Disadvantages:

- Restricted to areas of differential heating histories; this implies a rough terrain to provide shading.
- Basic simulation models are valid for dry, bare rocks. Modeling moisture and vegetative cover can be difficult.
- Requires accurate ortho-rectification of image in rough terrain.
- Requires accurate atmospheric correction.
- Computationally intensive.

2.2 Digital Elevation Extraction from Multiple MTI Data Sets

2.2.1 Introduction

To be able to calculate the exposure history of each pixel at the time the image is acquired, a significant requirement for determining thermal inertia (TI) from a single image is an accurate Digital Elevation Model (DEM). The DEM extraction process traditionally uses a stereo pair of aerial photographs that are sequentially captured using an airborne metric camera. Standard DEM extraction techniques extend naturally to satellite imagery. However, the particular characteristics of satellite imaging can cause difficulties in extracting a DEM. The ephemeris of the spacecraft (with respect to the ground test site during image collection) affects the elevation extraction process. When the angle of separation between the stereo images is small, the extraction process typically produces measurements with low accuracy. A large angle of separation can cause an excessive number of erroneous points in the output DEM. Also, significant variations in topography can introduce occluded areas in the images, preventing elevation calculations in the blind spots. Extracting elevation information from three or more images registered to the same ground area may reduce these problems and improve DEM accuracy. The pointing capability of the Multi-spectral Thermal Imager (MTI) allows for multiple collections of the same area to be taken from different perspective views. This section describes work sponsored by the RemoteGeo LDRD and the MTI Data Exploitation Project to develop algorithms for extracting DEMs from multi-look MTI imagery. Follow-on work will develop semi-automated ENVI/IDL routines and interfaces that allow a user to select three or more MTI images of the same site and corresponding match points to produce an accurate DEM that matches the resolution and registration of the MTI imagery.

The DEM extraction process requires multiple images that are geometrically corrected and registered to the same ground location. Because MTI is a push-broom imaging sensor with pointing capabilities, wide variations in the satellite attitude can introduce very different image geometries. Furthermore, the push-broom motion changes the position of the sensor continuously during the collect. Thus, geometrically correcting and registering multiple MTI images to the same ground location presents a challenge. Because geometric correction is not a standard MTI data product, we developed a correction model for MTI to precede the cross-correlation, match-point selection, and parallax extraction steps. (Resampling used in the geometric correction process corrupts integrity of the spectral data.) We tailored the geometric correction model to supply parameters required by the elevation extraction process. Section 2.2.2 describes the development of the geometric model. Section 2.2.3 describes the point-matching algorithms. Section 2.2.4 describes the proposed method for extracting the elevation information. Also included are the intended methods for integrating the various algorithms to produce the final DEM product.

2.2.2 MTI Geometric Correction

2.2.2.1 General

Figure 2.3 shows a typical geometric correction model. The model defines line/sample mappings that resample the raw input data to produce the corrected output image. The algorithm produces not only the resampled image, but also a look-up table containing line-of-sight vectors for every pixel in the resampled image. The elevation extraction process can benefit from the availability of line-of-sight vector information. Figure 2.3 illustrates that creating the geometric model requires three separate files. In general, the geometric calibration file specifies a static camera model and contains all the interior orientation information. The housekeeping file contains specific image acquisition and exterior orientation information. The product parameters file contains adjustable parameters defining the desired output image coordinate system, such as ground sample spacing and map projection, as well as image processing parameters such as the selected resampling method.

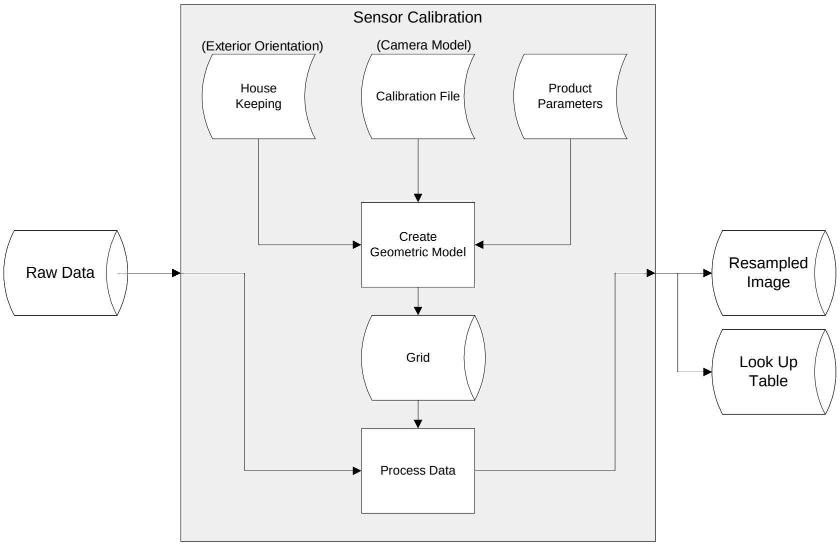

Figure 2.3 Geometric correction model

2.2.2.2 Interior Orientation

The most significant component of the interior orientation model is the field angle look vector for every detector on the focal plane. The MTI focal plane contains three staggered sensor chip assemblies, each containing 828 detectors per visible band. The visible band detector arrays are laid out in an odd/even manner in which the center point of the odd pixels is shifted by one pixel width in the positive along-track direction and the even pixels are shifted by the same amount in the negative along-track direction.

Because the DEM extraction process requires only a single band, we proposed selecting one of the first four MTI bands, A-D, because of their higher 5-meter spatial resolution. Because the 5-meter bands use linear silicon detector arrays, we considered both the silicon absorption sensitivity and the solar radiation in selecting the band with the strongest signal. The peak absorption wavelength of the silicon is approximately 0.96 µm; the peak transmission wavelength of the solar radiation model is approximately 0.49 µm. Combining the two models yields peak signal strength at approximately 0.65µm. Band C is the visible red band with a wavelength absorption range from 0.62 to 0.68 µm. To simplify the image registration and elevation extraction processes, we used band C only.

Figure 2.4 shows the band locations and SCA layout of the focal plane assembly. In addition to the detailed FPA design, engineers collected measurements from the focal plane after its construction. Using the measurement data, we generated an accurate (x,y) focal plane location for every detector in band C. To generate a look vector for every detector, we needed the position at which the telescope's optical axis would intersect the focal plane. During the telescope alignment process, engineers measured the angles between the optical alignment mirror and several specific detectors. We found the optical axis intersection location by triangulating between the angular measurements from the optical alignment mirror and the known focal plane distances between the specific detectors. We stored the distance between the measured focal plane center and the point of optical axis intersection as an offset in both the along-track and cross-track directions. Applying the offset to previously calculated measurements of every detector's location provided the (x,y) detector locations converted to the telescope's coordinate system.

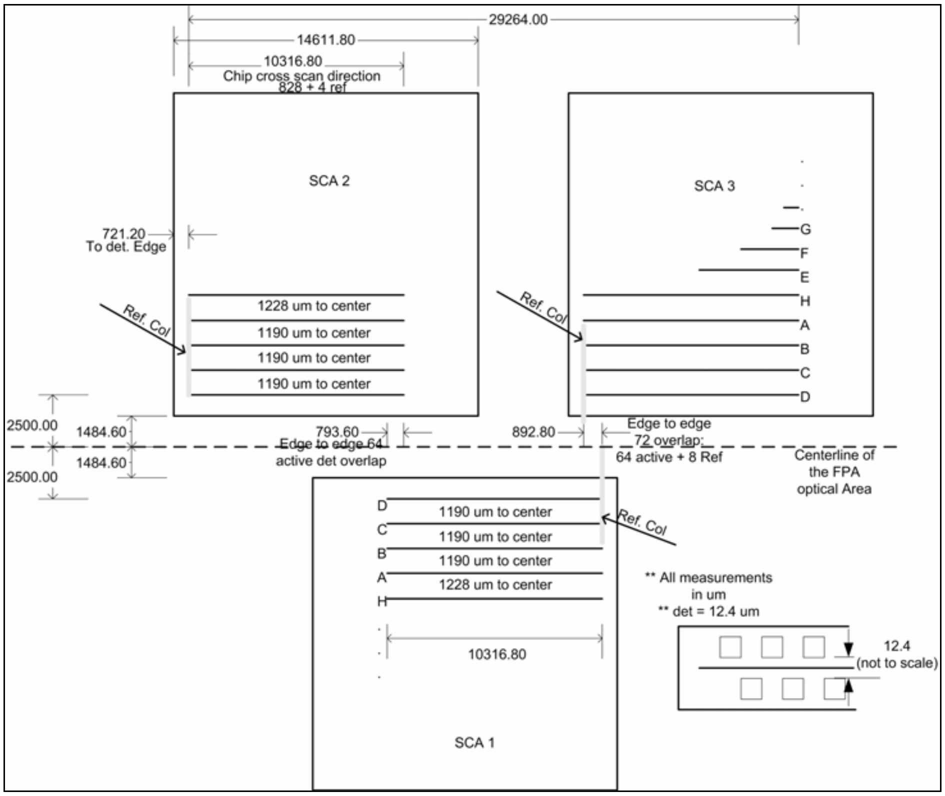

Figure 2.4 MTI focal plane detail

The telescope distortion model equations provide (x, y) focal plane locations (mm) from the relative focal plane center in terms of field angles (θ_x and θ_y) from the optical axis as follows:

$$Y = -23.773\theta_y - 0.36361(\theta_x^2+\theta_y^2) - 0.05176(\theta_x^2\theta_y+\theta_y^3) + 0.00001(3\theta_x^2\theta_y-\theta_y^3)$$
$$-0.00129(\theta_x^4+2\theta_x^2\theta_y^2+\theta_y) + 0.00151(\theta_x^4-\theta_y^4)$$

$$x = -22.498\theta_x - 0.3743\theta_x\theta_y - 0.05033(\theta_x^3+\theta_x\theta_y^2)$$
$$-0.00022(\theta_x^3-3\theta_x\theta_y^2) - 0.00214(\theta_x^3\theta_y+x\theta_y^3)$$

To apply the telescope distortion model to the detector locations, we solved for the field angles in terms of focal plane locations. We knew the (x, y) locations for all 2496 detectors in band C. Rather than invert the six-term polynomial, we applied an iterative least squares algorithm to solve for the distorted (x, y) field angle of every detector.

Figure 2.5 shows a plot of the actual versus nominal locations over the angular limits of the focal plane due to the telescope distortion. The gray bars in Figure 2.5 indicate the general locations of the band C detectors on all three SCAs. The close proximity of band C to the FPA center provides the additional advantage that telescope distortion effects are minimal.

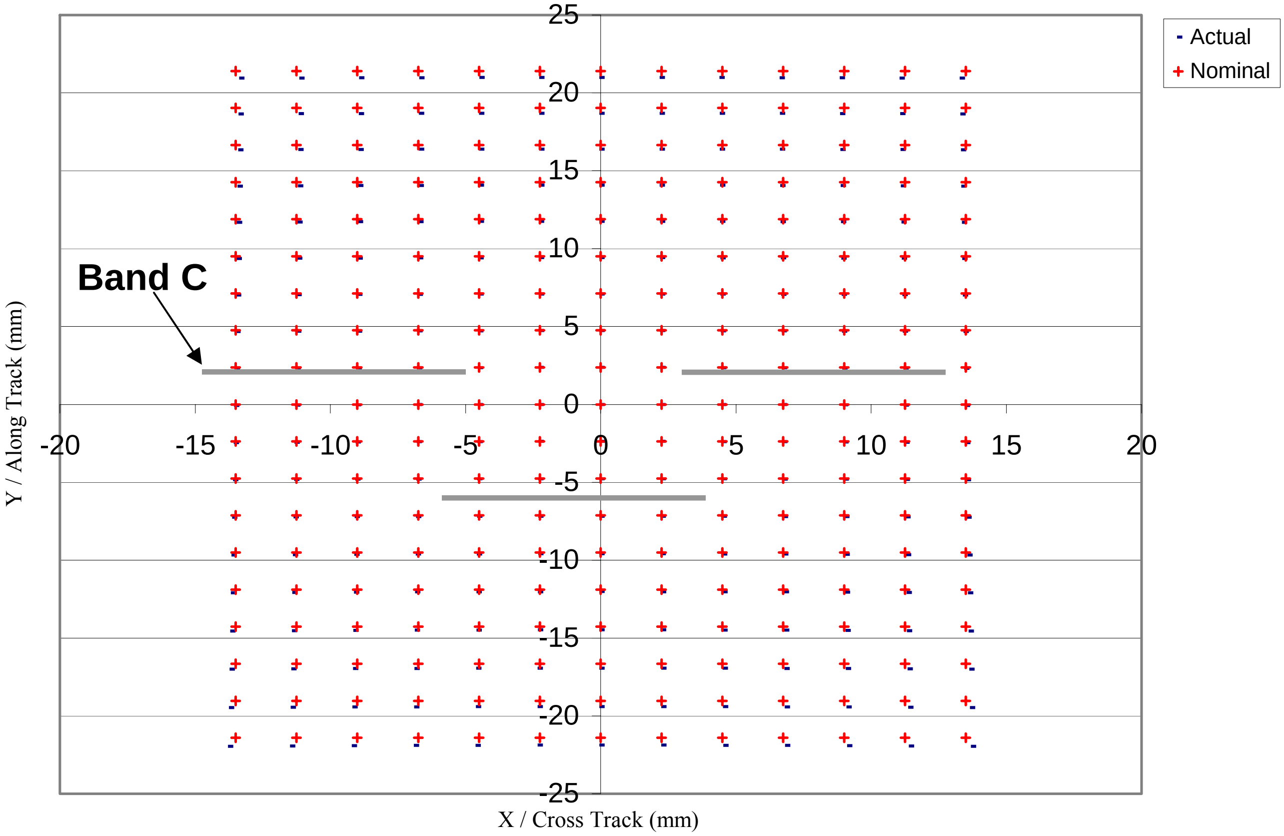

Figure 2.5 MTI telescope distortion plot

We needed timing information to complete specification of the interior orientation and we needed time-of-collection information for every detector. Because the SCA has a staggered layout, all pixels for a single band are not collected at the same time. Figure 2.4 shows that each band on SCA 2 and SCA 3 is located at the same along-track location and was collected at the same time. The matching band on SCA 1 would need an offset time to sample the same ground location. The satellite reports the times for both initialization and completion of the data collection. Data collections begin on SCA 2/3 at the band farthest from the FPA center, band L. Every other band is triggered by an offset from that initial time. We created a mapping to document the collection times for every line/sample in the image.

2.2.2.3 Exterior Orientation

In general, exterior orientation refers to a spacecraft model that describes the attitude and ephemeris throughout a given collect. An onboard GPS provides an accurate ephemeris of MTI with a maximum error of +/- 100 m in position and +/- 100 m/s in velocity. Unfortunately a gyro failure in December 2002 significantly decreased the accuracy of the attitude information available for the MTI satellite. The current pointing knowledge is accurate only within +/- 5 km. Accurate geometrical corrections require precise attitude knowledge, preferably across the entire collection. To work around this lack of information for MTI, we propose the following method of attitude estimation. We uniquely identify a feature in the image for which we have accurate latitude, longitude, and elevation information. Using the location and collection time of the detector that corresponds to the image feature as well as the satellite coordinates at collection time, we can calculate an accurate attitude. Every MTI collection specifies the desired coordinates of the target. We assume that the target can be identified visually and that the image contains the target, although perhaps not at the image center (i.e., pointing errors are less than +/- 7 km). Thus, we can deduce the attitude for at least one ground location. We can use more visually identifiable features with ground truth coordinates if they are available. We interpolate the attitude information over the entire image.

2.2.2.4 Product Parameters

Once we compute the attitude and ephemeris over the entire imaging interval, we combine them with the detectors' sample times to create a location and pointing map for every image point. We rotate the line-of-sight vectors from the camera coordinate system to the orbital coordinate system using the spacecraft attitude at each sample. We then map the line-of-sight vectors from the orbital coordinate system to an earth-fixed coordinate system using the spacecraft position and velocity at each sample. After mapping all image points onto the earth ellipsoid, we resample the image to regrid the data to a common ground sample distance and location. The product parameters file contains all of the information pertinent to the resampling function and the geometric regridding. After resampling, we run a correlation algorithm to identify stereo match points across the images. We store not only the resampled image, but also a lookup table of the line-of-sight vectors corresponding to every point in the resampled image. After match point identification, we extract elevation information using a ground-up space intersection technique described in Section 2.2.4.

2.2.3 Stereo Point Matching

The traditional method for identifying matching points in stereo images is a correlation-based approach that uses a shifting window. The location of the fixed-size window with the highest correlation value indicates the location of the match point. With the window cross-correlation method, we can construct a resolution pyramid, as shown in Figure 2.6. At lower resolutions (i.e., toward the top of the pyramid) we can measure the coarse shift information. The shift information from the top level provides a starting point for the next step down the pyramid, which has higher resolution. Using the resolution pyramid can both reduce the processing time and decrease the frequency of erroneous match points. The shifting window point-matching algorithm assigns one image to be the reference image and the other to be the target image, as shown in Figure 2.7. Although the shifting window correlation method does not yield high processor efficiency, it does allow for the use of previous knowledge. The capability of accepting lower-resolution information makes this method a good candidate for every level of the pyramid, with the exception of the top level. The method centers the search at the starting point provided by the previous level and can bound the search to reduce processing time. Without starting point information, the method centers the search at the same location in the target image as the center location of the window in the reference image. The major drawback to identifying match points with the window-based cross-correlation is processing time. In an attempt to increase processing efficiency, we have developed a second method—parallel-image correlation—to identify matching points. We implement the parallel-image correlation algorithm at the top level of the pyramid, where all matching points between the images are identified in parallel rather than calculating them one pixel at a time.

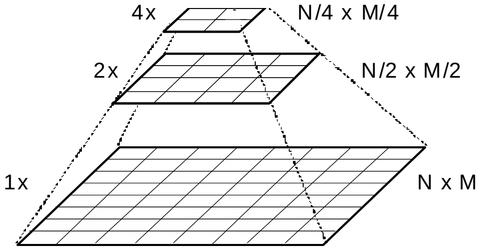

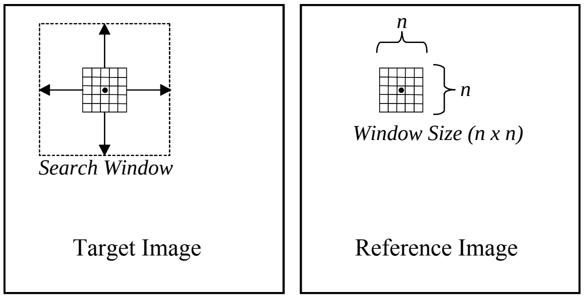

Figure 2.6 Resolution pyramid

Figure 2.7 Shifting window point matching

2.2.3.1 Parallel Image Correlation

The shifting–window algorithm performs many recurring multiplications. However, given an adequate amount of memory, we can implement image-sized matrix multiplications to eliminate redundant calculations. To identify the cross correlation value at every pixel, with no shift, the two images can be multiplied element by element. Convolving a normalized box filter with the multiplication result matrix produces the same result as the shifting-window method, provided that the window and filter sizes are equivalent. This calculation provides the correlation values at every location in the reference image with zero shift.

Figure 2.8(a) shows how the same calculation would be performed to generate the correlation values for a shift in both the x and y directions. The target image is shifted by all increments that would be covered by the search window from the shifting window algorithm. Each shift increment produces an image-sized matrix of normalized correlation values, at each pixel location, for the corresponding shift of the target image. As the calculation is performed at every increment, the result is stored in a three-dimensional array, as shown in Figure 2.8(b). In order to identify which shift value holds the highest correlation value (i.e., the best match) the three-dimensional array must be searched in the z direction at every (x,y) location. The z index of the maximum correlation value uniquely identifies the (x,y) shift amounts at that location.

Using typical window sizes and shift amounts, both algorithms have been benchmarked on images of various sizes. Holding all other variables constant, the parallel-correlation algorithm run time is, on average, 15% of the shifting-window algorithm run time. With such a drastic increase in performance, there is an inclination to entirely avoid the resolution pyramid and focus on only a single, full resolution, parallel correlation. However, using only the parallel technique requires a memory size of $(2*n+1)^2 * (x\text{-size}) * (y\text{-size})$, where n is the maximum expected shift. Using normal MTI dataset sizes with n equal to 25 requires approximately 73G of memory. Fortunately, if the images are resampled to the 4x pyramid level, all three variables are one-fourth the size, yielding approximately 300M of required memory.

Because the parallel-correlation method is computationally efficient for smaller images and because it requires no previous knowledge, it was a good candidate for point matching at the top level of the resolution pyramid. We conducted sample test data sets with both three and four pyramid levels, with the parallel correlation run at the top level, 4x and 8x, respectively. The tests revealed that the addition of the fourth level increased processing time but provided no improvements in point-matching accuracy. Thus, we implemented three-level pyramids. The top (4x) resolution level implements the parallel-correlation algorithm. The bottom two levels (2x and 1x) implement the shifting-window algorithm for which the coarse shift locations are inherited from the level above.

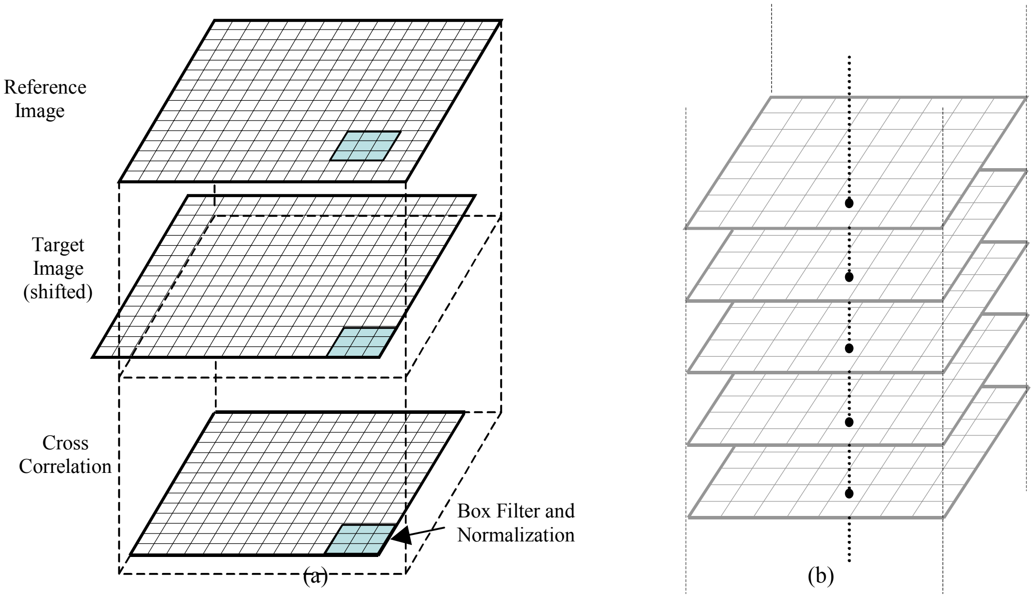

Figure 2.8 Parallel image correlation

2.2.3.2 Current Correlation Results

Because we had not yet fully implemented the geometric correction model, we ran initial correlation algorithm tests using sample data without geometric corrections or resampling. Off-nadir collections with no geometric correction introduce a strong bias in the match-point shift trends. In addition, the lack of geometric corrections and resampling precludes matching stereo images because of differences in pixel ground sample size.

As an initial proof of concept, we calculated the parallax between a single pair of stereo MTI collects. Figure 2.9(a) shows the corresponding surface plot. Figure 2.9(b) is a coarse estimate of the same ground coordinates cropped from a Department of Defense 100-meter Digital Terrain Elevation Data (DTED) set.

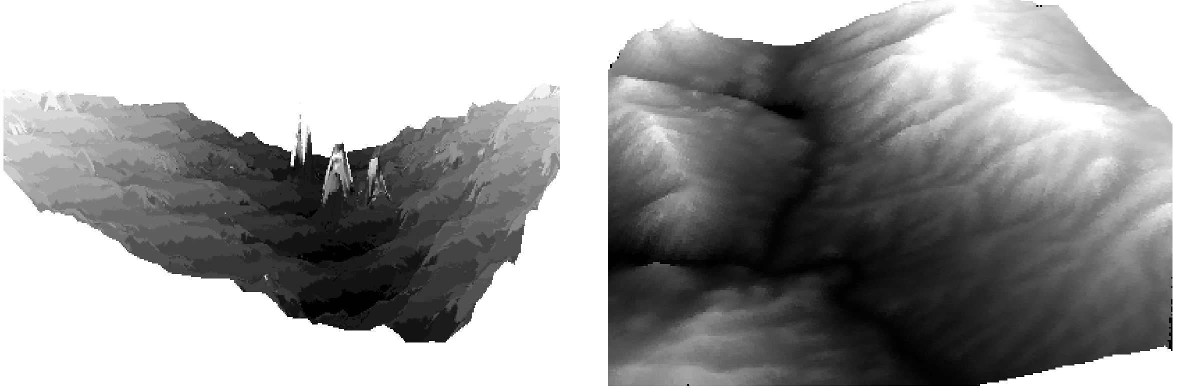

(a) (b)

Figure 2.9 Initial correlation results versus DTED surface plot

Without having the look vectors for every pixel in the image, we can calculate only relative elevation differences. Given all of the reasons that the simple correlation should fail to provide accurate elevation information, we are reassured to see that the general trend of the terrain is similar. The current approach includes no provisions for detecting and correcting erroneous match points. When the search produces an area of identical correlation values larger than the search window, the algorithm can not select the best match location. If multiple points exist with the same correlation value, the current algorithm will arbitrarily assign the location of the first occurrence. The noise found in the valley of Figure 2.9(a) is a result of such an assignment. To correct such errors, we propose to flag locations where multiple match locations are found and then interpolate across the flagged areas.

2.2.4 Elevation Extraction

The geometric correction process will produce resampled images that include a line-of-sight vector back to the spacecraft for every pixel location. If we convert the imaging geometry through multiple coordinated systems from the spacecraft to the ground, we can store the line-of-sight vectors in the ground coordinate system as look vectors. Projecting the look vectors onto the WGS84 ellipsoid surface facilitates using ground-up space intersection to estimate the elevation. Figure 2.10 shows that the two corresponding image points (X_1,Y_1) and (X_2,Y_2) can locate and identify the ground point (X,Y,Z). With the ground points projected onto the ellipsoid, the implicit elevation is zero. The look vector magnitudes are arbitrary and can therefore be rescaled such that the z component is equal to 1. If all look vectors are scaled in such a manner, we need to store only the (Δx, Δy) components of the vectors. Each image observation provides two equations relating the three unknowns (X, Y and Z). Using two matched images, the three variables can be solved for as follows:

$$Z = \frac{(x_1 + x_2)}{(\Delta x_2 - \Delta x_1)} = \frac{(y_1 + y_2)}{(\Delta y_2 - \Delta y_1)}$$

$$X = x_1 + \Delta x_1 \frac{(x_1 + x_2)}{(\Delta x_2 - \Delta x_1)} \qquad Y = y_1 + \Delta y_1 \frac{(y_1 + y_2)}{(\Delta y_2 - \Delta y_1)}$$

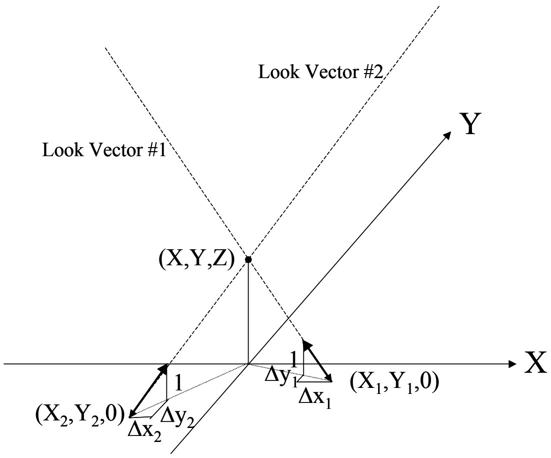

Figure 2.10 Ground–Up space intersection

Because of its pointing capability, MTI can collect multiple data sets of the same ground area from drastically different space coordinates. Traditionally, only two stereo images are used in the ground-up calculation. We propose to utilize three or more images to generate a denser, more accurate DEM than would be possible using only two images.

Multiple approaches are possible for extracting elevation from more than two images. The simplest approach would be to match all possible combinations of image pairs, treating each pair as a separate elevation extraction procedure. After extracting elevations from all the pairs, we can combine the multiple DEM to improve the accuracy over any given single pair. This implementation can become inefficient as the number of images increases. The number of image pairs grows quickly as the number of images increases. With three images there are only three combinations, but with five images, there are ten possible pair combinations. With a large number of images, many pair combinations may produce poor match points because of the drastic differences in look angles. To avoid the inefficiency of using every pair combination, we proposed a pair selection subroutine. The subroutine could use lower resolution copies of the original images to identify which pairs may be useful. Once the possible pairs are identified, we can apply the standard algorithm to full resolution images.

The second method for elevation extraction would use all of the images at one time rather than using one pair combination at a time. First, we identify one image, most likely the collect taken nearest to nadir, as the reference image. For each point in the reference image, we scan all of the other images for potential match points and calculate the elevation using all available match points, along with their previously stored look-up table. Not every image will contain a match point because not every point is visible from every collect angle. Thus, the space intersection algorithm must function using a variable number of points. If a match to the reference point exists in every other image, the appropriate algorithm would extend the standard two-ray space intersection to an N-ray intersection. Such ray intersection algorithms would be susceptible to noise spikes. To compensate for this susceptibility, we propose a disparity threshold to remove outlier rays during the space intersection routine.

2.2.5 Conclusions and Future Work

In summary, we propose a method for using three or more MTI data sets for accurate elevation extraction. We have developed and implemented multiple point matching algorithms for stereo image parallax determination. In follow-on work, after completing implementation and testing of the geometric model, we will examine sources of noise and test which point matching algorithm provides the highest accuracy. As a component of the geometric correction, we have developed a detailed interior orientation model of the satellite. We will continue to investigate methods of improving spacecraft attitude estimates for the exterior orientation model. When we complete the exterior orientation model, we will implement and apply the geometric correction model and conduct testing.

2.3 IR Response Model for Simulating Ground Temperature

2.3.1 Description of Original IR Response Code Model

As a preliminary step, we explored the feasibility of detecting measurable temperature differences from different rock types with different illumination histories. To do this, we applied a one-dimensional heat-transfer model code, called the IR (Infrared) Response Code, developed by Dykhuizen and Helmich (1994). The code numerically solves the one-dimensional heat-transfer partial differential equation subject to time-varying boundary conditions:

$$\rho C \frac{\partial T}{\partial t} = \frac{\partial}{\partial z}\left(k \frac{\partial T}{\partial z}\right) \tag{2.1}$$

or

$$\frac{\partial T}{\partial t} = \alpha^2 \frac{\partial^2 T}{\partial z^2} \tag{2.2}$$

where

ρ is the material density (Kg/m^3)
C is the material heat capacity (J/Kg•K)
k is the material thermal conductivity (W/m•K)
T is the Temperature Kelvin (K)
z is the depth (m)
t is time (sec)
α the diffusivity: $\sqrt{\frac{k}{\rho C}}$
p is thermal inertia: $\sqrt{k\rho C}$.

(The definition of diffusivity (α), as used here, is different than the conventional definition of diffusivity: $\alpha^* = k / \rho C$. This modified definition is used in our revisions to the IR Response Code and in presenting the results simulation and optimization. In the actual code, p and α are converted to k and ρC immediately on input.)

The model assumes two layers of (possibly) different materials with each layer divided into a (non-uniform) mesh or grid. The boundary condition at the bottom of the lower level, *z=D,* is the geothermal gradient (*G*).

$$k\left.\frac{\partial T}{\partial z}\right|_{z=D} = G = \text{Geothermal Gradient}. \tag{2.3}$$

The time-dependent boundary conditions at the surface are:

- Solar flux (absorbed),
- Thermal radiation (radiated and absorbed), and
- Convection transfers (dependent on air temperature and wind velocity).

The thermal flux at the surface is given by:

$$\left.\frac{\partial T}{\partial z}\right|_{z=0} = f\left(T_0,t\right) \tag{2.4}$$

with: $f\ \left(T_0,t\right) = f_{convection} + f_{IR\_radiation} - f_{solar}$

the solarflux is given by:

$$f_{solar} = N\alpha\left(A\frac{\left(C+\sin\beta\right)}{e^{B/\sin\beta}}\right) \tag{2.5}$$

N is Clearness number;

α is material solar absorptivity;

β is solar altitude (elevation) angle;

A is apparent solar irradiation at air mass zero ($\mathrm{W/m^2}$) , i.e. top of atmosphere;

B is the atmospheric extinction coefficient; and

C is the ratio of diffuse solar radiation on a horizontal surface to direct normal irradiation.

In applying this equation, we set $f_{solar} = 0$ if the solar elevation angle (β) is less than zero. If β is greater than zero but less that the horizon elevation angle (as determined by the topography and solar azimuth angle), we set $\sin\beta = 0$ so that only diffuse illumination is considered. *A, B,* and *C* are stored in a look-up table as a function of the day of the year, as listed in Table 2.1. Tabular values for *A*, *B*, and *C* used in the IR Response code from the ASHRAE Handbook are presented in Table 2.1.

Table 2.1 Solar Coefficients for IR Response Code*

Day of Year	Solar Declination	A	B	C
-10	-23.45	1416	0.142	0.057
21	-20.00	1415	0.142	0.058
52	-10.80	1401	0.144	0.060
80	0.00	1380	0.156	0.071
111	11.60	1356	0.180	0.097
141	20.00	1336	0.196	0.121
172	23.45	1325	0.205	0.134
202	20.60	1325	0.207	0.136
233	12.30	1337	0.201	0.122
264	0.00	1358	0.177	0.092
294	-10.50	1379	0.160	0.073
325	-19.80	1404	0.149	0.063
355	-23.45	1416	0.142	0.057
386	-20.00	1415	0.142	0.058

* **Note**: This table is a correction of the original. A mistake was found while using the above coefficient table that was traced to a verified mistake in the ASHRAE Handbook. This has been corrected in the IR Response Code.

Thus, the solar flux in this basic model depends on three simple broadband parameters. We have also included optional enhancements to the IR response code, one that accounts for the effects of non-horizontal surfaces, one that includes an amplitude-scaled generic MODTRAN estimate of the atmospheric transmittance (as described in Section 2.3.2) and one that includes a more site-specific MODTRAN estimate of the atmospheric transmittance (as described in Section 2.12). (As discussed below, we have modified the use of this formula.)

The sky radiation is given by:

$$f_{IR\_radiation} = \varepsilon\sigma\left(T_{sky}^4 - T_0^4\right) \tag{2.6}$$

where:

σ is Boltzmann constant (5.67e-8 W/m^{2}K^4),
ε is material emissivity, and

the sky temperature in Equation 2.6 is given by:

$$T_{sky} = T_{air}\left(0.8 = \frac{T_{dew}}{250}\right)^{0.25} \tag{2.7}$$

in which T_{dew} is dew point temperature (Bliss [1960]).

The air temperature is a simple sinusoidal:

$$T_{air} = T_{average} + \Delta T \sin\left(\pi \frac{t-8}{12}\right) \tag{2.8}$$

where:

$T_{average}$ is average air temperature (for a full day),

ΔT is half daily air temperature variation (i.e. amplitude),

the time t is such that t=0 is midnight, t=12 is noon.

The convected heat flux is given by:

$$f_{convetion} = h\left(T_{air} - T_0\right) \tag{2.9}$$

where h is convective heat transfer coefficient ($\text{W/m}^2\text{K}$).

From ASHRAE Handbook, 1989, p. 22.15, we have:

$$h = C'\left(\frac{2}{1.8\left(T_0 + T_{air}\right)}\right)^{0.181} \left(1.8\left|T_0 - T_{air}\right|\right)^{0.266} \sqrt{1 + 2.857V} \tag{2.10}$$

where C' is a constant depending on sign of temperature difference:

= 5.383 for $T_0 > T_{air}$

= 2.676 for $T_0 < T_{air}$

V is the wind velocity (m/sec).

The code accepts tabulated environmental parameters as functions of time. These optional tabulated parameters include time, air temperature, clearness number, dew point, solar flux and wind velocity. When only partial tabular data is available, the program uses the default formula to calculate the missing value. This feature facilitates the use of measured atmospheric weather data and/or solar radiation measurements, which improves simulation accuracy.

The code also requires inputs to specify the layer thickness, the grid or mesh spacing, and the time step size. Optional inputs include minimum and maximum length of simulation run-time and temperature accuracy tolerance. This temperature tolerance can stop a simulation run when the temperature at a fixed time of day is within the tolerance for subsequent simulation days. It also allows running a repetitive set of simulation days until the temperature at a certain time of day corresponding to an image collect time stabilizes, which minimizes effects of the initial conditions. However, using the temperature tolerance as a stopping criterion resulted in instabilities when using the thermal model with the Design Analysis Kit for Optimization and Terascale Applications (DAKOTA) optimization code, developed by M. S. Eldred, et al. at Sandia National Laboratories (Eldred, et al. [2002]). Our simulations ran for a fixed time, typically seven identical simulation days.

Equation 2.11 calculates the thermal radiation (irradiance) leaving the surface (*Lrad*).

$$Lrad = \sigma \varepsilon T_{surface}^{4} \tag{2.11}$$

This quantity more closely represents the radiation measured at the sensor than does the temperature. It also incorporates the emissivity parameter.

2.3.2 Modifications to IR Response Code

The original IR Response Code assumed that the surface was horizontal. In order to apply the code to real terrains, we modified it to account for non-horizontal ground samples, or pixels. The solar flux on the pixel is determined by the dot product between the incident flux and the surface normal. Section 2.3.2.1 describes the code modifications in terms of the angular definitions adopted. We also refined the contribution of the diffuse sky illumination term, which Section 2.3.2.2 describes. The IR Response code uses a simple atmospheric model that depends on a single extinction coefficient (*B* from Table 2.1) to represent the total vertical loss through the atmosphere. The extinction coefficient is integrated over both space and spectral frequency. Section 2.3.2.3 describes code modifications that incorporate a more complete atmospheric model, which includes spectral and spatial dependence.

To use the IR Response code with DAKOTA optimization, we needed to add the capability to do multi-pixel calculations and spectral band calculations. The objective function depends on the errors averaged over both multiple pixels and bands within pixels. Section 2.3.2.4 describes modifications for multi-pixel and spectral band calculations. We determined early in the simulations that using the variables thermal inertia and diffusivity rather than thermal conductivity and heat capacity as search or optimization variables gave superior results. This also required code modifications, which Section 2.3.2.5 describes. In addition, because DAKOTA needs variables scaled to the same order of magnitude, we modified the IR Response code to scale the input optimization variables, as described in Section 2.3.2.6.

2.3.2.1 Surface Normal

Initially let both vectors (incident flux and surface normal) be in polar form:

$$\bar{r} = \begin{bmatrix} x \\ y \\ z \end{bmatrix} = \begin{bmatrix} r\sin\theta\cos\varphi \\ r\sin\theta\sin\varphi \\ r\cos\theta \end{bmatrix} \tag{2.12}$$

where

θ is the polar (or zenith) angle (co-latitude or co-elevation) and

φ is the azimuth angle (counter clockwise from x = east);

then for unit vectors: $\bar{r} = \hat{n}$ (where subscripts refer to the two vectors)

$$\cos\Theta = \hat{n}_1 \bullet \hat{n}_2 = \cos\theta_1 \cos\theta_2 + \sin\theta_1 \sin\theta_2 \cos(\phi_1 - \phi_2). \tag{2.13}$$

In the present code, the solar angles are given as elevation $\beta = (90° - \theta)$ and azimuth from north $\phi = (90° - \varphi)$. For surface normal angles we use zenith angle and azimuth clockwise from north.

The notation for solar and surface normal angles is as follows:

ϕ = solar azimuth bearing (clock-wise from north);

β = solar elevation or altitude above horizon;

ψ = surface normal azimuth bearing (clock-wise from north); and

ξ = surface normal zenith (polar) angle, or tilt.

Let the subscripts be as: 1 => solar => sol, 2=>surface normal => surf

$$\begin{aligned} \theta_1 &= (90^\circ - \beta) \\ \varphi_1 &= (90^\circ - \phi) \\ \theta_2 &= \xi \\ \varphi_2 &= (90^\circ - \psi) \end{aligned} \tag{2.14}$$

$$\begin{aligned} \cos\theta_1 &= \cos\left(90^\circ - \beta\right) = \sin\beta \\ \cos\theta_2 &= \cos\xi \\ \sin\theta_1 &= \sin\left(90^\circ - \beta\right) = \cos\beta \\ \sin\theta_2 &= \sin\xi \\ \cos\left(\varphi_1 - \varphi_2\right) &= \cos\left((90^\circ - \phi) - (90^\circ - \psi)\right) = \cos\left(\psi - \phi\right) \end{aligned} \tag{2.15}$$

$$\cos\Theta = \hat{n}_{solar} \bullet \hat{n}_{surface} = \sin\beta\cos\xi + \cos\beta\sin\xi\cos\left(\psi - \phi\right) \tag{2.16}$$

As a check it is seen that for a horizontal surface, $\xi = 0$, $\hat{n}_1 \bullet \hat{n}_2 = \sin\beta$ as before.

2.3.2.2 Diffuse Illumination

As part of the flux incident on a surface, we must consider the diffuse contribution, which is the total irradiance coming from the sky that is not part of the direct irradiance. Let the direct-normal irradiance be given by I_{DN} following the notation in ASHRAE Handbook (1989). The diffuse irradiance falling on a horizontal surface is a fraction (*C*) of this

$$I_{diffuse} = CI_{DN} \tag{2.17}$$

If the surface is non-horizontal but rather has a surface normal zenith angle (or tilt) of ξ, only a fraction, F_{sky}, of the sky is visible from the surface (neglecting the part of the sky that is hidden by terrain (i.e., self shading only)). Thus the diffuse irradiance is

$$I_{diffuse} = F_{sky}CI_{direct} \tag{2.18}$$

where the fraction of the sky visible is (ASHRAE Handbook [1989])

$$F_{sky} = \frac{1 + \cos\xi}{2} \tag{2.19}$$

so that

$$I_{\;diffuse} = \left[C\left(\frac{1+\cos\xi}{2} \right) \right] I_{DN} \tag{2.20}$$

2.3.2.3 Atmospheric Effects

Now let us consider the transmission of the direct irradiance through the atmosphere. Let the incident radiation at the top of the atmosphere on a plane normal to solar direction be given by I_0. For vertical propagation (i.e., solar elevation of 90 degrees) the radiation at the surface (assumed to be sea level) is then $\tau_{vertical} I_0$ where $\tau_{vertical}$ is the vertical transmittance of the atmosphere (integrated over all wavelengths). The original code expresses this transmittance in terms of the atmospheric extinction (*B*) which is the sum of the scattering and absorption coefficients, $\sigma + \kappa$, integrated over all wavelengths. The transmittance is given by $\tau_{vertical} = e^{-B}$ or, for radiation incident from an *elevation* angle of β,

$$\tau(\beta) = e^{-B/\sin\beta} \tag{2.21}$$

Thus the total direct irradiance at the surface (on a surface normal to the solar direction) is:

$$I_{DN} = I_0 e^{-B/\sin\beta}\,. \tag{2.22}$$

2.3.2.3.1 Atmospheric Model

Notice that we have the following relationships for the transmittance $\tau_\alpha = e^{B/\sin\alpha}$ for any elevation angle α. Thus, denoting the vertical transmittance as $\tau_{vertical} = \tau$,

$$\begin{aligned}
&-B = \ln\tau = \sin\alpha \ln\tau_\alpha \\
&\ln\tau_\alpha = \frac{\ln\tau}{\sin\alpha} \\
&\tau_\alpha = e^{\frac{\ln\tau}{\sin\alpha}} = \left(e^{\ln\tau}\right)^{1/\sin\alpha} \\
&\tau_\alpha = \tau^{1/\sin\alpha}
\end{aligned} \tag{2.23}$$

In this formulation, with $\tau_\alpha = \tau^{1/\sin\alpha} = \tau^m$, *m* is identified as the “air-mass,” which is the ratio of the atmosphere transited relative to the vertical (air-mass of one). The above accounts for the non-vertical transmission. We extend the basic solar flux model when we account for the elevation above sea level of the pixel. This correction is given by:

$$m'(z) = m e^{-\frac{z}{z_{ref}}} \tag{2.24}$$

where

$m'(z)$ is the air mass at altitude z above sea level and

z_{ref} is the altitude at which the atmospheric pressure is reduced to $1/e$ of its sea level value (Campbell and Norman [1998]).

Care is required in using these formulations. To further extend the solar flux model, we use the atmospheric radiative transfer model MODTRAN (MODTRAN ([998]) to calculate the radiance, irradiance, transmittance, and other parameters directly from the site elevation and solar and sensor angles. See Section 2.12 for details on the atmospheric model.

2.3.2.3.1.1 Down-welling Irradiance

The total irradiance at the surface on a ground sample with surface normal $\hat{n}_{surface} = (\xi, \psi)$, illuminated by the sun in the direction $\hat{n}_{solar} = (\beta, \phi)$, is then given as**:**

$$\begin{aligned}
I &= I_{DN}(\hat{n}_{solar} \bullet \hat{n}_{surface}) + I_{diffuse} \\
I &= I_{DN}\left[\hat{n}_{solar} \bullet \hat{n}_{surface} + \left[C\left(\frac{1+\cos\xi}{2}\right)\right]\right] \\
I &= I_0 e^{-B/\sin\beta}\left[\hat{n}_{solar} \bullet \hat{n}_{surface} + \left[C\left(\frac{1+\cos\xi}{2}\right)\right]\right] \\
I &= I_0 e^{-B/\sin\beta}\left[\sin\beta\cos\xi + \cos\beta\sin\xi\cos(\psi-\phi) + \left[C\left(\frac{1+\cos\xi}{2}\right)\right]\right]
\end{aligned} \tag{2.25}$$

This is the general expression used in the modified code for non-horizontal pixels.

For a horizontal pixel, $\xi = 0$, this reduces to

$$I = I_0 e^{-B/\sin\beta}\left(C + \sin\beta\right), \tag{2.26}$$

which corresponds to Equation 2.5 of Dykhuisen and Helmich (1994):

$$f_s = N\alpha\left(A\frac{(C+\sin\beta)}{e^{B/\sin\beta}}\right) = N\alpha I \tag{2.27}$$

for the absorbed flux, f_s,

where

$$I = I_0 e^{-B/\sin\beta}\left(C + \sin\beta\right) = \left(A\frac{(C+\sin\beta)}{e^{B/\sin\beta}}\right) \tag{2.28}$$

2.3.2.3.1.2 Up-welling Radiation

The radiation received at the top of the atmosphere (TOA) is given by

$$L_{TOA} = \tau L_{surface} + L_{path} \tag{2.29}$$

where $L_{surface}$ is the radiation leaving the surface (either reflected (VNIR) or emitted (LWIR) or both), τ is the effective attenuation from the surface to the sensor and L_{path} is the path radiance, the radiation from the atmosphere arriving at the sensor (scattered for VNIR or emitted for

LWIR). All these quantities can be either spectral or broadband. As in the case for the down-welling transmittance, Equations 2.23 and 2.24, the up-welling transmittance is a function of the actual atmosphere and the geometry. If we are given the transmittance as a vertical transmittance at sea level, τ_{vert}, then the effective transmittance is

$$\tau = \tau_{vert}^{m} \qquad \text{with the air mass} \qquad m = \left(\frac{1}{\sin\alpha}\right) e^{-\frac{z}{z_{ref}}} \tag{2.30}$$

as in Equations 2.23 and 2.24 where α is the elevation angle of the sensor. In some cases the geometry of the air mass is not needed since the effective transmittance is given directly by the atmospheric model.

2.3.2.3.2 Atmospheric Corrections

Different types of atmospheric corrections are available in the modified code. These range from Type 0 in which the down-welling visible radiation is calculated as in the original code to Type 4 that includes a complete radiative transfer model of the atmospheric radiation. The types of correction are discussed here. The down-welling (visible and near IR) radiation which is used as a broadband flux boundary condition and the up-welling (usually LWIR), at-sensor, top of the atmosphere (TOA), radiation are handled separately in the code.

2.3.2.3.2.1 Type 0: None

This is the case of the original code. The broadband radiation down-welling radiation at the surface is calculated from Equation 2.25 and the coefficients are obtained from Table 2.1, the table of coefficients. Values for the coefficient *C* used in Equation 2.25 can also be specified as a spectral input variable. (It is available from atmospheric models.) If a negative value is specified on input, the value from the coefficient table is used.

The TOA radiance is just the surface radiance, i.e., no atmospheric correction.

2.3.2.3.2.2 Type 1: Up-welling: Average extinction

The down-welling radiation is as in Type 0. For the up-welling correction, we use

$$L_{TOA} = \tau L_{surface} + L_{path} \tag{2.31}$$

with τ given by

$$\tau = \tau_{vert}^{m} \qquad \text{with the air mass} \qquad m = \left(\frac{1}{\sin\alpha}\right) e^{-\frac{z}{z_{ref}}}$$

The value for the vertical transmittance is given by Equation 2.21 with the value of the extinction coefficient, *B*, obtained from the coefficient table, Table 2.1. That is, the transmittance in the LWIR is assumed to be the same as the average visible transmittance. This correction is used when no better estimates of the atmosphere are available.

2.3.2.3.2.3 Type 2: Up-welling: Vertical spectral transmittance input

For down-welling, this case is the same as Type 0. For up-welling radiation, it uses the same equations as Type 1. The difference is that rather than using the transmittance derived from the tabular coefficient *B,* we use vertical spectral transmittance given as inputs. The air-mass is determined from the geometry and location.

2.3.2.3.2.4 Type 3: Down-welling and Up-welling: MODTRAN air-mass zero

For down-welling, this case is the same as Type 0. For up-welling radiation, it uses the same equations at Types 1 and 2. The difference is that we use an effective input spectral transmittance directly. That is the air-mass is zero. This can be done when the atmospheric model, MODTRAN, gives effective values based on the location and elevation above sea level of the site and the geometry of the sun and sensor locations.

2.3.2.3.2.5 Type 4: Down-welling and Up-welling: MODTRAN

Note: This type is not implemented.

This is a general atmospheric correction using atmospheric model parameters for both down-welling and up-welling radiation. In the case of the down-welling, if the broadband irradiant flux is not directly available it must be calculated from the atmospheric parameters.

In addition to using model atmospheric parameters (assumed better than the climatology of Table 2.1) we can convert the measured at-sensor VNIR radiances to surface reflectances. This not only improves the rock classification but also can be used to calculate broadband absorption, which is used in the boundary value flux calculation.

2.3.2.6 Multiple Pixel Calculations

The original code was modified to allow for the calculation of temperature (and radiance) of more than one pixel on the ground. In this formulation of the code, each pixel is assumed to be of the same rock type; that is all the rock parameters are identical for each pixel. However the slope or surface normal of each pixel can be different, as can the times of local sunrise and sunset, resulting in differential heating histories**.**

2.3.2.7 Thermal Inertia & Diffusivity vs. Capacity & Conductivity and Scaling

In the original code, the only thermal parameters of the rocks are**:**

- Emissivity (ε),
- Reflectance (*r*),
- Thermal capacity (ρC), and
- Thermal conductivity (*k*).

We modified the input code to permit entries of thermal inertia (*p*) and diffusivity (α). The user specifies two of the four input thermal parameters: thermal capacity, thermal conductivity, thermal inertia, and diffusivity. From these, the code calculates the values of thermal capacity and thermal conductivity, which are then used as they were used in the original code. Because the optimization code needs to scale its optimization parameters to the same order of magnitude, the IR Response Code rescales its input parameters to physically realistic levels (see Section 2.6.2.1).

Relationships among Thermal Parameters

Definitions:

Conductivity k

Capacity ρC

Thermal Inertia P

Diffusivity α

$$\alpha = \sqrt{\frac{k}{\rho\, C}}$$

$$P = \sqrt{k\, \rho\, C}$$

Conversions: Calculate

Given:

	k	ρC	α	P
$k, \rho C$	•	•	$\sqrt{\frac{k}{\rho C}}$	$\sqrt{k\rho C}$
k, α	•	$\frac{k}{\alpha^2}$	•	$\frac{k}{\alpha}$
k, P	•	$\frac{P^2}{k}$	$\frac{k}{P}$	•
$\rho C, \alpha$	$\alpha^2 \rho C$	•	•	$\alpha\rho C$
$\rho C, P$	$\frac{P^2}{\rho C}$	•	$\frac{P}{\rho C}$	•
α, P	αP	$\frac{P}{\alpha}$	•	•

2.3.2.8 Broadband vs. Spectral MTI Bands

The original IR Response Code does not use spectral values but assumes all calculated quantities are spectrally integrated or “broadband.” For example, the top of the atmosphere solar constant (A in the coefficient table) is the integral over all wavelengths. The parameters of emissivity, reflectance, extinction (or transmittance), and radiance are interpreted similarly. We have modified the code to allow the use of average spectral values, which are the convolution of the spectral radiance with the normalized MTI band response. In some cases, we simply use the narrow band approximation as a substitute for the convolution. The code is able to accept either broadband or spectral data as input. Given spectral data, the input processing routine calculates the broadband average. For example, suppose MTI band spectral emissivities were input for a few thermal bands. On input, the broadband emissivity (which is used in the flux equations) is calculated as the average of the band emissivities. If broadband data is entered, the input processor assigns the broadband value to every spectral band to generate a flat spectral response. The usefulness of these conventions will become clear when we discuss the use of DAKOTA to estimate rock parameters using the IR Response Code

We have modified the code to allow the use of atmosphere parameters such as transmittance, path radiance, and diffuse radiation. The atmospheric modeling using MODTRAN is discussed more thoroughly in Section 2.12.

2.3.3 Summary of Model Limitations and Modifications

The original code was written to predict the temperature history of a flat area of soil subject to full sun all day long. It is a straightforward implementation of the Fourier heat transfer equation with time-variable boundary conditions. It assumes a two-layer soil, each layer of which can be set to different thermal properties. It is a strictly one-dimensional (vertical) model and does not account for horizontal heat transfer. It does not incorporate any consideration for moisture. The soil porosity is accounted for only in the thermal parameters of heat capacity and conductivity. It does not take into account any effects of vegetation such as transpiration or the effects of heat transfer at the surface due to vegetation. When used in the normal mode, the atmospheric and weather conditions are modeled based on historical climatology. (Actual weather can be simulated using tabular data input.) In addition, the code does not consider the spectral nature of radiation and it uses only broadband or spectrally integrated radiation measures.

We modified the code to correct for some of these limitations and to allow the use of spectral radiance to match the characteristics of a multi-spectral sensor such as MTI. We also incorporated means of exploiting advanced atmospheric modeling using radiative transfer, MODTRAN. We made a few structural changes to the code to implement our optimization concept using DAKOTA.

The effects of surface tilt and the illumination history introduced by surrounding terrain were modeled as discussed in Section 2.3.2.1. We have incorporated a simple soil moisture model (see Section 2.8), but have not exercised it extensively. We have also included the effects of the moisture content altering the thermal properties of the soil as a function of time. To date none of these additions have been verified and the code is not completely implemented. Our plan was to verify the bare dry-soil model before proceeding to the more complicated conditions.

We made a few modifications to the original code to allow for better interaction with a multi-spectral sensor. Rock and atmospheric properties, broadband or spectral, such as emissivity, reflectance, transmittance, path radiance, and diffuse radiance can be specified as inputs or used as optimization variables. We also transform between irradiance and radiance as needed. Thus, we can compute at-sensor spectral radiance, based on the model, when surface temperature and the atmospheric and surface properties are provided. Because multi-spectral sensors measure radiance, this allows a direct comparison of model-predicted and measured spectral radiance. We can also specify emissivity as an optimization parameter to estimate temperature and emissivity separately. Reconciling broadband and spectral measures was done in the simplest manner. If spectral properties are specified, we calculate the broadband properties by averaging. If broadband properties are specified, we calculate the spectral properties by assigning each band the same value of broadband property. Radiance is calculated as irradiance divided by π, thus assuming Lambertian surfaces. All conversions are done outside the basic heat transfer code and are essentially input/output unit conversions.

In the original code, the effects of the solar radiation and atmosphere were modeled using historical averaged data and the local solar ephemeris. These historical data include extinction coefficient (a measure of transmittance, assumed to be measured vertically at sea level), top-of-atmosphere direct solar broadband irradiance, and a strictly empirical “clearness factor.” Our enhancements to the basic model use improved atmospheric models. We consider the effects of “air-mass” to account for non-vertical radiation paths (both from the sun and to the satellite) and the site’s elevation above sea level. In some cases, the MODTRAN atmospheric transmittance estimates already include site and geometry effects.

The original code was able to use actual measured environmental data using an input table. Each entry is for a particular time and consists of the following parameters: time, air temperature, clearness number, dew point temperature, solar flux and wind velocity. Validation tests of the original code (Dykhuisen and Helmich [1994]) showed that including tabular inputs to define these parameters produce much closer matches to measured temperatures. If a particular tabular variable is not available, its value in the table is negative and its value is computed using the default code. We have not used this capability of the original code since such data will probably not be readily available for remotely sensed data. We attempted to maintain the tabular input capability but have not debugged any of our modifications using tabular input.

A simple—but important—change that we made was to provide for calculating the thermal response of multiple pixels. We assumed that a segmentation algorithm (such as the one described in Section 4.3), when applied to the spectral reflectance portion of the spectra, can identify regions of same-material pixels. Thus, each pixel in the region of interest is assumed to be of identical material and only its illumination, surface tilt, and altitude can be specified individually. These are derived from the terrain DEM and the solar ephemeris for the site. To date, the effects of using pixels of different rock types (through poor segmentation identification) have not been investigated. For each time step, temperature and at-sensor radiance were calculated for each pixel. In order to provide the DAKOTA optimization with an objective function to minimize, we calculated the root-mean-square of the difference between the measured sensor radiance (obtained from the image) and the predicted radiance (obtained from the model at the time of day corresponding to the sensor collect, using then current optimization variables) averaged over all pixels. A detailed description of the code and required support files is found in Walker (2003).

2.4 Sun/Shade Times from DEM

In order to account for the different heating time histories for different pixels we need some means of incorporating the times of sunrise and sunset (perhaps multiple) into the code. Initially the results were simulated using a simple “wall” or “ridge” model of topography. We also developed a program to calculate the times of sunrise and sunset of a particular pixel in a scene by using the DEM of the neighboring terrain.

2.4.1 Ridge Simulation

The simple model consists of an observation pixel and a ridge (or wall) extending from a peak of height z in a direction α with a slope of β. The observation point is at a horizontal distance, r, from the peak. The angle to the peak from the pixel is γ. The elevation angle, ξ, of the ridge (i.e. the horizon angle) as seen from the pixel in a direction θ (which corresponds to the solar azimuth) is given by

$$\tan\xi = \frac{\left(\frac{z}{r}\right)\sin(\alpha-\theta)-\sin(\theta-\gamma)\tan\beta}{\sin(\alpha-\gamma)} \tag{2.32}$$

All angles are measured counter-clockwise from east. In the temperature simulations, we assumed a ridge slope of zero (i.e. a constant height) and ridge directions of east-west and north-south. The above equation then simplifies to

$$\tan\xi = -\left(\frac{z}{r}\right)\sin\theta \tag{2.33}$$

for the east-west case and

$$\tan\xi = \left(\frac{z}{r}\right)\cos\theta \tag{2.34}$$

for the north-south case.

We modified the original IR Response code to calculate temperatures (on a horizontal surface) for a set of pixels located distances r_i from a ridge of constant height z (nominally taken as 3000 meters). We used a simplified solar ephemeris, in which a look-up table gives the solar declination for the Julian date of interest. We use the same geographic latitude for all the pixels. Time is local time. We run the simulation for each of the pixels in the set, which all have the same thermal rock parameters, but different solar histories because of their differing distances from the ridge. We run the simulation for a fixed time (nominally seven days) using identical days (e.g., the solar declination is not changed from day to day).

We pre-calculated the times of sunrise and sunset for each pixel based on the solar altitude and azimuth and the elevation angle of the horizon. We applied the sunrise/sunset times as a mask to set the solar flux to the diffuse value when the pixel was in the shade. Using sunrise/sunset times simplifies the data structures that characterize the pixel topographies. Thus, for a given image, a pixel is completely described by its thermal rock parameters (including emissivity and reflectance), its sunrise/sunset times (multiples are allowed) and its surface normal direction.

2.4.2 DEM Sunrise/Sunset Calculations

Under contract Research Systems Incorporated (RSI), the producers of the image processing software ENVI used in most of this effort, developed code for ENVI to calculate the times of sunrise and sunset for a selected group of pixels (a Region of Interest or ROI) in a scene. The calculation uses a DEM of the vicinity. In the initial version, the procedure is straightforward. It is assumed that the image and DEM are rectified to the same coordinate system. This is required to determine the location in the DEM (geographic coordinates) for each image pixel (in image coordinates). For a given pixel in the image, its DEM position is determined. For a fixed time steps the azimuth of the sun for the location and date of image collection is calculated. Given the azimuth of the sun at that time the elevation of the horizon, as determined by the DEM, is calculated. If the solar elevation is less than the terrain horizon elevation angle, the pixel is shaded. The time of sunrise is set when consecutive times result in shaded/non-shaded conditions. Time of sunset is similarly determined. These times of sunrise and sunset are then used in the calculation of solar illumination history in the modified IR Response code.

As might be expected the straightforward version of the sunrise/sunset code is inefficient and execution times are long. Subsequent versions should use better algorithms and modified to run on parallel processors.

2.5 Optimization to Estimate Thermal Parameters of Rock

2.5.1 A Method to Estimate Thermal Parameters

The initial study showed that different rock types subject to varying solar/shade histories produce measurable temperature differences at a particular time of day. In the following paragraphs, we propose a procedure to estimate the rock parameters using radiance/temperature information estimated from MTI thermal imagery. For a given set of MTI pixels, we predict the sun/shade history from the known collection time, solar ephemeris, and DEM of the local topography. With this predicted solar history and an initial estimate of the rock parameters, we apply the forward thermal model to predict the radiance/temperature of the surface rocks. We then apply an iterative optimization code to search for the set of rock parameters that minimizes the mean square difference between the model-predicted radiance/temperature and the MTI-measured radiance/temperature. The basic rock parameters considered are the thermal conductivity (k) and thermal capacity (ρC). Equivalently, we can determine the rock's thermal inertia (p) and diffusivity (α) or any combination of two of these parameters, from which the other two can always be calculated.

Two other rock parameters of interest are the emissivity and VNIR reflectance, which are both surface properties. Other researchers have conducted theoretical and experimental efforts to estimate absolute reflectance and emissivity from spectral radiance image data. The proposed procedure applies iterative optimization to estimate the reflectance and emissivity. However, we could also estimate emissivity and/or reflectance directly from the spectral radiance image and provide these estimated parameters as inputs to the optimization. Further study will help determine which approach produces the more accurate estimates of the bulk rock parameters.

Procedure:

1. Obtain one or more MTI images of the target area.
2. Obtain a DEM of the area (preferably using the MTI images).
3. Select regions of interest (ROI) in the image adjacent to terrain-induced shadows.
4. Apply robust spectral segmentation algorithms to MTI VIS, NIR, and SWIR bands to segment regions of spectrally similar materials within the ROI; assume that every pixel in a segment has the same rock parameters; and, from the shape of the reflectance spectra, predict the general class of rock type.
5. Perform radiance calibration and atmospheric corrections to estimate the VNIR reflectance and emitted thermal radiance (or, alternatively, temperature and emissivity) of each pixel in the ROI and, to improve estimation accuracy, minimize image re-sampling.

6. For all pixels in the ROI using the DEM, location, and date of image collection, calculate sunrise and sunset times.
7. For each rock type of interest, use DAKOTA optimization code to estimate the rock parameters that minimize the mean-square difference between the MTI-estimated thermal radiances and the thermal-model-predicted radiances.

To evaluate the feasibility of the proposed procedure for rock parameter estimation, we generated a simulated set of truth data. First, we assumed a set of true rock parameters and applied the forward thermal model to predict associated image pixel temperatures. We then applied Step 7 of this procedure to test the ability of the optimization procedure to estimate the true rock parameters from the simulated pixel temperatures. This approach tests the ability of the optimization procedure to approximate the inverse thermal model and accurately estimate rock parameters from simulated temperatures. Heretofore, we will refer to this approach as a simulated temperature test, which should produce rock parameter estimates identical to the true rock parameters input to the forward thermal model. This report describes the results of these simulations using both error-free simulated temperatures and temperatures with induced errors in a sensitivity analysis. The sensitivity analysis will aid in determining error bounds for Steps 1 through 6. In the simulations, we used model-predicted temperatures to simulate measured values.

2.5.2 Optimization Procedures

In Step 7, we applied the DAKOTA optimization software package, which is a general, integrated collection of optimization algorithms that facilitate rapid implementation of a wide variety of optimization problems (Eldred [2002]). The DAKOTA optimization process depends on a target function (e.g., the IR Response Code) with variable input parameters to generate the objective function. DAKOTA passes input parameters to the target function and the target function passes the computed objective to DAKOTA via text files on the computer disk. Thus, DAKOTA can maintain a loose connection between itself and the target code. Although DAKOTA has been designed to operate on parallel and multiple processor machines, its basic operation is best described sequentially. During each iteration, DAKOTA uses the current parameter set and the objective function output (which can be multi-valued) to estimate a new parameter set. The goal is minimizing the objective function (e.g., root-mean-square temperature errors). It passes the new parameters to the target function, which calculates a new value of the objective function and passes it back to DAKOTA. Iterative computation continues until the objective criteria are met. To minimize the objective, DAKOTA contains many separate optimization procedures ranging from steepest descent to genetic algorithms. In addition, it incorporates a variety of constraints. When tolerance criteria are met, DAKOTA halts the iterative optimization and outputs the parameter values corresponding to the minimum value of the objective function. However, many of the optimization methods can search for a local minimum only. We modified the IR Response Code to produce the following objective function at its output: the sum of square differences between the calculated temperature/radiance at each pixel (i.e., the rms value), given the input parameters and the true or measured temperature/radiance at the pixel.

There are three sets of inputs to the modified IR Response Code (called IR_Dak*, where "*" is a wild-card substituting for the various version names). The first input set describes the mechanisms of the simulation (e.g., time step, maximum simulation time, location, date, time of image collection, etc.). Also included in this group are any rock parameter values that: 1) we can estimate from another source, and 2) will not be modified in the optimization iterations. For example, if we can estimate reflectance from the MTI VNIR bands, we do not need to predict its value in the optimization, but instead can use the estimated value in the forward thermal model to predict the surface temperature. When available, atmospheric correction data is input. This set also includes a number of logical input variables that can change the behavior of each run.

The second input set includes the ground truth and measured data corresponding to each pixel in the region of interest. These are the measured temperatures (or radiances), sunrise and sunset times (based on topography), and surface normal direction. The third input set specifies those parameters that define the search space, which we call the discovery parameters or optimization variables. For our application, the discovery parameters comprise the unknown rock parameters to be estimated. During each iteration of the optimization procedure, IR_Dak reads the updated discovery parameters from the DAKOTA output file.

On execution, IR_Dak reads its inputs and calculates a temperature/radiance for each pixel by running a complete seven-day simulation. It extracts the predicted temperature from the seventh day at the time of image collection. It calculates the differences between the predicted temperatures and the measured temperatures for all pixels, computes the root-mean-square errors, and writes this out as the objective function. Other output files are optional. An echo file has the same format as the basic initialization file, which contains the first two sets of inputs. In the echo file, the predicted temperatures for the current iteration replace the input measured temperatures. Thus, if we input a set of true rock parameters corresponding to a particular rock type, the echo file will contain the predicted temperatures for that rock type.

We have written a few auxiliary programs to support the basic DAKOTA-IR_Dak optimizations. These aid in preparing input files for the sensitivity analysis and in computing sunrise-sunset times for the "ridge" simulation. A number of Perl scripts are available to prepare execution scripts and to handle the DAKOTA output files.

2.6 Simulation

2.6.1 Forward Model

We ran a number of IR Response Code simulations to determine whether variations in shading time histories and different rock types produced measurable temperature differences. Table 2.2 shows thermal parameters of a number of different soil/rock materials. We derived the values for thermal inertia and diffusivity from the known values for conductivity and capacity. A scatter plot of these parameters is shown in Figure 2.41. At the time these simulations were run, better values of these for individual rock types were not available. In these initial runs, we created a simple model to incorporate the effects of topography. This model is discussed in Section 2.4.

Figure 2.11 gives simulation results for granite (granite17 in Table 2.2) and dirt or soil (alldirt03 in Table 2.2) for pixels located north of an east-west ridge. (In all cases run to date, we have assumed that both layers allowed in the IR Response code are the same material.) In the simulation, we used 30° N latitude on 22 December and calculated temperatures every 0.01

hours. We simulated seven days to eliminate any residual effects of the initial conditions. The results in Figure 2.11 show that shading produces distinct temperature differences and that the two rock types produce significantly different temperature histories. While these results can be considered typical, we should note that the details of the temperature histories would be quite different for different latitudes, dates, and topographies. The differences in temperature between the rock types are sufficient to indicate the feasibility of the proposed approach. In addition, examination of the thermal imagery in Figure 2.2 shows that measurable temperature differences exist in terrain with shadows.

Initially we attempted to find some simple, empirical relationship between time-of-day or time-since-sunrise and the temperature of the different rock types. None was found. However, in light of the results of the “simple model” described in Section 2.8.2 we believe that it might be worthwhile to revisit this topic.

Table 2.2 Material Properties of Selected Rocks*

Reference	Material	Rock_ID	K = Thermal Conductivity	rho*C	P = Themal Inertia= sqrt (k*rho*c)	a = Diffusivity = sqrt (k/rhoC)
			k (W/m-K)	(J/m^3-K)		
ASHRAE	Marble	Marble01	2.60	2.28E+06	2.43E+03	1.07E-03
ASHRAE	Sand	Sand02	0.33	1.21E+06	6.32E+02	5.22E-04
Default IR Code	**"All dirt"**	**Alldirt03**	**0.52**	**3.60E+06**	**1.37E+03**	**3.80E-04**
Edwards, et al.	Earth	Earth04	0.52	3.77E+06	1.40E+03	3.71E-04
Edwards, et al.	Earth (wet??)	Earth_wet05	2.60	5.23E+06	3.69E+03	7.05E-04
Hillel	Clay (100%wet)	Clay_100wet06	1.60	2.90E+06	2.15E+03	7.43E-04
Hillel	Clay (50%wet)	Clay_50wet07	1.20	2.10E+06	1.59E+03	7.56E-04
Hillel	Clay (dry)	Clay_dry08	0.25	1.30E+06	5.70E+02	4.39E-04
Hillel	Sand (100%wet)	Sand_100wet09	2.20	2.90E+06	2.53E+03	8.71E-04
Hillel	Sand (50%wet)	Sand_50wet10	1.80	2.10E+06	1.94E+03	9.26E-04
Hillel	Sand (dry)	Sand_dry11	0.29	1.30E+06	6.14E+02	4.72E-04
Holman	*Granite*	*Granite12*	*1.70*	2.16E+06	1.92E+03	8.86E-04
Holman	*Granite*	*Granite12_LR*	*4.00*	2.16E+06	2.94E+03	1.36E-03
Holman	***Limestone***	***Limestone13***	***1.26***	**2.25E+06**	**1.68E+03**	**7.48E-04**
Holman	*Limestone*	*Limestone13_LR*	*1.33*	2.25E+06	1.73E+03	7.69E-04
Holman	*Marble*	*Marble14*	*2.08*	2.00E+06	2.04E+03	1.02E-03
Holman	*Marble*	*Marble14_UR*	*2.94*	2.16E+06	2.52E+03	1.17E-03
Holman	*Marble*	*Marble14_LR*	*2.94*	2.00E+06	2.42E+03	1.21E-03
Holman	*Marble*	*Marble14_UL*	*2.08*	2.16E+06	2.12E+03	9.81E-04
Holman	*Sandstone*	*Sandstone15*	*1.83*	1.53E+06	1.68E+03	1.09E-03
Holman	*Sandstone*	*Sandstone15_UL*	*1.83*	1.63E+06	1.73E+03	1.06E-03
Incropera	Clay	Clay16	1.30	1.28E+06	1.29E+03	1.01E-03
Incropera	**Granite**	**Granite17**	**2.79**	**2.04E+06**	**2.38E+03**	**1.17E-03**
Incropera	Limestone	Limestone 18	2.15	1.88E+06	2.01E+03	1.07E-03
Incropera	Marble	Marble19	2.80	2.22E+06	2.50E+03	1.12E-03

Reference	Material	Rock_ID	K = Thermal Conductivity	rho*C	P = Themal Inertia= sqrt (k*rho*c)	a = Diffusivity = sqrt (k/rhoC)
Incropera	Sand	Sand21	0.27	1.21E+06	5.72E+02	4.72E-04
Incropera	**Sandstone**	**Sandstone22**	**2.90**	**1.60E+06**	**2.16E+03**	**1.35E-03**
Incropera	Soil	Soil23	0.52	3.77E+06	1.40E+03	3.71E-04
Kreith	Limestone (dry)	Limestone_dry24	0.69	1.55E+06	1.03E+03	6.68E-04
NIST	Water	Water25	0.56	4.22E+06	1.54E+03	3.64E-04
Incropera	Quartzite	Quartzite20	5.38	2.92E+06	3.96E+03	1.36E-03

Suffixes LR, UR, UL indicate range of values.

* From: Yocky and Dykhuizen (1993)

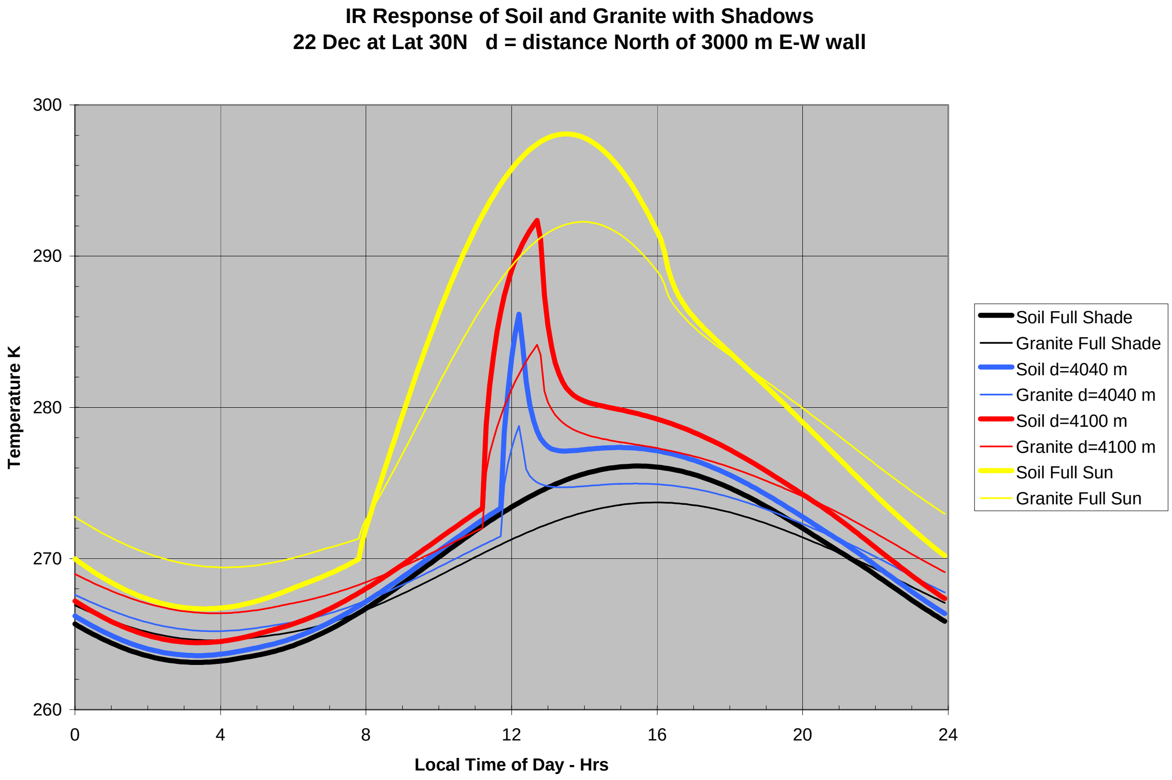

Figure 2.11 Simulated temperatures for full sun and full shade: granite and soil

2.6.2 Noiseless Optimization Methods

This section describes the results of simulating temperature data from a set of true rock parameters and testing the accuracy and sensitivity of the proposed optimization procedure for estimating the true rock parameters from the simulated temperature data.

The first set of runs exercised DAKOTA-IR_Dak with only two rock discovery parameters—conductivity and capacity. We assumed that emissivity and reflectance were known. We assumed a set of true rock parameters from Table 2.2 and applied the forward thermal model to simulate the corresponding measured temperatures for a set of 16 pixels located various distances north of an east-west ridge, a location of 30°N on 22 December, a 11:30-a.m. collection time and a seven-day simulation length. With the simulated temperatures as input, we applied DAKOTA-IR_Dak to estimate the rock parameters and compare the optimized k and ρC to the assumed truth values. DAKOTA requires an input file to specify the optimization parameters, which include the desired optimization method, the names, initial values, and optional minimum and maximum constraints of the variables to be optimized, as well as various optimization control parameters, which have reasonable default values.

We first used a nonlinear least-squares Gauss-Newton procedure from the OPT++ package. For detailed information on algorithms, see the DAKOTA Users' Manual and the DAKOTA Reference Manual (Eldred, et al. [2002]). We tried both unconstrained and bound-constrained (i.e., maximum and minimum limits on the variable) runs. The Gauss-Newton procedure failed to converge for many initial points, producing a large final objective value.

As an alternative, DAKOTA developers recommend using the Fletcher-Reeves conjugate gradient algorithm with bound constraints from the CONMIN package. Without bound constraints, DAKOTA can give IR_Dak physically meaningless values (e.g., negative thermal conductivity) that violate the physical model. This model proved successful and is the main one used to date.

2.6.2.1 Parameter Scaling

We also discovered a need to scale the optimization variables. To ensure proper operation of the optimization algorithms, we must scale all of the variables to the same order of magnitude. DAKOTA does not do its own scaling. Without scaling, estimating the granite parameters (e.g., $k = 2.79$ and ρC = 2.038E+06) prevented ρC from changing much during a run. Thus, we allowed DAKOTA to estimate $\rho C/10^6$ and required IR_Dak to scale the parameter value up by 10^6. Then we scaled all optimization parameters accordingly. (Note: Many of the accompanying figures, graphs, and tables present the scaled values rather than the actual values.)

2.6.2.2 Parameter Choice: Thermal Inertia

When the optimization routine converged properly with small objective function values and gradients, it still produced estimated values for k' and $(\rho C)'$ that varied widely from the truth values, k and ρC. However, we found that $\sqrt{k'\rho C'}$ closely matched $\sqrt{k\rho C}$. Thus, the optimization correctly estimated the TI of the rock, which is $\sqrt{k\rho C}$. We also found that the optimization correctly estimated the rock diffusivity $\sqrt{\frac{k'}{\rho C'}} \approx \sqrt{\frac{k}{\rho C}}$, but with much higher errors than those corresponding to TI estimates. These results led to an investigation of the error surface.

DAKOTA has a parameter-study mode that facilitates examining the error surface of a function. If $f(x_1, x_2, \cdots)$ is the value of a function (in our case temperature) for true values, $x_1, x_2, \cdots$ and $f'(x'_1, x'_2, \cdots)$ is the value at estimated parameters $x'_1, x'_2 \cdots$, then

$F(x'_1, x'_2, \cdots) = \left(f(x_1, x_2, \cdots) - f'(x'_1, x'_2, \cdots)\right)^2$ is the error surface of the function *f*. *F* is also the objective function used. (We often use the equivalent root-mean-square (rms) measure where the average is over the set of pixels.) We calculated the error surface for a specific rock type for the estimated parameters *k'* and $\rho C'$. The surface has a deep trough located approximately along a line $p = \sqrt{k' \rho C'}$. Figure 2.12 shows this error surface and the curve of constant thermal inertia.

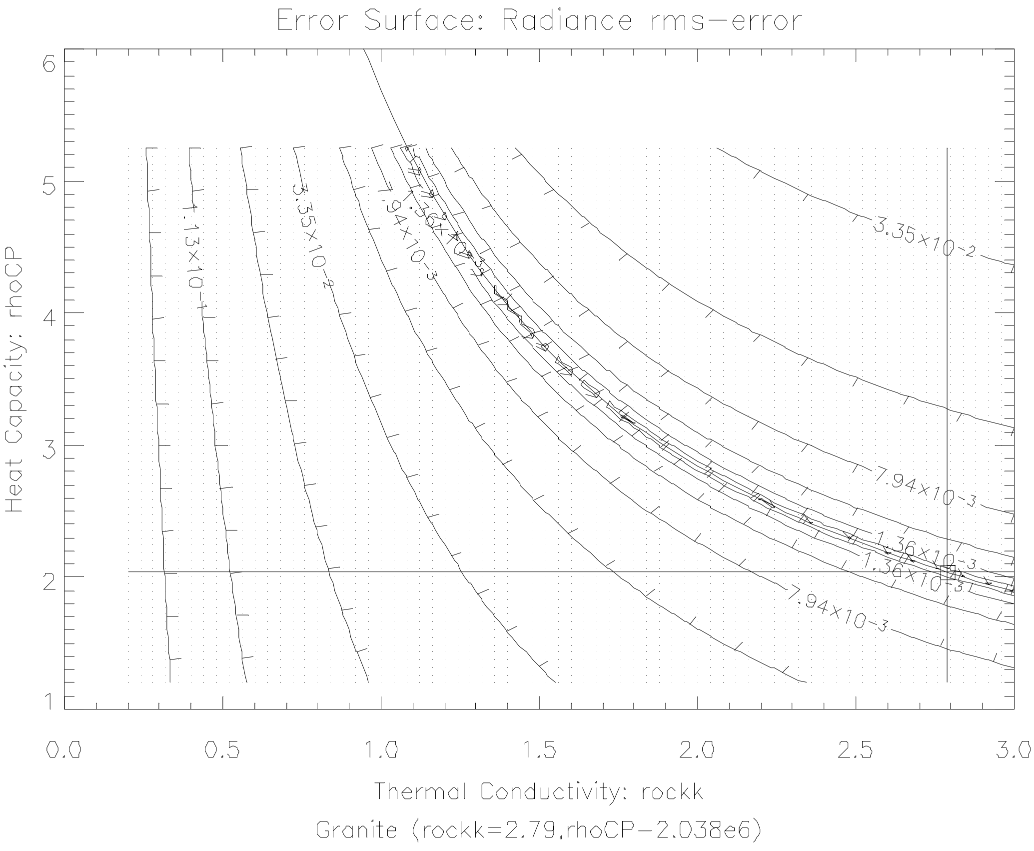

Figure 2.12 Error Surface: Thermal Conductivity vs. heat capacity.

(curve in trough is $\rho C = \frac{p^2}{k}$)

The CONMIN algorithm is a gradient descent algorithm, which can find only local minima. Thus, it will converge within the trough and produce correct estimates of thermal inertia, but has difficulty estimating accurate values of thermal conductivity and heat capacity independently because the gradient of the error surface along the trough (line of nearly constant thermal inertia) is small. A major criterion for the optimization procedure CONMIN to halt is a small gradient. It thus has difficulty in "following" the trough to the absolute global minimum. The error surfaces for the variables thermal inertia, *p*, and diffusivity, α, (Figures 2.13 and 2.14) are more well behaved in the sense that the gradients near the minima are much stronger along one direction (the thermal inertia axis) than in the perpendicular direction (the diffusivity axis). This structure of the error surface in thermal inertia vs. diffusivity suggests that the gradient descent algorithm will give better results for thermal inertia than for diffusivity, which has been demonstrated by the results to date.

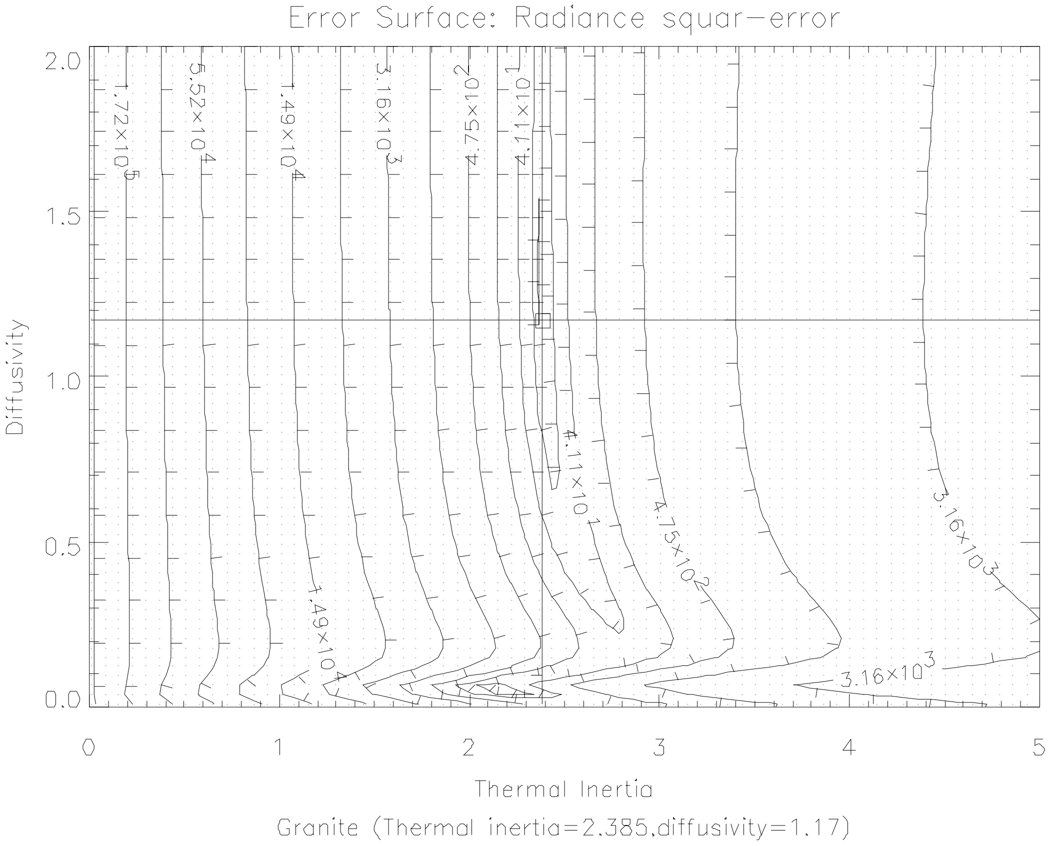

Figure 2.13 Error surface: thermal inertia vs. diffusivity; granite

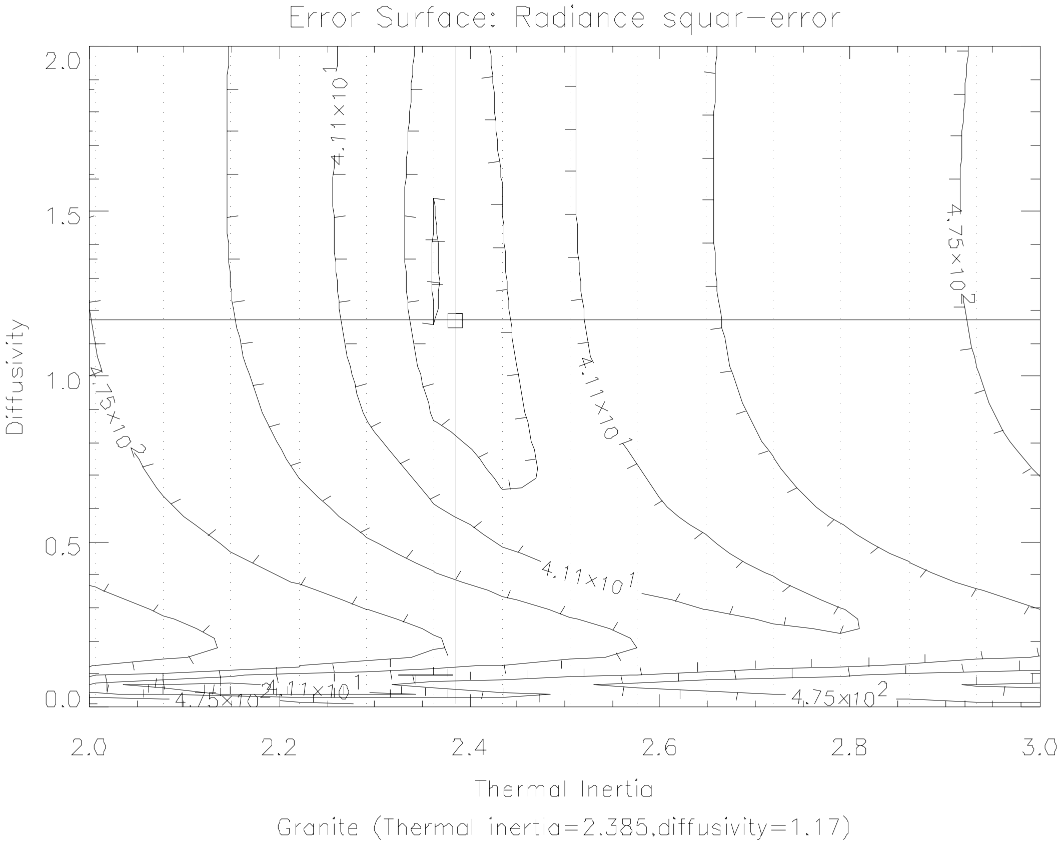

Figure 2.14 Error surface: thermal inertia vs. diffusivity; granite (expanded view)

2.6.2.3 Emissivity

An objective function based on the sum-square temperature error requires that we extract temperature estimates from the MTI thermal images. However, estimating the temperature from the thermal imagery also requires estimating the emissivity, which is difficult at best. Because emissivity is a rock property, this suggests that we can include emissivity as an optimization variable and calculate radiance (using Equation 2.11 or Planck's Law Equation 2.102 in Section 2.12) to be used in an objective function. Thus, we use the basic IR Response model, with input optimization variables of emissivity and, say, thermal inertia and diffusivity, to calculate surface temperature. We then convert temperature to spectral radiance (Planck's Law) and correct this to produce an at-sensor radiance. This model radiance is compared to the radiance measured at the sensor to calculate the objective function. We used the direct temperature objective function in the initial stages of our investigation but soon switched to using radiance-based measures.

When we applied DAKOTA-IR_Dak with a temperature-based objective function to estimate emissivity, thermal inertia and diffusivity of two surface materials, alldirt03 and granite17, from a number of initial estimates that uniformly spanned the bound parameter space, the worst case errors (relative err = (true-calc)/true) were as follows:

Emissivity error= 6.5e-06
Thermal Inertia error= 5.0e-03
Diffusivity= 1.4e-02

Thus, with no-noise temperature measurements, applying DAKOTA-IR_DAK with a temperature-based objective function can accurately estimate emissivity and thermal inertia. A plot of the initial and final estimates for optimization with a temperature-based objective function shows that the final values cluster tightly around the true values. An error surface of emissivity vs. thermal inertia, for a case in which the optimization variables were these two plus diffusivity is shown in Figure 2.15. Similar results were obtained using radiance and other rock types from Table 2.2.

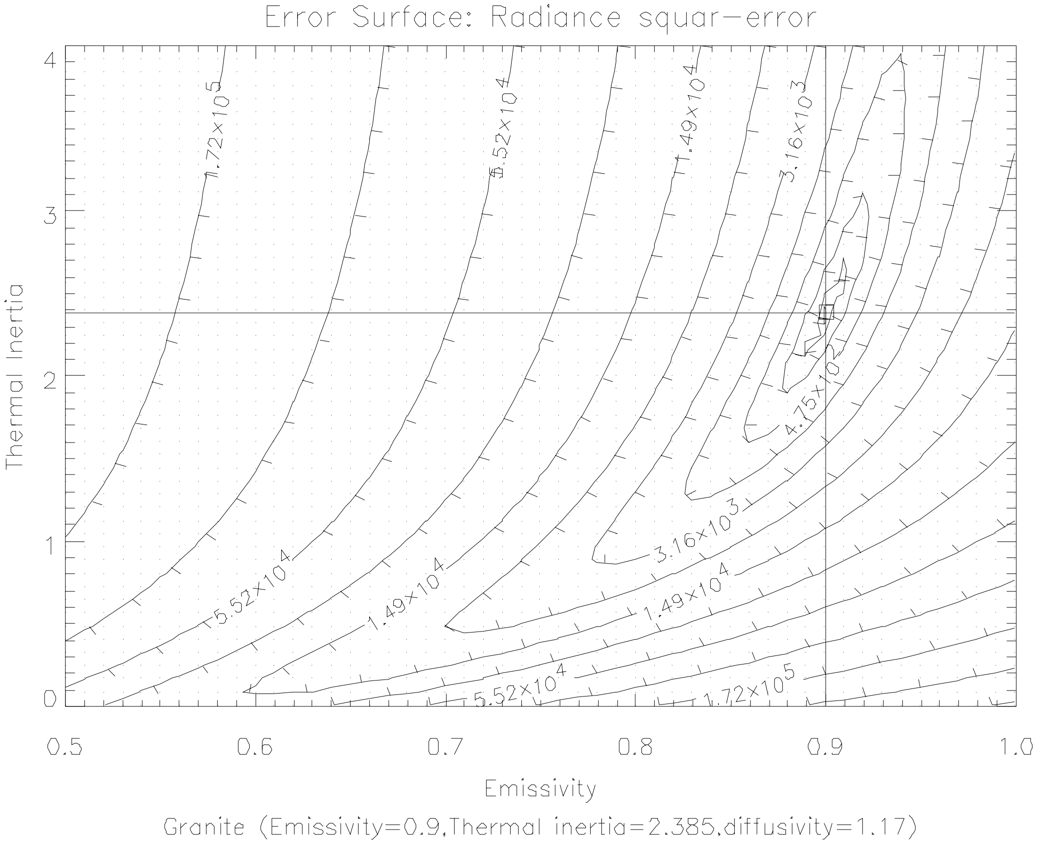

Figure 2.15 Error surface: emissivity vs. thermal inertia; granite

2.6.2.4 Summary of Initial (Noiseless) Rock Parameter Estimation Using Optimization

We use the term “noiseless” here to distinguish the case in which all of the parameters that are not used as optimization parameters are the same values used to compute the “measured” values. In addition, these “measured” values are not perturbed in any way. This is distinguished for the “noise” case discussed below in the sensitivity analysis.

Heat capacity and thermal conductivity error surface formed a trough in which the locus of minima formed a power-law curve closely matched to

$$\rho C = \frac{p^2}{k} \tag{2.35}$$

where p is thermal inertia. Optimization runs would thus result in different $(\rho C, k)$ pairs; however, the pairs fell on a well-defined curve that defined a constant thermal inertia.

Thermal inertia and diffusivity should therefore be used as parameters. The thermal inertia minima were all the same. The "trough" in the error surface was along a line of constant thermal inertia with the diffusivity having a very broad minimum. (As an interesting observation, the early results of the NASA Earth Heat Capacity mission led to substituting thermal inertia rather than heat capacity as the best property to measure remotely (Short and Stuart [1982]).

Noiseless simulation results were excellent. We obtained very low rms errors (i.e., objective function) in temperature and radiance and small errors in optimization parameters.

As part of the simulations, we experimented with using irradiance rather than temperature as the basis of the objective function. As part of this experiment we also included emissivity as an optimization variable. Using irradiance in the objective function measure yielded accurate simultaneous estimates of emissivity and thermal inertia, which obviated the intermediate step of estimating the surface temperature and emissivity directly from the measured at-sensor radiance. Even when the objective function depends on irradiance, the internal IR Response model calculates the temperature so that it is available, if needed.

We conclude that the objective function should depend on irradiance rather than temperature and that the optimization should include emissivity as one of its search variables. The objective function is the rms difference between the model-predicted radiance and the measured radiance, which is averaged over a number of pixels with different heating histories. Thus, spectral radiance, measured at the sensor and corrected for atmospheric effects, is the best basis for the objective function.

2.6.3 Sensitivity

2.6.3.1 Approach

We developed the following sensitivity analysis to investigate the theoretical performance limitations on the process of applying optimization code to estimate the thermal rock parameters from image-derived temperature estimates. The sensitivity analysis establishes the expected parameter estimation errors in the presence of temperature measurement errors. For example, errors in estimates of the measured temperature, T, induce errors in estimates of thermal inertia, p. The sensitivity function, $\frac{\Delta p}{\Delta T}$, depends on Δp, the error in thermal inertia, and ΔT, the temperature error. Temperature measurement error sources include such errors in MTI imagery as:

- Sensor noise,
- Sensor calibration,
- Atmospheric correction errors, and
- Errors in simultaneously estimating emissivity and temperature.

In addition, geometric errors in the DEM can lead to errors in calculating the local sunrise and sunset times as well as the surface normal directions of ground samples. These errors naturally propagate to errors in temperatures and radiances predicted by the IR Response code. Also, the procedure assumes that all pixels in a particular segmented region near a shadow have identical thermal parameters. However, even with MTI's high spatial resolution, it is likely that some segmented regions and some ground samples will contain more than one rock type.

Further errors can occur if we violate the assumptions of the IR Response Code. To date, this investigation has considered only a single type of rock as a function of depth. The IR Response Code allows for two layers of different rock parameters. The model neglects the effects of ground moisture and vegetation in the simulations and image analysis. (We added a simple moisture model to the IR Response Code but have not fully implemented or tested it.)

A complete analysis of all these error sources is beyond the scope of this effort but a limited investigation is important. We will characterize the rock parameter errors as functions of temperature and radiance errors. We can also use the IR Response Code in a forward calculation to predict the errors in temperature/radiance induced by the other errors such as DEM position or elevation errors.

We considered the effects of bias errors and random noise separately. A bias error is an offset from the true value of a measurement. We applied bias errors identically to each pixel in a segmentation set. For random noise, we generated random samples from a normal distribution centered at the true value of the measurement for each pixel. Bias calculations were deterministic and could be calculated readily. Random variations required multiple runs to establish statistical validity.

2.6.3.2 Methodology

We have written an auxiliary program to facilitate the sensitivity investigation. In it, we incorporated provisions to vary the following predicted values:

- Temperature (measured),
- Radiance (measured),
- Position (offset positions of a pixel in topography), and
- Times of sunrise and sunset..

We can vary these predictions individually or simultaneously. However, temperature and irradiance are closely related though $Lrad = \sigma\varepsilon T_{surface}^4$, and position and sunrise/sunset times are also related. This sensitivity analysis program reads the standard initialization file and a sensitivity parameter file. This auxiliary file contains a bias and standard deviation for each of the sensitivity terms, as well as logical control variables. It writes an echo file that is a copy of the initialization file with the value of the sensitivity variable changed. For example, it will echo the temperature for sensitivity runs as $T_{sens} = T_{orig} + T_{bias} + T_{std\_dev}$, where

T_{sens} is the modified temperature for input to the DAKOTA-IR_Dak run;

T_{orig} is the original measured temperature;

T_{bias} is a bias term; and

T_{std_dev} is a random temperature from a zero mean normal distribution with variance as specified.

The code uses similar formulas for varying the other predicted values. After varying the position values, we applied the sunrise/sunset program to generate corresponding variances in the sunrise/sunset times.

2.6.3.3 Bias Results

We have completed two types of optimization simulations investigating temperature bias errors. These include optimizations for a set of three discovery parameters and for a set of four discovery parameters, designated as 3epa and 4erpa with the optimization discovery parameters as follows:

3epa => emissivity, thermal inertia and diffusivity with reflectance fixed at 0.4
4erpa => emissivity, thermal inertia, diffusivity and reflectance

We applied optimization runs to estimate both parameter sets for four rock types: alldirt03, limestone13, granit17 and sandstone22 (parameters shown in Table 2.2). Figures 2.16 through 2.20 show the relative parameter errors (calculated as (true-model)/true) and corresponding objective functions as functions of temperature bias for the 3epa case. Figures 2.21 through 2.33 include the 4erpa case and comparisons between the two. The data are presented in a number of ways to emphasize significant points. For example, in Figures 2.16 through 2.18, we plot relative errors and objective functions vs. temperature bias on a linear temperature scale. In Figure 2.17, the objective function is plotted on a logarithmic scale to emphasize that the objective function increases rapidly from very small values corresponding to small biases as the temperature bias increases. In Figure 2.18, the signs of the parameter errors are emphasized to show their correspondence with the sign of the bias.

Figures 2.19 and 2.20 show the absolute value of the relative errors or objective functions vs. biases on a logarithmic scale. The lines connect points with the same sign (+ or -) before the absolute value was taken. We concluded that temperature bias errors in excess of 1K lead to unacceptable errors in rock parameters. The effects of *noise* errors were not so great as shown below.

Figures 2.16 through 2.19 show that, when the temperature biases are high, the objective function is large. Figure 2.33 shows the direct relationship between parameter errors and objective function. Thus, for these experiments, highly biased temperatures yielded high objective functions, implying that there are no solutions that are physically consistent with the thermal model. There are no rock parameters that produce the biased temperature distributions. The large objective value suggests that the input temperature values are invalid.

Figure 2.24 shows effect of the bounds of the parameters. For example, when the emissivity value reaches 0.999, its upper bound, a relative error of 0.1 (10%) results. Relative error might not be a good measure in this case.

Guided by Figures 2.16, 2.17 and 2.33, we propose a possible procedure for correcting temperature biases in the no-noise case. A high objective function value at the end of an optimization indicates the possible presence of a temperature bias. The relationship between temperature bias and objective function is shown in Figures 2.17 and 2.18. This indicates a distinct minimum value of objective function for a particular bias. We could include the temperature bias as a discovery parameter in the DAKOTA optimization. The optimization would produce a small objective function only when the temperature bias estimate is accurate. After estimating the temperature bias, we would apply the bias to the temperature measurements and run the optimization to estimate the rock parameters more accurately. If random noise is present but acts independently of the bias, then the proposed procedure may allow bias estimation even in the presence of noisy temperature measurements. When we apply this procedure to estimate atmospheric interferences, such as up-welling IR path radiances from the atmosphere, we apparently improve performance. See Coyote Canyon results below.

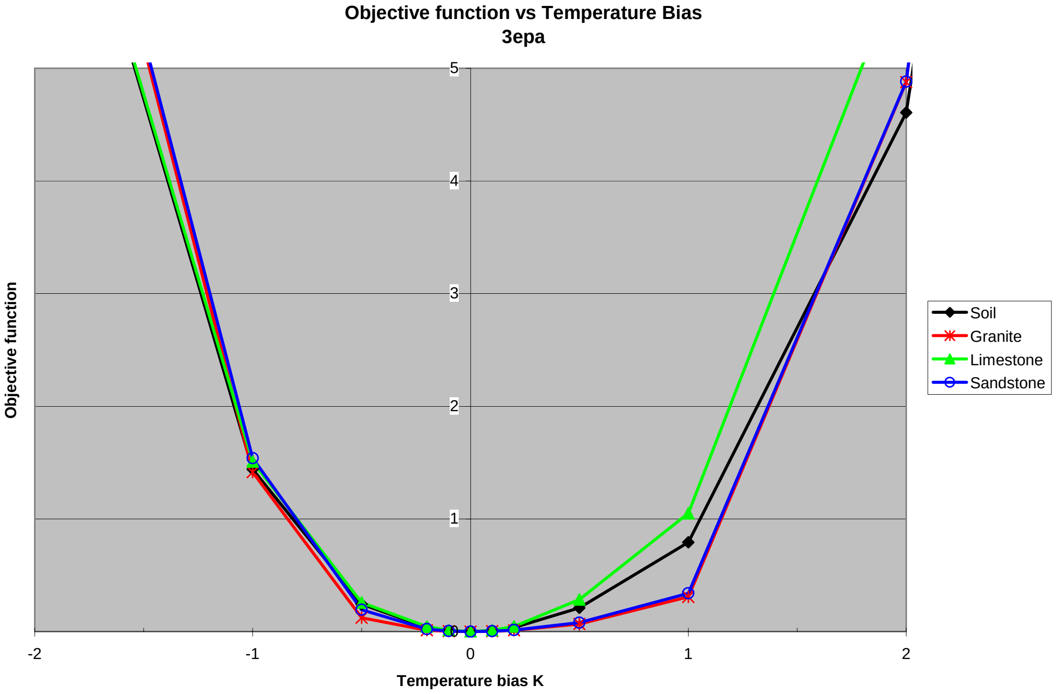

Figure 2.16 Temperature bias: Objective functions for different rock types (linear scales)

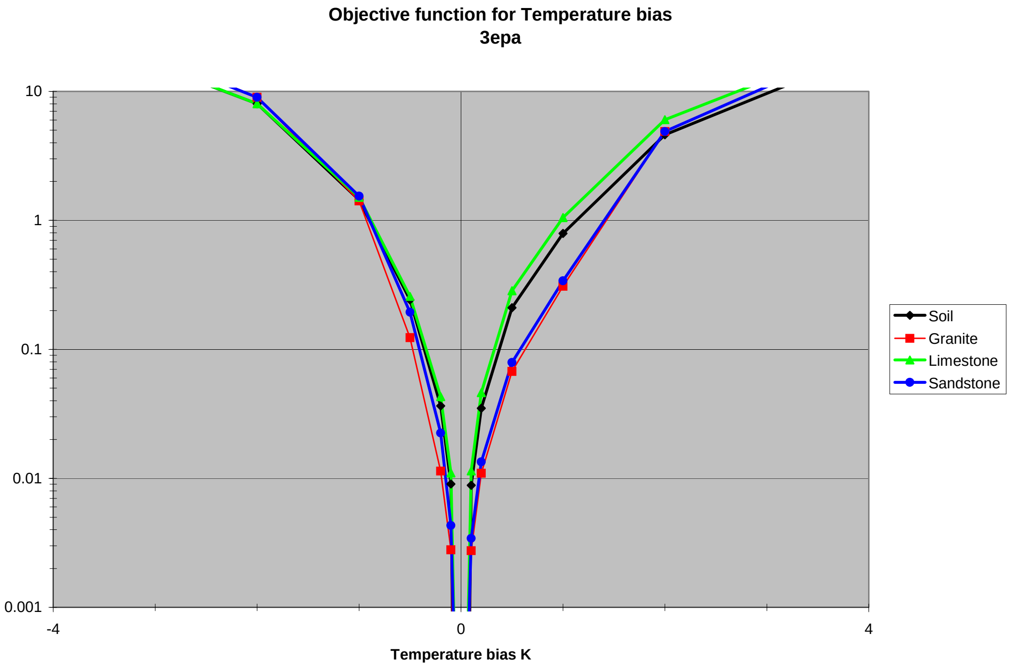

Figure 2.17 Temperature bias: Objective function

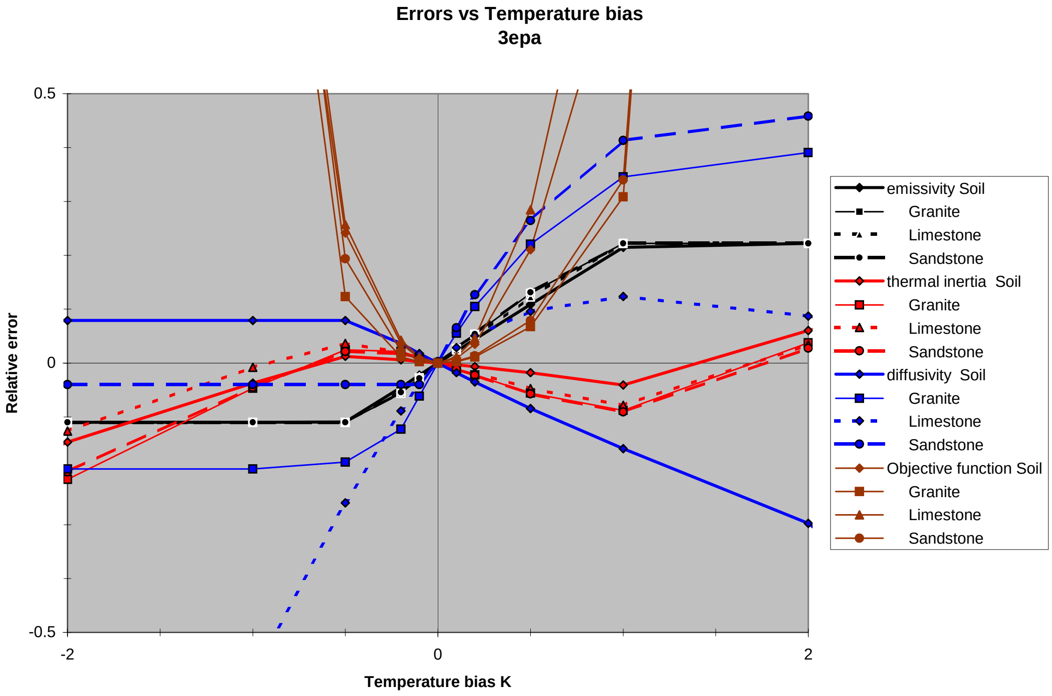

Figure 2.18 Temperature bias: Relative errors and Objective function for 3epa

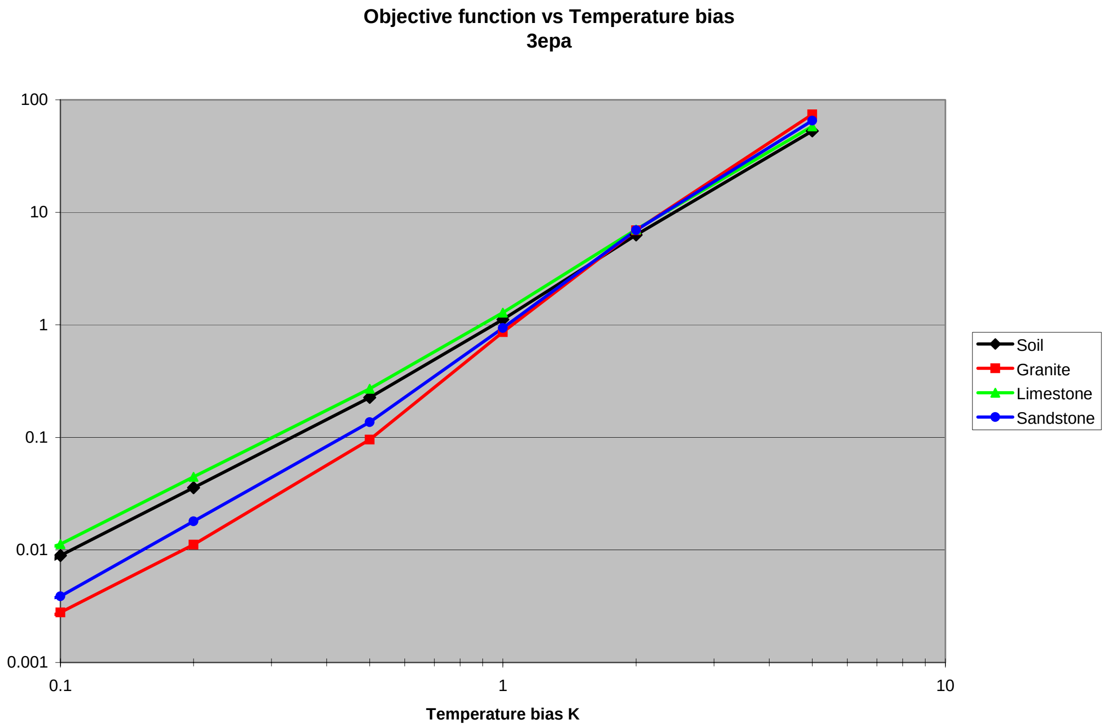

Figure 2.19 Temperature bias: Objective function (log-log plot)

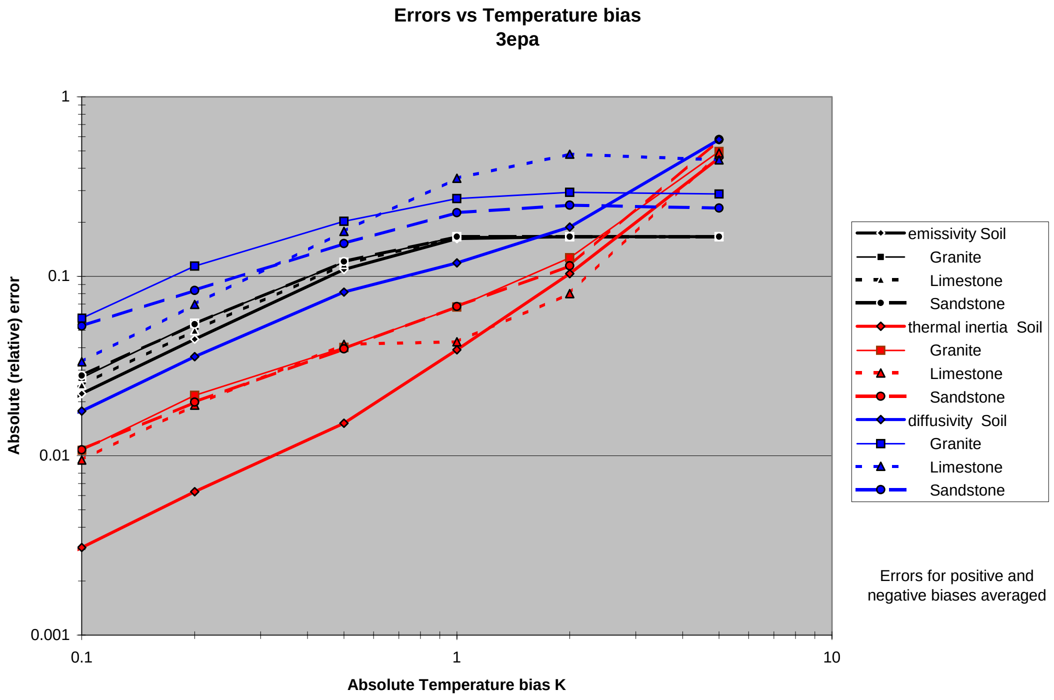

Errors for positive and negative biases averaged

Figure 2.20 Errors vs Temperature bias (optimizing emissivity, thermal inertia and diffusivity: 3epa)

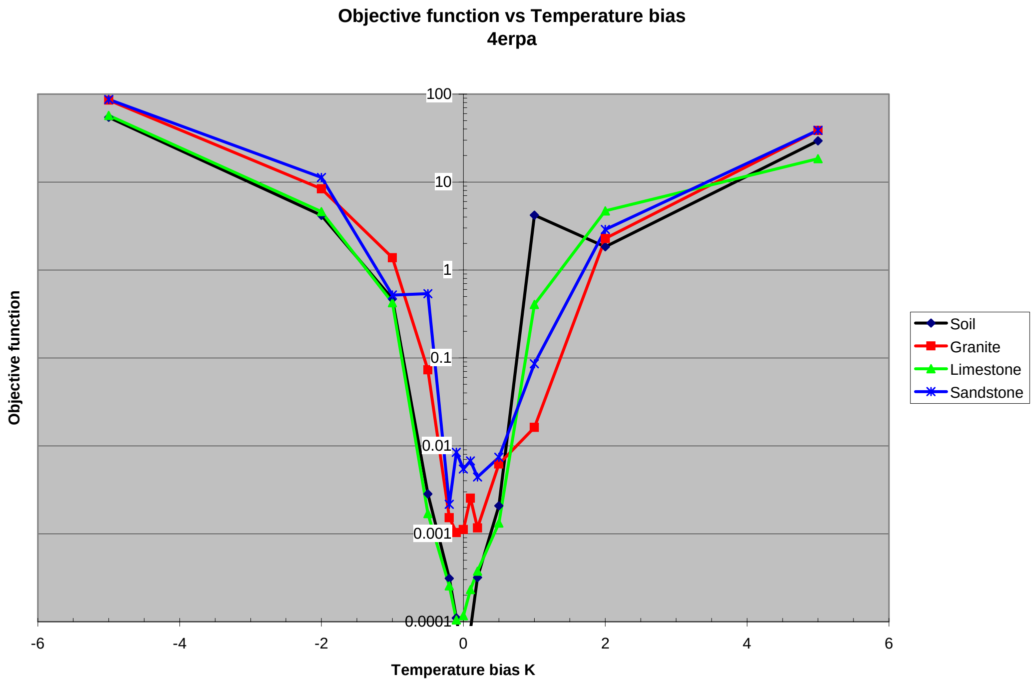

Figure 2.21 Temperature bias: Objective functions for 4erpa (emissivity, reflectance, thermal inertia and diffusivity)

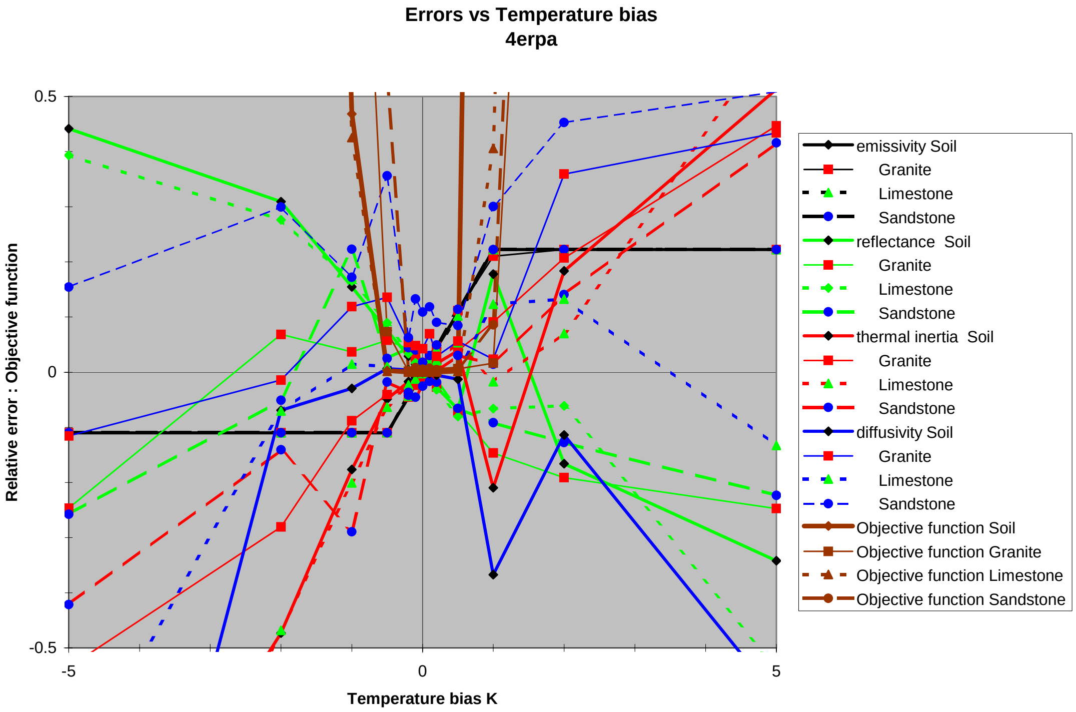

Figure 2.22 Temperature bias: all errors and Objective functions 4erpa

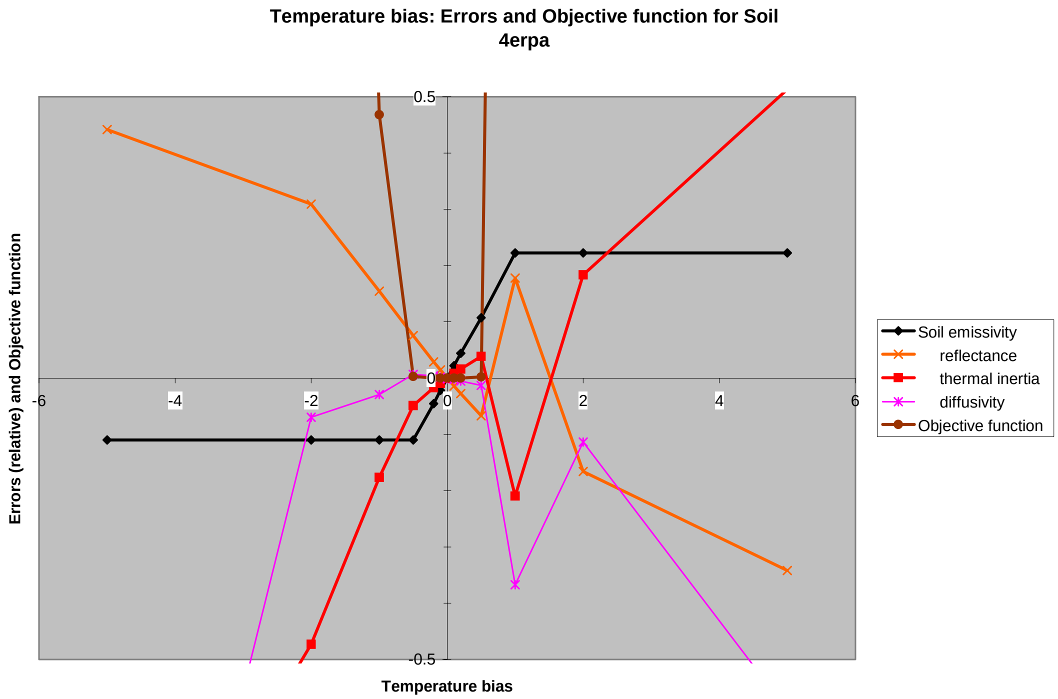

Figure 2.23 Temperature bias: Relative errors and Objective functions: Soil (4erpa)

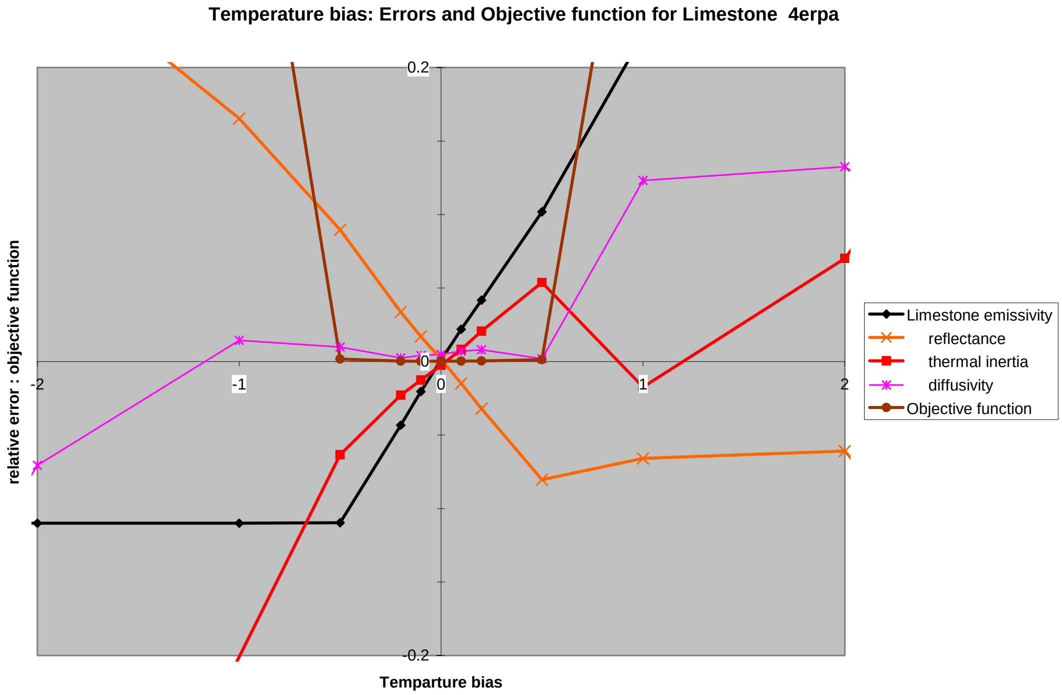

Figure 2.24 Temperature bias: Relative errors and Objective funtions: Soil (4erpa). Note scale difference from preceding figure.

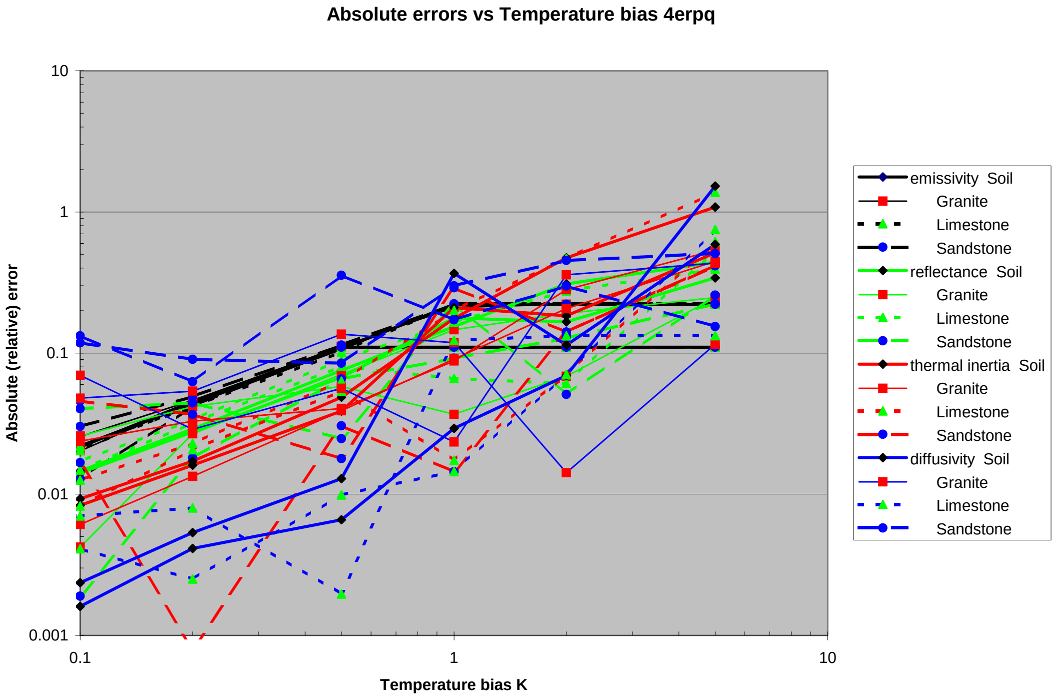

Figure 2.25 Temperature bias: Absolute relative errors (duplicate lines are for positive or negative errors)

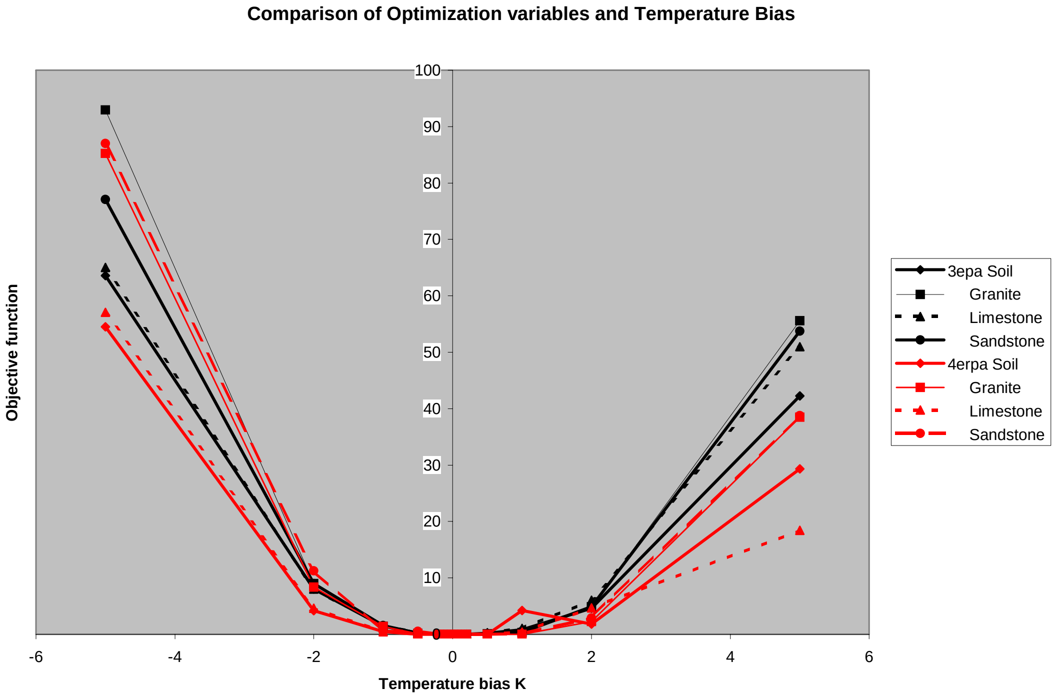

Figure 2.26 Temperature bias Comparison of Objective functions for 3epa and 4erpa

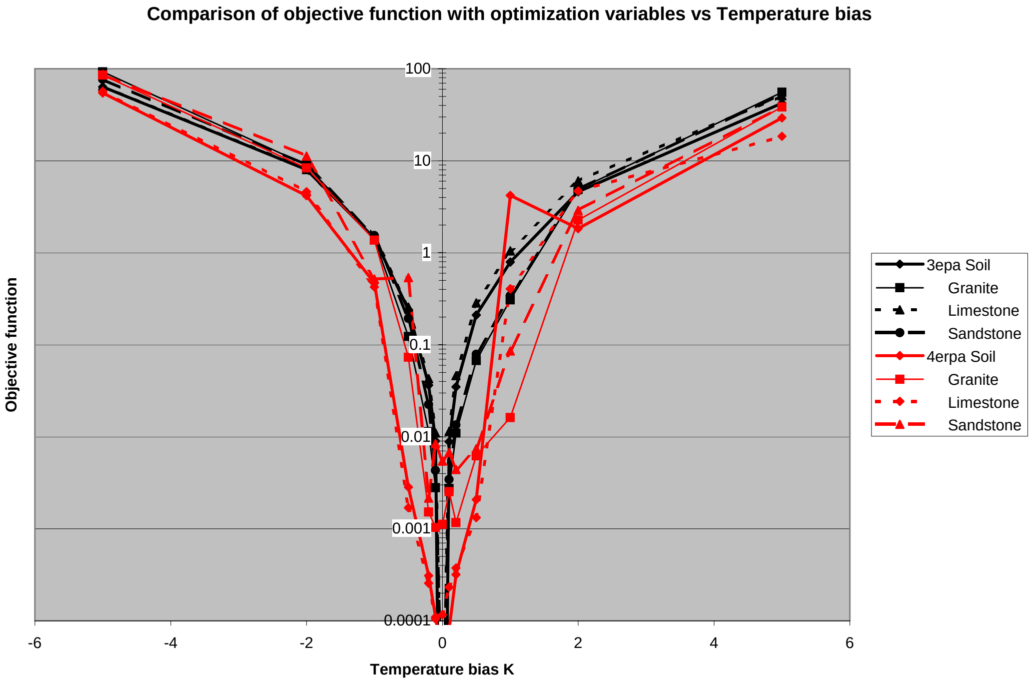

Figure 2.27 Temperature bias Comparison of Objective functions for 3epa and 4erpa (semi-log plot)

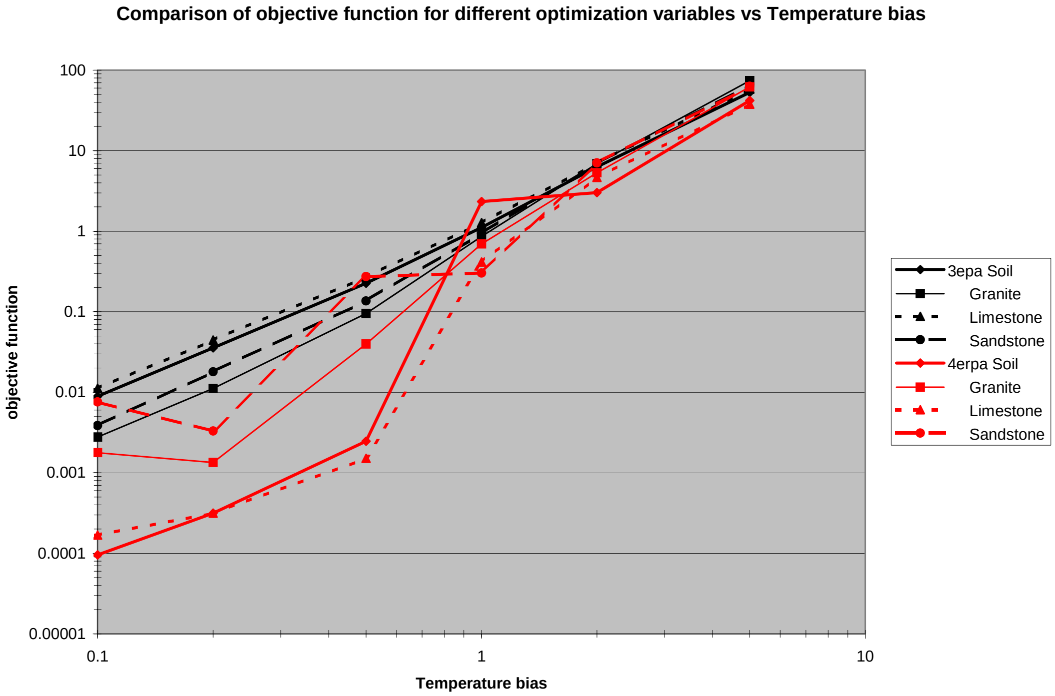

Figure 2.28 Temperature bias Comparison of Objective functions for 3epa and 4erpa (log-log plot)

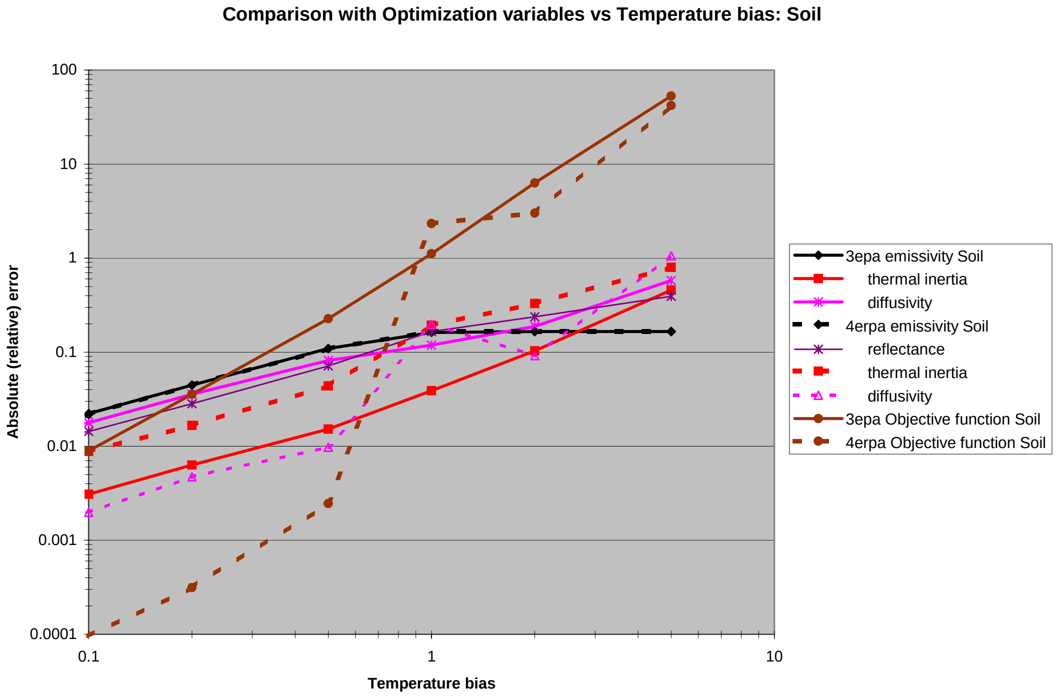

Figure 2.29 Temperature bias: Comparison of Optimizations 3epa and 4erpa for Soil

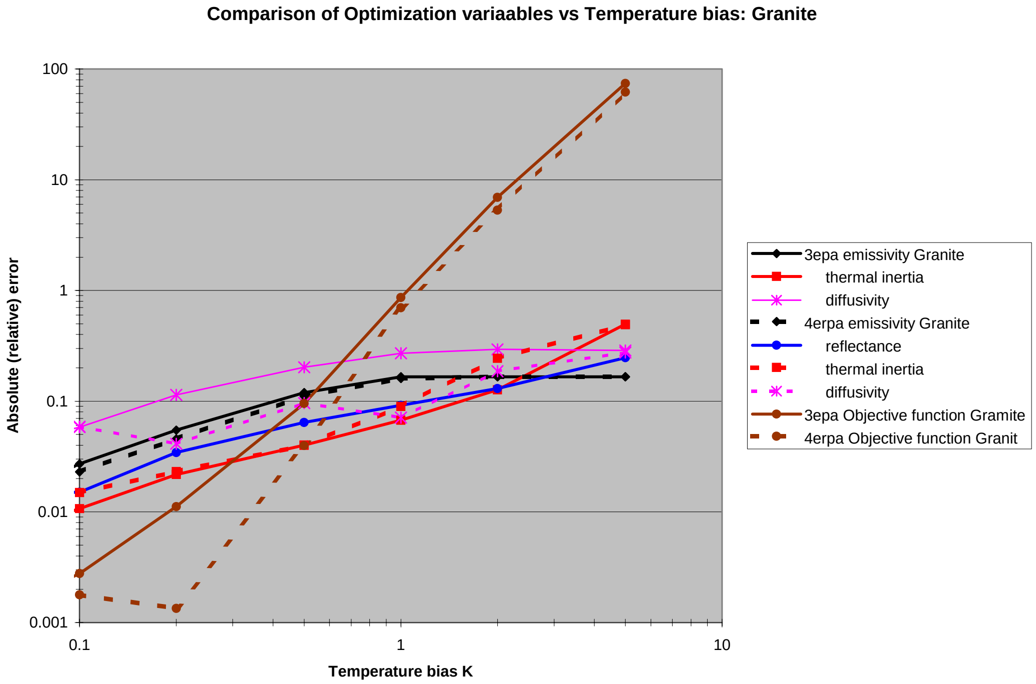

Figure 2.30 Temperature bias: Comparison of Optimizations 3epa and 4erpa for Granite

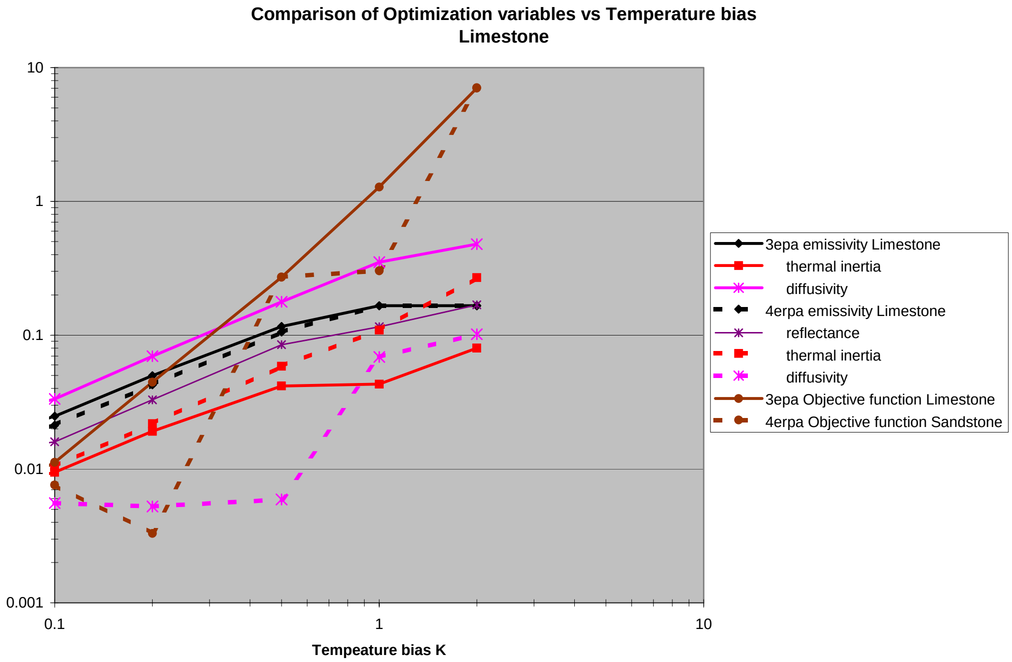

Figure 2.31 Temperature bias: Comparison of Optimizations 3epa and 4erpa for Limestone

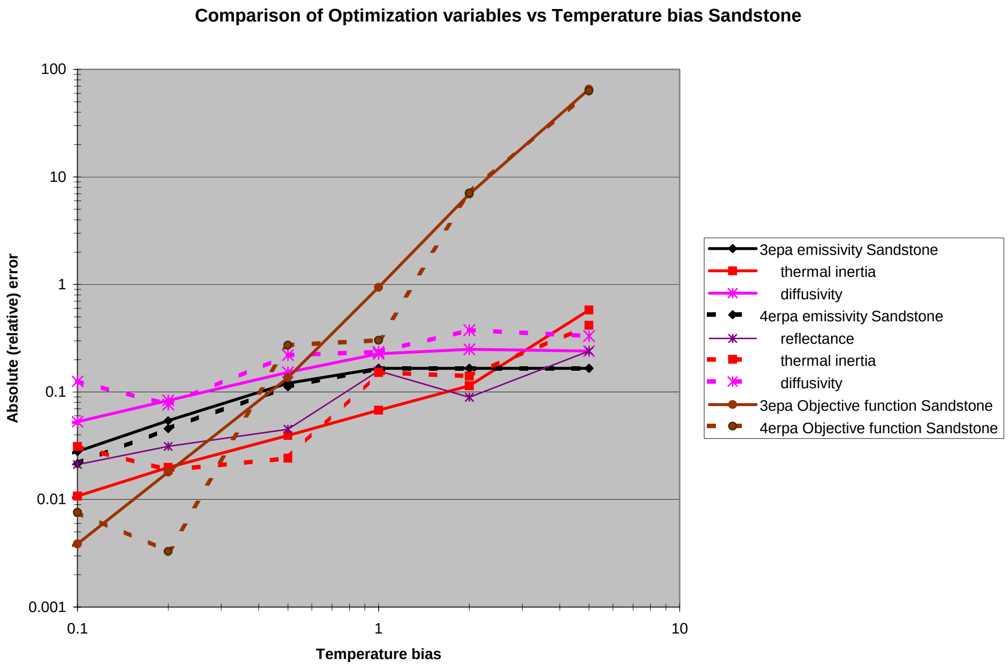

Figure 2.32 Temperature bias: Comparison of Optimizations 3epa and 4erpa for Sandstone

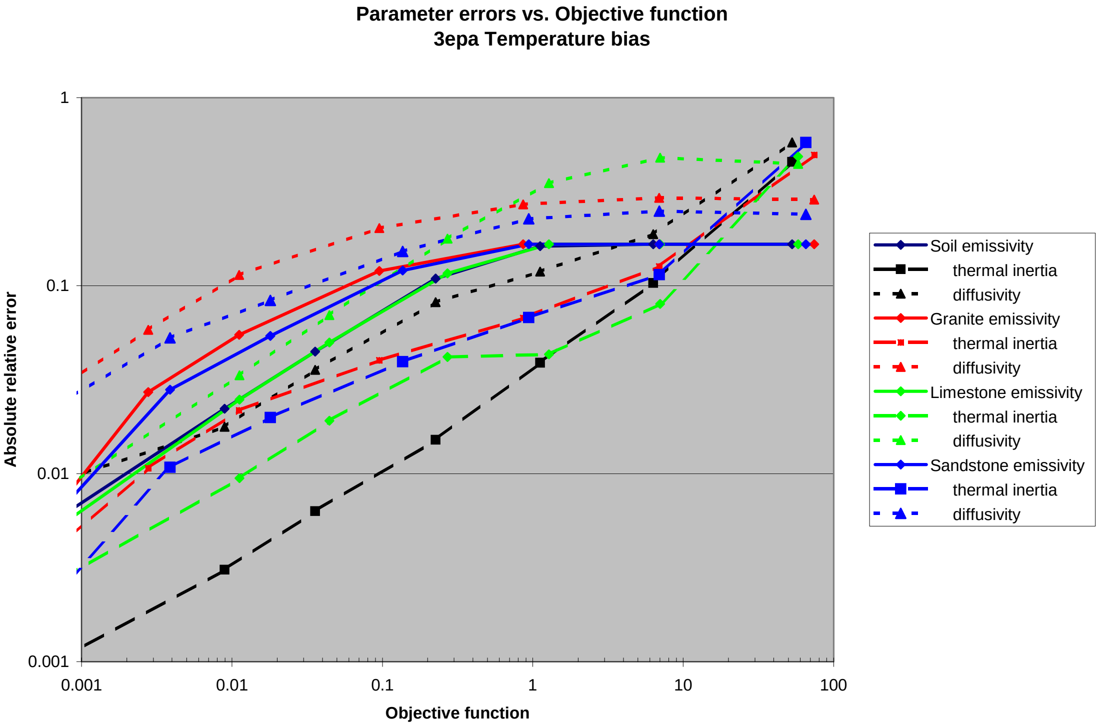

Figure 2.33 Parameter errors vs. Objective function: Temperature bias

2.6.3.4 Noise Sensitivity

In the current context, we define noise as the case of a different value assigned to each pixel. This is to be contrasted against the bias case in which the same value is assigned to each pixel. This use of the term "noise" is different than in the discussion of "noiseless" simulations.

A number of input files were created to simulate the addition of noise to the temperatures or radiances (i.e., the measured values) in DAKOTA optimization. Noise values were distributed according to a zero mean normal distribution with a specified standard deviation. These values were then added to the "true" temperature/radiance in order to construct the noise input files.

A few (typically ten) separate input files were calculated for each standard deviation. For each of these files with the same standard deviation, each pixel had different measured values while the same pixel in different files also had different measured values. For each file, a set of rock parameters was estimated using a Dakota optimization. For each run, we obtained a set of parameter errors calculated as the difference between the estimated value at convergence and the true values of the defined rock parameters. The relative error is defined as:

$$\text{Error}_{\text{relative}} = \frac{\text{Value}_{\text{Dakota}} - \text{Value}_{\text{True}}}{\text{Value}_{\text{True}}} \tag{2.36}$$

Using multiple runs with identical standard deviations allows one to calculate ensemble averages of the resulting parameter estimation errors for a given standard deviation.

Most of the DAKOTA optimizations were used to estimate emissivity, thermal inertia, and diffusivity (type 3epa). A summary of the results of noise sensitivity of the rock parameters emissivity, thermal inertia, and diffusivity is shown in Figures 2.34 through 2.36. In all cases, the errors in diffusivity were relatively large. However, we are not very concerned with diffusivity, as the discussion on error surfaces demonstrates.

Figure 2.34 shows the resulting absolute values of the actual (non-relative) errors in emissivity and thermal inertia for all the runs using all of the rms standard deviations for irradiance. Each point in this figure is an error value obtained for a particular rock type (dirt, granite, limestone, sandstone). Figures 2.35 and 2.36 show the ensemble averages of the same data (plus the diffusivity errors). In these figures, the errors shown are the mean absolute relative errors. In Figure 2.36, the abscissa is the irradiance noise standard deviation (rms W/m^2), while the abscissa in Figure 2.35 is equivalent temperature noise (rms K), which is a little more intuitive to interpret. The equivalent temperature noise is related to the irradiance noise through Equation 2.11. Upon differentiation, this equation becomes:

$$\frac{dT}{T} = \frac{1}{4}\left(\frac{dE}{E} + \frac{d\varepsilon}{\varepsilon}\right)., \qquad (2.37)$$

where we have used the symbol E for irradiance. If we set the emissivity error in this equation to zero, we have equivalent temperature standard deviation as a function of irradiance standard deviation. This relationship is examined in detail in Appendix A.

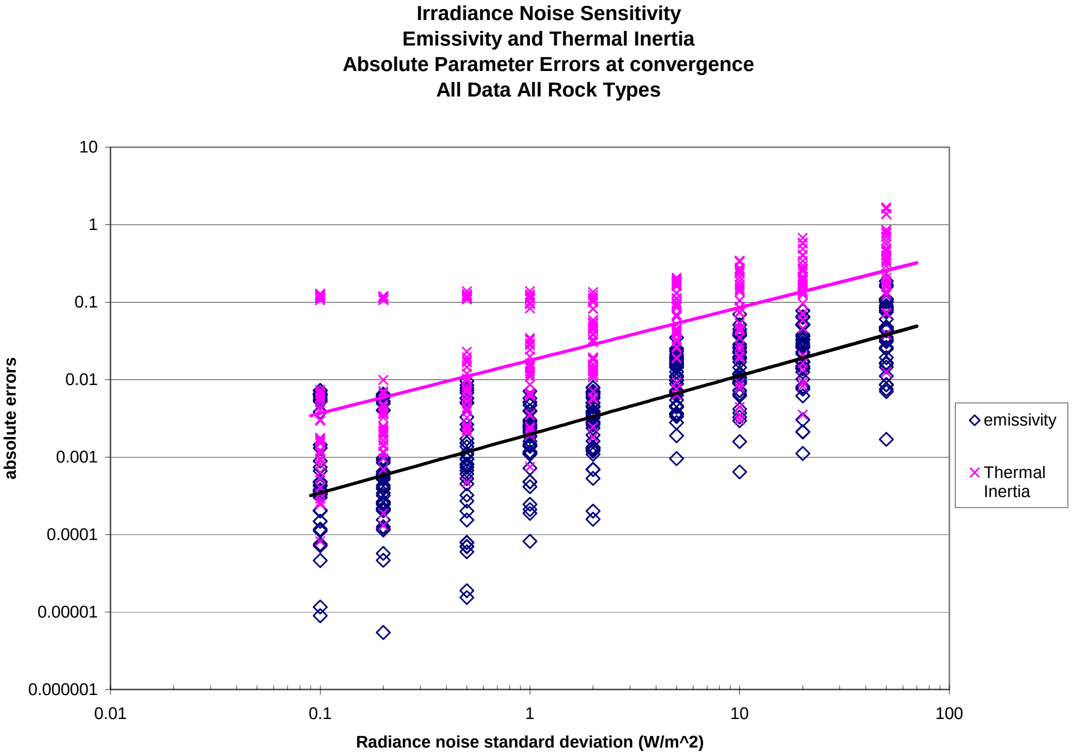

Figure 2.34 Irradiance noise sensitivity: Absolute parameter errors for emissivity and thermal inertia (3epa)

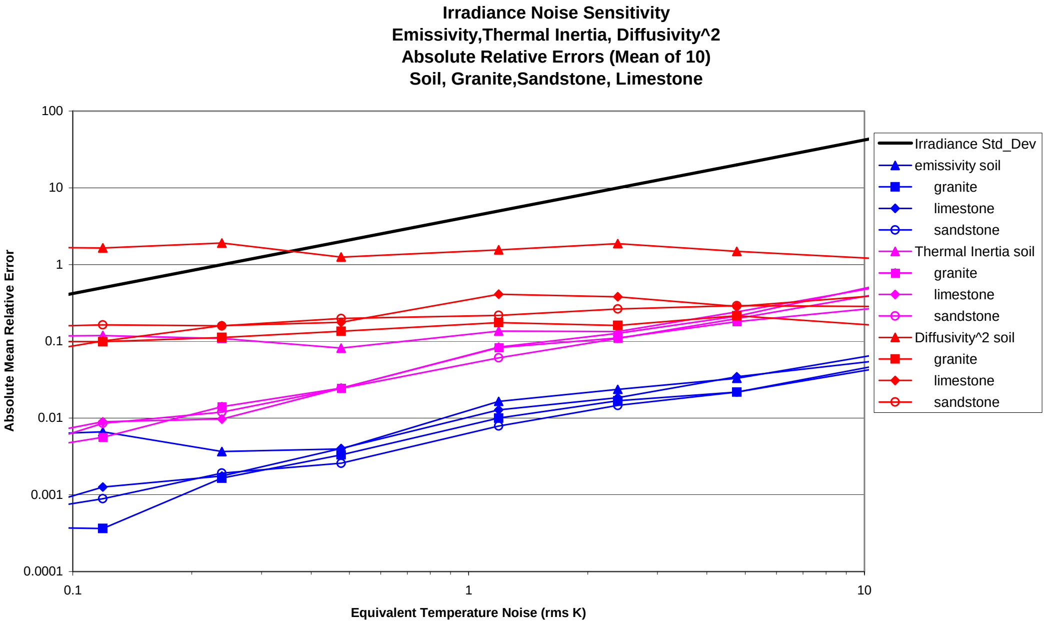

Figure 2.35 Irradiance noise sensitivity: Equivalent Temperature noise: vs. Relative errors (each point is mean of 10 instances)

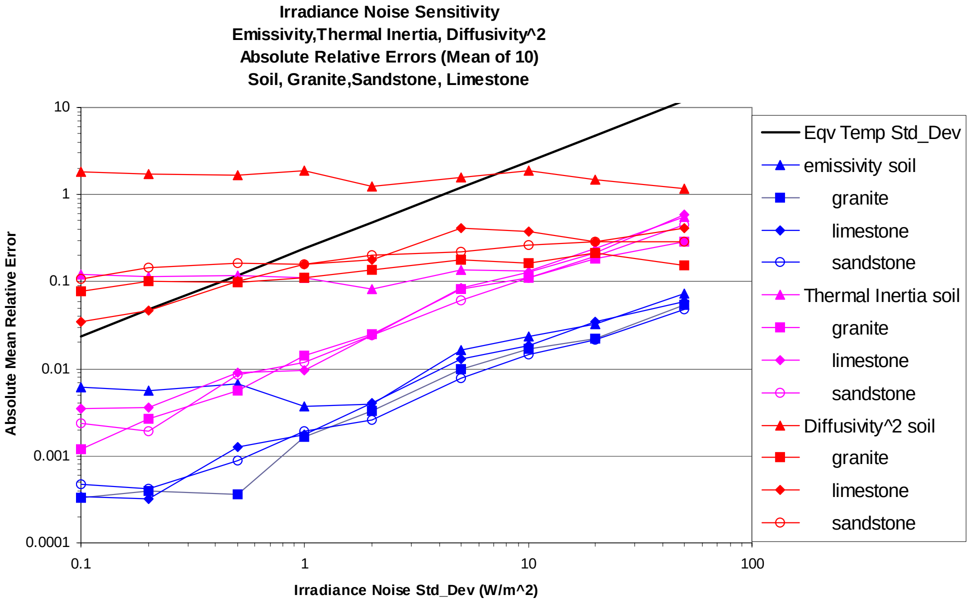

Figure 2.36 Irradiance noise sensitivity: Errors vs. Irradiance standard deviation

Using equivalent temperature noise, we see that the sensitivities of emissivity and thermal inertia are well within reasonable limits. For a 1 K rms temperature noise, the emissivity errors are less that 1%, the thermal inertia errors less that 5%. We have not duplicated the sensitivity analysis using spectral band radiances or determined the effects of errors in atmospheric correction. However, we can estimate these effects from the results already obtained. The radiance received at the sensor at a particular wavelength can be given as

$$L_{sens} = \tau L_{surf} + L_{path} \tag{2.38}$$

where

L_{sens} is the radiance received at the sensor
τ is the atmospheric transmittance
L_{surf} is the radiance emitted at the surface
L_{path} is the upwelling IR radiance from the atmosphere

In another section of this report, we have shown that the path radiance can be considered as a bias term and thus can be corrected. We convert radiance L_{surf} to irradiance at the surface as $E = \pi L_{surf}$. Neglecting the path radiance, substituting and differentiating we get:

$$\begin{aligned} L_{sens} &\approx \tau \frac{E}{\pi} \\ dL_{sens} &\approx \frac{\tau dE}{\pi} + \frac{E d\tau}{\pi} \end{aligned} \tag{2.39}$$

$$\frac{dL_{sens}}{L_{sens}} = \frac{d\tau}{\tau} + \frac{dE}{E} \tag{2.40}$$

Thus, the relative errors in spectral radiance and irradiance are comparable if the atmospheric correction for transmissivity is good.

Figure 2.37 shows the result of a direct sensitivity investigation of positional errors. In the normal execution of the simulation data set, each pixel is offset from the ridge by a different amount to simulate the effects of differential heating. To determine the sensitivity of the estimated rock parameters with respect to positional inaccuracy, we repeated the construction of an input data set by deviating the pixel distance to the ridge in an identical way.

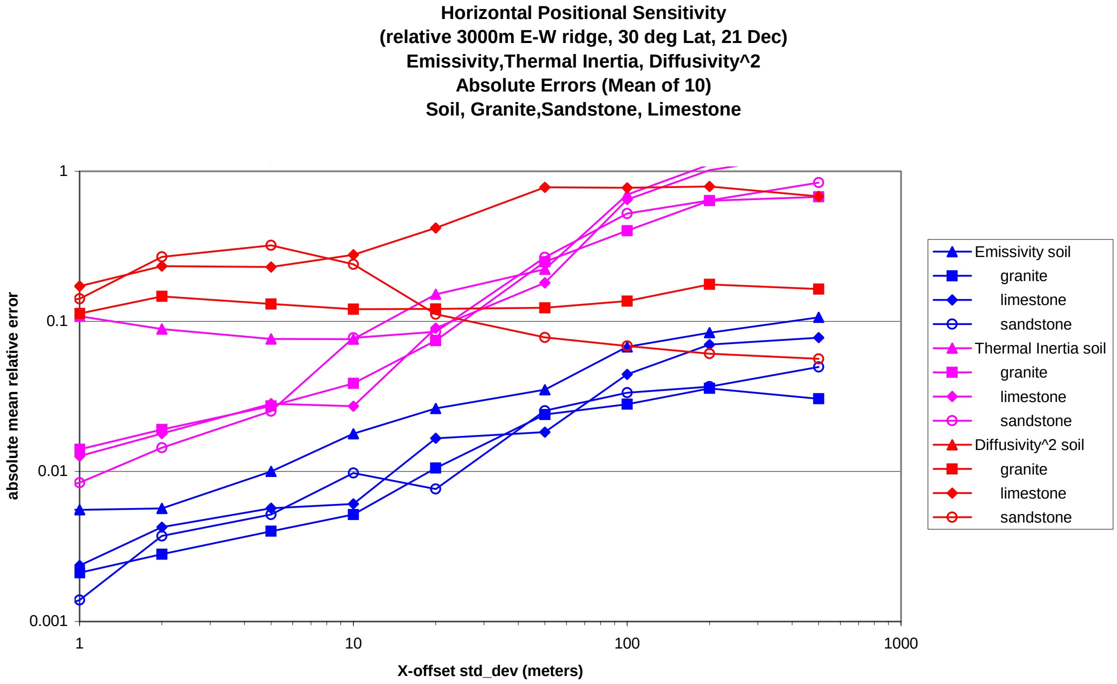

Figure 2.37 Horizontal positional sensitivity by direct simulation

Scatter plots of emissivity vs. thermal inertia and thermal inertia vs. diffusivity using the irradiance sensitivity results are shown in Figures 2.38 through 2.40 as a function of rock types. The interpretation of Figures 2.38 through 2.40 is that rock parameter separability in the presence of noise is satisfactory. Laboratory and field measurements of thermal rock properties also tend to indicate parameter separability difficulties for different rocks types, as shown in Figure 2.41. However, the proposed relationship between thermal inertia and rock "strength" might make the issue of separability irrelevant. That is to say, if two different rock types have similar thermal inertias their "strength" might be comparable.

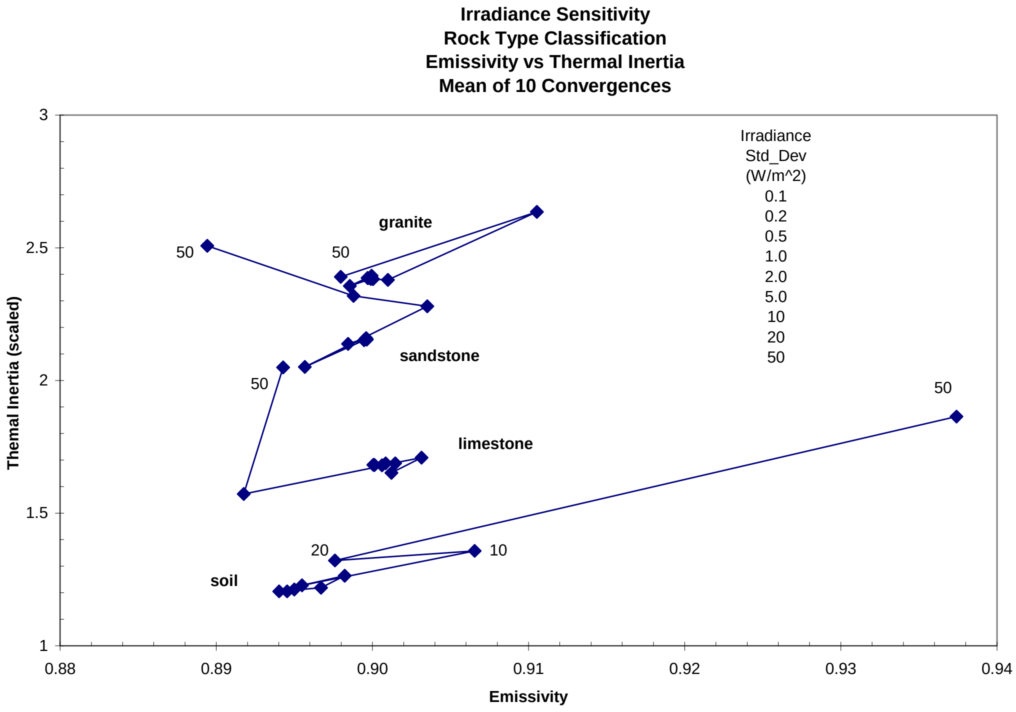

Figure 2.38 Rock type separability in presence of irradiance noise: emissivity vs. thermal inertia

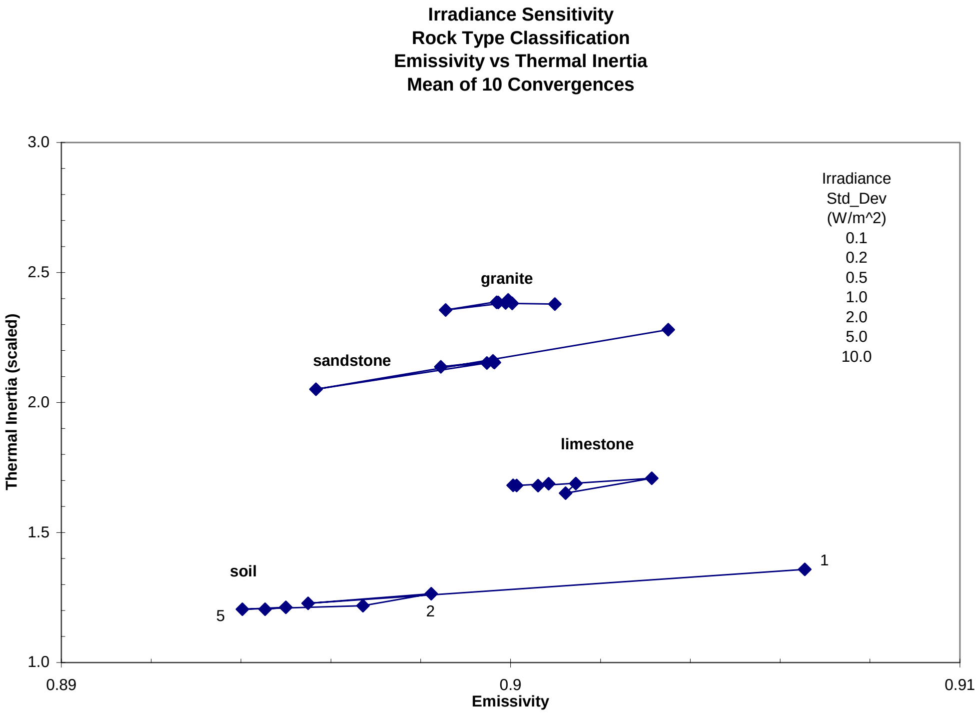

Figure 2.39 Rock type separability in presence of irradiance noise; emissivity vs. thermal inertia (maximum std_dev=10: expanded scale)

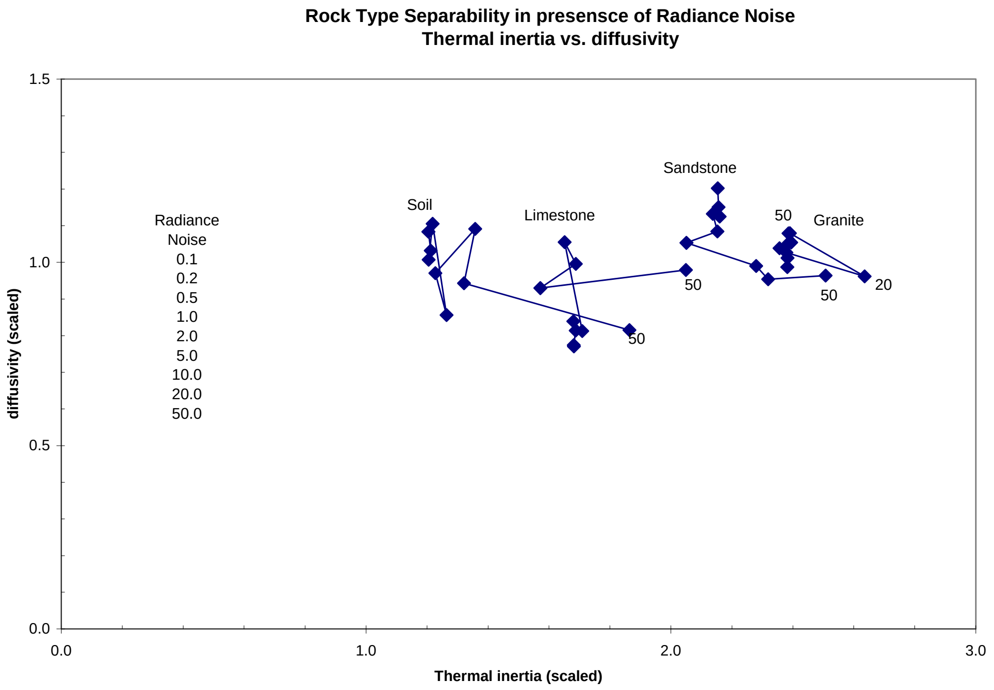

Figure 2.40 **Rock type separability in presence of radiance noise (0.1 to 50.0): thermal inertia vs. diffusivity**

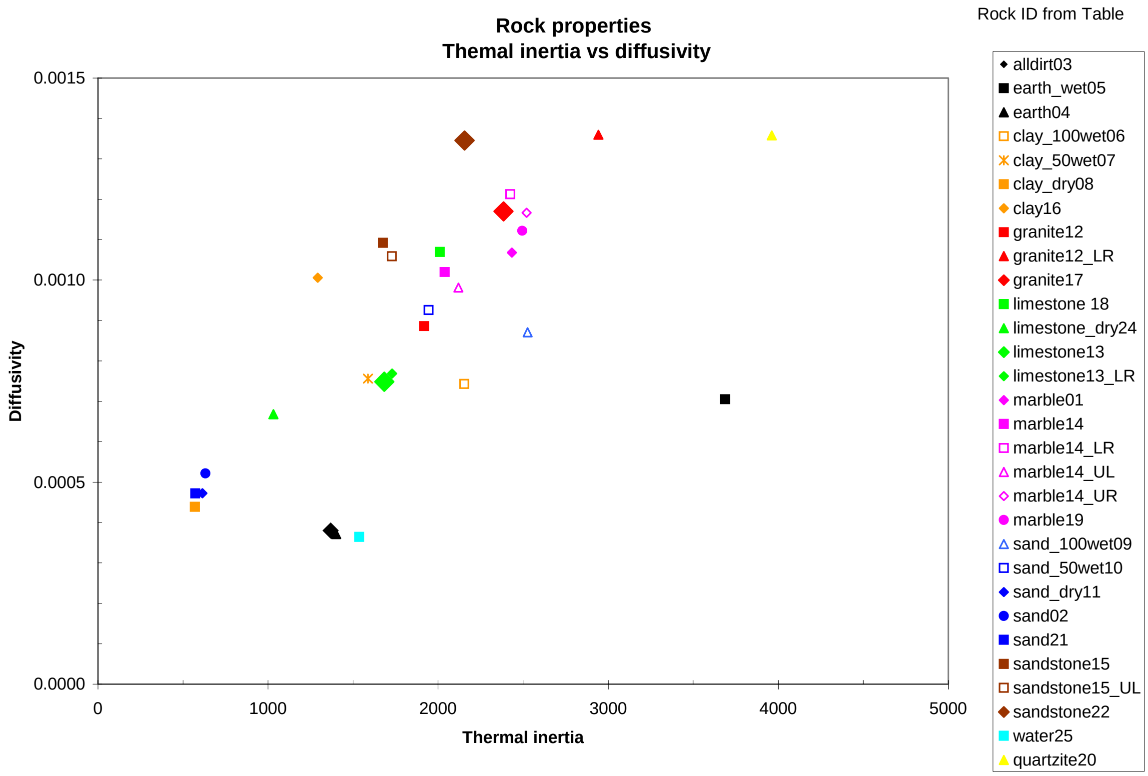

Figure 2.41 **Rock properties: thermal inertia vs. diffusivity**

2.6.3.5 Sensitivity Summary

The major conclusion of the sensitivity study is that the simulated errors in rock parameter estimates introduced by bias or noise in the temperature, radiance, or location (which effects heating history) are low enough to give some confidence that the method will produce satisfactory results with real imagery if the assumptions of the model are met. Furthermore, due to the nature of the errors introduced by bias, we should be able to use the relationship between the bias and the rms error in the Objective Function to estimate and correct for bias offsets that apply equally to all pixels used.

2.6.3.6 Summary of Rock Parameter Optimization Simulation Results

We have modified the IR Response Code to run with the DAKOTA optimization package in a manner that simulates the terrain-shading situation. We simulated shading of multiple pixels by positioning pixels at varying distances from a simulated ridge, resulting in varying times of local sunrise and sunset for different pixels.

We have demonstrated, in a no-noise simulation, that DAKOTA can estimate the rock parameters (thermal inertia, diffusivity, emissivity, reflectance) by minimizing the sum of square errors between truth temperatures obtained from direct model application and model-predicted temperatures. The use of emitted IR irradiance or band radiance, rather than temperature, as the optimization objective gave results comparable to temperature. An added advantage of using radiance is that the rock thermal emissivity can be used as an optimization variable. This gives a direct estimate of the rock emissivity. We believe that this is a unique method of estimating emissivity from remote imagery.

The IR Response code has been used to investigate the sensitivity of rock parameter estimation to errors in temperature, radiance, DEM, and sunrise/sunset times. Sensitivity analysis includes both bias error (all pixels get same offset from true) and random errors (each pixel gets an independent error offset). Errors in rock parameter estimates due to temperature bias greater than ± 1°C are excessive. However, the presence of temperature or radiance bias in a no-noise situation can be detected and corrected to estimate both the bias value and obtain correct rock parameter estimates. The same conclusion is valid for bias in an additive noise case. Because the atmosphere between the ground and the sensor approximately affects every pixel the same, it can be considered as a bias. Thus, we can estimate the atmosphere parameters (transmittance and up-welling atmospheric IR radiance) and essentially correct the measured values. This has been demonstrated, to a certain degree, in the analysis of the Coyote Canyon SW image discussed below.

The sensitivity analysis of the noise case in which each pixel was assigned a different value (temperature, radiance, location) taken from random distribution indicated that much higher rms deviations produce rock parameter estimates with tolerable errors. For example, an irradiance rms variation of 5 $\mathrm{W/m^2}$ produced emissivity relative error of about 1% (all rock types) and thermal inertia relative errors slightly less than 8%. These errors were small enough to allow reasonable rock type separation.

An important conclusion to be drawn from the sensitivity work was that, in no case, did addition of noise or bias lead to a parameter solution for the "wrong" rock. The algorithm never converged (with a small objective function) to a set of parameters different from the "truth" values. In all cases in which the objective function was relatively small, the rock parameters given by the optimization were close to the true rock parameters. An interpretation of this phenomenon is that the one-dimensional heat transfer model used restricts solutions to physically sensible ones.

2.7 Application to MTI Imagery

2.7.1 Description of MTI

MTI is a Department of Energy research and development project executed by Sandia National Laboratories, Los Alamos National Laboratory, and Savannah River Technology Center. Other government participants include the Air Force Research Laboratory, the National Institute of Standards and Technology, and the Air Force Space Test Program; major private industry participants include Ball Aerospace, Raytheon Optical Systems, Raytheon Infrared Center of Excellence, and TRW.

The MTI satellite is a push-broom imager that collects imagery in 15 spectral bands from the visible (VIS) through the long wave infrared (LWIR). Figure 2.42 shows band pass filter ranges of the sensor overlaid on the solar and emission spectra as attenuated by a typical atmosphere. Ground sample distances are approximately 5 meters in the visible and shortest near infrared (NIR) band and 20 meters in the remaining longer wavelength bands. The swath length is approximately 12 km, and a standard image is nominally 12 km x 12 km.

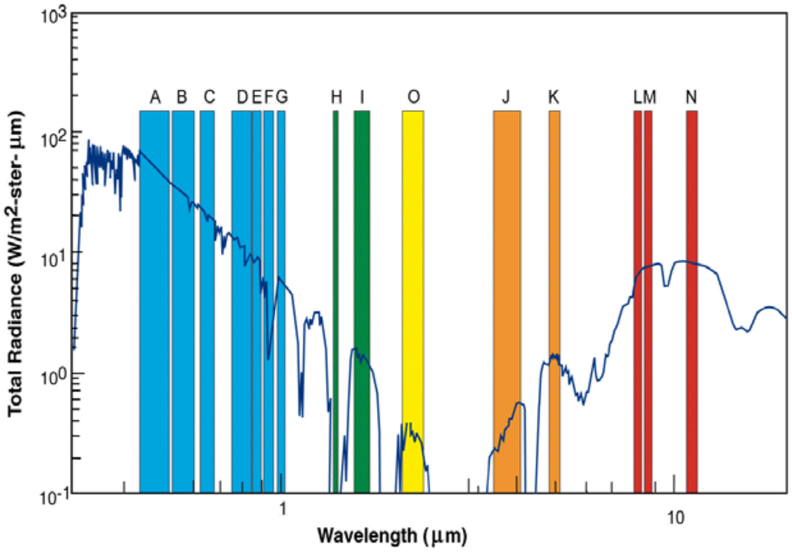

Figure 2.42 MTI Band Response

2.7.2 Experimental Sites

A number of sites were considered for a proof-of-concept demonstration. These sites were selected in concert with ongoing studies being performed by the Interagency Geologic Assessment Team (IGAT). The sites represented a wide variety of geologic conditions, climates, and terrain. Images from two sites were used with the proposed method of determining rock properties by matching measured and computed spectral radiances in the LWIR using Dakota and the modified IR Response code. These are the Coyote Canyon South West site at Kirtland AFB, close to Sandia National Laboratories and the Red Wing mine site at China Lake NWC.

MTI images of Coyote Canyon SW are shown in Figures 2.43 and 2.44. Figure 2.45 is a shaded relief map based on a 30-meter DEM illustrating the terrain of the Red Wing Mine area. The Coyote Canyon site was chosen for its ready access to Sandia National Laboratories, its terrain, and the availability of MTI imagery. Unfortunately, it does not meet all the current restrictions of the model, namely lack of vegetation. The Red Wing Mine site fits the constraints more accurately and has been characterized in related projects.

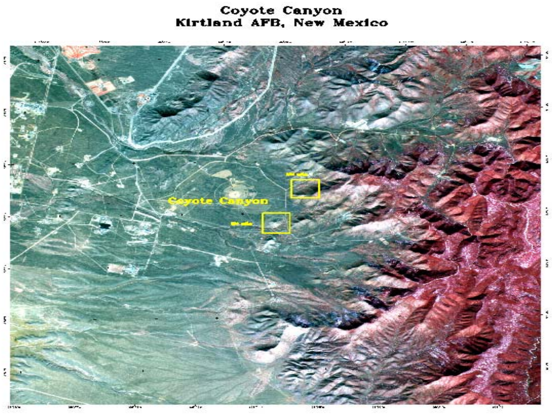

Figure 2.43 Coyote Canyon test sites (MTI false color IR)

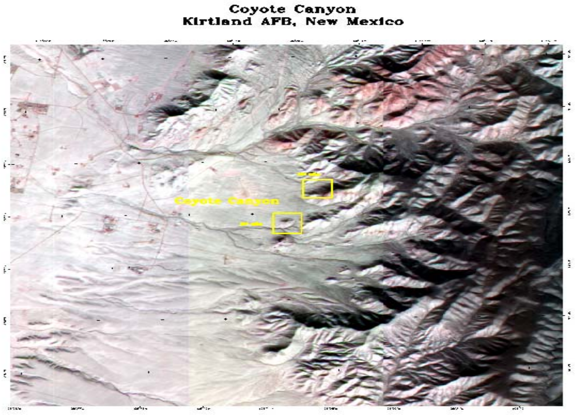

Figure 2.44 Coyote Canyon test site (MTI: RGB=NML)

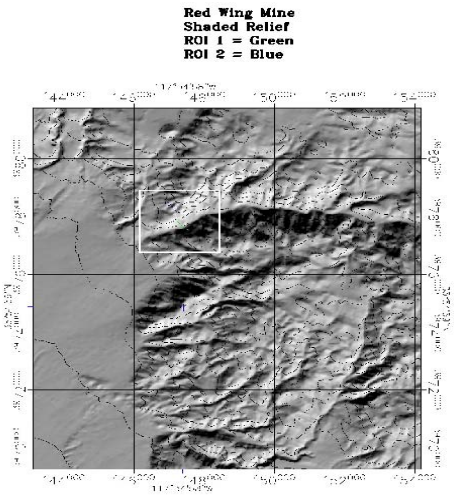

Figure 2.45 Red Wing Mine test site (Shaded relief from DEM)

A single Region of Interest (ROI) for the Coyote Canyon was used consisting of 48 points spread evenly around the small hill. From a cursory analysis of the image and actual ground inspection, the surface materials from all 48 points seem to be the same. Unfortunately, the surface at this test site was not bare soil; about 25-50% of it was evenly covered with a short senescent tuft grass. For the Red Wing Mine scene, two ROIs where chosen, consisting of 15 and 10 points respectively. Each of these ROI sets contained differential heating and appeared to be homogenous. It was thought that a set by the valley floor (ROI 1) and a set higher up (ROI 2) might give different results. We obtained weather data for the Albuquerque airport (about 5 miles SW of Coyote Canyon) for February 2001 in terms of daily averages and extremes. These are shown in Figures 2.46 and 2.47 and used as input data for the IR Response Code (daily averages only, not hourly tabular data). IR Response weather data for Red Wing Mine was estimated.

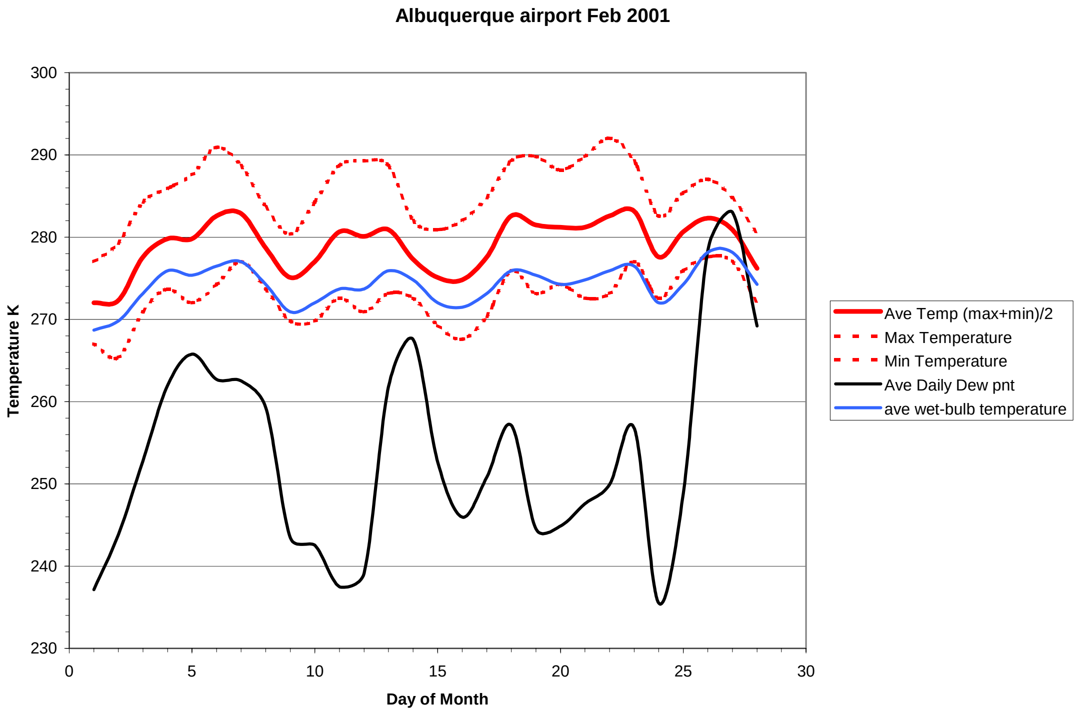

Figure 2.46 Temperature: Albuquerque Feb 2001

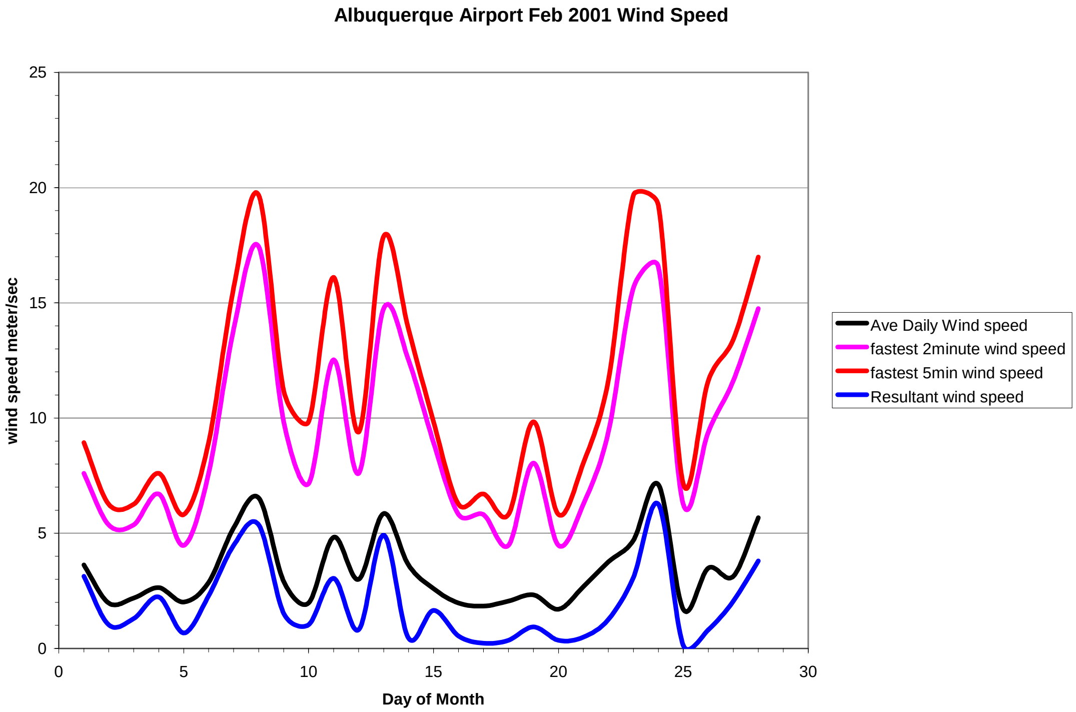

Figure 2.47 Wind Speed: Albuquerque, Feb 2001

2.7.3 Experimental Procedures

For both sites the procedure for estimating rock parameters from MTI imagery and DEMs were followed. Some minor exceptions will be noted. The MTI images used and date of collection are shown below.

Table 2.3 MTI Images Used at Test Sites

Site	Image ID	Date
Coyote Canyon SW	101995	02-12-2001
Red Wing Mine	111955	10-31-2002

2.7.4 Rectification to DEM

For Coyote Canyon, a 10-meter resolution DEM generated from SAR was used. This was provided to us by University of New Mexico, Earth Data Analysis Center. For the Red Wing Mine site, a USGS Level1 DEM at a nominal 30-meter elevation resolution and 30-meter post spacing was used. In both cases, they were interpolated to a 20-m resolution using nearest-neighbor resampling to match the LWIR band data resolution.

In order for the pixels in the image to be matched with the pixels in the DEM for use in the sunrise/sunset calculation and the calculation of surface tilt, the image should be ortho-rectified. However, this is not strictly required, we need to know only the geographic positions of the image pixels; the warping and resulting resampling does not need to be applied. Resampling is undesirable because it can degrade the radiance accuracy of the resulting resampled pixels. Thus for the Coyote Canyon data the DEM was rectified to the image. This was done using a traditional ground control point (GCP) method. The resampling method chosen was triangulation with a dense grid of GCPs to provide the most accurate registration.

For the Red Wing Mine site, the image was not ortho-rectified for the initial analysis. By overlaying the image and a shaded relief image of the DEM (constructed for the time of collect) and “flickering,” it was determined that we would be off by only a few pixels. For a more detailed analysis, the image and DEM should be handled the same as for the Coyote Canyon site.

2.7.5 Atmospheric Correction

Initially there was no good atmospheric correction data available for the Coyote Canyon site. A vertical, sea level transmittance was estimated using graphs in a textbook on remote sensing (Showengerdt [1997]). This was from a MODTRAN calculation for a mid-latitude summer with a visibility of 23 km. The algorithm failed to converge to a reasonable set of rock parameters (band emissivity, thermal inertia and diffusivity) using weather parameters estimated from the weather at the Albuquerque airport for the month of February 2001 (see Figures 2.46 and 2.47). This failure to converge was determine by the high best-objective function and the fact that all of the optimization variables were on the boundary of the maximum or minimum values specified to DAKOTA. The up-welling path radiance used in this initial test was zero. As mentioned in Section 2.6.3.3, the path radiance can be considered as a bias and the possibility of minimizing the objective function by using this bias as an optimization variable was tested. Rather than actually use path radiance as a DAKOTA variable, a number of atmosphere input files were constructed based on the atmosphere estimate we were using. DAKOTA –IR_Dak was exercised over a number of these and a minimum objective function was obtained with more reasonable rock parameters. (This is analogous to the error surface.) Once the Red Wing Mine atmosphere data became available, it was used and the results were much better. Both the Coyote Canyon and Red Wing images were obtained in a high desert in the winter and it was expected that the atmospheres would be similar.

A MODTRAN atmosphere was obtained for the Red Wing Mine site using the information in the image meta-data file. The results for transmittance (surface–to–satellite) and the up-welling atmospheric path radiance are shown in Figures 2.48 and 2.49. These were the basis for the Red Wing Mine calculations.

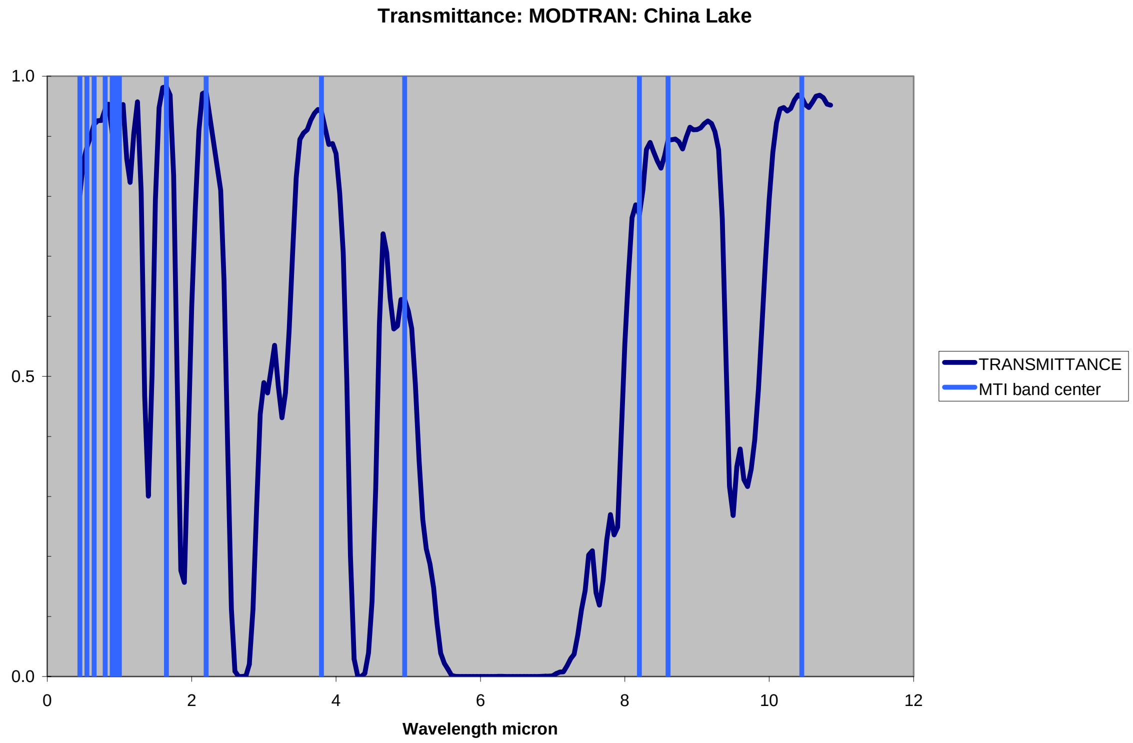

Figure 2.48 Transmittance: MODTRAN China Lake

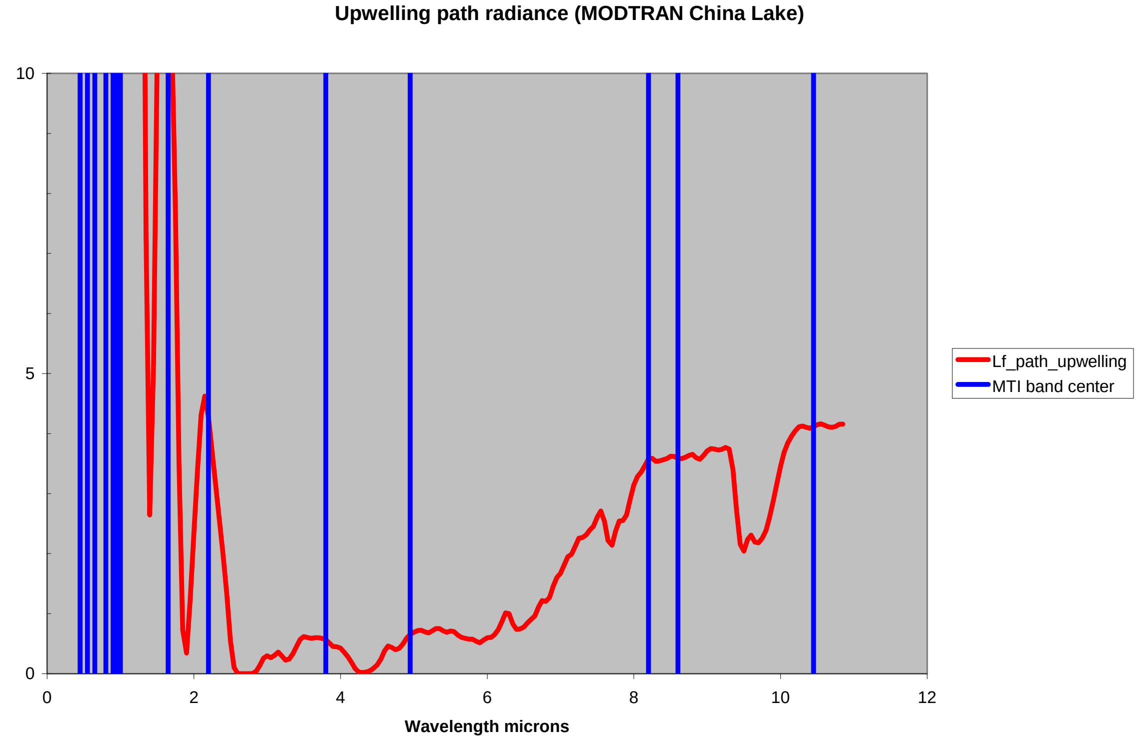

Figure 2.49 Up-welling path radiance: MODTRAN China Lake

2.7.6 Results

In addition to obtaining a single result (emissivity, thermal inertia, and diffusivity), we made a number of runs with various up-welling atmospheric path radiance offsets as suggested by preliminary results with the Coyote Canyon and the poorly matched atmosphere. We used the Red Wing Mine atmosphere for both sites. From this basis atmosphere, we derived alternate "path radiance offset" atmospheres by simply adding an offset value to the original basis path radiance in the basis atmosphere. The same offset was added to each LWIR band. The results of this for both sites are presented in Figures 2.50 through 2.53.

The interpretation of these results is problematic. It appears that, for the optimization variables, the offset that gives a minimum objective function (across all the offsets) yields somewhat reasonable results in terms of values. However, the details of the thermal inertia and diffusivity curves are puzzling, particularly the "spikey" nature of the thermal inertia as a function of bias offset. The large changes in thermal inertia at convergence do not seem consistence with the small differences in objective function.

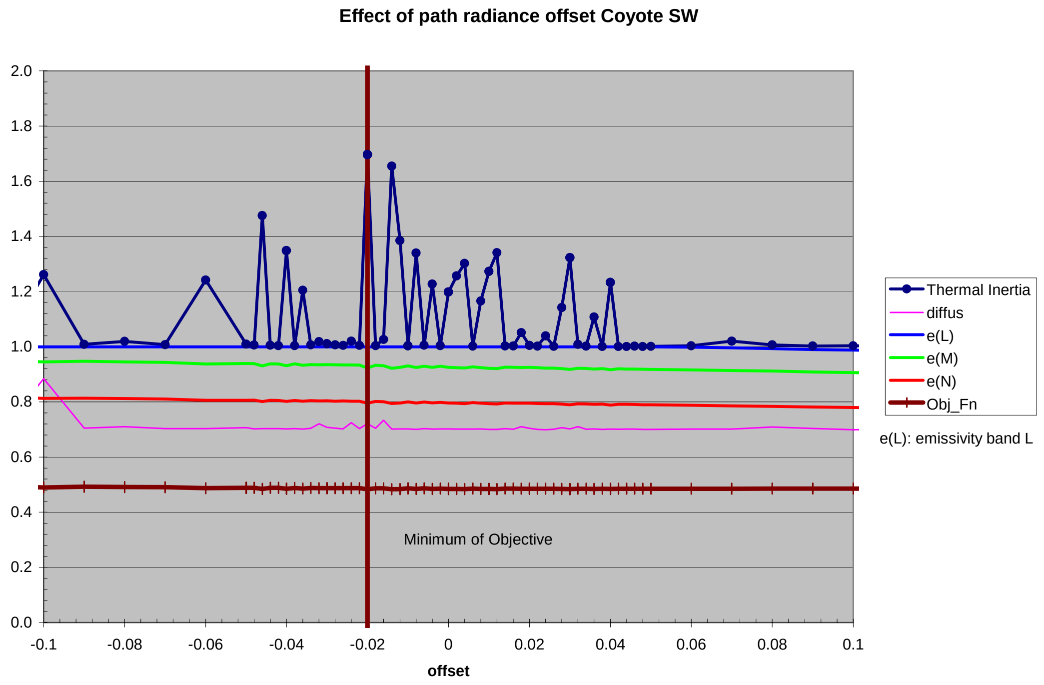

Figure 2.50 Effect of path radiance offset Coyote Canyon (high resolution)

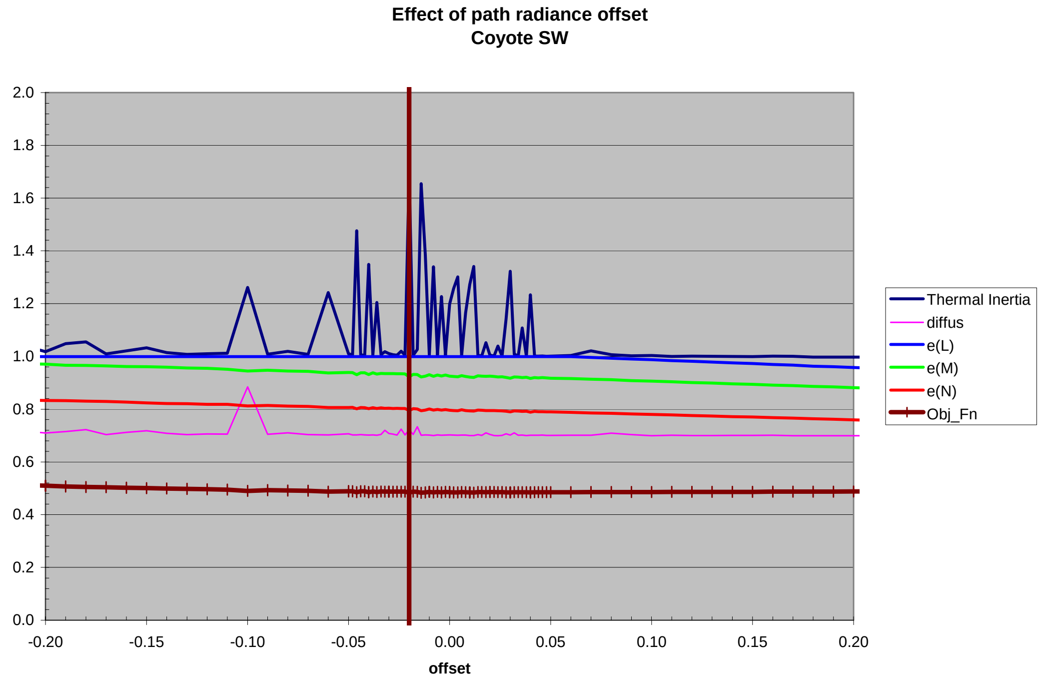

Figure 2.51 Effect of path radiance offset: Coyote Canyon (medium resolution)

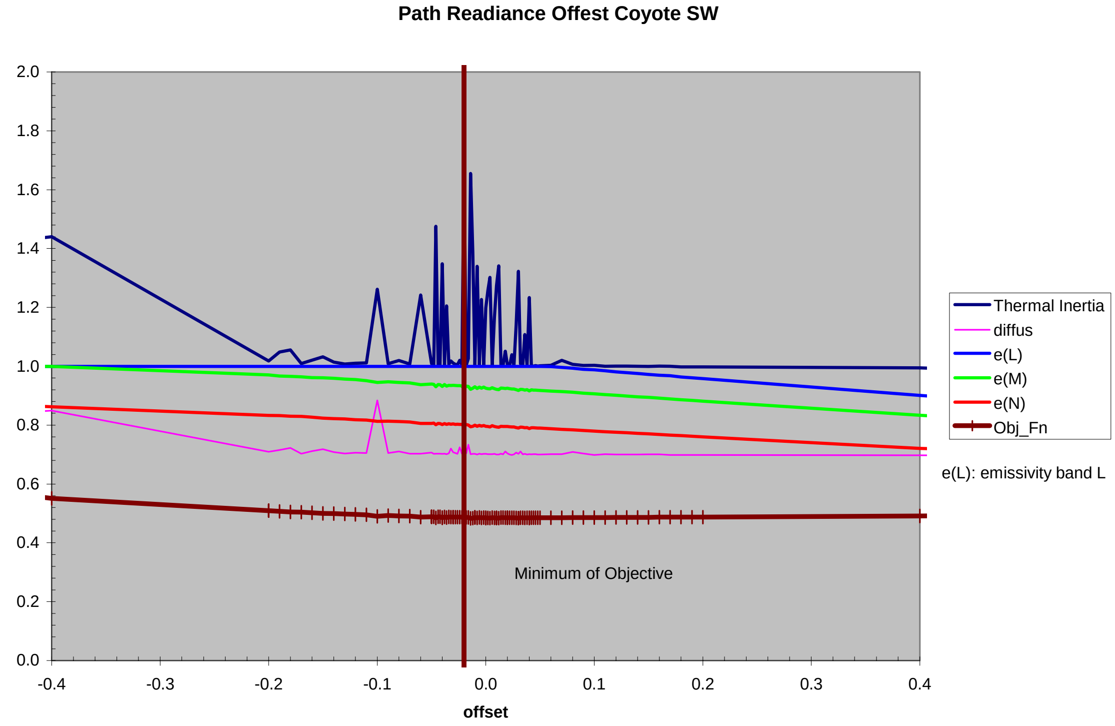

Figure 2.52 Path radiance Coyote (low resolution)

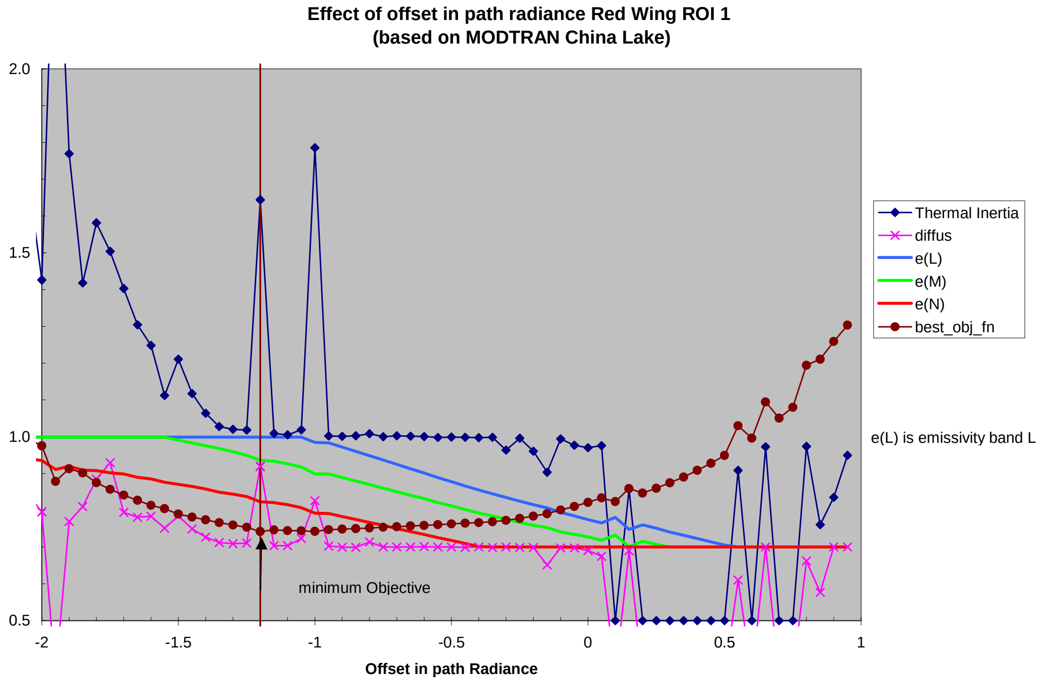

Figure 2.53 Effect of Path Radiance Offset: Red Wing Mine ROI 1

2.8 Analytical Models for Surface Temperature Differences in Sun and Shade

2.8.1 Introduction

Analytical models have been developed to predict the temperature difference between sunlit and shaded regions. The models were developed in order to gain insight into the influence and sensitivities of various parameters and processes on temperature differences. The models also provided guidance during the development of numerical predictive methods. The models are referred to as "simple" in that they permit use of a closed-form solution.

Development of the analytical models assumes two adjacent ground surface locations—one in full sunlight and one in complete shade. The locations are assumed identical in the sense that they have the same conditions with respect to moisture status, soil properties, amount and type of vegetation, and climatic conditions. The models are based on the energy balance at the soil or rock surface:

$$Rn = LE + H + G \tag{2.41}$$

where Rn is the net radiation flux, LE is latent heat flux, H is the sensible heat flux, and G is the ground heat flux.

Three models of temperature differences between sunlit and shaded surfaces were developed. First, a model without soil moisture was developed. This allowed the latent heat flux term to be set to zero. This model may be applicable to very dry bare soil conditions or areas where relatively intact rock is exposed on the surface. The second model includes soil moisture, expanding the capability of the model to include the bare soil with some moisture in the near-surface. The third model includes vegetation, permitting a mixture of bare soil and vegetation to be modelled. The intent of this model was to capture the influence of relatively sparse vegetation on sun-shade temperature differences. The models can be considered only approximate in nature due to the numerous assumptions and simplifications they contain; however, the models do provide some insight into how temperature differences in sun and shaded locations may be affected by near surface properties and conditions.

2.8.2 Model 1 - Model Without Soil Moisture

In the absence of any soil moisture and vegetation, the latent heat term in Equation 2.41 can be taken as zero, simplifying the energy balance.

2.8.2.1 Net Radiation

The net radiation Rn is given as

$$Rn = (R_b + R_d)\,(1-\alpha) + R_{sky} - R_s \tag{2.42}$$

where R denotes radiation, α is the surface albdeo, the subscripts b and d denote short-wave direct beam and diffuse radiation, respectively. The subscripts sky and s denote long-wave radiation emitted from the sky and ground surface, respectively.

The beam radiation on a horizontal plane surface can be given by (Campbell and Norman [1998])

$$R_b = Ro\ \tau^m \cos\psi \tag{2.43}$$

where Ro is the extraterrestrial flux density, τ is the atmospheric transmittance, m is the optical air mass number, and ψ is the solar zenith angle. The solar zenith angle can be calculated from the solar declination, latitude, and the diurnal phase of the sun with respect to local noon, and accommodate a non-level slope (Price [1977])

$$\cos\psi = \sin\delta \sin(\phi-\beta\cos\Psi) + \cos\delta \cos(\phi-\beta\cos\Psi) \cos(\Omega t - \beta \sin\Psi/\cos\phi) \tag{2.44}$$

where δ is the solar declination, ϕ is the latitude, Ω is the diurnal phase of the sun with respect to local noon, t is time, β is the slope angle, and Ψ is the slope strike. Ignoring local atmospheric pressure variations, m can be taken as the inverse of cos ψ. Usually, the atmospheric transmittance will be assumed to be 0.75, which is typical for clear sky conditions.

The ratio of diffuse radiation to beam radiation is nearly constant for clear sky conditions and is on the order of 30% of the beam radiation (Campbell and Norman [1998]). Thus, the diffuse radiation can be approximated by

$$Rd = 0.3\ Rb = 0.3\ Ro\ \tau^m \cos\psi \tag{2.45}$$

The long-wave radiation components can be expressed as

$$Rsky = \varepsilon s\ \sigma\ Tsky^4 \tag{2.46}$$

and

$$Rs = \varepsilon s\ \sigma\ Ts^4 \tag{2.47}$$

where σ is the Stephan-Boltzmann constant, T is temperature, ε is the emissivity and the subscripts sky and s denote sky and ground surface, respectively. Watson (1975) linearized the net long-wave radiation with respect to surface temperature as

$$Rsky - Rs = -4\ \varepsilon s\ \sigma\ Tsky^3\ (Ts - Tsky) \tag{2.48}$$

The sky temperature can be related to the local air temperature, Ta**.** Here, we use a linear expression given by Xue and Cracknell (1995)

$$Tsky = -129.3 + 1.387\ Ta \tag{2.49}$$

Combining the above expressions, the net radiation for a location that receives both beam and diffuse radiation becomes

$$Rn = 1.3\ (1-\alpha)\ Ro\ \tau^m \cos\psi\ - 4\ \varepsilon s\ \sigma\ Tsky^3\ (Tss - Tsky) \tag{2.50}$$

whereas a shaded location that receives only diffuse radiation, the net radiation will be

$$Rn = 0.3\ (1-\alpha)\ Ro\ \tau^{m} \cos\psi - 4\ \varepsilon s\ \sigma\ Tsky^{3}\ (Tsh - Tsky) \qquad (2.51)$$

Here we recognize that the surface temperatures may not be equal and distinguish them by the subscript ss, referring to the sun exposed surface temperature, and sh, referring to the shaded location surface temperature.

2.8.2.2 Sensible Heat Flux

The sensible heat flux, H, is given by

$$H = Ca\ (Ts - Ta)/r_{a} \qquad (2.52)$$

where Ca is the volumetric heat capacity of air, Ta is the temperature of the air, and r_a is the aerodynamic resistance of the air above the surface. Assuming neutral stability conditions and equal roughness lengths for heat and momentum, r_a can be expressed as a function of the wind speed.

$$ra = (UK^{2})^{-1}\ [\ln(z/zo)]^{2} \qquad (2.53)$$

where U is the wind speed, K is von Karmen's constant (0.4), z is a reference height, and zo is the roughness length. z and zo were taken as 2 m and 0.01 m, respectively, consistent with values used by others (e.g., Chung and Horton [1987]).

2.8.2.3 Soil Heat Flux

The soil or ground heat flux, G, depends upon the thermal properties of the surface materials and the thermal gradient

$$G = P\ \sqrt{\kappa}\ \ (\delta T/\delta z) \qquad (2.54)$$

where P is the thermal inertia, κ is the thermal diffusivity, and $\delta T/\delta z$ is the thermal gradient. The thermal gradient can be expressed as (Zhang [2001])

$$(Ts - Tg)/\Delta z \qquad (2.55)$$

where Δz is the distance to some depth below ground surface at which temperature varies very little from Tg, the nearly constant temperature of the ground at depth. This form of the gradient is easily to incorporate into the model, but its linear nature is problematic because the temperature profile, and consequently the gradient, is highly non-linear. In other words, the gradient may be substantially underestimated using this form.

Here, we will utilize the damping depth as Δz. The damping depth, Dd, is defined from the thermal properties as (Hillel [1998])

$$Dd = (2\ \kappa/\omega)^{1/2} \qquad (2.56)$$

where ω is the radial frequency of the temperature variation. A common expression for the temperature variation with depth is

$$Ts(z,t) = Tg + A[\sin\ (\omega t - z/Dd)]/ez/Dd \qquad (2.57)$$

where A is the maximum amplitude in surface temperature with respect to the constant ground temperature. Differentiating this expression, the maximum gradient at the surface occurs at solar noon and is equal to

$$(Ts-Tg)/Dd \tag{2.58}$$

2.8.2.4 Difference of Energy Balance Between Sunlit and Shaded Locations

The difference in the energy balance between the sunlit and shaded locations can be expressed as

$$(1-\alpha)/(Tss-Tsh) = (1/Rb)\{Ca/ra + P\sqrt{\kappa} / Dd + 4\,\varepsilon s\,\sigma\,Tsky^3\} \tag{2.59}$$

This assumes that a number of parameters are the same for the sunlit and shaded locations: the sky temperature, surface albedo, surface emissivity, wind speed, ground temperature, air temperature, thermal properties of the ground, and temperature variation with depth.

Consistent with other approaches and models for determining thermal inertia (see Cracknell and Xue [1996]), the temperature difference can be expressed as the amount of absorbed radiation divided by a term that includes the thermal inertia and referred to as the apparent thermal inertia (ATI)

$$\Delta T = (1-\alpha)/ATI \tag{2.60}$$

In this model, ATI is equal to the right hand side of Equation 2.59. ATI is comprised of three distinct factors that affect the temperature difference: sensible heat flux, ground heat flux, and thermal radiation flux from the ground.

2.8.2.5 Numerical Example

The model described above was used to calculate the maximum surface temperature difference with the inputs in Table 2.4 below. Input values were selected so that results could be compared with those calculated using the IR Response code by Walker (2002).

Table 2.4 Input Parameters

Parameter	Symbol	Value	Units	Reference
Extraterrestrial flux density	Ro	1382	W/m^2 sec	Price (1977)
Solar declination	δ	-23. 45	°	*
Latitude	ϕ	30 N	°	*
Slope angle	β	0	°	
Slope strike	Ψ	0	°	
Transmissivity	τ	0.75	-	Campbell and Norman (1998)
Local air temperature	Ta	290	K	
Specific heat of air	ca	0.718	kJ/(kg K)	
Wind speed	U	1	m/s	
Roughness length	zo	.01	M	Chung and Horton (1987)
Reference height	z	2	M	Chung and Horton (1987)
Thermal conductivity of ground	λ	Varied	W/(m K)	*
Heat capacity of ground	C	Varied	kJ/(m^3 K)	*
Emissivity	ε	0.9	-	*
Albedo	α	0.4	-	*

*values used to facilitate comparison with results of Walker (2002)

The magnitude of maximum temperature difference is compared to that of Walker (2002) for properties for granite and "dirt" in Figure 2.54. The temperature differences are smaller for the simple model here, but the trend is consistent. The dirt showed a greater temperature difference in both approaches compared to the granite. The comparison between the two approaches could be improved by ensuring that all of the input is comparable (e.g., the terms related to the thermal gradient, wind speed, local air temperature, etc.).

The model also allows the relative contribution of the three fluxes that comprise the apparent thermal inertia (sensible heat flux, thermal emissive flux and ground heat flux) to be assessed. The contribution of the ground heat flux is the largest component to the apparent thermal inertia, comprising 50% and 78% of the apparent thermal inertia for the dirt and granite, respectively. The contributions of the sensible heat flux and the thermal emissive flux are nearly identical at 25% and 11% each for the dirt and granite, respectively.

The model may be useful for simple parametric studies. With some additions, the model can be used to predict temperature differences as a function of time as well. The latent heat flux can also be added, but at the cost of additional assumptions and required meteorological input.

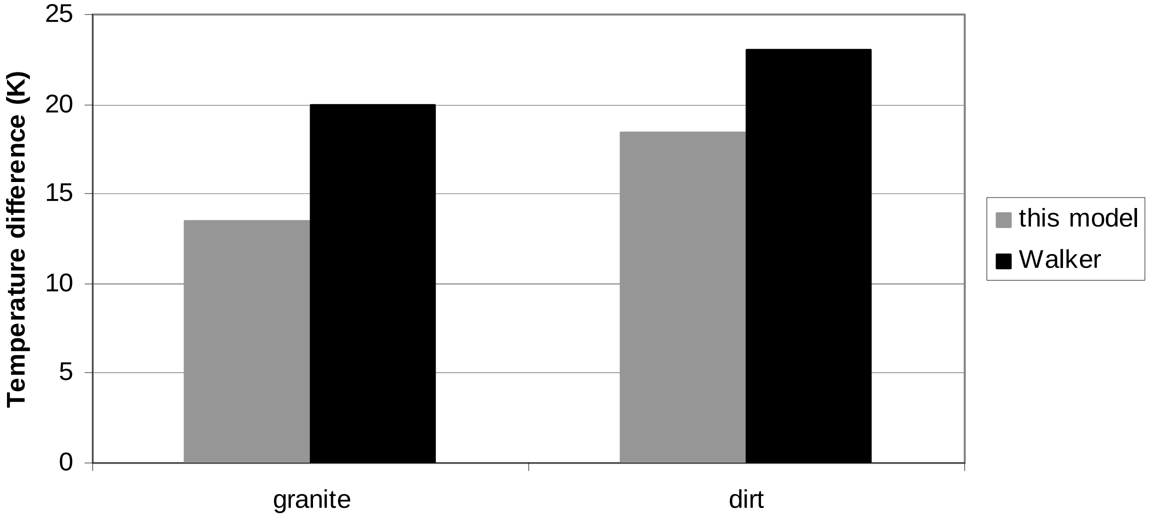

Figure 2.54 **Predicted temperature difference in sun and shade for granite and dirt properties from model described here and results of Walker (2002).**

2.8.3 Model 2 - Inclusion of Soil Moisture

The simple model was extended to include surface moisture. The original model will not be repeated here; only new material related to surface moisture will be presented in this section.

Surface moisture has two important effects on the surface temperature that are considered here. First, it modifies the thermal properties of the surface material (soil or rock). Second, evaporation of surface moisture affects the surface energy balance by consuming some of the incident solar radiation, resulting in less surface heating than occurs in dry soils. The effect of surface moisture on albedo is not considered.

2.8.3.1 Effect of Moisture on Thermal Properties

Models of the variation of the thermal properties of soil as a function of water content and porosity have been developed (Farouki [1986]), and indicate that moisture increases thermal inertia. The greater the thermal inertia, the less temperature difference would be expected between sunlit and shaded locations. The dependence of thermal properties on moisture can be accommodated in the model by incorporating these functions into the model so that the thermal conductivity and heat capacity are calculated as functions of the moisture content.

2.8.3.2 Soil Water Evaporation

The evaporation of soil moisture results is the conversion of liquid water at or near the ground surface to vapor and its transpiration to the atmosphere. This process requires energy to convert the water from the liquid to vapor phase. This amount of energy, expressed on a unit mass basis, is called the latent heat of vaporization and is about 2.47×10^6 J/kg at temperatures of interest here.

The latent heat flux, LE, is the product of the evaporation rate and the latent heat of vaporization, and can be expressed as a diffusion-type process driven by the differences in the water vapor pressure at the ground surface and in the atmosphere (e.g., Camillo, et al. [1988])

$$LE = c\ (e_s - e_a) \qquad (2.61)$$

where e_s is the vapor pressure of the soil air at the ground surface and e_a is the vapor pressure of the atmosphere. The constant c can be given by

$$c = (\rho\ ca\ )/\ (\gamma\ ra) \qquad (2.62)$$

where γ is the psychrometric constant, ρ is the density of air, ca is the specific heat of air, and r_a is the aerodynamic resistance of the air above the surface. r_a can be expressed as a function of the wind speed

$$ra = (UK2)^{-1}\ [\ln(z/zo)]^2 \qquad (2.63)$$

where U is the wind speed, K is von Karmen's constant (0.4), z is a reference height, and zo is the roughness length.

The vapor pressure of the soil (that is, the vapor pressure in the gas phase of the soil) can be expressed as a function of the relative humidity (rH) and the saturated vapor pressure at the surface temperature (e_s*)

$$es = rH\ es^* \qquad (2.64)$$

The saturation vapor pressure at the ground surface can be given accurately expressed as a third-order polynomial of the ground surface temperature (e.g., Brutsaert [1982]). For our purposes, a linear relationship with temperature is desired. Linearizing this expression over a range of 280 to 310 K yields

$$es^* = 1.732\ Ts\ - 479, \qquad (2.65)$$

which yields an R^2 of 0.95.

The relative humidity of the soil at the surface is related to the energy state of the soil water (Jury, et al. [1991])

$$rH = \exp\ \{\ (\Psi\ g\ Mw)/(R\ T)\} \qquad (2.66)$$

where Ψ is the soil water potential, g is acceleration, Mw is the molecular weight of water, R is the universal gas constant, and T is temperature. The soil water potential will be assumed equivalent to the matric potential, that is, osmotic pressures are neglected and the potential is simply equal to the negative pressure of the water in the unsaturated soil.

Evaluation of Equation 2.66 reveals that the relative humidity remains very high (close to one) until the potential becomes a very large negative number. For example, the relative humidity of 98% is associated with a potential of –3000 kPa. For perspective, a soil that is so dry that plants are unable to extract moisture from it is at a potential of about -1500 kPa. This indicates that the latent heat flux is not limited by soil moisture until the soil is quite dry.

The relative humidity of the soil can be expressed as a function of soil moisture (water content or saturation) if a relationship between soil moisture and potential is known. This relationship, referred to as the moisture characteristic, is commonly given by (van Genuchten [1980])

$$\Theta = (1 + (\xi\Psi)^n)^{-m} \qquad (2.67)$$

where Θ is the effective saturation, which is equal to $(\theta - \theta s)/(\theta s - \theta r)$, where θ is the water content and the subscripts s and r refer to the saturated and residual water contents; and ξ, n and m are fitting parameters for a particular soil. m is assumed to be equal to 1/(1-n).

The rH can then be given as

$$rH = \exp\{ (\Theta^{-1/m} - 1)^{1/n}\, g\, Mw/ (\xi\, R\, T)\} \qquad (2.68)$$

It is important to emphasize that, in order to express the relative humidity at the ground surface in terms of the amount of moisture in the soil, the moisture characteristic curve for the particular surface soil of interest must be known.

Combining Equations 2.61, 2.62, 2.64 and 2.65 yields the following expression for the energy flux due to evaporation:

$$LE = (\rho\, ca)/ (\gamma\, ra)\{rH\, (1.732\, Ts - 479) - ea\} \qquad (2.69)$$

where rH can be expressed in terms of potential (Equation 2.66) or saturation (Equation 2.68). An additional assumption here is that the temperature in the rH expression is taken as a constant. The difference in latent heat flux in the sunlit and shaded region can be given as

$$\Delta LE = (\rho\, ca)/(\gamma\, ra)\{rH\, 1.732\, (Tss - Tsh)\} \qquad (2.70)$$

An important assumption in Equation 2.70 is that the moisture (expressed as either potential or saturation) is the same in the sunlit and shaded regions.

2.8.3.3 Temperature Difference Model Including Surface Moisture

The difference in the latent heat flux in the sunlit and shaded regions can be readily included in the previous model. The resulting equation that describes the relationship between the temperature difference and the components of the surface energy balance becomes

$$(1-\alpha)/(Tss-Tsh) = (1/Rb)\{Ca/ra + P\sqrt{\kappa} / Dd + 4\, \varepsilon s\, \sigma\, Tsky^3 + (\rho\, ca) / (\gamma\, ra)(rH\ 1.732)\} \qquad (2.71)$$

This equation is a modification of Equation 2.59 of the previous model. As described in the previous model, the right hand side of the above equation is the apparent thermal inertia. Thus, including the latent heat flux due to evaporation increases the apparent thermal inertia of the soil.

In order to utilize this model, additional input parameters related to the saturation and soil hydraulic properties are required.

2.8.3.4 Numerical Example

The model described above was used to calculate the maximum surface temperature difference with the inputs in Table 2.5 below. These values are largely the same as those used by in the previous numerical example with additional input of saturation and surface soil hydraulic properties.

Table 2.5 Input parameters

Parameter	Symbol	Value	Units	Reference
Extraterrestrial flux density	Ro	1382	W/m^2 sec	Price (1977)
Solar declination	δ	-23. 45	°	*
Latitude	ϕ	30 N	°	*
Slope angle	β	0	°	
Slope strike	Ψ	0	°	
Tranmissivity	τ	0.75	-	Campbell and Norman (1998)
Local air temperature	Ta	290	K	
Specific heat of air	ca	0.718	kJ/(kg K)	
Wind speed	U	1	m/s	
Roughness length	Zo	.01	m	Chung and Horton (1987)
Reference height	Z	2	m	Chung and Horton (1987)
Thermal conductivity of ground	λ	Varied	W/(m K)	
Heat capacity of ground	C	Varied	kJ/(m^3 K)	
Emissivity	ε	0.9	-	*
Albedo	α	0.4	-	*
Saturation	S	Varied	-	
Van Genuchten's n	N	Varied		Carsel and Parrish (1988)
Van genuchten's ξ	ξ	Varied	1/m	Carsel and Parrish (1988)
Saturated water content	θs	Varied	-	Carsel and Parrish (1988)
Residual water content	θr	Varied	-	Carsel and Parrish (1988)

*values used to facilitate comparison with results of Walker, 2002

The presence of soil moisture substantially affects the temperature difference; more than one-half of the total incident energy is consumed by evaporation from a wet soil. In Figure 2.55, temperature difference is given as a function of saturation for soils of three different textures**:** sand, silt and clay. The surface temperature difference increases with decreasing saturation. Two distinct responses are observed**:** a steep, abrupt increase, and a gradual increase. The gradual increase is due to the modification of the thermal properties of the near-surface soils. The steep increase occurs as the soil dries sufficiently so that the latent heat flux decreases. This increase occurs over a relatively small saturation range because of the moisture characteristic response**:** small changes in saturation are associated with very large decreases in potential.

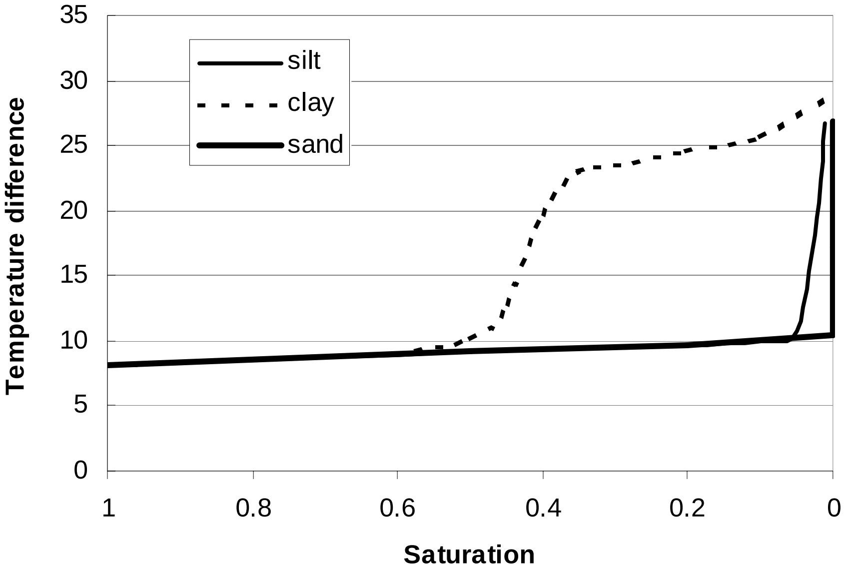

Figure 2.55 Surface temperature differences between sunlit and shaded regions as a function of saturation for three soil textures

The surface temperature response is shown to be a function of the hydraulic properties of the soil. In general, most soils will have a response similar to that shown for silt and sand. Until the saturations approach zero, the latent heat flux will significantly influence the thermal response. The clay is different because it retains significant water when it reaches potentials that are so small that the latent heat flux approaches zero.

This model may yield some insight into how changes in apparent thermal inertia as a function of time (i.e., multiple passes) can be exploited to infer characteristics of near-surface materials. A further step in the development of the model would be coupling the near-surface energy balance to moisture movement in near-surface soils. This coupling would require a numerical approach.

2.8.4 Model 3 - Inclusion of Vegetation

The simple model developed to predict surface temperature differences in sunlit and shaded locations was extended to include vegetation. Features common to earlier models will not be repeated in this section.

Vegetation significantly affects the near-surface energy balance by reducing the amount of incident solar radiation that reaches the ground surface. In addition, the remotely sensed surface temperature is a function of the amount of vegetation. Consequently, the utility of sun-shade temperature differences to deduce the thermal inertia of the ground decreases with increasing vegetation.

The approach developed here considers separately the energy balances of the vegetation and the bare soil. This approach, termed the two-layer approach, is in contrast to models that lump the vegetation and bare soil together in an “effective” single surface layer.

2.8.4.1 Surface Temperature

The remotely sensed temperature of the surface (Tr) is termed the radiometric temperature and can be approximated as a linear function of the temperature of the vegetation (Tv) and the temperature of the bare soil surface ground surface (Ts) (Anderson, et al. [1997]; Moran, et al. [1994])

$$Tr(\phi) = f(\phi)Tv + (1-f(\phi))\ Ts \qquad (2.72)$$

where $f(\phi)$ is the fraction of the radiometer view occupied by the vegetation and ϕ is the view zenith angle from which the surface is observed. $f(\phi)$ is often assumed to be of the form (e.g., Norman, et al. [1995])

$$f(\phi) = 1 - \exp(-0.5\ LAI/\cos\phi). \qquad (2.73)$$

where LAI is the leaf area index.

2.8.4.2 Energy Balances

The energy balances of the bare soil and vegetation are given as (Norman, et al. [1995])

$$Rn,s = Hs + LEs + Gs \qquad (2.74)$$

$$Rn,v = Hv + LEv \qquad (2.75)$$

where Rn denotes the net radiation at the surface, H is sensible heat flux, LE is latent heat flux, and G is the soil heat flux. The subscripts s and v denote the soil and vegetation, respectively. Note that this formulation assumes that there is no soil heat flux associated with the vegetation.

The net radiation that penetrates to the soil surface is given by (Anderson, et al. [1997])

$$Rn,s = Rn \exp(-\kappa\ LAI/\sqrt{(2\cos(\theta))}) \qquad (2.76)$$

where κ is an extinction coefficient and θ is the solar zenith angle. The net radiation absorbed by the vegetation is found from

$$Rn,v = Rn - Rn,s \qquad (2.77)$$

Assuming that the vegetation and the soil are in parallel (that is, there is no interaction between the heat fluxes from vegetation and soil surface), the sensible heat flux components are given by (Norman, et al. [1995])

$$Hs = (\rho\ Ca)\ (Ts - Ta)/\ (r_{ah} + r_s) \qquad (2.78)$$

$$Hv = (\rho\ Ca)\ (Tv - Ta)/\ (r_{ah}) \qquad (2.79)$$

where Ta is the air temperature above the soil and vegetation, ρ is the density of air, Ca is the specific heat of air, r_{ah} is the aerodynamic resistance to heat flow, and r_s is the resistance to heat flow in the boundary layer immediately above the soil surface.

The latent heat flux components are given by

$$LEs = (\rho\ Ca / \gamma)\ (es - ea)/\ (r_{ah} + r_s) \qquad (2.80)$$

$$LEv = (\rho\ Ca / \gamma)\ (ev - ea)/\ (r_{ah} + r_v) \qquad (2.81)$$

where r_v is the canopy resistance to transpiration, γ is the psychrometric constant, and ea, es and ev are the vapor pressures of the air, at the soil surface, and at the vegetation surface, respectively.

The vapor pressure of the soil can be expressed as a function of the relative humidity (rH) and the saturated vapor pressure at the surface temperature (e_s*)

$$es = rH\ es^* = rH\ e^*(Ts) \qquad (2.82)$$

The vapor pressure of the vegetation is assumed to be the saturated vapor pressure at the temperature of the vegetation surface

$$ev = ev^* = e^*(Tv) \qquad (2.83)$$

The saturation vapor pressure can be given accurately expressed as a third order polynomial of the temperature (e.g., Brutsaert [1982]). For our purposes, a linear relationship with temperature is desired. Linearizing this expression over a range of 280 to 310 K yields

$$e^* = 1.732\ T\ - 479 \qquad (2.84)$$

which has an R^2 of 0.95.

The latent heat fluxes can then be given as

$$LEs = (\rho\ Ca / \gamma)\ (rh\ (1.732Ts - 479) - ea)/\ (r_{ah} + r_s) \qquad (2.85)$$

$$LEv = (\rho\ Ca / \gamma)\ ((1.732\ Tv - 479) - ea)/\ (r_{ah} + r_v) \qquad (2.86)$$

2.8.4.3 Resistances

The aerodynamic resistance is given by the expression of Campbell and Norman (1998)

$$r_a = [\ln((z-d+z_h)/z_h) + \psi_H]\ [\ln((z-d+z_m)/z_m) + \psi_m]/(k^2U) \qquad (2.87)$$

where U is the wind speed measured at height z above the surface, d is the zero plane displacement, z_h and z_m are the roughness lengths for sensible heat and momentum, ψ_H and ψ_m are the stability correction factors for heat and momentum, respectively, and k is von Karmen's constant (0.4). Following others (e.g., Colaizzi, et al. [2003]), d and z_m can be estimated as a function of the vegetation canopy height h as $d = 0.67\ h$ and $z_m = 0.13\ h$, and z_h can be estimated as $0.2z_m$. The stability corrections depend on the sensible heat flux and require an iterative procedure to determine. To simplify the solution here, neutral stability will be assumed (i.e., the stability corrections will be assumed to be zero). Colaizzi, et al. (2003) found that including the stability corrections did not improve their energy-based solution for estimating crop soil moisture. Campbell and Norman (1998) discuss the conditions under which this assumption is reasonable. Note that assuming neutral stability (no correction) and equal roughness lengths for heat and momentum, the above equation reduces to the simple expression used in the previous models (Equations 2.53 and 2.63).

The soil surface resistance term can be thought of as the additional resistance due to heat moving through the boundary layer immediately above the soil surface (Anderson, et al. [1997]). r_s can be expressed as (Norman, et al. [1995])

$$r_s = (a + bUs)^{-1} \tag{2.88}$$

where a and be are empirical constants, and Us is a term that can be calculated based on wind speed, leaf area index, and vegetation height.

The resistance of the vegetation to transpiration is assumed to have the following form (van de Griend, et al. [1985])

$$r_v = r_o \exp(-r_1(\psi_{rz} - wp)) \tag{2.89}$$

where r_o and r_1 are empirical constants. The wilting point, wp, is the soil water potential below which plants can not extract moisture, and is typically assumed to be on the order of –160 m. ψ_{rz} is the soil water potential in the root zone.

2.8.4.4 Temperature Difference Models for Vegetated Surface and Bare Soil

Following the approach of the development of the previous models, sunlit areas are assumed to receive direct beam and diffuse radiation whereas shaded areas receive only diffuse radiation. The differences between the energy balances for the sunlit and shaded regions yields an expression for the sun-shade temperature difference of the form

$$(1-\alpha)/\Delta T = ATI \tag{2.90}$$

where ATI is the apparent thermal inertia. The expression for the bare soil is

$$(1-\alpha_s)/(T_{ss}-T_{sh})s = (1/Rb,s)\{ \rho Ca / (r_{ah}+r_s) + P \sqrt{\kappa} / Dd + 4 \varepsilon s \sigma Tsky^3 + \rho ca /(\gamma (r_{ah}+r_s))(rH\ 1.732)\} \tag{2.91}$$

and for the vegetation

$$(1-\alpha_v)/(T_{ss}-T_{sh})_v = (1/Rb,v)\{ \rho Ca / r_{ah} + 4 \varepsilon s\ \sigma\ Tsky^3 + (\rho\ ca) / (\gamma (r_{ah}+r_v)(rH\ 1.732)\} \tag{2.92}$$

where the subscripts ss and sh refer to sunlit and shaded locations, respectively. The radiometric temperature difference is from Equation 2.72. The expression for the bare soil is similar to the previous model but accounts for the reduction in incident solar radiation received by the bare ground due to vegetation. In addition, the expressions for the resistances are somewhat different than were used previously. The expression for the vegetation temperature difference does not include the soil heat flux and consequently does not involve the thermal inertia of the ground.

The increased capability of the model to include vegetation comes at the expense of more assumptions and simplifications as well as additional input. These input include leaf area index, root zone moisture, vegetation albedo, and soil and vegetation resistance model parameters.

2.8.4.5 Numerical Examples

The model described above was used to calculate the soil, vegetation and radiometric surface temperature differences for a combination of surface and root zone moisture conditions and amount of vegetation. The input values are in Table 2.6.

Table 2.6 Input Parameters

Parameter	Symbol	Value	Units	Reference
Extraterrestrial flux density	Ro	1382	W/m^2 sec	Price (1977)
Solar declination	δ	-23. 45	°	*
Latitude	ϕ	30 N	°	*
Slope angle	β	0	°	
Slope strike	Ψ	0	°	
Transmissivity	τ	0.79	-	Campbell and Norman (1998)
Local air temperature	Ta	293	K	
Heat capacity of air	Ca	1.01	kJ/(kg K)	
Wind speed	U	2	m/s	
Albedo of soil	αs	.3		
Albedo of vegetation	αv	.25		
Thermal conductivity of ground	λ	1	W/(m K)	
Heat capacity of ground	C	2x10^6	kJ/(m^3 K)	
Emissivity	ε	0.9		
Canopy height	H	0.5	m	
Leaf size	S	0.004	m	
Extinction coefficient	κ	0.5		
Wilting point	Wp	-160	m	
Stomatal resistance coefficient	Ro	20	s cm-1	van de Griend, et al. (1985)
Stomatal resistance coefficient	r1	2.6e-4	cm-1	van de Griend, et al. (1985)
Soil resistance coefficient	A	.004	m s-1	Norman, et al. (1995)
Soil resistance coefficient	B	.012		Norman, et al. (1995)
Fractional vegetation coefficient	F	Varied		
Surface soil moisture	Rh	Varied		
Root zone moisture	ψrz	Varied		

Soil, vegetation and radiometric temperatures are given in Figure 2.56 as a function of fractional vegetation coverage. The surface soil is modelled as partially dry by assigning the moisture factor described previously as 0.5. The vegetation is assumed to transpiring at its maximum rate because the root zone moisture is at the field capacity of the soil. The vegetation substantially affects the radiometric temperature difference, decreasing it until about 70% vegetation coverage, after which it rebounds. Because this model was developed with relatively sparse vegetation in mind, values beyond 50% vegetation have more uncertainty associated with them.

Radiometric temperatures are given in Figures 2.57 and 2.58 as a function of fractional vegetation coverage for a number of scenarios with respect to soil moisture. In Figure 2.57, the surface soil moisture decreases from saturated to fully dry, while the root zone moisture stays fixed at a value that allows the vegetation to transpire at its maximum rate. In Figure 2.58, the surface soil remains completely dry, and the root zone moisture decreases from its maximum value to the wilting point, below which the plant can not extract moisture from the soil for transpiration. Taken together, these figures may represent the progressive drying first of the surface soil (Figure 2.57) followed by drying of the root zone (Figure 2.58).

Both of these figures indicate the expected response: as the soil and vegetation dry**:** the temperature difference between sun and shade increases. The results suggest that fractional vegetation coverage is a crucial input to any attempt to interpret and utilize temperature differences in sunlit and shaded areas.

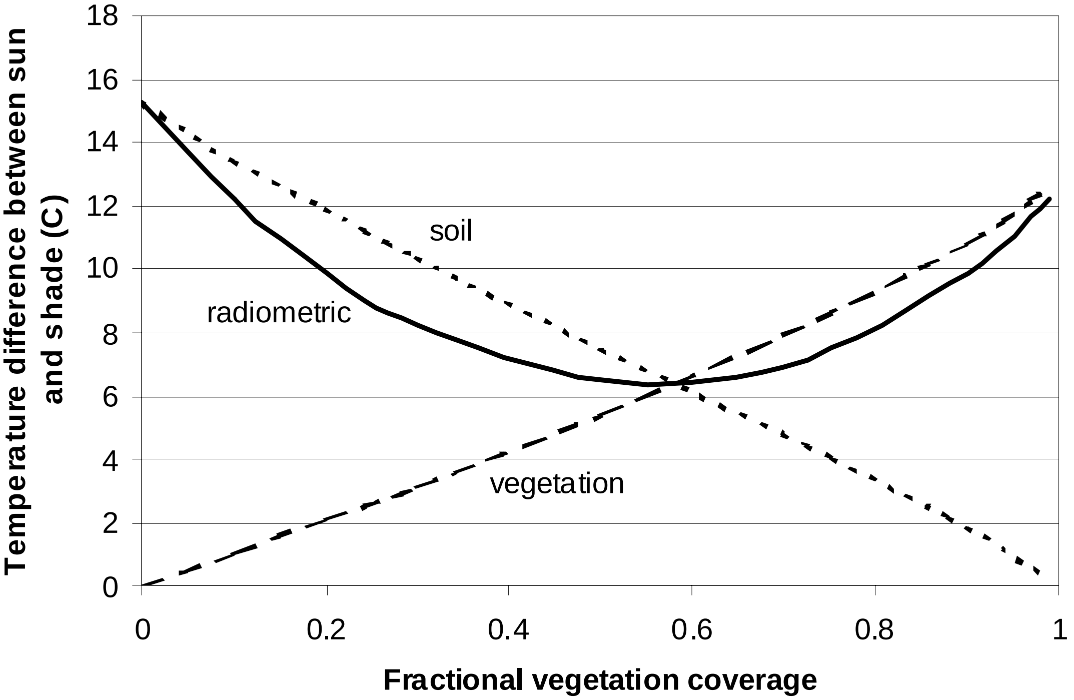

Figure 2.56 Soil, vegetation and radiometric temperatures as function of fractional vegetation coverage for a partially dry soil and fully transpiring

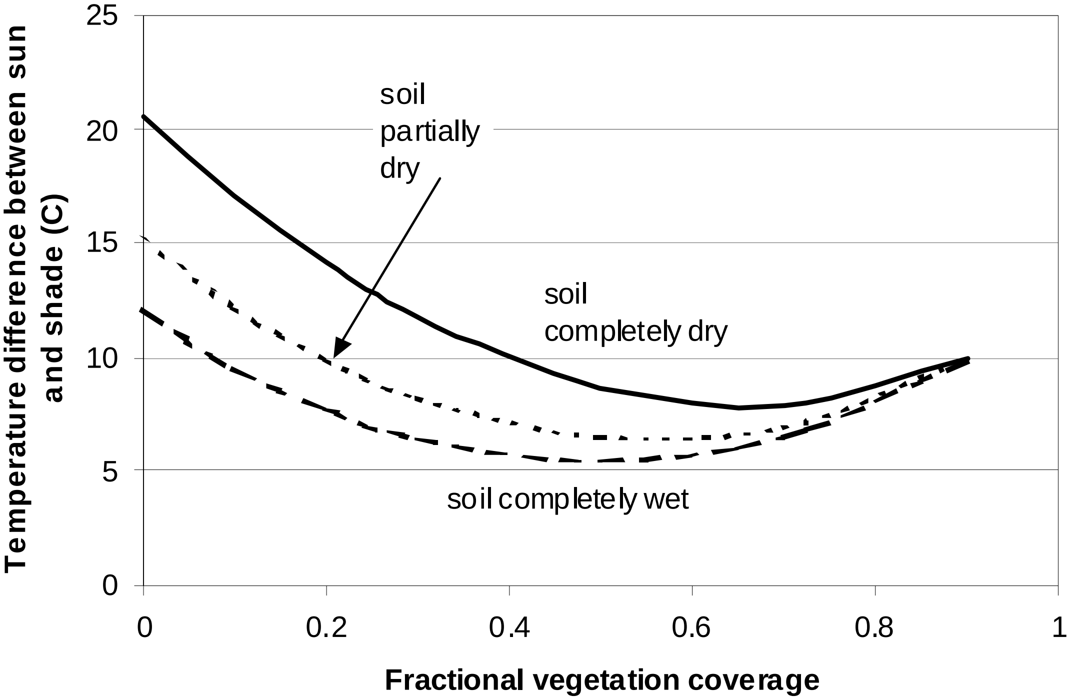

Figure 2.57 **Radiometric temperature as a function of fractional vegetation coverage for three different surface soil moisture values. The vegetation transpires at its maximum rate.**

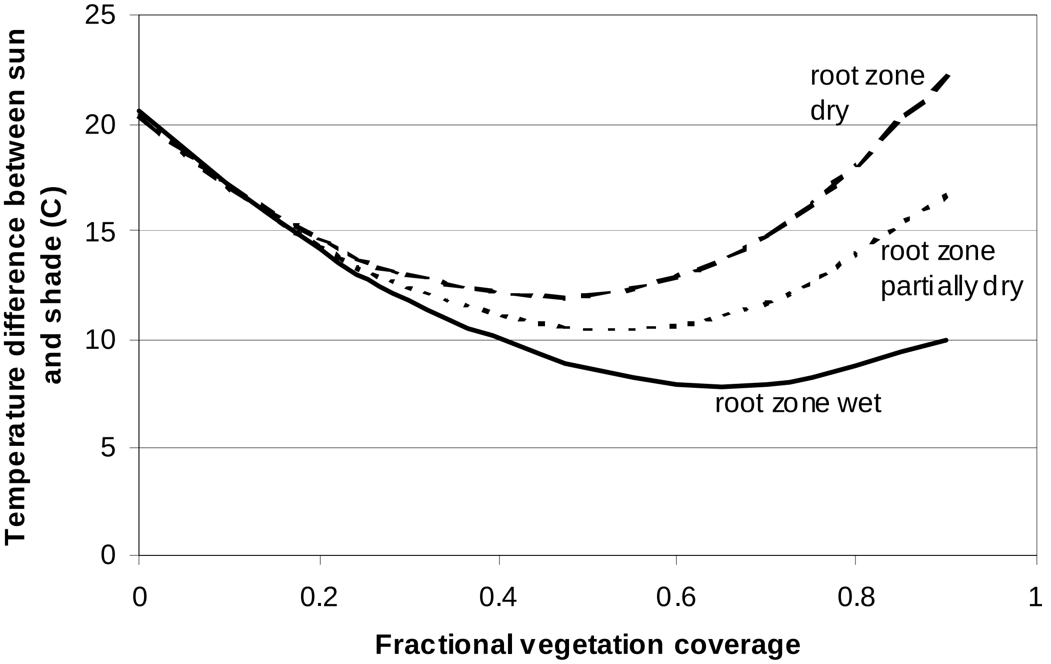

Figure 2.58 **Radiometric temperature as a function of fractional vegetation coverage for three different root zone moisture amounts. The soil surface is completely dry so there is no evaporation.**

2.8.5 Conclusions

The model substantiates the concept that sun-shade temperature differences develop and that the magnitude of the temperature difference will depend in part on the thermal properties of the near-surface materials. This suggests that identifying near-surface materials may be possible from sun-shade temperature differences.

The potential for extracting information regarding near-surface properties becomes increasingly difficult if soil moisture and vegetation are included. This is due to two factors:

1. Additional uncertainty is embedded in the way the model describes evaporation and transpiration, processes that are difficult to represent robustly yet simply.

2. Moisture and vegetation reduce the magnitude of the temperature difference between sunlit and shaded regions.

In order to apply an analytical model, some estimate of the moisture conditions and amount of vegetation has to be made. Even if the temperature differences are being used in an empirical or comparative fashion, the presence of moisture and vegetation can dominate the response and must be constrained to the extent possible. The model is also sensitive to local meteorological data. In areas where this data is not available, a unique interpretation of the data in terms of near-surface properties is not possible. It is certainly possible to develop more sophisticated models; however, it should be recognized that the trade-off for complexity is often more uncertainty and additional input requirements.

2.9 Field Measurements

2.9.1 Introduction

Field measurements were conducted to evaluate the concept of extracting information from sun-shade temperature differences. The measurements were conducted at an existing well-characterized and instrumented field test facility. These experiments focused on the near-surface processes and material properties that give rise to temperature differences. Temperatures were measured from the ground using hand-held, non-contact sensors; thus, important issues surrounding remote sensing of surface temperatures were not addressed.

The objectives of the field measurements were to:

- Demonstrate the concept that measurable sun/shade temperature differences will develop, and
- Assess utility of methods for discriminating properties and composition of near-surface soils.

The tests were conducted at the Alternative Landfill Cover Demonstration (ALCD) field test site in Sandia National Laboratories' Tech Area III. Measurements of surface temperatures were made at sunlit and shaded regions on soil, vegetation and rock surfaces. These measurement locations coincided with existing sub-surface arrays of thermocouples and moisture probes. An on-site meteorological station provided air temperature, humidity, wind speed and incident solar radiation. An additional advantage of the site is that the site and its soils have been well characterized.

For the vast majority of a typical year, the ambient surface conditions at this site are very dry. The surface can be wetted with an existing sprinkler system to allow the differences in the surface temperature in the sunlit and shaded regions to be measured in response to moisture.

2.9.2 Measurement Methods

2.9.2.1 Surface Temperature Measurements

Surface temperatures were measured with a hand-held infrared camera (Raytheon ExplorIR). The camera measures the spot temperature of objects with an accuracy of about 4%. The camera also captures and stores high-resolution thermal images of objects.

At first, shaded areas were created with tarps; but they were vulnerable to high winds. After that, surplus tables (1.5 m x .5 m surface area) were used.

The principal measurement location was on the crest of the capillary barrier cover. The surface soil at this location is a silty sand (a common near-surface soil in the Albuquerque area). The vegetation on this site was a sparse stand (estimated at 10% coverage maximum) of native grama and dropseed grasses. Measurements were also made on the evapotranspiration cover, which has a veneer of rounded stone, nominally 2 cm in diameter.

The site has a data collection system in place for the measurement of water balance components on the landfill covers. A meteorological station records hourly air temperature and humidity, wind speed and direction, and incident solar radiation. Measurement systems embedded in the ground include water content probes and thermocouples. Maintenance of the data collection system ceased in late 2002, and data collection capability has progressively degraded with time. Meteorological data could no longer be monitored, and a number of water-content probes went off-line. One important shortcoming of the data is that the sub-surface temperature measurements were recorded but were not included in the program for downloading the data. Consequently, these data were unavailable.

2.9.2.2 Thermal Properties of Near–Surface Soils

Measurements were made of the thermal properties of near-surface soils using a hand-held heat dissipation probe (Decagon Devices KD2). This device measures the response to a thermal pulse from a 10–cm–long rod inserted into the soil. From the measured response, the thermal conductivity and diffusivity are calculated and displayed. The interpretation method assumes constant soil properties. A concern with this measurement method applied to near-surface soils is that the water content is not constant with depth and, consequently, the thermal properties are not constant with depth.

A test was devised to obtain thermal properties as a function of water content on a relatively uniform soil. Near-surface soil was packed into a 10–cm–diameter, 14–cm–long PVC tube with a sealed bottom. The dry density and water content of the soil were 1.50 g/cm^3 and 1.3%, respectively. The water content of the soil in the cylinder was increased by introducing additional water on the top of the soil and letting it redistribute for at least 48 hours.

Measurements of thermal properties were made with the thermal probe at each value of water content.

Measurements of thermal properties as a function of depth in the field soil profile were also made. A hole was dug with a shovel, permitting the probe to be inserted horizontally into the soil at different depths. Samples for measurement of gravimetric water content and soil water potential were obtained at these depths as well.

2.9.2.3 Lysimeter Tests

A number of plastic tubes filled with soil, referred to as lysimeters, were placed in the ground and their temperatures were monitored. The purpose of the lysimeters was to create soil surfaces with known or measurable water contents so this effect on the surface temperature could be investigated.

The lysimeters are 10 cm (4") in diameter and nominally 15 cm (6") long. The soil was packed into the lysimeters at a dry density of 1.50 g/cm^3. Four lysimeters were installed: dry soil in sun, dry soil in shade, wet soil in sun, and ambient soil in sun. The dry soil lysimeters had an initial water content of 1.3%. The wet soil lysimeter included a perforated plastic tube that penetrated the soil along its depth to facilitate wetting of the soil. Water was added to the wet lysimeters prior to surface temperature measurement to ensure that the surface soil was very wet and presumably experiencing maximum evaporation. The ambient lysimeter was constructed with an initial water content of 10.4%.

The ambient lysimeter was removed (dug up) periodically and weighed so that evaporative loss could be measured. Due to the extremely windy conditions experienced after the lysimeters were in place, as the ambient lysimeter dried, a portion of the surface soil was lost to wind erosion, thus compromising the evaporation measurement.

2.9.2.4 Potential Measurements

Soil water potential measurements were made with a field portable psychrometer (Decagon Instruments WP-4). This device, which utilizes small samples of soil (nominally 10 g), can measure potentials to about –80 MPa. Thermal equilibrium between the soil and the device is an important factor in the accuracy of the measurement.

Measurements of potential were often made when soil samples were taken for water content measurements. In addition to measurements on surface soils, potentials were measured on soils as a function of depth below ground surface.

Some of the soil samples obtained as a function of depth below the surface were used to investigate the relationship between potential and surface temperatures. Once the potential of the soil samples was measured, they were set in the sun and their temperatures were re-measured.

2.9.3 Results

2.9.3.1 Temperatures of Soil and Vegetation

Measurements of the soil surface temperature were made periodically during the spring and early summer of 2003. These measurements were most often made as a pair, with one measurement in complete sun and one in complete shade. On occasion, temperature measurements were made of the vegetation as well.

The surface temperature measurements were made under a wide range of climatic conditions, particularly with respect to air temperature and wind speed. While there were some precipitation events during the spring of 2003, the ground surface at the time of the measurements always appeared “dry,” never “damp.” The soil at the surface had a potential below the resolution of the pyschrometer, that is, less than about –80 MPa. A few centimeters below the surface, the soil was noticeably wetter, consistent with the conceptual view that water from within the soil profile was moving upward and evaporating at (or just below) the ground surface.

An example of the sun-shade temperature contrast is shown in Figure 2.59, which includes a photograph and thermal image of the sun-shade boundary on the capillary barrier cover where the majority of the measurements were made. The field of view is approximately 1 m for both images. The thermal image confirms the substantial temperature difference between sun and shaded regions. The sun-shade transition is fairly sharp, occurring over a distance of 10 cm or so. The small amount of vegetation at this location can be identified by its cooler temperature.

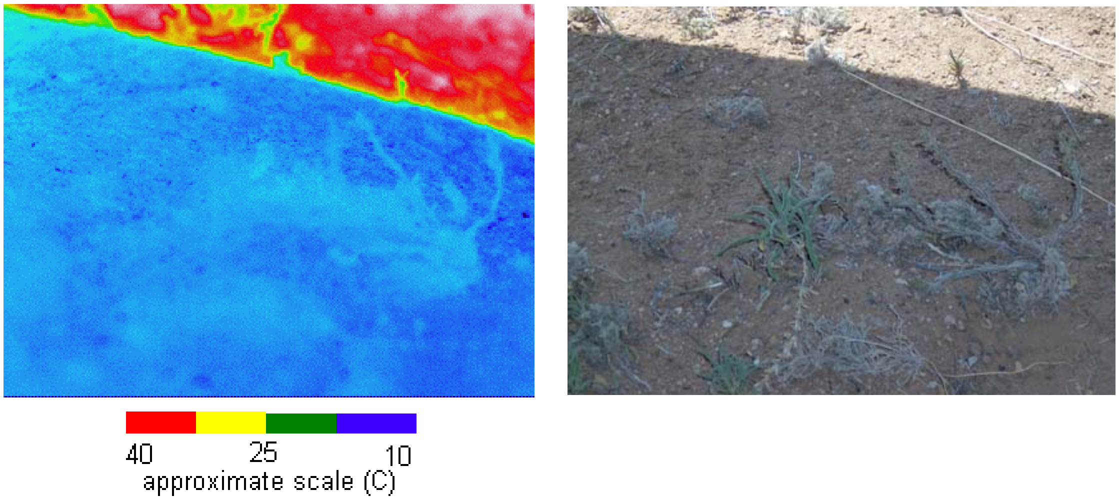

Figure 2.59 Thermal image and photograph showing sun-shade boundary

Measured sun-shade temperature differences are summarized in Table 2.7 and Figure 2.60. The majority of these tests were conducted on ambient soil. In addition, the lysimeters with dried soil in the sun and shade are included, as well as the few sun-shade measurements of vegetation and stones.

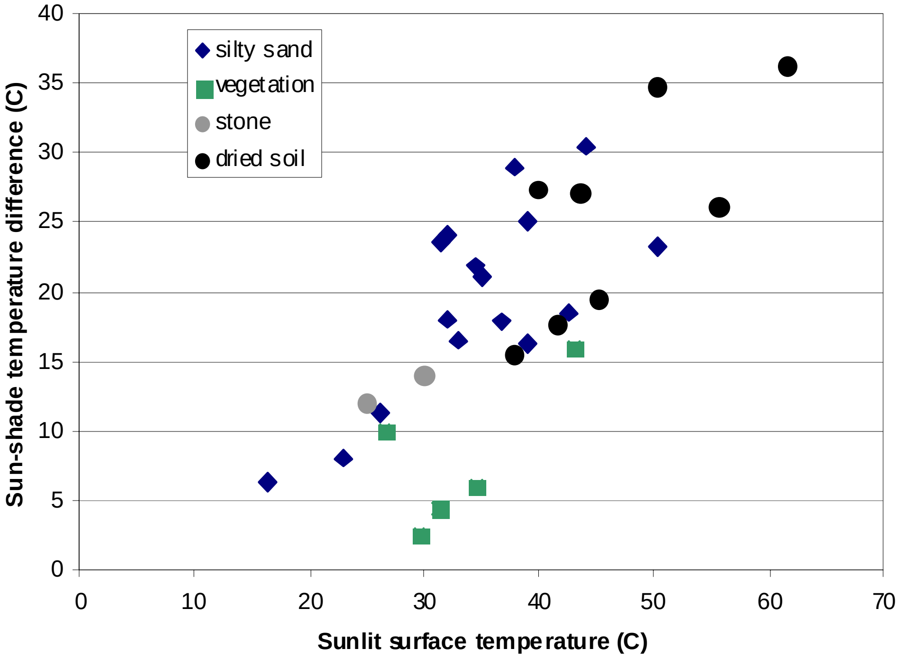

Figure 2.60 Summary of sun-shade temperature difference vs. sunlit temperature

Table 2.7 Summary of sun-shade temperature measurements on soils and vegetation

Material	**Soil Surface Temperature (C)**			**Air Temperature (C)**
	Sunlit	**Shade**	**Sun–Shade**	
Silty sand	37.8	8.9	**28.9**	17
Silty sand	33	16.5	**16.5**	20.3
Silty sand	39	14	**25**	20.3
Silty sand	35	14	**21**	20.3
Silty sand	32	14	**18**	20.3
Silty sand	23	15	**8**	14.1
Silty sand	16.3	10.1	**6.2**	17.6
Silty sand	32	8	**24**	17.6
Silty sand	31.4	7.9	**23.5**	9
Silty sand	26.1	14.9	**11.2**	9
Silty sand	34.5	12.7	**21.8**	13
Silty sand	44	13.6	**30.4**	19
Silty sand	36.8	19	**17.8**	19.7
Silty sand	39	22.8	**16.2**	20.2
Silty sand	42.5	24.1	**18.4**	24
Silty sand	50.2	27	**23.2**	26
Silty sand - dried	40	12.7	**27.3**	13
Silty sand - dried	43.6	16.5	**27.1**	18
Silty sand - dried	50.2	15.5	**34.7**	19
Silty sand - dried	37.8	22.3	**15.5**	18
Silty sand - dried	41.7	24.1	**17.6**	19
Silty sand - dried	45.3	25.9	**19.4**	24
Silty sand - dried	55.7	29.7	**26**	26
Silty sand - dried	61.5	25.4	**36.1**	22
Vegetation	43	27	**16**	22
Vegetation	31.3	27	**4.3**	26
Vegetation	29.5	27	**2.5**	26
Vegetation	34.5	28.5	**6**	26
Vegetation	26.5	16.5	**10**	20.3
Light stone	25	13	**12**	20.3
Dark stone	30	16	**14**	20.3

At the beginning of the test program, the focus was on bare soil temperature and only a few measurements of vegetation temperature were made. Nonetheless, the thermal images revealed that the vegetation was cooler than the soil, even during the early spring when the plants are expected to be dormant or nearly dormant. Figure 2.61 shows examples of a thermal image and corresponding photograph of typical native vegetation.

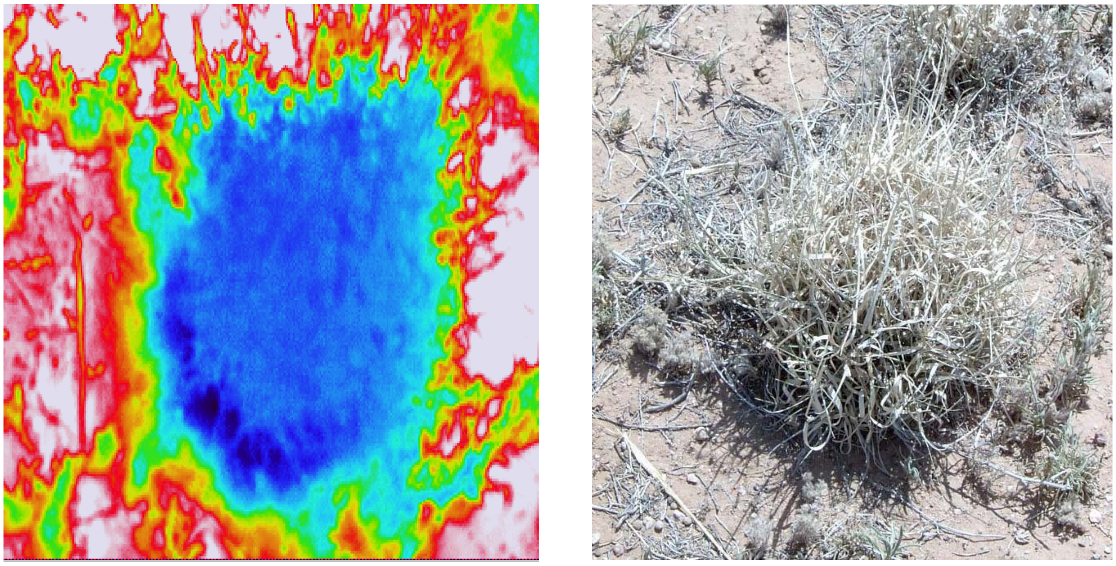

Figure 2.61 Thermal image and photograph of grama grass at ALCD test site

A thermal image of a pile of rounded cobble is shown in Figure 2.62. This image indicates that the stones “self-shade” themselves, and depending on their position, temperatures can readily vary by more than 20° C. This result highlights the variability or non-uniformity of surface temperatures, and highlights the need to specify the scale of the temperature measurements.

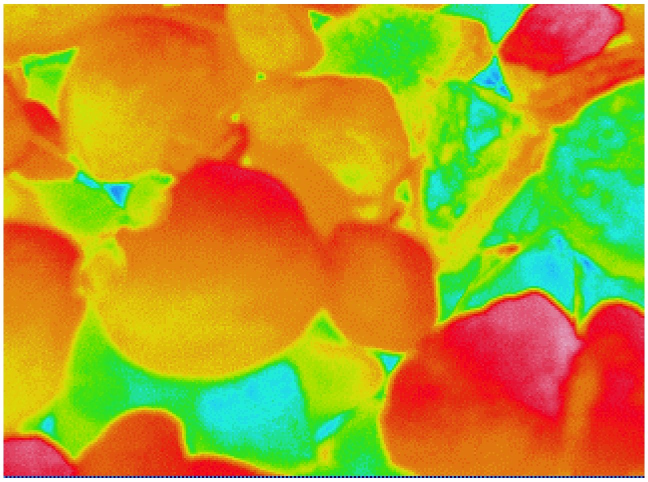

Figure 2.62 Thermal image of cobble pile

In addition to significant spatial variability, on occasion, considerable temporal variation was observed. In particular, surface temperatures fluctuated a few seconds after a rapid change in the wind speed such as during gusty periods. This was a relatively frequent occurrence during the blustery spring of 2003. The temperature change was in the direction expected, that is, the temperature would decrease with increasing wind speeds. The magnitude of the temperature change was variable, but often the temperature would vary by more than 5° C over just a few seconds.

2.9.3.2 Lysimeters

Temperatures of the soils in the dry, wet, and ambient lysimeters are given in Figure 2.63 along with the air temperature. The surface temperature of the ambient soil remains between the dry and wet soils, as expected. Generally, the air temperature tracks close to the wet soil temperature. The data that deviates from this trend may be due to the test procedure. Typically, water was added to the wet lysimeter and the surface temperature measurement was made after a few hours. In the case of the wet soil's being much warmer than the air temperature (day 60), it is believed that the water added to the lysimeter was relatively warm and the measurement was made shortly after the water was added. Similarly, for measurements taken when the air temperature is significantly above the wet soil temperature (perhaps day 11), the water added may have been relatively cold and there may have been insufficient time for equilibrium to come about between adding the water and the temperature measurement.

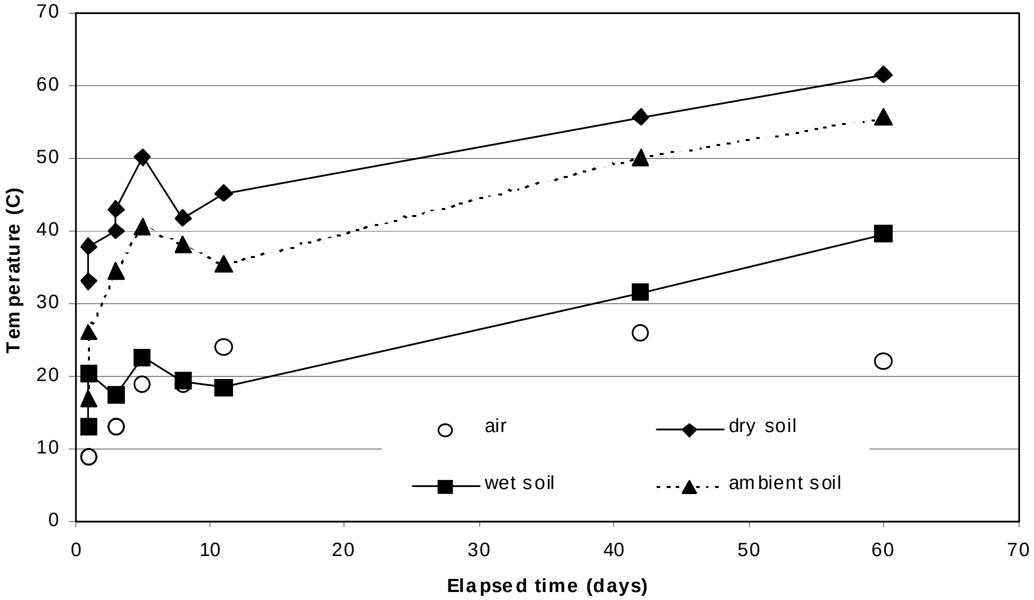

Figure 2.63 Lysimeter and air temperatures

The surface temperatures can be used to estimate evaporation from the soil (e.g., Qiu, et al. [1999]). By rewriting the energy balance and assuming that albedo and net radiation do not change as a soil dries, a soil evaporation transfer coefficient, h, can be defined as

$$LE/(Rn - G) = (Td - Ts)/(Td - Ta) = h \qquad (2.93)$$

where Td is the dry soil temperature, Ta is the air temperature, Ts is the temperature of the ambient (drying) soil, LE is the latent heat flux due to evaporation, and Rn-G is the difference between the net radiation and the soil heat flux. These ratios are proportional to the evaporation occurring in the soil. The greater the ratio, the more evapotranspiration will be occurring. A similar ratio can be defined for the case of the wetted soil, substituting Tw for T in Equation 2.93. In this case, the evaporation (LEmax) should approach the maximum amount and the surface temperature of the wet soil will be nearly equal to the air temperature as the value of h approaches one. The lysimeter data, expressed in terms of h, are given in Figure 2.64.

Under the condition of a very wet soil, the evaporation rate will approach the maximum evaporation rate, or the potential evaporation. Priestly and Taylor (P–T) [1972] estimated the potential evaporation rate as

$$\mathrm{Lemax}/(\mathrm{Rn}-\mathrm{G}) = 1.26\ \Delta / (\Delta + \gamma) \tag{2.94}$$

where Δ is the slope of the vapor saturation vs. temperature and γ is the psychrometric constant. Equation 2.94 is also given in Figure 2.64. The predicted values from the P–T expression compare favorably to the wet lysimeter data. The two data points that deviate the most from the P–T expression (for days 11 and 60) are suspect because of the temperature of the water added to the lysimeter to wet the soil as previously noted.

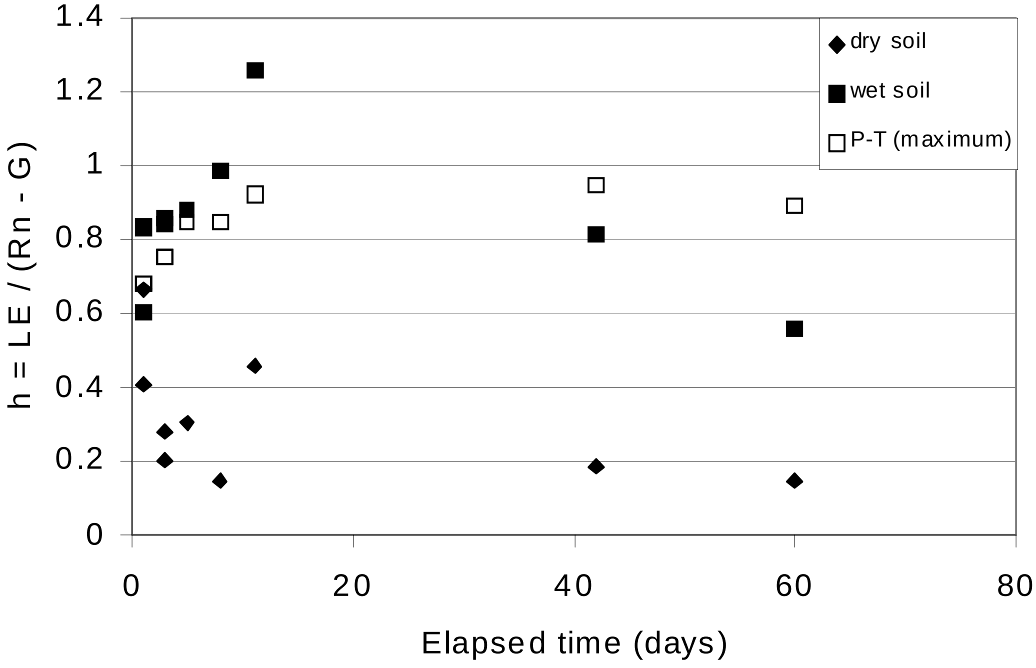

Figure 2.64 **Soil transfer coefficient, h, for dry and wet soil, and theoretical maximum from P–T approximation**

These results from this simplified analysis suggest that surface temperature measurements may provide a useful means of deducing evaporation rates. In addition to its importance to certain agricultural and water resources issues, evaporation (as latent heat) is a principal element in the energy balance. Some estimate of the amount of evaporation (if any) occurring from a soil surface must be made in order to accurately use surface temperatures (including sun-shade differences) to deduce near-surface thermal properties.

2.9.3.3 Thermal Properties

Thermal conductivity as a function of water saturation is given in Figure 2.65 for the data collected from the PVC tube (denoted test data). These data are compared to predicted values from the models of Johansen and DeVries (described in Farouki [1986]). These models predict thermal conductivity as a function of soil properties such as density, water content, and quartz content. In an evaluation of numerous thermal models, these two were found by Farouki to be two of the more useful models for estimating thermal properties. The results here suggest that the Johansen model provides a good estimate of thermal properties as a function of water content.

Also shown in the figure are in situ data collected from inserting the heat dissipation probe horizontally at different depths in holes. The water content was obtained from samples taken close to the probe location. These data do not fit the Johansen model as well, and may fit the DeVries model at least as well. However, issues with these data include non-uniformity of density, water content, and soil type in the soil exposed in the side of the hole.

2.9.3.4 Potential Measurements

Measurements of the water potential of the soils at the surface were most often below the resolution of the psychrometer, that is, less than about –80 MPa. These values of potential correspond to what would be qualitatively described as "dry soil," but do not necessarily mean that the soil was completely dry. It should be pointed out that a relatively dry surface layer does not rule out substantial evaporation with water being supplied from within the soil profile.

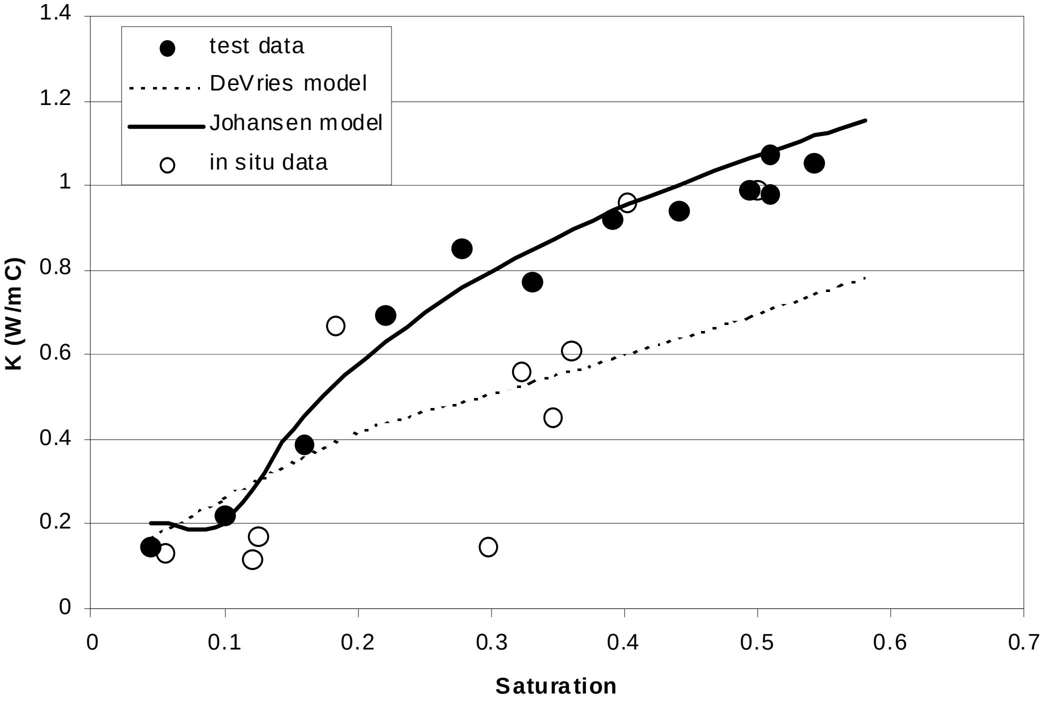

Figure 2.65 Thermal conductivity as a function of soil saturation

The speed at which the immediate soil surface dries is illustrated by data from the ambient soil lysimeter. On the day it was placed in the field in a pre-wetted condition, the soil had a potential of –1.4 MPa. Within two days, the potential was less (–80 Mpa).

Below the immediate surface, there is more water in the soil and potentials are smaller. On two occasions, measurements of potential were made on samples taken at a number of depths below the surface. These results, shown in Figure 2.66, reveal the strong upward gradient that exists in the top 5 cm (2") or so that drives evaporation.

The significance of these results for the problem of estimating soil characteristics from temperature differences is that, even when the soil surface appears to be very dry, there may still be significant evaporation and the latent heat term can not be neglected when solving for thermal properties of near-surface soils.

The measurements made to investigate the viability of determining potential from surface temperatures were inconclusive. A principal problem with this method was that the samples were so small that they lost moisture very fast in the sun and it was difficult to measure the sample temperature with the thermal camera. Further investigation of this method should be conducted under controlled laboratory conditions.

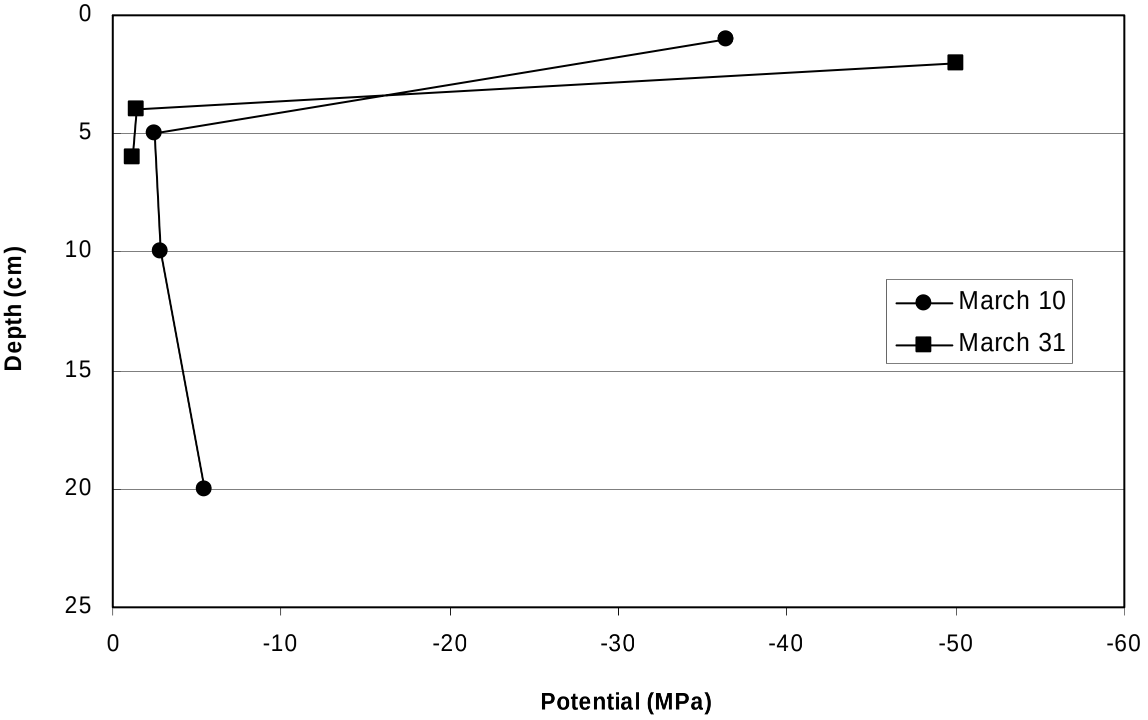

Figure 2.66 Potential as a function of depth below surface

2.9.4 Discussion

Significant temperature differences between sunlit and shaded regions were measured in the field. These differences are clearly a function of near-surface properties. For example, consider the temperature differences measured on March 12, 2003 given in Figure 2.67 for four materials: soil, grama grass, light-colored stone and dark-colored stone. The relative values of the temperature differences can be qualitatively explained. Even for stones that have the same thermal properties, light-colored stones will reflect more of the incident radiation, and consequently develop a lower temperature and temperature difference than will darker stones. The grass is transpiring water, which consumes a significant portion of the incident radiation, which will reduce its temperature. The soil was relatively dry and, although it is likely that there is some evaporation occurring, more of the incoming solar radiation is available to increase its temperature. Compared to the stones, the greater temperature difference measured in the soil indicates that it has a lower effective thermal inertia. This is expected from the known influence of air and water-filled porosity on thermal properties.

An important lesson from the field measurements is the significance of water on temperatures that develop near the surface. The effect of water is clearly illustrated by the lysimeter data shown in Figure 2.63. The temperatures varied by 20° C or more between the dried and wetted soil in the sun. The wet soil and the vegetation had very similar temperatures (within a few degrees), which is consistent with both materials' evaporating water at a maximum rate controlled by the atmosphere. This result suggests that the moisture status of the near-surface material can be more important to the surface temperatures that develop than are thermal properties.

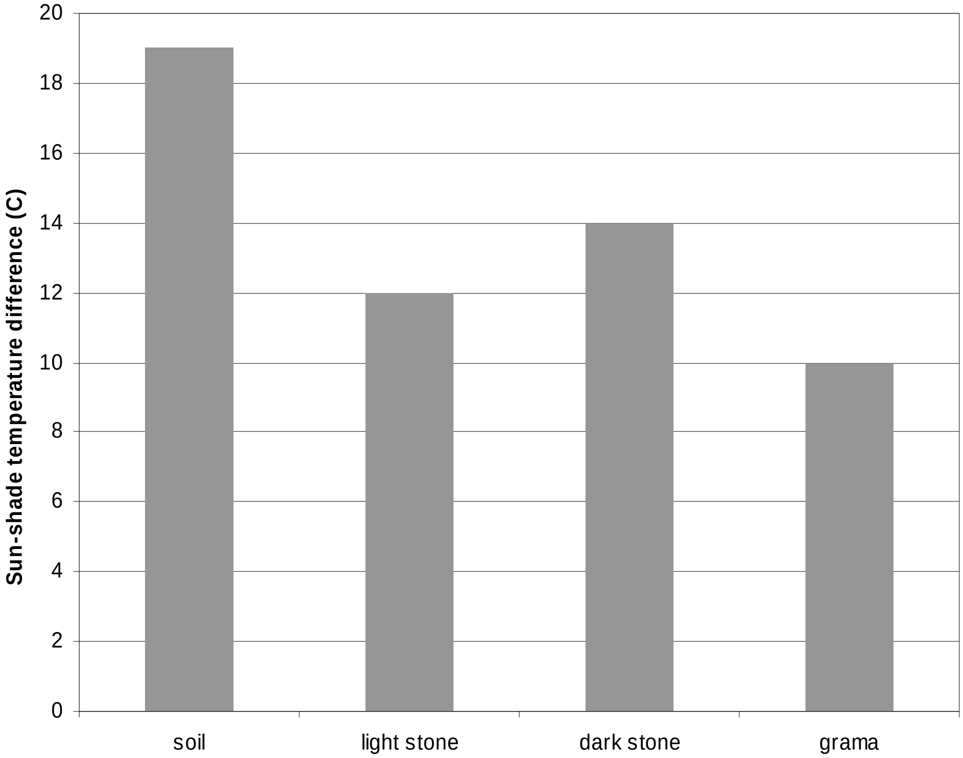

Figure 2.67 **Comparison of temperature differences measured on March 12, 2003 for four different surface materials**

An important conclusion from the field measurements is the significance of water on the temperatures that develop in the near surface. The effect of water is clearly illustrated by the lysimeter data shown in Figure 2.63. The temperatures varied by 20° C or more between the dried and wetted soil in the sun. The wet soil and the vegetation had very similar temperatures (within a few degrees), consistent with both materials evaporating water at a maximum rate controlled by the atmosphere. This result suggests that the moisture status of the near-surface material can be more important to the surface temperatures that develop than the thermal properties.

Another conclusion regarding water is that even apparently dry soil can evaporate water and this dry-soil evaporation, although well below the maximum amount, is significant enough to affect the surface temperatures and temperature differences that develop in the soil. The lysimeter data bear this out: the ambient soil never reached the temperature of the dry soil, indicating that it continued to experience evaporative cooling. Thus, in support of our goal of being able to discriminate near-surface materials, it is imperative that some information regarding moisture status be available.

Field measurements also highlighted issues regarding the scale of the thermal measurements. Consider the thermal image of the cobble shown in Figure 2.62. The temperature of the cobble depends on the scale of the measurement. If the scale is small, say on the order of a centimeter, then temperatures can be measured for sunny exposures and self-shaded areas, and for different types and colors of cobble. As the scale is increased, more of these materials are included in the sensed region and a composite temperature is measured. This result suggests caution in interpreting remotely sensed temperatures in terms of laboratory or small-scale derived thermal response of near-surface materials. The variation in surface temperature with wind speed is another important observation. The temperature difference that is measured at any point in time depends on both the average wind speed and the wind speed near the time of sensing. This identifies another challenge for using remotely sensed temperatures for deducing near-surface properties or characteristics.

In summary, the field measurements indicate that measurable temperature differences develop in sunlit and shaded regions and these temperature differences are related to the thermal properties of the materials. The presence of moisture, the sensing of areas including vegetation and self-shaded regions, and variable wind speeds are some of the issues that make using temperature differences to discriminate material properties challenging.

2.10 Evaluation of Analytical Models with Field Data

2.10.1 Introduction

Data collected in the field were evaluated and compared to the predicted response from the analytical models. The purpose of the evaluation was to:

- Evaluate ability of the analytical models to predict field values, and
- Investigate sensitivities of temperatures to factors such as moisture status, wind speed, etc.

Each time field measurements were made, there was an opportunity to compare the measured values with those predicted using the analytical models. Input to the analytical models included date and time of day (for solar zenith angle calculations), air temperature, relative humidity, and wind speed from the meteorological data available at the field test site. An important input parameter for which there was no measured value was albedo. In addition, some terms used in calculating the surface resistances such as roughness length were not measured.

The primary output from the models was the sun-shade temperature difference. In addition, the models provided predictions of the energy balance terms, such as predicted net radiation, soil heat flux, etc.

Generalizations regarding model capabilities include:

- The models usually predict the net radiation at the field site to within a few percent.
- The model output is quite sensitive to surface moisture and wind speed. The model is also sensitive to albedo and roughness length (a surface characteristic that is not well known).
- Model output that matches the measured data is, to some extent, non-unique. Different combinations of input parameters can yield predictions that are reasonably close to the measured data.

2.10.2 Evaluation of Data from Bare Soil Surface

On March 10, 2003, surface temperatures were measured on a nearly bare soil surface exposed to sun and shaded conditions. Measurements of water content, soil water potential and thermal properties were made as a function of depth from the surface. Climatic data was also collected.

Some comments on the data used as input in the model follow. The surface water potential was very low (below the resolution of the measurement system), consistent with the appearance of the surface as quite dry. The resolution of the potential measurement was –85 MPa, which corresponds to a moisture factor of 0.54 in the simple model. In other words, measurements indicated that the surface moisture factor could range from 0 to 0.54. The wind speed was recorded within about a minute of the measured surface temperatures. However, wind speed was observed to be quite variable, and there was no certainty that the recorded value was the actual wind speed at the time of temperature measurement.

Model results are given in Figure 2.68 (solid lines) as a function of the moisture factor for three assumed wind speeds. The model utilized the measured thermal properties of the near surface soil. Also shown in the figure is the measured sun-shade temperature difference as well as the region of possible moisture factors based on the field measurement. For the wind speed of 1.7 m/s, the corresponding moisture factor would be 0.3, a value consistent with the measured range.

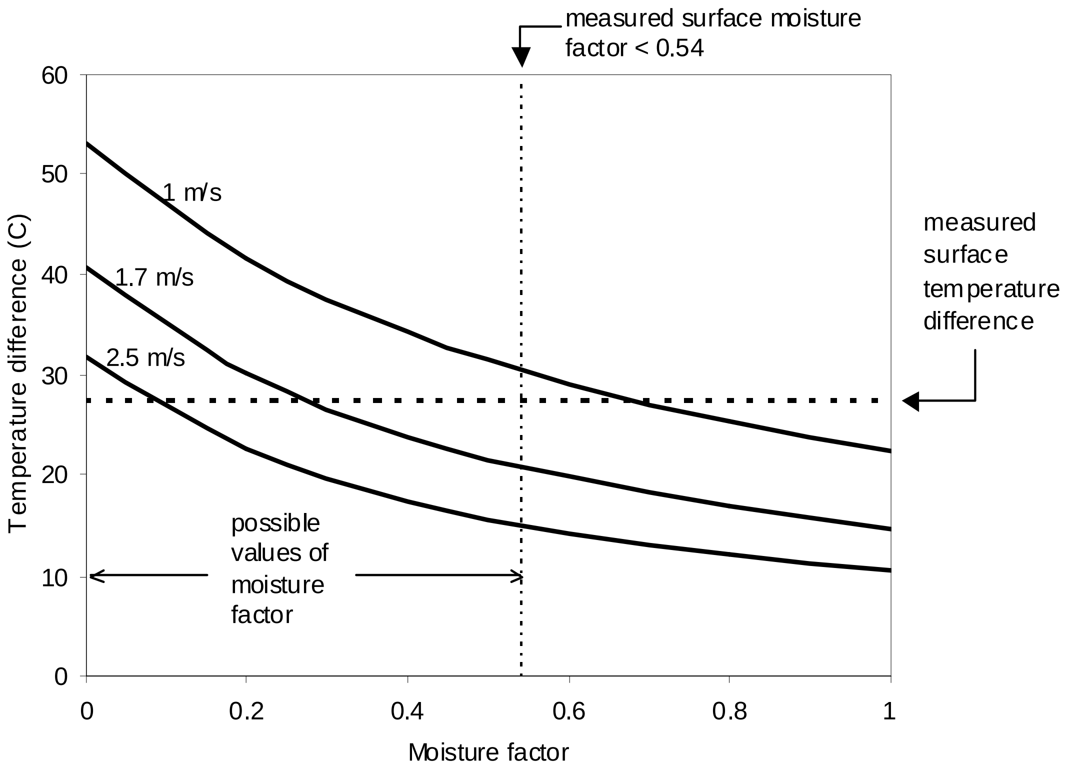

Figure 2.68 **Predicted temperature difference as a function of the moisture factor for three different wind speeds. Recorded wind speed was 1.7 m/s within about 1 minute of measurement. Measured surface temperature difference and moisture factor values are for bare soil at ALCD site on March 10, 2003.**

On March 12, 2003, sun-shade temperature measurements were repeated. During these measurements, the wind speed varied noticeably. At the same time, the surface temperature was observed to change. (As expected, with increased wind speed, the surface cooled). Coincident with measurements of surface temperatures, estimates of the wind speed were made. These data are shown in Figure 2.69. Also shown in this figure is the model prediction (solid line) as a function of wind speed, assuming a moisture factor of 0.3 (from the 3/10 data analysis). The model provides a reasonable estimate of the trend of the sun-shade surface temperature difference with wind speed.

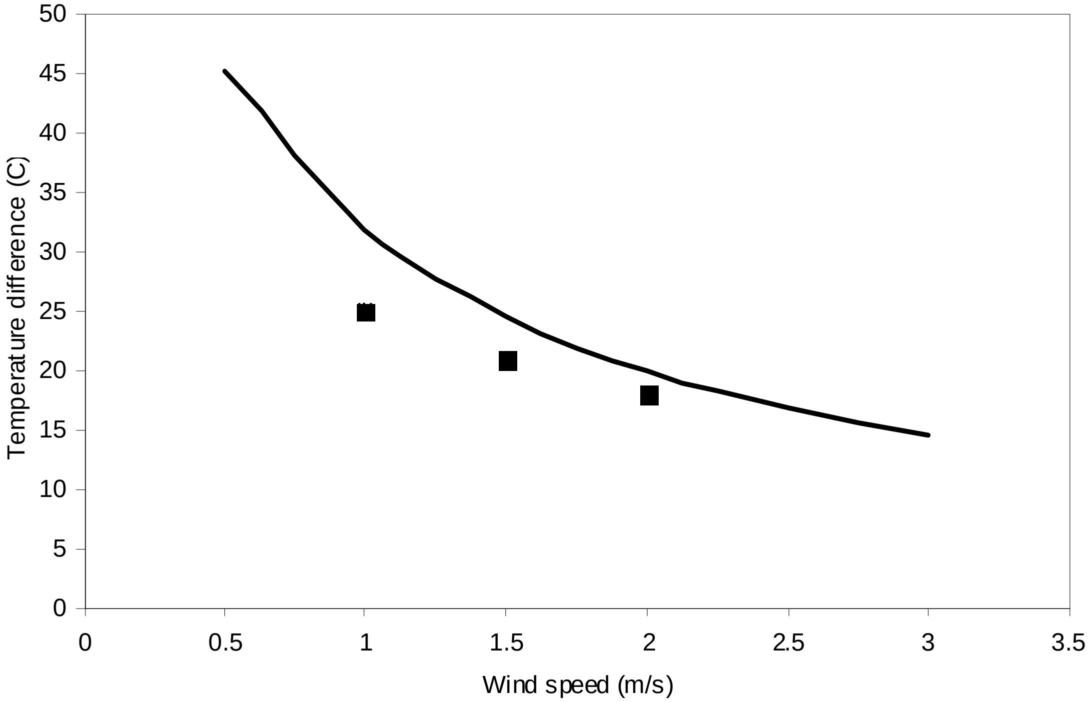

Figure 2.69 **Solid line is predicted temperature difference as a function of wind speed for bare soil with moisture factor of 0.3. Symbols denote measured temperatures at estimated wind speed on March 12, 2003 at ALCD site with bare soil.**

2.10.3 Evaluation of Data from Stone–Covered Surface

On March 12, 2003, sun-shade temperature differences were made on a surface comprised of stones of variable composition in the 2 to 10 cm size range. In contrast to the bare soil site, it was not possible to make independent thermal properties measurements with the Decagon thermal probe on the stone.

There was considerable variation in the surface temperature, especially in the sunlit area. Sun-shade temperature differences varied from 24 to 12 °C. As expected, dark colored stones tended to be warmer and have greater temperature differences. Two stones that exhibited much different surface temperatures, one dark and one light, were collected for cursory identification. The dark stone was identified as a basalt or andesite, and the light-colored stone was identified as rhyolite with perhaps up to 20% quartz (Borns, personal communication).

In Figure 2.70, model predictions of surface temperature differences are calculated for the light-colored stone (albedo=0.4) and the dark-colored stone (albedo = 0.1) as a function of thermal inertia. These calculations assumed no moisture. For the measured temperature difference, the thermal inertia for the two albedos can be found. These values of thermal inertia are quite high (>2500 TIUs), even for intact rock, suggesting that the model is lacking with this surface condition. Including moisture (even though the surface of the stones seemed dry) and accounting for the rough surface in the energy balance may be ways of improving the model.

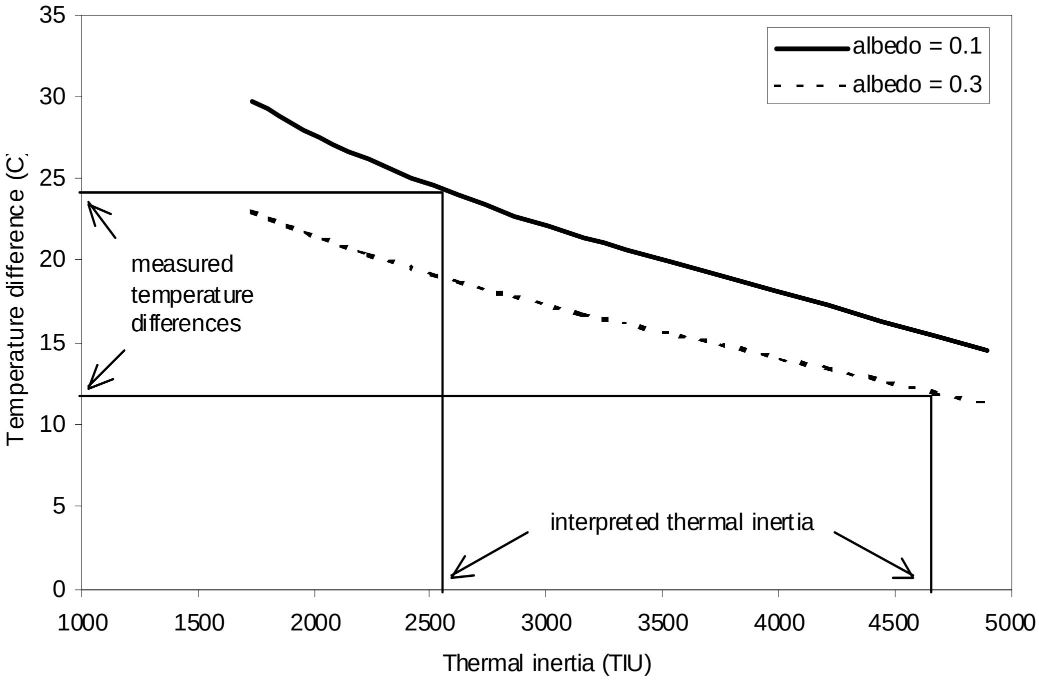

Figure 2.70 **Model prediction of sun-shade temperature difference as a function of thermal inertia for two different values of albedo, corresponding to light and dark colored stone. Field measured temperature differences and interpreted thermal inertia are also given.**

2.10.4 Evaluation of Albedo from Dry Soil

The data from the dry soil in sun and shade lysimeters can be used to exercise the analytical model without including a latent heat flux. In particular, these data can be used to estimate the albedo of the dry soil surface. Model predictions corresponding to measurements made on April 11 and May 19 as a function of albedo are shown in Figure 2.71. The predicted temperature differences are greater for the April 11 date because the wind speed was lower on that day. The measured temperature differences for these days are used to define, for each day, an albedo that results in a good match with the model. The interpreted albedos of about 0.3 and 0.35 are in the reasonable range based on the literature, but have not been confirmed by measurement.

The albedos should be the same on both days because the soil conditions were the same. Not unexpectedly, the results were very sensitive to the wind speed used in the models. For example, changing the wind speed in the May 19 simulation by 20% yields a good match to the April 11 albedo estimate.

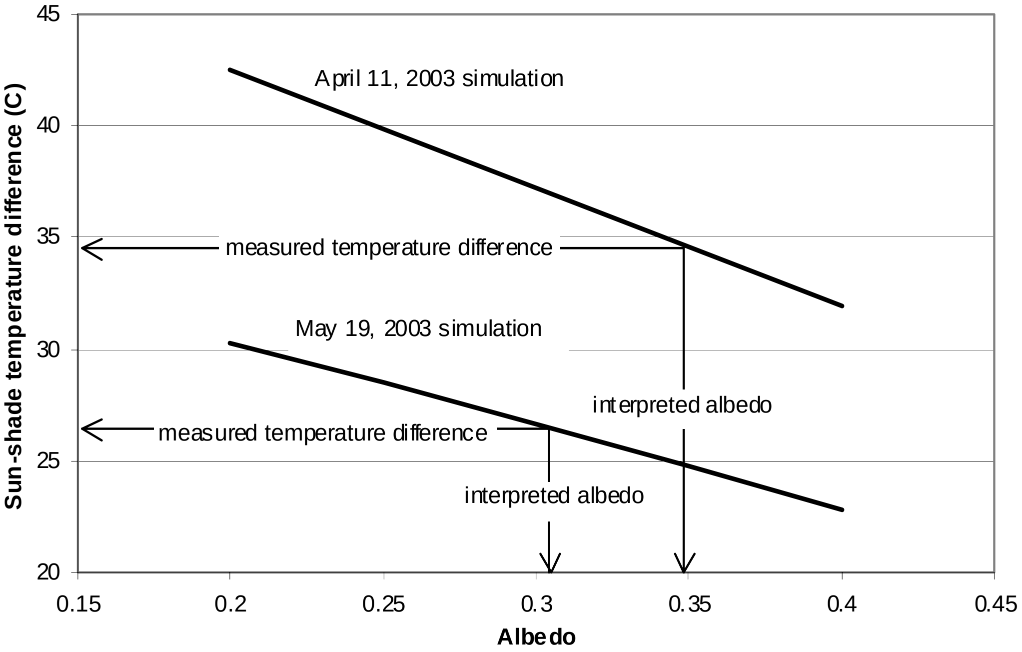

Figure 2.71 **Interpreted albedos for April 11 and May 19 measured temperatures by matching to model simulations for these dates with variable albedos (solid lines)**

2.10.5 Evaluation of Vegetation Temperature Differences

A limited number of measurements of sun-shade temperature differences of vegetation were made. The temperatures varied considerably in the clumpy grass at the field site and the minimum temperatures in the "heart" of the vegetation were recorded. Typical values are given in Table 2.8.

Table 2.8 Typical sun-shade temperature difference for vegetation

Date	Temperature Difference (°C)
March 12	10
May 19	8
June 16	16

The analytical model that includes vegetation was applied to the conditions of May 19. The model predicted temperatures ranging from 12 to 23 °C as the root zone moisture decreased from fully wet to the wilting point. This result suggests that the model predictions are in the range of the measured values. However, because the resistance model and the numerous vegetation parameters were taken from the literature, these results should not be viewed as verifying the model.

2.10.6 Discussion

The analytical models predict temperature differences that are consistent with those measured, which suggests that the models capture much of the important behavior and processes that control the development of temperature differences.

At the same time, evaluation of the models with the field data reveals that there are so many unknowns (non-constrained input parameters) that it is not likely that predicted temperature differences can be used to extract precise thermal properties of surface materials. This suggests that the most fruitful approach may be to pursue empirical and/or comparative data analysis methods with the analytical models.

One of the most problematic aspects of the analytical models is the definition and parameterization of resistances for soil and vegetation. First, the model descriptions of the soil and vegetation resistances utilized in the analytical models were developed for specific applications and conditions, and they have not been verified or confirmed as being appropriate for the conditions under consideration here. Resistances are very difficult to measure and thus it is very difficult to verify a resistance model. Second, the input parameters for the resistance models are not always well known or easy to determine. Wind speed is an important input parameter; but it should be measured locally, which may be problematic at remote or hostile sites. The vegetation and soil resistances contain parameters that have been empirically derived from very limited data. Extrapolating these parameters to different conditions introduces more uncertainty. These considerations suggest that an approach that avoids explicitly describing resistances may be worthwhile.

2.11 A Method for Estimating Bare Soil Temperature from Radiometric Temperatures that Include Vegetation

2.11.1 Introduction

A principal objective of the RemoteGeo project is to interpret thermal inertia of the ground surface. This objective is complicated by the presence of vegetation. In the vegetated portions of the ground surface, the soil heat flux, and consequently the influence of the thermal properties of the soil on the energy balance, is generally assumed as negligible (Kustas and Norman [1997]). Consequently, for purposes of obtaining near-surface properties of the ground, it is the temperature of the bare surface we need, not the radiometric temperature, which is a composite of both the vegetation and bare soil temperatures.

The radiometric temperature (Trad) is given as a function of temperatures of the bare soil (Ts) and vegetation (Tv)

$$Tr(\varphi) = [f(\varphi)\, Tv^n + (1 - f(\varphi))\, Ts^n]^{1/n} \qquad (2.95)$$

where f(φ) is the fraction of the sensor field of view occupied by vegetation when viewed at the angle φ, and n is the power in the Stephan-Boltzman equation and is typically taken as 4. This equation assumes a single emissivity. Anderson, et al. [1999] indicated that the linear approximation to (1) is adequate for most applications

$$Tr(\varphi) = f(\varphi)\, Tv + (1 - f(\varphi))\, Ts \qquad (2.96)$$

One means to extract the bare soil temperature from the radiometric temperature is to measure the radiometric temperature at more than one view angle (Francois [2002]). An alternative to this approach, which may be useful if directional viewing is not available, is given below.

2.11.2 Vegetation Indices (VIs)

Vegetative indices (VIs) are algebraic combinations of reflectances in red and near infrared bands. The VIs provide spatial and temporal information related to vegetation-related variables such as leaf area index and fractional vegetation cover. The most common VI is the Normalized Difference Vegetation Index (NDVI)

$$\mathrm{NDVI} = (\mathrm{NIR} - \mathrm{R})/(\mathrm{NIR} + \mathrm{R}) \tag{2.97}$$

The Soil Adjusted Vegetation Index (SAVI) is believed to be a more useful VI in the case of sparse vegetation

$$\mathrm{SAVI} = (\mathrm{NIR} - \mathrm{R})/(\mathrm{NIR} + \mathrm{R} + \mathrm{L}) * (1 + \mathrm{L}) \tag{2.98}$$

where L is an “adjustment factor,” typically taken as 0.5.

One application of VIs has been to produce scatterplots of VI vs. radiometric temperature. These data should fall within a theoretical area that often resemble a trapezoid (Moran, et al. [1994]). The boundaries of the trapezoid can be interpreted in terms of the amount of vegetation (full bare soil to fully vegetated, which is a function of VI) and moisture status (from wet to dry, which affects the temperature).

2.11.3 Vegetation Index Applied to Sun–Shade Exposure

We propose to map a vegetation index as a function of sun-shade status rather than moisture status. Four bounding conditions can be considered:

- Bare soil, full sun,
- Bare soil, complete shade,
- Full vegetation, full sun, and
- Full vegetation, complete shade.

The shape in VI – Tr space by which sunlit and shaded regions are bounded can be estimated by considering separately the soil and vegetation temperatures.

The minimum value of VI is associated with bare soil. At this condition, a temperature difference between sunlit and shaded regions of the soil develops. With increasing VI, the net radiation that penetrates to the soil decreases. By combining Equations 2.73 and 2.76, it can be shown that, with increasing VI, this decrease in net radiation is expected to be linear. The temperature difference between the sunlit and shaded regions is shown to be a linear function of soil net radiation in Equation 2.91. Although not explicitly derived previously (because the focus was on temperature differences), by following the same line of reasoning as above, the temperatures of the sunlit and shaded regions of soil would be expected to also be linear with VI. This assumed relationship is shown in Figure 2.72.

The temperature of the vegetation can be estimated in a manner similar to that for the soil. The maximum temperature difference between sunlit and shaded vegetation would be expected to occur at the maximum VI. The temperature difference will decrease linearly with the net radiation that strikes the vegetation (Equation 2.92), which is linearly related to the VI. The vegetation temperatures in sunlit and shaded regions would be expected to be linear in VI as well, as shown in Figure 2.72.

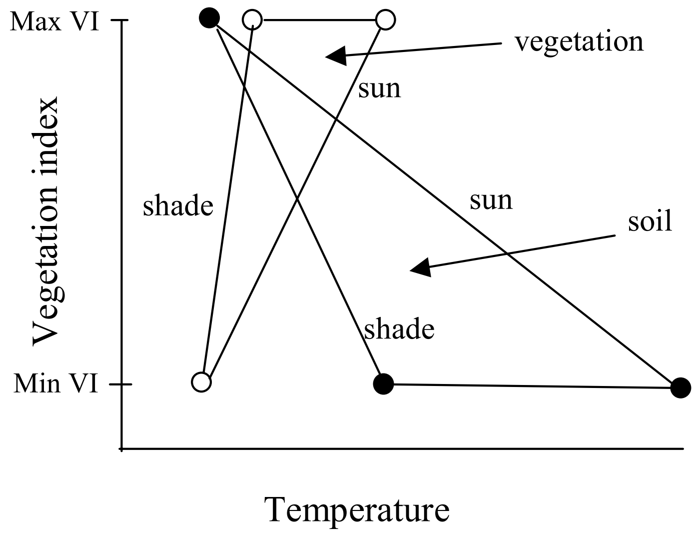

Figure 2.72 Soil and vegetation temperatures with sunlit and shaded conditions

The radiometric temperatures can be calculated as the linear combination of the soil and vegetation temperatures in the sunlit and shaded regions (Equation 2.96) and as shown in Figure 2.73. This figure reveals the bounding shape of the VI – Tr response as a curvilinear trapezoid. This shape defines all of the possible temperatures for regions of varying amounts of vegetation and shading conditions. It is important to recognize that, for every combination of surface and root zone moisture, there is a curvilinear trapezoid that describes the relationship.

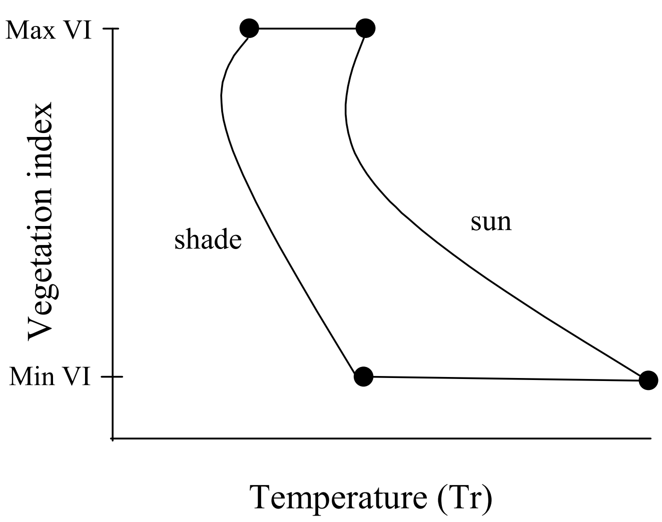

Figure 2.73 Radiometric temperature in sunlit and shaded conditions

The approach described above can also be developed for temperature differences between sunlit and shaded regions. With this approach, only the temperature difference and not the absolute values of temperatures in the sunlit and shaded regions need be measured. This response is shown in Figure 2.74.

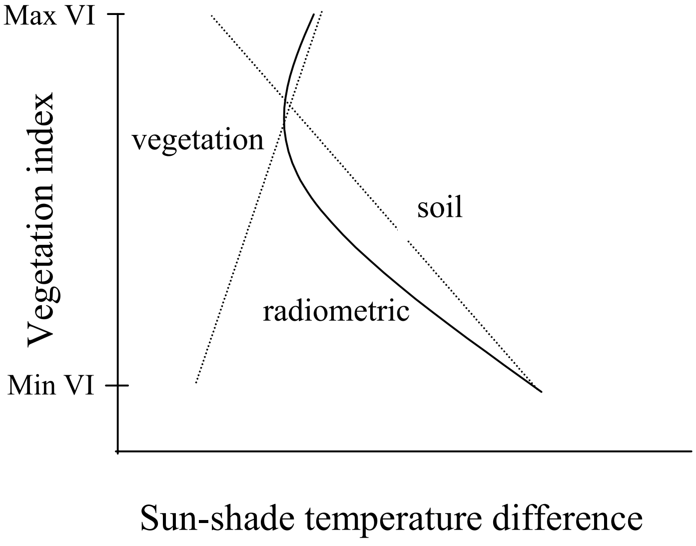

Figure 2.74 Radiometric, soil and vegetation sun-shade temperature differences

2.11.4 Comparison of Theoretical and Calculated VI – Tr Response

The so-called "simple model" described in Section 2.8.4 is an energy balance model that provides an analytical solution for the temperature difference between sunlit and shaded areas and includes surface and root-zone moisture and the amount of vegetation. We can use the simple model to estimate the temperature difference as a function of a vegetation index such as SAVI.

Results of example calculations using the simple model are given in Figure 2.75. Two conditions were simulated: one in which the soil surface was assumed to be dry, and another in which the soil surface was assumed to be sufficiently wet to maximize soil evaporation. In both cases, the vegetation was assumed to be transpiring at the maximum rate. The calculated radiometric temperature difference variation with SAVI is qualitatively similar to that expected (Figure 2.74). Further, the two curves indicate that a wide range of temperature differences is possible at any VI value.

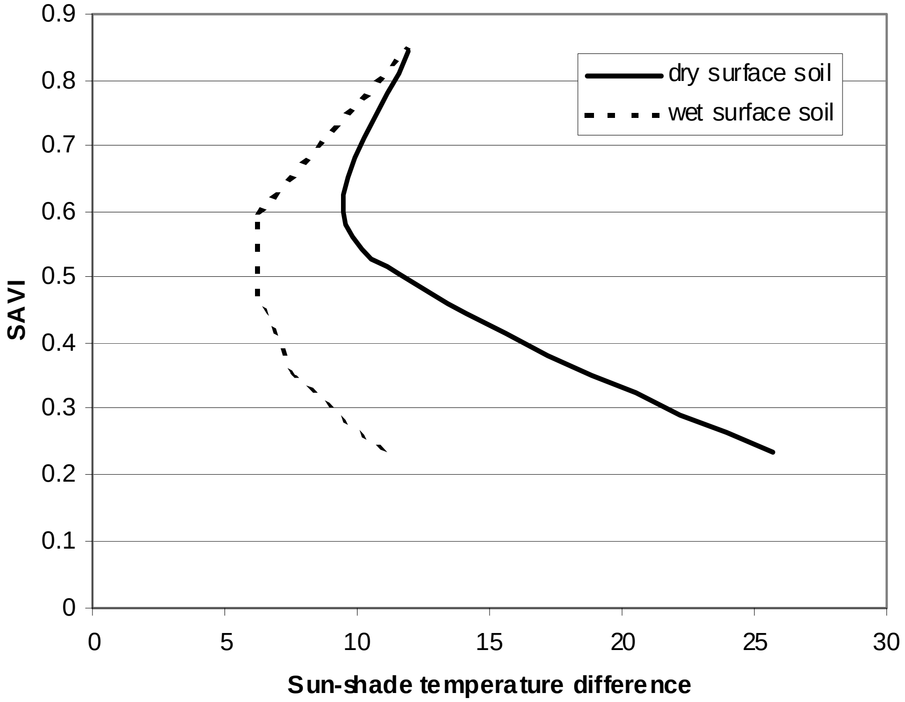

Figure 2.75 Temperature differences from example calculations using simple model

For certain conditions, the simple model can be used to estimate temperatures (not just temperature differences). For the case in which the root zone moisture is plentiful and does not limit the transpiration rate, the Priestly-Taylor (P–T) equation can be used to estimate the maximum transpiration rate LEmax (Norman, et al. [1995]):

$$\mathrm{Emax} = 1.26\ [\gamma/(\Delta+\gamma)]\ (\mathrm{Rn} - \mathrm{G}) \tag{2.99}$$

where Rn is the net radiation at the surface, G is the soil heat flux, Δ is the slope of the saturation vapor pressure versus temperature, and γ is the psychrometric constant.

For dry, bare soil, the soil temperature can be estimated from (Moran, et al. [1994])

$$s = [r_{ah} (Rn - G) / (\rho C)] + Ta \qquad (2.100)$$

where r_{ah} is the aerodynamic resistance and Ta is the air temperature. For saturated bare soil, the soil temperature can be estimated from (Moran, et al. [1994])

$$s = [r_{ah} (Rn - G) / (\rho C)] [\gamma/(\Delta+\gamma)] - [VPD/(\Delta+\gamma)] + Ta \qquad (2.101)$$

where VPD is the vapor pressure deficit of the air.

By incorporating Equations 2.99, 2.100, and 2.101 into the model, estimates of surface temperatures can be made for the following two special cases:

- Wet root zone, dry surface and
- Wet root zone, wet surface.

Results from an example calculation with the model are given in Figure 2.76. This particular calculation assumes a wet root zone and a dry soil surface. These results compare qualitatively with the expected behavior shown in Figures 2.72 and 2.73. Although not completely linear, the soil and vegetation temperatures in the sun and shade were nearly linear over a significant range of SAVI. Further, they are linear over the range of SAVI on which they have the greatest impact—the radiometric temperature. The vegetation response deviates significantly from a nearly linear response at low values of SAVI when it will not greatly influence the radiometric temperature. The soil temperature response is nearly bi-linear, with the inflection at a SAVI value of about 0.6. Note that there was no attempt to adjust input parameters (such as parameters in the resistance models for the soil and vegetation) in order to produce a more linear response.

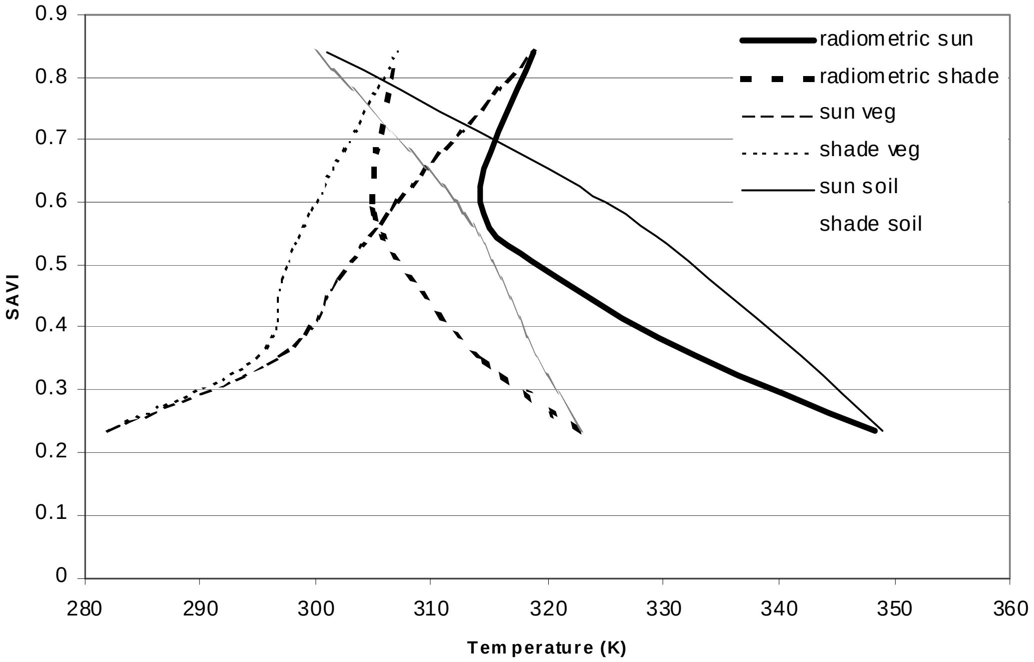

Figure 2.76 Predicted temperatures from simple model

2.11.5 Application Approach

From the remotely sensed image, a VI-Tr pair can be determined for each pixel. A scatterplot in VI-Tr space can then be developed for an image. From the scatterplot, data that correspond to full sun and complete shade locations can be selected. Preferably, these locations would be adjacent to one another so that moisture conditions and surface properties would be similar. The viability of this approach increases as the pixel size decreases. Thus, it may be appropriate for the relatively small pixel size of the MTI.

These data can be compared to a family of curves generated from the simple model or another model for different soil types (i.e., thermal properties) and moisture conditions (Figure 2.77). Once a match between the data and a curve is found, the curve is followed to the minimum VI line. This would provide the temperature difference associated with the bare soil, which can be used to interpret the thermal properties of the ground. In this way, the influence of the vegetation is removed. A similar approach can be used for temperature measurements rather than temperature differences.

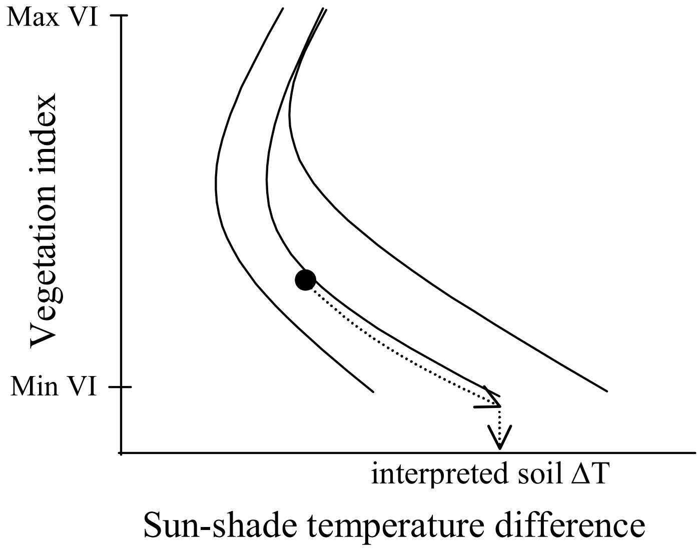

Figure 2.77 Example of data interpretation method using radiometric sun-shade temperature difference to estimate soil temperature difference

2.12 Atmospheric Correction for Thermal Infrared Satellite Imagery

2.12.1 Introduction

Satellite systems provide an essential platform for probing the thermal emissions and emissivity spectra of terrestrial materials on a global scale. These measurements are made possible by the direct relationship between surface emitted radiance, emissivity and temperature. Specifically, the unscattered surface-emitted radiance [$L^{eu}(\lambda,T)$] is related to the material's temperature by the Planck blackbody formula [$B(\lambda,T)$].

$$L^{eu}(\lambda,T)=\varepsilon(\lambda)\frac{C_1}{\pi}\lambda^{-5}\left[e^{(C_2/\lambda T)}-1\right]^{-1}=\varepsilon(\lambda)B(\lambda,T) \tag{2.102}$$

where, C_1,C_2 are known constants. The multiplicative factor, $\varepsilon(\lambda)$, represents the material's spectral emissivity, defined as a ratio between the object's emitted spectral radiance at a temperature T and the spectral radiance of a blackbody at the same temperature. For nontransmissive objects at thermal equilibrium with the environment, the material's spectral emissivity is related to its spectral reflectance by Kirchoff's law

$$\rho(\lambda)=1-\varepsilon(\lambda) \tag{2.103}$$

In fact, within the visible region of the spectrum, Equation 2.103 is often used to calculate spectral emissivity from solar reflected radiance.

In order to utilize the thermal properties of materials in classification algorithms, at-sensor radiance must first be converted into unscattered surface emitted radiance which is then related to the material’s temperature by Equation 2.102. For the later process, emissivity and temperature must be decoupled. This requires solving an underdetermined problem with N equations (radiance measures at each spectral band) for N+1 unknowns (emissivity at each spectral interval and a single temperature). The following sections describe currently accepted methods of both removing the effects of intervening atmosphere (Section 2.12.2). Each method is evaluated for its applicability to imagery from the multi-spectral thermal imager (MTI).

2.12.2 Atmospheric Correction

The general goal of atmospheric correction algorithms is to remove the effects of the intervening atmosphere and thereby to reduce the at-sensor radiance to the ground reflected and/or ground emitted radiances. In general these factors include:

1. unscattered, surface emitted radiance $\left[L^{eu}(\lambda)\right]$,
2. down-emitted, surface reflected radiance $\left[L^{ed}(\lambda)\right]$
3. path emitted radiance $\left[L^{ep}(\lambda)\right]$
4. unscattered surface reflected solar radiance $\left[L^{su}(\lambda)\right]$
5. surface reflected skylight $\left[L^{sd}(\lambda)\right]$ and
6. path scattered solar radiance $\left[L^{sp}(\lambda)\right]$. (Schowengerdt [1997])

See Figure 2.78 for a depiction of each of these contributions. In the thermal infrared (TIR), reflected and scattered solar radiation introduce negligible contributions to the at-sensor radiance and thus are largely ignored. This approximation is readily justified by comparing solar reflected radiance to typical terrestrial emissions. For a terrestrial emissivity of 0.9, the solar reflected and earth emitted radiances are approximately equal at a wavelength of 3.8 microns; whereas, satellite-based sea surface and land surface temperature (SST and LST, respectively) retrievals are attempted using radiance values from the 8-14 μm atmospheric window. (Schowengerdt [1997]; Salisbury and D’ArÌ´a [1992]; Gillespie, et al. [1999])

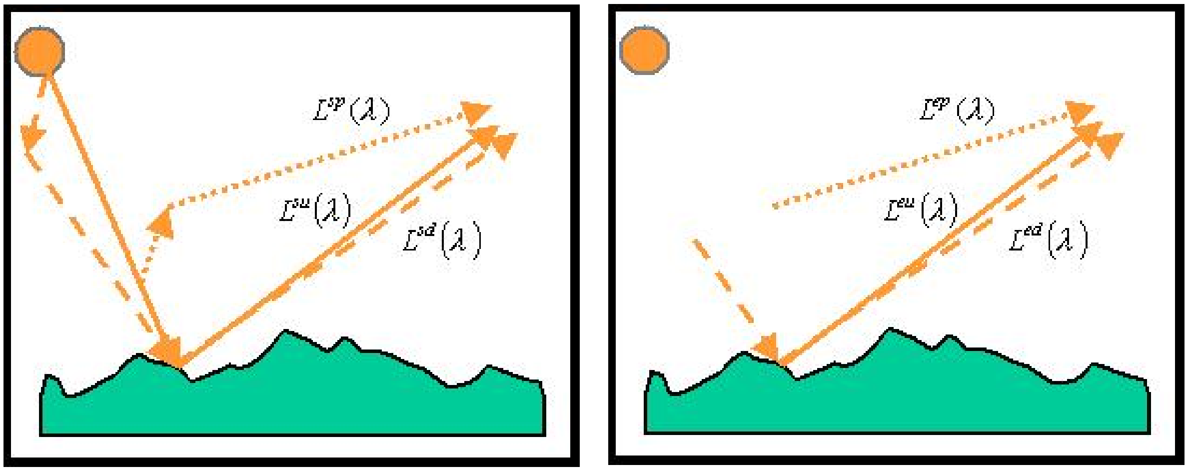

(a) (b)

Figure 2.78 (a) Contributions to at sensor radiance within solar reflective regime (b) Contributions to at-sensor radiance from atmospheric and ground surface emissions

By disregarding these solar contributions, the radiative transfer equation (RTE) for the thermal region of the spectrum reduces to

$$L^{e}(\lambda)=L^{eu}(\lambda)+L^{ed}(\lambda)+L^{ep}(\lambda) \tag{2.104}$$

$$L^{e}(\lambda)=\varepsilon(\lambda)\tau_{s}(\lambda)B(\lambda,T_{s})+F\rho(\lambda)\tau_{a}(\lambda)B(\lambda,T_{a})+L^{ep}(\lambda), \tag{2.105}$$

for each pixel. In Equation 2.105, $\tau_s(\lambda)$ and $\tau_a(\lambda)$ are the atmospheric transmission for paths corresponding to the surface emission to sensor and path emission to sensor, respectively, T_s is the temperature of the surface object, T_a is the temperature of the emitting atmosphere and F is a geometrical factor associated with the amount of sky seen by each pixel. Of the three contributing factors on the left hand side (LHS) of Equation 2.104, it is the final term, which extends the greatest atmospheric influence to at-sensor radiance. In contrast, the reflected down-welling can be ignored for objects with large emissivities and thus small reflectivities.

Thus, atmospheric correction is largely concerned with the determination of atmospheric transmission and atmospheric path radiance. Sections 2.12.2.1 through 2.12.2.4 provide descriptions of four commonly employed methods to extract these quantities either from information contained within the collected images or auxiliary measurements of atmospheric parameters. The applicability of each method to MTI imagery is also addressed.

2.12.2.1 In-Scene atmospheric correction

In-scene atmospheric correction (ISAC) is one of the simplest and most commonly applied methods of atmospheric correction in TIR (Kaiser [1999]). The method assumes (1) a single layer approximation to the atmosphere and (2) a negligible reflected down-welled radiance for materials with large emissivity values ($\varepsilon(\lambda)$> 0.85). The validity of this approximation is based upon the correspondingly low reflectances for such materials. Examples of materials that readily meet this later criterion are water and dense vegetation. Given these assumptions the RTE becomes

$$L^{e}(\lambda) \approx L^{eu}(\lambda) + L^{ep}(\lambda) \tag{2.106}$$

For this algorithm, a brightness temperature is first calculated for each TIR pixel. The brightness temperature is defined as the temperature of a blackbody $[\varepsilon(\lambda) = 1]$ having a spectral radiance equivalent to that measured by the satellite sensor.

$$L^{e}(\lambda) = \varepsilon(\lambda)\tau_{s}(\lambda)B(\lambda, T_{s}) + L^{ep}(\lambda) \tag{2.107}$$

From Equation 2.107, the emitted path radiance is equivalent to the y-intercept for a plot of $B(\lambda, T)$ vs. $L^{e}(\lambda)$. By including only those pixels that are darkest in the solar reflective region, atmospheric transmission and path radiance can be determined from the slope and y-intercept, respectively.

This assumes that the darkest pixels in the solar reflective region correspond to those objects whose radiances approach that of true blackbodies with an $\varepsilon(\lambda) \approx 1$. The quantity of interest, namely surface emitted radiance is then calculated using

$$L^{u}(\lambda) \equiv \frac{L^{e}(\lambda) - L^{p}(\lambda)}{\tau_{s}(\lambda)} = \varepsilon(\lambda)B(\lambda, T_{s}) \quad . \tag{2.108}$$

The main difficulty associated with this algorithm is that of trying to find the appropriate pixels to use for the linear interpolation. In general, one is not guaranteed to find a pure pixel of water or dense vegetation to use as an upper bound. This is especially problematic due to the relatively low spatial resolution of most TIR sensors. Due to the lower resolution, $L^{ed}(\lambda, T)$ and $\varepsilon(\lambda)$ are typically measured as average values for a mixture of many different materials contained within the satellites instantaneous field of view. In this regard, MTI offers the advantage of significantly higher spatial resolution in this spectral region (ground sampling distance, GSD = 20 m). Although this resolution increases the probability of finding pure pixels within the scene, another problem still remains. Specifically, an appropriate choice of materials (e.g., water) may not exist at the site of data collection such as in regions of bare rocks and soils with sparse vegetation. As these scenes are of particular value within this mission, the ISAC algorithm will not be generally applicable to this project.

2.12.2.2. Atmospheric Sounding

Provided the measurement of certain atmospheric parameters at the time and location of image collects, radiative transfer programs (LOWTRAN, MODTRAN) can be used to predict atmospheric transmission and emitted path radiance. This versatile method allows for the correction of a wide range of imagery including that from sensors with only a single TIR channel. The parameters of greatest interest in the 8-14 μm window are the vertical profiles of temperature and water vapor content. Due to the spatial and temporal variability of these parameters, it is essential that the atmospheric measurements be performed simultaneous to the collection of image data. Typical methods of atmospheric sounding include the use of radiosondes, meteorological models, and vertical sounding instruments (TOVS, VAS).

In general simultaneous sounding information is not available during the collection of MTI imagery. This will especially be the case for collections at denied sites. Therefore, approaches requiring such information will not be applicable to this MTI mission. It is possible, however, to acquire low resolution weather information from global meteorological databases. Although these datasets may require significant interpolation, they may still enhance the predictive capabilities of radiative transfer codes.

Throughout the course of this project, graphical user interfaces (GUI) have been generated to allow for the intuitive interaction between a user and the radiative transfer code, MODTRAN. (MODTRAN User's Manual [1998]) MTI specific functions have been added allowing for the derivation of target location, collection time, and sensor and solar geometries from header files of MTI imagery. The program also allows the user to select MTI filter functions during the process of final data extraction. This program will thus provide a basis for atmospheric correction of MTI imagery using numerical modeling of the atmosphere. See Figure 2.79 for an image of the main GUI window.

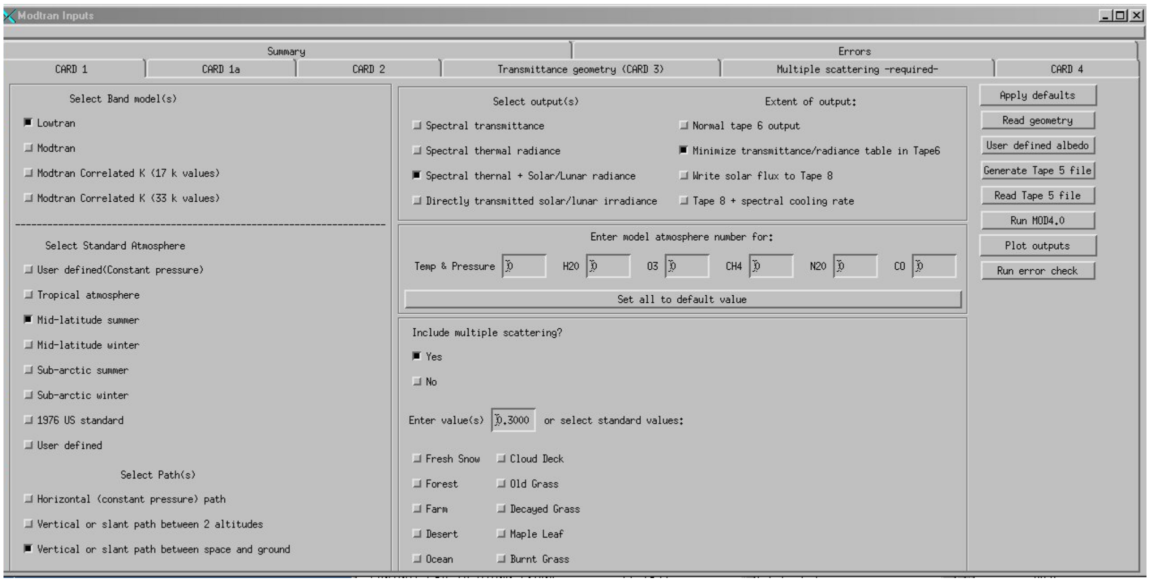

Select Band model(s)

☒ Lowtran
☐ Modtran
☐ Modtran Correlated K (17 k values)
☐ Modtran Correlated K (33 k values)

Select Standard Atmosphere

☐ User defined(Constant pressure)
☐ Tropical atmosphere
☒ Mid-latitude summer
☐ Mid-latitude winter
☐ Sub-arctic summer
☐ Sub-arctic winter
☐ 1976 US standard
☐ User defined

Select Path(s)

☐ Horizontal (constant pressure) path
☐ Vertical or slant path between 2 altitudes
☒ Vertical or slant path between space and ground

Select output(s)

☐ Spectral transmittance
☐ Spectral thermal radiance
☒ Spectral thermal + Solar/Lunar radiance
☐ Directly transmitted solar/lunar irradiance

Extent of output:

☐ Normal tape 6 output
☒ Minimize transmittance/radiance table in Tape6
☐ Write solar flux to Tape 8
☐ Tape 8 + spectral cooling rate

Enter model atmosphere number for:

Temp & Pressure 0 H20 0 O3 0 CH4 0 N20 0 CO 0

Include multiple scattering?

☒ Yes
☐ No

Enter value(s) 0.3000 or select standard values:

☐ Fresh Snow ☐ Cloud Deck
☐ Forest ☐ Old Grass
☐ Farm ☐ Decayed Grass
☐ Desert ☐ Maple Leaf
☐ Ocean ☐ Burnt Grass

Figure 2.79 Screen capture image of MODTRAN GUI in IDL interface generated to allow users a more intuitive interaction with the radiative transfer code. [Interactive Data Language, Research Systems, Inc.] The "read geometry" button located in the left column allows for the selection of an MTI image file, from which solar, sensor, and target geometry are read. In plotting MODTRAN outputs, the user has the option of applying MTI filter functions to all data outputs. Finally, the GUI provides the user with a means of generating LUT, which correlate atmospheric transmission and radiance values to a range of atmospheric parameters such as column water vapor.

2.12.2.3 Split Window methods

A group of algorithms that require less auxiliary information are becoming a popular method of correcting hyperspectral datasets. These split window methods utilized radiance information for 2 channels within the same atmospheric window to derive atmospheric transmission and path radiance. These methods assume that the radiance measured by the 2 channels have been impacted by the same atmospheric constituents with any differences being attributed to variations in water vapor content rather than emissivity.

A typical wavelength range for these two measurements extends from 10.5 to 12.5 μm. Not that MTI has only a single filtered channel within that spectral range [Band N: 10.2-10.7].

In other words, emissivity is an unknown constant across the two spectral bands. Although this method provides a simple interpretation of atmospheric correction, the underlying assumption are often not valid. However, several groups have made significant advances in improving the utility of this method for use with Channel 4 and Channel 5 on the Advanced Very High Resolution Radiometer (AVHRR). (Price [1984]; Sobrino [1991]; Becker [1990]; Coll [1994]; Becker [1995]) Such a customization of the method would be required to justify its application to the IR bands specific to MTI [Bands L, M, and N]; however, at this time there is not enough evidence to justify the application of this method to MTI imagery. ne reason for continued efforts on this front is the simplification it lends to surface temperature retrieval. If the assumptions are valid for a given ground sample, then there exists a linear relationship between the ground surface temperature and the brightness temperatures calculated in the two spectral bands. For example, the relationship originally derived for AVHRR is

$$T_s = T_4 + a(T_4 - T_5) + b \tag{2.109}$$

where, T_s is the ground surface temperature, T_4 and T_5 are the brightness temperatures for channel 4 and channel 5, respectively, and a and b are empirically derived constants. (Dash, 2002) One additional drawback of this method is that the empirically derived constants must be derived for each new dataset resulting in a computationally inefficient method of correction.

2.12.2.4 Multi-angle method

A promising technique for satellites with MTI's flexible maneuvering capabilities is the mutli-angle method (MEM). This set of techniques requires multiple images to be acquired of the same target site from multiple view angles. For example, MTI was designed with the capability to acquire a nadir image followed by a back look at 50-55 degrees off nadir. Assuming vertical atmospheric profile is uniform across the image scene and the angular dependence of emissivity is negligible, the atmospheric parameters are then empirically derived from the differences in at-sensor radiance between the two view angles. A similar capability was first made available with the launch of ERS-1 (1991), which carried the Along Track Scanning Radiometer (ATSR). (Mather,1993)

Unfortunately, the capability to accurately perform such a maneuver was lost in December of 2002 when MTI lost its IRU gyro. Due to the concomitant reduction in pointing accuracy, this method of atmospheric correction is no longer available to MTI users. This correction can however be applied to multi-look imagery acquired prior to December 2002.

2.13 References

Anderson, M.C., Norman, J.M., Diak, G.R., Kustas, W.P., and Mecikalski, J.R., 1997, A Two-Source Time-Integrated Model for Estimating Surface Fluxes Using Thermal Infrared Remote Sensing, Remote Sensing of the Environment, Vol. 60, pp. 195-216.

American Society of Heating, Refrigerating and Air-Conditioning Engineers ASHRAE Handbook, Fundamentals, 1985.

Becker, F., and Li, Z.-L., 1990, Towards a local split window method over land surface. *International Journal of Remote Sensing*, **11**, 369–394.

Becker, F., and Li, Z.-L., 1995, Surface temperature and emissivity at different scales: definition, measurement and related problems. *Remote Sensing Reviews*, **12**, 225–253.

Bliss *Solar Energy*, 1961, Vol. 5, p.103.

Burt, P. and Adelson, E., 1983, "The Laplacian pyramid as a compact image code," *IEEE Transactions on Communications*, Vol. 31:4, pp. 532–540.

Brutsaert, W., 1982, Evaporation into the atmosphere, Reidel Publishing.

Camillo, P.J., Gurney, R.J., and Devaney, J.E., 1988, A two-dimensional model of the hydrological response of a hillslope, *Land Surface Evaporation*, Schmugge and Andre eds., p. 121–135.

Campbell, G.S., and Norman, J.M., 1998, An Introduction to Environmental Biophysics, 2nd Edition, Springer, New York.

Carlson, T.N., 1986, Regional-Scale Estimates of Surface Moisture Availability and Thermal Inertia Using Remote Thermal Measurement. *Remote Sensing Reviews,* Vol. 1, pp 197–247.

Carsel, R.F., and Parrish, R.S., 1988, Developing joint probability distributions of soil water retention characteristics, *Water Resources Research*, Vol. 24, No. 5, pp. 755–769.

Chen, A.J., Liu, C.H., Rau, J.Y., and Chen, L.C., 1994, "Adaptive Stereo Matching for SPOT Multi-Spectral Image Pairs", *SPIE Proc.*, Vol. 2357, pp. 98–103.

Chung, S.O., and Horton, R., 1987, Soil heat and water flow with a partial surface mulch, *Water Resources Research*, Vol. 23, No. 12, pp. 2175–2186.

Colaizzi, P.D., Barnes, E.M., Clarke, T.R., Choi, C.Y., and Waller, P.M., 2003, Estimating Soil Moisture Under Low Frequency Surface Irrigation Using Crop Water Stress Index, ASCE *Journal of Irrigation and Drainage Engineering*, Vol. 129, pp. 27–35.

Coll, C., Caselles, V., Sobrino, J. A., and Valor, E., 1994, On the atmospheric dependence of the split-window equation for land surface temperature. *International Journal of Remote Sensing*, **15**, 105–122.

Cracknell, A.P., and Xue, Y., 1996, Review Article: Thermal inertia determination from space – a tutorial review, *International Journal of Remote Sensing*, Vol. 17, No. 3, pp. 431–461.

Dash, P., Gottsche, F.-M., Olesen, F.-S., Fischer, H., 2002, Land Surface temperature and emissivity estimation from passive sensor data: theory and practice-current trends, *International Journal of Remote Sensing*, Vol. 23, No. 13, pp. 2563–2594.

Dykhuizen, R.C. and Helmich, D.R., 1994, "Users Manual for IR Thermal Response Code," Sandia National Laboratories Memorandum Report, June 20.

Eldred, M.S., Giunta, A.A., van Bloemen Waanders, B.G., Wojtkiewicz, S.F., Jr., Hart, W.E., Alleva, M.P., 2002, DAKOTA, A Multilevel Parallel Object-Oriented Framework for Design Optimization, Parameter Estimation, Uncertainty Quantification, and Sensitivity Analysis, Version 3.0 Reference Manual, SAND2001-3515, February.

Farouki, O.T., 1986, Thermal Properties of Soils, Series on Soils and Rocks, Vol. 11, Trans Tech Publications.

Francois, C., 2002, "The potential of directional radiometric temperatures for monitoring soil and leaf temperature and soil moisture status," *Remote Sensing of the Environment*, Vol. 80, pp. 122–133.

Gillespie, A.R., Rokugawa, S., Hook, S.J., Matsunaga, T., Kahle, A.B., 1999, Temperature and emissivity separation algorithm basis document.

Hensen, T., Krumel, L., Blake, D., Bender, S., Byrd, D., Christensen, W., Rappoport, W., and Shen, G., 1999, "Multispectral Thermal Image Optical Assembly Performance and Integration of the Flight Focal Plane Assembly", *SPIE Proc.* Vol. 3753, pp. 359–368.

Hillel, D., 1998, Environmental Soil Physics, Academic Press.

Hoek, E. and Brown E.T., 1980, Underground Excavations in Rock, London Inst of Mining and Metallurgy.

Im, H., Chul-Soo, Y., and Kwae-Hi, L., 2000, "Digital Elevation Model Extraction Using KOMPSAT Images," *Journal of the Korean Society of Remote Sensing*, Vol. 16, pp. 347–353.

Interactive Data Language, Research Systems, Inc, Boulder, Colorado

Jury, W.A., Gardner, W.R., and Gardner, W.H., 1991, Soil Physics, John Wiley and Sons.

Kaiser, R.D., 1999, Quantitative comparison of temperature/emissivity algorithm performance using SEBASS data, Proceedings of the SPIE: algorithms for multispectral and hyperspectral imagery V, vol. 3717, eds. S. Chen and M. Descour, Orlando, FL, 47–57

Kay, R., Bender, S., Henson, T., Byrd, D., Rienstra, J., Decker, M., Rackley, N. Akau, R., Claassen, P., Kidner, R., Taplin, R., Bullington, D., Marbach, K., Lanes, C., Little, C., Smith, B., Brock, B., and Weber, P., 1999, "Multispectral Thermal Imager Payload Overview," *SPIE Proc.* Vol. 3753, pp. 347–358.

Kustas, W.P., and Norman, J.M., 1997, "A two-source approach for estimating turbulent fluxes using multiple angle thermal infrared observations," *Water Resources Research*, Vol. 33, No. 6, pp. 1495–1508.

Lee, H.Y., Park, W., Kim, T., and Lee, H.K., 1999, "Accurate DEM Extraction from SPOT Stereo Pairs: A Stereo Matching Algorithm Based on the Geometry of the Satellite," *Asian Conference on Remote Sensing Proc.*

Li, M., 1991, "Hierarchical Multipoint Matching," *Photogrammetric Engineering & Remote Sensing*, Vol. 57, pp. 1039–1047.

Lotti, J., and Giraudon, G., 1994, "Correlation Algorithm with Adaptive Window for Aerial Image in Stereo Vision," *SPIE Proc.* Vol. 2315.

Mathur, A.K. and Agarwal, V.K. 1993, Multichannel dual angle approach for sea surface temperature retrieval in context of ERS-1 scenario. *Proc. of the 1st ERS-1 Symposium*, Cannes 1992, ESA SP-359, 767–771.

MODTRAN User's Manual, 1998, Versions 3.7 and 4.0, Air Force Research Laboratory – Space Vehicles Directorate, Hanscom AFB.

Moran, M.S., Clarke, T.R., Inoue, Y., and Vidal, A., 1994, Estimating Crop Water Deficit Using the Relation between Surface-Air Temperature and Spectral Vegetation Index, *Remote Sensing of the Environment*, Vol. 49, pp. 246–263.

Norman, J.M., Kustas, W.P., and Humes, K.S. 1995, Source approach for estimating soil and vegetation energy fluxes in observations of directional radiometric surface temperature, *Agricultural and Forest Meteorology*, Vol. 77, pp. 263–293.

Percious, D. J., and Shellum, C., 2001, "Integrated Red-Blue Report for the U16b Tunnel Test Bed Site, NTS, Nevada," HTD Program Technical Review, January 24.

Price, J.C., 1984, Land surface temperature measurements from the split window channels of the NOAA-7 AVHRR. *Journal of Geophysical Research*, **89**, 7231–7237.

Price, J.C., 1977, Thermal Inertia Mapping: A New View of the Earth, *Journal of Geophysical Research,* **82,** 2582-2590.

Priestley, C.H.B., and Taylor, R.J., 1972, "On the assessment of surface heat flux and evaporation using large scale parameters," Monthly Weather Review, Vol. 100, pp. 81-92.

Quam, L.H., 1987, "Hierarchical Warp Stereo," *Readings in Computer Vision,* Morgan Kaufmann Publishers, inc. Los Altos, CA. pp. 80–85.

Rienstra J., and Ballard, M., 1999, "MTI Focal Plane Assembly Design and Performance," *SPIE Proc*., Vol. 3753, pp. 369–379.

Salisbury, W., and D’ArÌ´a, D.M., 1992, Emissivity of terrestrial materials in the 8–14 mm atmospheric window. *Remote Sensing of Environment*, **42**, 83–106.

Schowengerdt, R.A., 1997, Remote Sensing: Models and Methods for Image Processing, 2nd Edition, Academic Press, San Diego.

Schultz, H., Hanson, A.R., Riseman, E.M, Stolle, F.R., and Zhu, Z., 2002, "A Self-consistency Technique for Fusing 3D Information," *IEEE Fifth International Conference on Information Fusion*, pp. 1106-1112.

Short, N.M., and Stuart, L.M, Jr., 1982, The Heat Capacity Mapping Mission (HCMM) Anthology, NASA SP–465.

Sobrino, J.A., Cool, C., and Caselles, V., 1991, Atmospheric correction for land surface temperature using NOAA-11 AVHRR channels 4 and 5. *Remote Sensing of Environment*, **38**, 19–34.

Sobrino, J.A., El Kharraz, M.H., Cuenca, J., and Raissouni, N., 1998, Thermal Inertia Mapping from NOAA-AVHRR Data *Adv. Space Res*, Vol. 22 No. 5 pp. 655–667.

Storey, J.C., 1993, "Hybrid Stereopairs from Space-based Sensors; A New Approach for Creating Digital Terrain Models", presented at *Pecora 12 Symposium*, Land Information from Space-Based Systems, Sioux Falls, South Dakota, pp. 55–60.

Stormont, J.C., 2002, Thermal inertia as a function of porosity and water content, memo to Charles Walker, October 1.

Stormont, J.C., 2003, “Inclusion of vegetation in a simple model for surface temperature differences in sun and shade,” Sandia National Laboratories letter report, May 19.

van de Griend, A.A., Camillo, P.J., and Gurney, R.J., 1985, Discrimination of Soil Physical Parameters, Thermal Inertia, and Soil Moisture from Diurnal Surface Temperature Fluctuations, *Water Resources Research*, Vol. 21, No. 7, pp. 997–1009.

Van Genuchten, M., 1980, A closed form equation for predicting the hydraulic conductivity of unsaturated soils, *Soil Science Society of America Journal*, Vol. 44, pp. 892–898.

Walker, C.L., 2002, Rock Thermal Parameter Estimation using DAKOTA Optimization Feasibility Study, Progress Report, Sandia National Laboratories, September 19.

Walker, C.L., 2003, User’s Manual: IR Response Code for DAKOTA Optimization and Supporting Software, Sandia National Laboratories memorandum report, September (in preparation).

Wan, Z., v3.3, MODIS Land-surface temperature algorithm theoretical basis document.

Watson, K., 1975, Geologic Applications of Thermal Infrared Images, *Proceedings of the IEEE*, p. 128–136.

Weber, P., Brock, B., Garrett, A., Smith, B., Borel, C., Clodius, W., Bender, S., Kay, R., and Decker, M., 1999, "Multispectral Thermal Imager Mission Overview", *SPIE Proc*., Vol. 3753, pp. 340–346.

Wolf, P.R., Elements of Photogrammetry: with Application in GIS, Third Ed. New York, NY: McGraw-Hill.

Xue, Y., and Cracknell, A.P., 1995, Advanced thermal inertia modeling, *International Journal of Remote Sensing*, Vol. 16, No. 3, pp. 431–446.

Yocky, D. and Dykhuizen, R.C.,“Thermal Properties for Various Terrestrial Materials IR Radiometric Compensation: Thermal Modelly,” Sandia Systems Research Report, Appendix C, October 1, 1993.

Zhang, R., Li, Z., Sun, X., Tang, X., and Becker, F., 2001, The potential information in the temperature difference between shadow and sunlit of surfaces and a new way of retrieving the soil moisture, Science in China, Series D, Vol. 44, No. 2, pp. 112-123.

3 Spectral Separation and Classification of Rock Types

3.1 Introduction

This study examined the possibility of using remotely-sensed multi-spectral data to classify rocks into seven generic types. We conducted comprehensive separability and classification analysis on seven multi-spectral data sets, each representing one of the seven geologically-categorized rock-type groups. We included the effects of imperfections introduced by the presence of other materials such as water and various types of soil and vegetation. To emulate multi-spectral data, we filtered laboratory spectrometer spectra with Multi-spectral Thermal Imager (MTI) filters. We obtained laboratory spectral reflectance data corresponding to the rocks and other materials from the spectral libraries of the Advanced Space-borne Thermal Emission and Reflection Radiometer (ASTER) (http://asterweb.jpl.nasa.gov/). We applied and tested a number of supervised parametric classifiers. The purpose of this study is to determine the classification techniques that produce the best results and to identify challenges associated with multi-spectral classification of generic rock types. Another outcome of this study is the identification of the "important" features (viz., MTI spectral bands) that dominate the spectral information needed to separate and classify the main rock types.

Section 3.2 includes a summary of the results of our literature survey on rock classification using multi-spectral (and some hyper spectral) remotely-sensed data. Section 3.3 contains an overview of the Bayesian decision theory and its application to pattern classification. Section 3.4 contains a description of the generic rock classes, defined by SNL geologists. In Section 3.5, we discuss the generation of the original multi-spectral training data (and the difficulties associated with its limited size) and provide a methodology for enlarging it through limited mixing with appropriate impurities. In Section 3.6, we define all the training data and testing data that we use in the separability and classification analysis. Section 3.7 includes the separability and classification results. A number of linear and nonlinear feature extraction techniques are also discussed in Section 3.7. Section 3.8 presents results using compressed features. The conclusions and future work are included in Sections 3.9 and 3.10, respectively.

3.2 Prior Work on Rock Classification

A number of technical articles, both published and unpublished, are relevant to our study. Jackson and Landgrebe (2001) and Shahshahani and Landgrebe (1994) considered the problem of small-size training sets, which can severely affect the recognition rate of the classifier when the dimensionality of multi-spectral data is relatively high. Solutions to mitigate this problem are provided, such as using unlabeled samples to enlarge the training set and using a self-learning and self-improving adaptive classifier. A self-improving adaptive classifier iteratively trains on new semi-labelled samples and the original training set. To control the influence of semi-labelled samples, the proposed method gives full weight to the training data and reduced weight to semi-labelled samples. Results show that training with supplementary semi-labelled samples can enhance statistic estimation and hence improve classifier performance. Ninomiya and Yoshiki (2002) attempted to map quartz, carbonate materials, and bulk SiO_2 content in silicate rocks with the indices defined for ASTER TIR multi-spectral data. Using the specific spectral features of different rocks and minerals, several indices were defined as the ratio of these features. The results were compared with the information from the field and the laboratory geological investigations, including the TIR spectra of the rocks collected at the site and a published geological map. The potential ability of the indices for mapping quartz, carbonate minerals and silicate rocks was suggested.

Patel (2002) focused on establishing the degree of discrimination between three types of rocks based on the observing band pairs. Using multi-spectral data from the Lansat-5 Thermal Imager (TM) in the visible and near infrared (NIR) spectral range (seven bands), this study identified which band pairs would produce the best discrimination. Weathering produced identical mineralogical composition on the surfaces of all three rock types and caused difficulties in discriminating them. The size of the training data for each type was about 20. The types were not totally separable, and the misclassification probabilities ranged from ~24% up to 55%, depending on the type of training data.

Chen (1998) examined the role of topographic normalization in improving classification for fourteen classes of rock with a Maximum Likelihood Classifier. The topographic variation resulted from variations in the angle of observation, slopes, and shaded areas of the object. Chen concluded that topographic normalization for the multi-spectral data rendered no noticeable classification improvement because it also removes spectral features. The presence of vegetation also causes difficulty in normalization and classification.

Ientilucci (2001) focuses on spectral unmixing, considering the multi-spectral data of a rock as a linear superposition of the spectra of the exemplars (center of the classes). Given a multi-spectral vector of any rock, he formed the projection of the unknown vector onto each one of the exemplars and matched it with the exemplars (using an inner product) to find the “energy” component of the unknown vector in the dimension spanned by each class. The component with the highest energy wins. A possible limitation of the proposed orthogonal subspace projection (OSP) method is that the number of bands must be no fewer than the number of classes (this is not the case for the MTI sensors, however). This problem can be remedied using the generalized OSP, reported by Ren, et al. in 2000. This approach may be particularly useful in classifying samples from fine-grain rocks, as the linear model may be applicable.

Fogler (2003) reports recent efforts conducted under an SNL/Lockheed-Martin joint vision project for improving autonomous ground–vehicle navigation. Fogler developed a method to search for the pairs of hyperspectral bands that produced the best discrimination between types of vegetation and other potential obstacles. His goal was to distinguish hard obstacles from soft obstacles, as well as impassable thickets and other sources of entrapment. Spectral-based classification may provide a means to identify obstacles, such as plant species that tend to snag small robotic vehicles, plant species that grow near the edge of hidden water hazards, and tree species that tend to suppress undergrowth and provide a potentially clear path. Additionally, it may be useful to be able to identify road paving materials in order to exploit any road(s) in the area. The report also addresses a few design issues such as sensor resolution, sensor configurations with and without complementary sensors, and day/night operation.

The research papers reviewed in this project provided us with numerous perspectives on multi-spectral data and the problems associated with its separation and classification.

3.3 Theory and Background

For our research, we adopted the Bayesian classification technique, which has been proven to be an effective parametric classification approach in numerous applications, including remote sensing. We begin by reviewing the fundamentals of this approach. Our presentation closely follows Fogler (2003).

3.3.1 Bayes Theory

In a typical classification problem, the objective is to assign a class label to an incoming observation from a set of predefined labels. To make a classification decision for a set of data, we need to know the *a posteriori* probabilities that the sample (data point) belongs to each of the classes, labeled as $i = 1, \ldots, c$, (assuming c classes), conditional that the sample has the feature value $\mathbf{x}$ (e.g., in a d-dimensional Euclidean feature space). This *a posterior* probability, denoted by $p(i|\mathbf{x})$, may be calculated using Bayes Rule as follows:

$$p(i \mid \mathbf{x}) = p(\mathbf{x} \mid i)p(i) / p(\mathbf{x}) \tag{3.1}$$

where

$$p(\mathbf{x}) = \sum_{i=1}^{m} p(\mathbf{x} \mid i)p(i) \tag{3.2}$$

$p_{\mathbf{X}}(\mathbf{x})$ is the probability density function (pdf) of the data vector $\mathbf{x}$, and $p_I(i)$, $i=1, \ldots, c$, are the prior probabilities of the classes (assumed to be known). A Bayesian (or maximum *a priori*, MAP) decision rule may now be formed with the *a posteriori* probabilities of Equation 3.1. More precisely, if a sample has feature value $\mathbf{x}$, the MAP classification rule is to assign the sample $\mathbf{x}$ to a class i if and only if $p(i|\mathbf{x}) \geq p(j|\mathbf{x})$ for all $j \neq i$. Because $p_{\mathbf{X}}(\mathbf{x})$ is independent of the classes (see Equation 3.1), it can be ignored in the maximization. Thus, we obtain the following equivalent representation for the Bayes (or MAP) decision rule: A sample belongs to class i if and only if $p(\mathbf{x}|i)p_I(i) \geq p(\mathbf{x}|j)p_I(j)$ for all $j \neq i$. (In the event that the two *a posteriori* probabilities are equal, a randomised tie-breaking rule is arbitrarily employed.) It can be shown that the above Bayes decision rule minimizes the average probability of error (Fogler [2003]). Throughout this report, we will assume that all the prior probabilities $p_I(i)$ are equal. This is a safe assumption because, at this point, we do not have any information on the likelihood of occurrence of the rocks (considered in this project) in nature.

3.3.2 Discriminant Function

Using the above classification rule, we can define the discriminant function, $g_i(\mathbf{x}), i = 1, \ldots, c$, and use it to classify the data. More precisely, we assign the class i to the data point $\mathbf{x}$ if and only if $g_i(\mathbf{x}) \geq g_j(\mathbf{x})$ for all $j \neq i$. Thus, the classifier computes c discriminant functions and selects the category corresponding to the largest discriminant value.

From the various pdfs that have been investigated, none has received more attention than the multivariate normal (or Gaussian) pdf. To a large extent, this attention is due to its analytical tractability (as well as its validity in the many cases by appealing to the central-limit theorem). The general multivariate normal pdf in n dimensions is given by:

$$p(\mathbf{x}) = \frac{1}{(2\pi)^{d/2} |\Sigma|^{1/2}} \exp\left[-\frac{1}{2} (\mathbf{x} - \boldsymbol{\mu})^t \Sigma^{-1} (\mathbf{x} - \boldsymbol{\mu}) \right], \tag{3.3}$$

where *p is the n-dimensional mean vector of* **X**, Σ *is its n* x *n covariance matrix, and* $|\Sigma|$ and Σ^{-1} are its determinant and inverse, respectively. Formally, we have:

$$\boldsymbol{\mu} \equiv E[\mathbf{X}] = \int \mathbf{x} p_{\mathbf{X}}(\mathbf{x}) d\mathbf{x} \text{ and } \Sigma \equiv E\left[(\mathbf{X} - \boldsymbol{\mu})(\mathbf{X} - \boldsymbol{\mu})^t\right] = \int (\mathbf{x} - \boldsymbol{\mu})(\mathbf{x} - \boldsymbol{\mu})^t p_{\mathbf{X}}(\mathbf{x}) d\mathbf{x}, \tag{3.4}$$

The covariance matrix Σ is always *symmetric* and *positive semi-definite*. In the general multivariate normal case, the covariance matrices are different for each category and the discriminant functions are inherently quadratic. For example, if **X** belongs to class *i*, then its discriminant function is:

$$g_i(\mathbf{x}) = \mathbf{x}^t W_i \mathbf{x} + \mathbf{w}_i{}^t \mathbf{x} + \mathbf{w}_{i0}, \tag{3.5}$$

where

$$W_i = -\frac{1}{2} \Sigma_i^{-1}, \tag{3.6}$$

$$w_i = \Sigma_i^{-1} \boldsymbol{\mu}_i \tag{3.7}$$

and

$$w_{io} = -\frac{1}{2} \boldsymbol{\mu}_i^t \Sigma_i^{-1} \boldsymbol{\mu}_i - \frac{1}{2} \ln |\Sigma_i| + \ln p_I(i). \tag{3.8}$$

Here, $\boldsymbol{\mu}_i$ and $\boldsymbol{w}_i$ are the mean vectors and covariance matrix associated with *i*th class. We estimate these parameters as follows: To calculate any mean vector $\boldsymbol{\mu}$ we use the simple mean estimator, defined by $\hat{\boldsymbol{\mu}} = \frac{1}{N} \sum_{p=1}^{N} X_p$, where $X_p, p = 1, \ldots. N$, are the independent observation of a normal random variable. This estimator is implemented in the Matlab function mean. For matrix A, with rows corresponding to different observations and columns corresponding to data dimensionality, mean (A) is a row vector, containing the mean value of each column.

3.3.3 Error Bounds

We can obtain additional insight into the operation of a Bayesian classifier if we consider the classification error (Fogler [2003], Duda [2000]). We first observe the two-category (binary) case and assume that feature space is divided into two (2) regions, R_1 and R_2, in a possibly "non-optimal way." Classification error may occur in two ways: either an observation **x** falls in R_1, while its true membership is 2, or **x** falls in R_2, while its true membership is 1. Because these events are mutually exclusive and exhaustive, the average probability of error is:

$$
\begin{aligned}
&P_E = P(\mathbf{x} \in R_2, 1) + P(\mathbf{x} \in R_1, 2) = \\
&P(\mathbf{x} \in R_2 \mid 1) p_I(1) + P(\mathbf{x} \in R_1 \mid 2) p_I(2) = \\
&\int_{R_2} p(\mathbf{x} \mid 1) p_I(1) d\mathbf{x} + \int_{R_1} p(\mathbf{x} \mid 2) p_I(2) d\mathbf{x}.
\end{aligned}
\tag{3.9}
$$

In general, if $p(\mathbf{x}|1)p_I(1) > p(\mathbf{x}|2)p_I(2)$, it is beneficial to classify **x** as a member of region R_1 so that the smaller quantity will contribute to the error integral, which is exactly what Bayes decision rule achieves.

In the multi-category case, there are more ways to be misclassified and so it is easier to compute the probability of success. Clearly,

$$
\begin{aligned}
&Pc = \sum_{i=1}^{c} P(\mathbf{x} \in R_i, i) = \\
&\sum_{i=1}^{c} P(\mathbf{x} \in R_i \mid i) p_I(i) = \sum_{i=1}^{c} \int_{R_1} p(\mathbf{x} \mid i) p_I(i) d\mathbf{x}
\end{aligned}
\tag{3.10}
$$

Then average error probability is:

$$
P_E = 1 - P_c = 1 - \sum_{i=1}^{c} \int_{R_i} p(\mathbf{x} \mid i) p_I(i) d\mathbf{x}\,, \tag{3.11}
$$

where P_c denotes the average probability of correct classification. This is a general result that depends neither on the partitioning of the feature space nor on the form of the underlying distribution (Duda [2000]). Bayes classifier yields the smallest probability of error because it maximizes the above probability by choosing the regions so that the integrand is maximal for all **x.**

However, in most cases, calculation of P_E is computationally impractical. Fortunately, simple upper bounds are available, which in some cases give very tight approximations. A simple upper bound on P_E is obtained by examining the compliment $\overline{R_i}$ of the decision region.

$$
\begin{aligned}
&P_E = P(\mathbf{x} \in \overline{R_i}, j \text{ occurs}) = \\
&= P(\mathbf{x} \in \bigcup_{i \neq j} R_{i,j}, j \text{ occurs}) \leq \sum_{i \neq j} P(\mathbf{x} \in R_{i,j}, j \text{ occurs}) = \\
&\sum_{i \neq j} P\left(\ln \frac{p(\mathbf{x} \mid i)}{p(\mathbf{x} \mid j)} \geq 0, j \text{ occurs} \right) = \\
&= \sum_{j \neq i} P_E(j \to i),
\end{aligned}
\tag{3.12}
$$

where $P_E(j \to i)$ denotes the pairwise (binary classification) error associated with class j, specifically, the probability of selecting the class i over j when class i is the only alternative to class j. This inequality becomes equality whenever the regions $R_{i,j}$ are disjoint. This occurs in the trivial case where c=2. This bound is called a *union bound*. A weaker but completely general error bound can be obtained by estimating $P_E\left(j \to i\right)$ from above by using the so-called *Bhattacharya bound* and its negative logarithm, the *Bhattacharya distance* (BH),

$$P_E(j \to i) \le \sqrt{p_I(i)p_I(j)}\int \sqrt{p(\mathbf{x}\mid i)p(\mathbf{x}\mid j)}d\mathbf{x} = \sqrt{p_I(i)p_I(j)}e^{-BH_{i,j}}. \tag{3.13}$$

For the Gaussian case we have:

$$BH_{i,j} = 1/8\left[(\boldsymbol{\mu}_i - \boldsymbol{\mu}_j)^t\left[\frac{\Sigma_i + \Sigma_j}{2}\right]^{-1}(\boldsymbol{\mu}_i - \boldsymbol{\mu}_j)\right]^{1/2} + \frac{1}{2}\ln\frac{\left|\frac{\Sigma_i + \Sigma_j}{2}\right|}{\sqrt{|\Sigma_i||\Sigma_j|}}. \tag{3.14}$$

The quantity $BH_{i,j}$ is called the Bhattacharya distance between the pdf's of classes i and j. It can be calculated for any pair of classes and it is often used to quantify the separation between classes. A final bound on the error probability

$$P_E \le \sum_{i\neq j} P_E(j \to i) \le \sum_{i\neq j}\sqrt{p_I(i)p_I(j)}e^{-BH_{i,j}}, \tag{3.15}$$

can be obtained by combining the union bound with the general Bhattacharya. A special case of the Bhattacharya distance is the Mahalanobis distance, defined by

$$MH_{i,j} = \left[(\boldsymbol{\mu}_i - \boldsymbol{\mu}_j)^t\left[\frac{\Sigma_i + \Sigma_j}{2}\right]^{-1}(\boldsymbol{\mu}_i - \boldsymbol{\mu}_j)\right]^{1/2}. \tag{3.16}$$

Note that $MH_{i,j}$ is zero when the means of the classes coincide. Thus, the Mahalanobis distance is not appropriate for class separability when classification is solely based on inter-class variability.

3.3.4 Minimum Distance Classifier

A commonly used, simple algorithm for image classification is the minimum distance classifier. With this algorithm, each unknown sample with feature vector $\mathbf{x}$ is classified by assigning it to the class whose mean vector $\boldsymbol{\mu}_i$ is closest to $\mathbf{x}$. In addition to the obvious intuitive appeal and computational simplicity of this approach, it can be shown that it is a very special case of maximum-likelihood (Bayesian) classifier, when the covariance matrices for different classes are identical. If we assume that the covariance matrices for all classes are equal, i.e.,

$$\Sigma_i \equiv \Sigma_0, \tag{3.17}$$

and that the prior probabilities are equal, i.e.,

$$p_I(i) = p_I(j) \equiv p_0. \tag{3.18}$$

Then the discriminant function of Equation 3.5 becomes

$$g_i(\mathbf{x}) = \mathbf{x}^t\left(-\frac{1}{2}\Sigma_0^{-1}\right)\mathbf{x} + \left(\Sigma_0^{-1}\boldsymbol{\mu}_i\right)^t\mathbf{x} - \frac{1}{2}\boldsymbol{\mu}_i^t\,\Sigma_0^{-1}\,\boldsymbol{\mu}_i - \frac{1}{2}\ln\left|\Sigma_0\right| + \ln p_0 \qquad (3.19)$$

or

$$g_i(\mathbf{x}) = A - \frac{1}{2}\left(\mathbf{x}-\boldsymbol{\mu}_i\right)^t\,\Sigma_0^{-1}\left(\mathbf{x}-\boldsymbol{\mu}_i\right), \qquad (3.20)$$

where the constant A is given by $A = -\frac{1}{2}\ln\left|\Sigma_0\right| + \ln(p_0)$ and may be ignored in a comparison of g_i for different classes. If the covariance matrix is further constrained to be diagonal, i.e., the features are uncorrelated each with variance $\sigma_0{}^2$ and if we further have equal variance along each feature axis, then

$$g_i(\mathbf{x}) = A - \frac{\left(\mathbf{x}-\boldsymbol{\mu}_i\right)^t\left(\mathbf{x}-\boldsymbol{\mu}_i\right)}{2\sigma_0{}^2}. \qquad (3.21)$$

The quantity $\left(\mathbf{x}-\boldsymbol{\mu}_i\right)^t\left(\mathbf{x}-\boldsymbol{\mu}_i\right) = \|\,\mathbf{x}-\boldsymbol{\mu}_i\,\|^2$ is simply the square of the Euclidian distance between vectors $\mathbf{x}$ and $\boldsymbol{\mu}_i$, and Equation 3.21 therefore is the discriminant function for the minimum-distance classifier. In particular, $g_i(\mathbf{x})$ will be largest for the class i for which the distance from the data point to the “center” of the class is at a minimum (i.e., the class with nearest mean to the data point). However, unlike the maximum-likelihood classifier, the minimum-distance classifier does not generally minimize the average classification error. This classifier will be initially used in this work to show its inadequacy since we will encounter a high degree of inter-class variability among rock classes.

3.4 Rock-Type Class Definitions

Geologists define three general categories of rock type: igneous, metamorphic, and sedimentary, which correspond to the different processes that form the rocks. We selected a number of spectra of common rock samples from the ASTER hyperspectral database. Tables 3.1 and 3.2 show the samples included in the training set. We selected other samples for inclusion in Testing set 3, which is described in Section 3.6.2. The brief description that follows is borrowed from Ientilucci (2001).

Igneous rocks are any of a variety of glassy rocks formed by the cooling and solidification of molten earth material. A great majority of igneous rocks are composed of silicate materials such as pyroxene, amphibole, olivine, and mica. Minor occurrences of carbon-rich igneous rocks, e.g., containing sodium carbonate but low in silicates, have been found.

The bonding of sediments from broken down minerals creates *sedimentary* rocks. There are two principle types–detrital and authigenic. Detrital rock is formed by the accumulation and lithification of sediment composed of grains of minerals such as quartz and feldspar that may have been transported to the depositional site. Authigenic rock is formed from minerals such as calcite, halite and gypsum within the depositional site in response to geochemical processes.

Metamorphic rocks are formed by the alteration of pre-existing rocks in response to changing environmental conditions such as temperature, pressure, mechanical stress, and the addition or removal of chemical components. Metamorphic rocks may be formed from igneous, sedimentary, or other pre-existing metamorphic rocks.

SNL geologists have further divided the three rock categories into seven generic classes relevant to the sites of interest, as follows:

Metamorphic Rocks

- Unfoliated or faintly foliated
  - Horfelsic (Group 1)
  - Granoblastic (Group 2)
- Foliated
  - Schistose (Group 3)
  - Semischistose (Group 4)

Igneous

- Igneous (Group 5)

Sedimentary

- Clastic Sedimentary (Group 6)
- Chemical sedimentary (Group 7)

The database contains data from samples of different grain sizes: solid rock (taken to mean a whole-hand sample) whole chips, 0-75 µm, and 500-1500 µm groups. The samples in the different size groups are taken from the same original sample type and were further broken down into the two grain-size categories. In most cases, the rock chips and the smaller grained samples were extracted from different original samples, which belong to the same geological type but are not identical to each other.

Tables 3.1 and 3.2 show all the members of the original training data.

Table 3.1 Members of the original training data of groups 1-4. Letter "C" denotes the coarse-grain rocks and the letter "F" denotes the fine size rocks

GROUP 1 *HORNFELSIC*	GROUP 2 *GRANOBLASTC*	GROUP 3 *SCHISTOSE*
Hornfels-F	Pink Quarzite-C	Chlorite(Ap-961-197)
Hornfels-C	Gray Quarzite-C	Chloritic Shist-C
	Pink Quarzite-F	Gray Slate-C
	Marble-F	Chloritic Shist-F
	Marble-C	Gray Slate-F

Table 3.2 Continuation of Table 3.1. This table lists members of the original training data for groups 5 -7. The letter "C" denotes the coarse-grain rocks and the letter "F" denotes the fine size rocks.

GROUP 5 *IGNEOUS*		GROUP 6 *CLASTIC SEDIMENTARY*	GROUP 7 *CHEMICAL SEDIMENTARY*
1. AU	Andesite-F	Shale-C	Limestone-C
Augite-Hypersthene	Basalt-F	Shale-F	Limestone-F
Andesite-C	Diorite-F	Siltstone-C	Dolomite
Basalt-C	Gabbro-F	Siltstone-F	CAMGCO3RO368-C
Diorite-C	Granite-F	Fossiliferous	Limestone
Gabbro-C	Rhyolite-F	Limestone-C	CACO3RO360-C
Granite-C	Tan Rhyolite (Ap-981-176)	Red Sandstone-F	
Rhyolite-C	Tuff-9	Red Sandstone-C	
Augite-Hypersthene	Tuff-8	Fossiliferous	
		Limestone-F	

3.5 Original Multi-Spectral Training Data and a Methodology for Training Set Enlargement

Our first step in generating the training set is to transform the hyper spectral data signatures available from the ASTER database to an MTI-based multi-spectral signature. The *spectral signature* can be defined in the solar reflective region by its reflectance as a function of the wavelength, measured as an appropriate spectral resolution (Viterbi [1979], Schowengerdt [1997]). The main premise of multi-spectral remote sensing is that *different types of materials can be distinguished on the basis of difference in their spectral signatures*. A number of factors can avert the success of multi-spectral remote sensing, such as:

- Natural variability for a given material type.
- Coarse spectral quantization of many remote-sensing systems.
- Modification of the signature by atmospheric effect.

Therefore, there is no guarantee that different materials will exhibit measurably different signatures in the natural environment. All the spectral reflectance data are unique to the sample and the environment, in which they are measured. Consequently, laboratory or field reflectance data should be used judiciously because they give only an approximation of the real signatures (Viterbi [1979]).

We passed the available training data through the MTI filters using the post-launch filter parameters. Table 3.3 shows the 15 MTI filter bands (Band H has two filters). The multi-spectral data was then generated and *normalized* by dividing the output of each filter by the area under the filter for each band. This step forces the value of multi-spectral data to be between 0 and 1, thus resembling reflectance. Typically, we use a numerical designation for the band, as documented in Tables 3.3 through 3.5. Bands **F** and **H** (and the spectral regions associated with them) are avoided altogether for remote sensing of the earth's surface since the molecular absorption bands of water and carbon dioxide cause "deep" absorption, which completely blocks the transmission of radiation to earth (Viterbi [1979]). The water absorption bands near 0.9 µm are much narrower and block the energy completely for narrowband remote sensors when the water vapor content of the atmosphere is high. These bands can be useful for detections of cirrus clouds. Such clouds are not easily distinguished from lower altitude clouds or surface features at other wavelengths. Table 3.4 shows the 13 bands we used in the preliminary analysis and the correspondence between the band's number and the actual MTI band. Section 3.5.4 describes the preliminary analysis, which estimated the rank of the augmented training set to be 11 and established the required number of dimensions for preliminary feature extraction. Table 3.5 shows the 11 bands remaining after preliminary feature extraction, which were used in the separability and classification analysis.

Table 3.3 The numbering system for MTI- bands (red letters denote the bands that we initially avoided)

Bands	A	B	C	D	E	F	G	H1	H2	I	O	J	K	L	M	N
#	1	2	3	4	5	6	7	8	9	10	11	12	13	14	15	16

Table 3.4 Bands used in the preliminary analysis (Bands C and L visually identified to have low variance)

Bands	A	B	C	D	E	G	I	O	J	K	L	M	N
#	1	2	3	4	5	6	7	8	9	10	11	12	13

Table 3.5 Bands used in the separability and classification analysis

Bands	A	B	D	E	G	I	O	J	K	M	N
#	1	2	3	4	5	6	7	8	9	10	11

3.5.1 Inadequacy of Classification Using the Euclidian Distance as a Metric for Separability

First, we applied the minimum-distance classifier to the available training sets (original training data shown in Tables 3.1 and 3.2), without applying any additional preprocessing techniques. We calculated the average error in classification of the training data, which are shown in Table 3.6. The large errors clearly indicate that the Euclidian-distance alone cannot provide good inter-class separability. The Euclidean distance only measures absolute distance from the mean of each class. It does not take into account the distribution of the points in the group. Thus, it cannot discriminate overlapping classes with similar means. As seen from the table, the average error (when classifying the original training data) is approximately 57%. The error results from the inability of the Euclidean distance to detect differences among the spread (covariance) of the various classes.

To improve the class separability, we must move beyond the first-order statistics to second-order statistics, which can be used, in turn, to perform a full-fledged Bayesian classification. However, the small size of the training set is a fundamental challenge in our ability to estimate the second-order statistics of the classes reliably. Section 3.5.2 discusses methods for training from limited data sets.

Table 3.6 Results of the separation of the original training data (Tables 3.1 and 3.2) among all seven groups, according to the Euclidean minimum-distance criterion

Average Error = 0.55	GROUP 1	GROUP 2	GROUP 3	GROUP 4	GROUP 5	GROUP 6	GROUP 7
Number of Members	2	5	5	2	15	8	4
Correctly Classified	0	3	3	1	5	3	3
Incorrectly Classified	2	2	2	1	10	5	1
Error	1	0.4	0.4	0.5	0.67	0.625	0.25

3.5.2 Mean and Covariance-Matrix Estimation from a Limited Size Training Data

The question of how to determine the adequate number of training samples for a given number of features has been a subject of intensive empirical and analytical research efforts. One frequently used rule-of -thumb is to take ten times the dimension of the data. It is reasonable to expect that as the number of spectral bands increases, the ability to detect more detailed classes should also increase, leading to an improved accuracy in the classification. But in our case, as it often happens in practice, the number of training data is limited. Here we come to the well-known and extensively discussed problem of parameter estimation from training samples of limited size, to which the following remarks apply (Jackson and Landgrebe [2001], Shahshahani and Landgrebe [1994]):

- Most of the classification algorithms are based solely on second-order statistics.
- We are dealing with multidimensional data.
- As in most remote-sensing applications, the number of available labelled samples is limited.

All of the above reduce the precision with which class characteristics can be estimated. Therefore, the limited number of training samples severely restricts practical application of statistical pattern recognition procedures for multi-dimensional data. Next, we discuss our strategy for enlarging the set of training data.

3.5.3 Augmentation of the Training Set

For covariance-matrix estimation, we used Matlab function cov. For matrices, were each row is observation and each column is variable, cov(x) gives an estimate of the covariance matrix. This estimate is normalized by *N*-1, where *N* is the number of observations. However, when the dimension of data is relatively high compared to the number of samples in the training set for each group, the estimate of the covariance matrix becomes singular and cannot be used in Bayesian classification (since it cannot be inverted). In fact, because of the limited size of the training set, the covariance matrix fails to be of full rank for six of the seven groups. Only group five has rank thirteen, since initially it is the highest populated group. For groups 1 through 7, the ranks of the covariance matrices, calculated on the bases of the original training data are 2, 4, 4, 1, 13, 7 and 3, respectively. This fact forces us to purposefully increase the number of training set members by perturbing the original rock samples. We create these perturbations by mixing the original training data with different types of minerals, vegetation, soil and water. We use random mixture ratios ranging from 0% to 10%. We also create mixtures between fine and coarse size rocks, according to their geological properties, as shown in Table 3.7. As a result, the augmented training set contains perturbation of the original training data with fine and coarse size rocks, minerals, vegetation, water and soil. We named this enlarged set *training set 1*.

Table 3.7 Elements used to perturb the original training data and to create the enlarged training data set (training set 1). The odd number columns contain the perturbation's identification number (ID), according to the database and to the corresponding library and the even number columns contain the sample's name.

Identification #	**Perturbation Spectra**	**Identification #**	**Perturbation Spectra**	**Identification #**	**Perturbation Spectra**
3	Sea water	5	Dark brown fine sandy loam	22.2 Fine	Basaltic andesite
		20	Brown–to–dark–brown sand	26.5 Coarse	Diorite gneiss
				27.6 Fine	Diorite gneiss
				210.15 Coarse	“Limestone" siltstone
				211.13 Fine	“Lim*estone"* siltstone

In the mixing process, we must rescale the reflectance of the perturbing spectra so that they are comparable with the reflectances of the members of the original training data. We pursued this normalization procedure because we noticed that there are several perturbing spectra (e.g., dolomite 368, limestone 360), which have higher reflectivity than the training spectra. Without this rescaling, even a 5% perturbation can totally distort the original sample and overwhelm the spectral features of the original member. To visualize the effect of the mixing process, Figure 3.1 shows the reflectivity for Hornfels, a representative member of original training data of group 1, and Figures 3.2 through 3.6 show the reflectivity of some of the perturbations used.

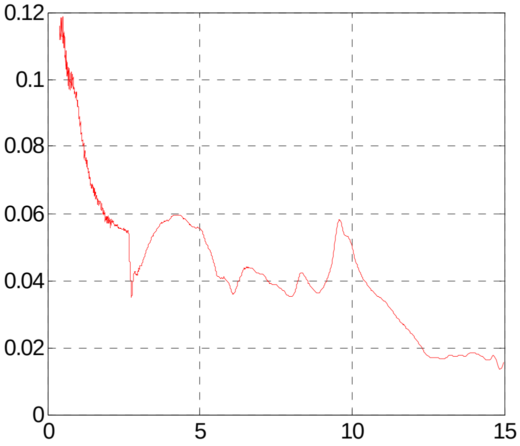

Figure 3.1 Hyperspectral signature of coarse hornfels, member of original training data for group 1

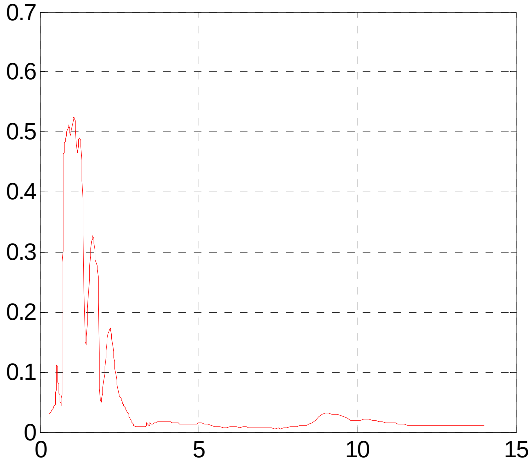

Figure 3.2 Hyperspectral signature of green grass, used to perturb the original training data

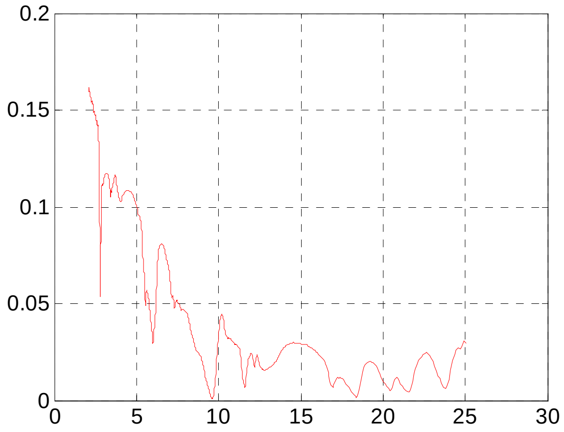

Figure 3.3 Hyperspectral signature of andradite mineral, used to perturb the original training data

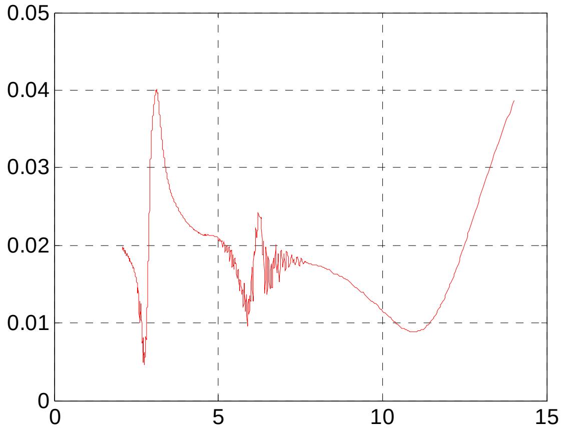

Figure 3.4 Hyperspectral signature of distilled water, used to perturb the original training data

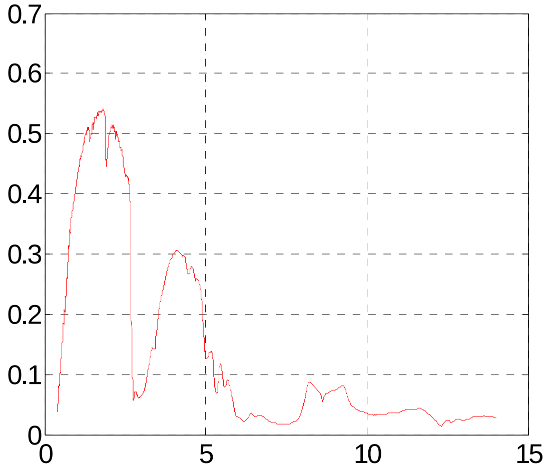

Figure 3.5 **Hyper spectral signature of brown silty loam, used to perturb the original training data**

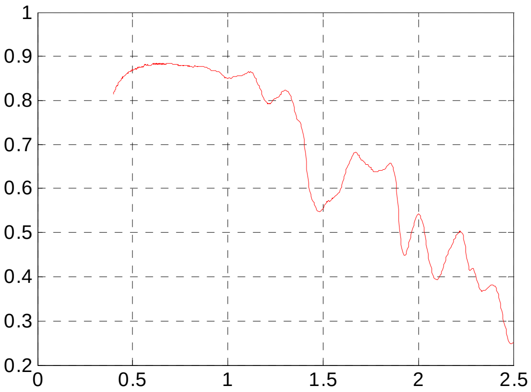

Figure 3.6 **Hyper spectral signature of Cellulose, used to perturb the original training data**

Through the above perturbation procedure, we enlarged our training data by a factor greater than ten. This caused the rank of the multi-spectral training data to reach eleven (particularly for groups one and four, which initially had the smallest population). Note that since most of the new members are linear combinations of existing data, their addition does not significantly alter the relevant spectral characteristics of each group. Figure 3.7 shows the multi-spectral signature of original training data for group 1. Figures 3.8 and 3.9 show the resulting mixtures of the original training data of group 1 with minerals and soils, respectively. Figures 3.10 and 3.11 show perturbation of the same original training data with green vegetations and water, respectively.

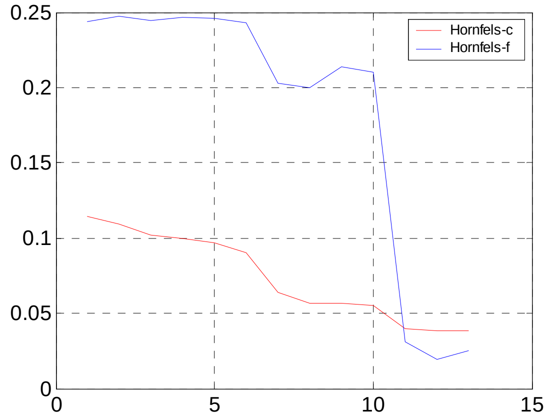

Figure 3.7 **Multi-spectral signatures of the original training data for group 1**

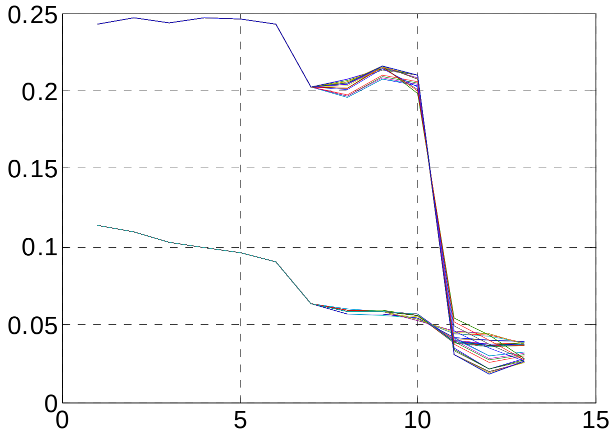

Figure 3.8 **Multi-spectral signatures of original training data for group1, perturbed with the mineral**

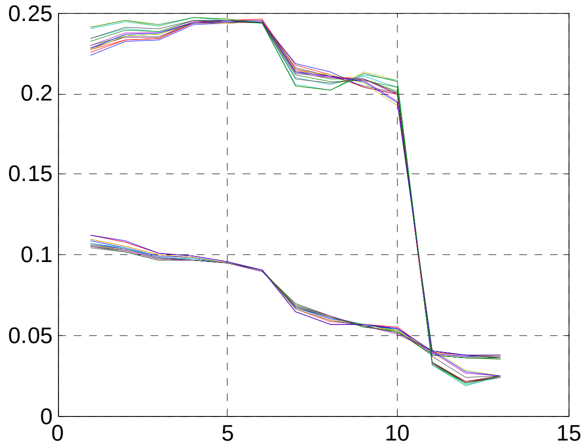

Figure 3.9 **Multi-spectral signatures of the original training data for group 1, perturbed with soil**

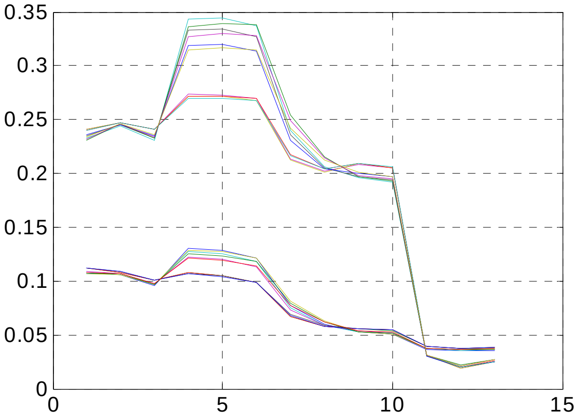

Figure 3.10 **Multi-spectral signatures of original training data for group 1, perturbed with green vegetation**

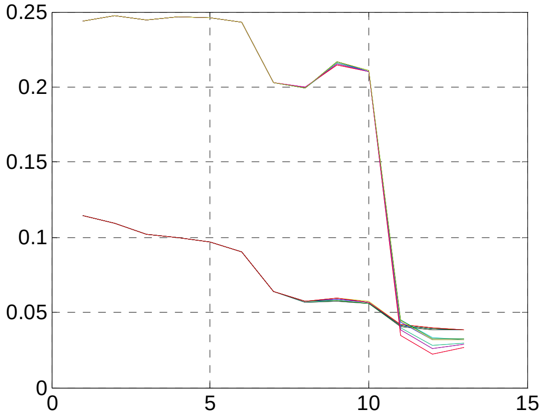

Figure 3.11 **Multi-spectral signatures of original training data for group 1, perturbed with water**

Only the addition of green vegetation visibly modifies the multi-spectral characteristics of the training data in the 0.4 - 2.4 micron range, because of higher reflectivity of green vegetation in this range. Adding minerals and water changes the multi-spectral characteristics of the original data from bands eight to thirteen. Adding dry vegetation affects the multi-spectral signatures of the original data from bands one to eight. Perturbation with soil and green vegetation changes the whole multi-spectral signature of the original data from bands one to thirteen. Adding all these elements helps us to achieve a good estimation accuracy of the covariance matrices. However, augmenting the data increased the rank of the training set to 11, which falls short of full-rank for the 13-dimensional data and precludes inversion of the covariance matrix. Section 3.5.4 describes the heuristic feature extraction method we used to reduce the dimensionality to 11.

3.5.4 Preliminary Feature-Space Reduction

We elected to avoid statistics-based feature reduction methods because they depend on accurate statistical estimates, which require large training sets (Schowengerdt [1983]) and (Haertel and Landgrebe [1999]). Instead, we applied heuristic band selection. High correlation between adjacent bands justifies band selection. Furthermore, we suspect that not all bands are equally important and useful. Consequently, finding a set of bands that reduces the data dimension and at the same time preserves most of the relevant information is desirable. Indeed, in real applications, strongly correlated bands can be eliminated and only those bands, bearing significantly different information are required for data processing (Jimnez and Langrebe [1999]). We elected to eliminate two bands, **C** and **L**, using the heuristic criteria described in the following paragraph. Table 3.4 shows the eliminated bands highlighted in red. Table 3.5 shows the remaining 11 bands used in the separability and classification analyses, described in the next section.

We attempted to select bands that would uniformly cover the entire spectral range. We visually inspected the multi-spectral signatures for all the seven geological groups. We noticed that the MTI filters' responses for bands C and L were very similar across the different geological groups. The response of these bands exhibited little variability for different members of the groups. These bands, therefore, did not seem to aid in distinguishing between the groups.

The next section describes the separability and classification analysis of rock's groups and defines the data sets used to conduct the experiments.

3.6 Definition of the Data Sets Used in the Separability and Classification Analysis

3.6.1 Overview

There are two important aspects in our study:

i) *We want to investigate to what extent the data we have at our disposal can be separated and what can be said about the size of the training data which would allow separability*. Essentially, this is an iterative process that attempts to achieve performance that is as close as possible to the optimal performance for the given data set. However, there is always a tradeoff between the size of the training data and the separability error. While an overly complex system may allow perfect classification of an existing training set, it is unlikely to perform well on a new pattern. This situation is known as an *overfitting* (Fogler [2003]). Because our methodology imposes a bias toward "simple" classifiers, we will stop searching when the classifier performance is good enough. One of the most important issues is to adjust the complexity of the classification model. The model should not be too simple so as to prevent it from discriminating the categories, yet it shouldn't be too complex so as to yield a poor classification on a novel pattern.

Separability can also be used to determine combination of features that is best, on average, at distinguishing among the given classes (Viterbi and Omura [1979]). As a tool for feature selection, a measure for separability is typically computed for all possible pairs of classes and for all combinations of *k* features out of *n* total features. The average separability over all class pairs is computed and the subset of features that produces the highest average separability is found.

One may then use that subset for classification and save computational time in the classification stage. It is important to match the separability measure to the classifier for the feature subset analysis.

ii) Once separability is established, we wish to study the performance of various classifiers when applied to various testing data sets.

3.6.2 Testing Data Sets

The experiments conducted to investigate separability and classification performance use the following data sets:

Testing set 1: The original training data (Tables 3.1 and 3.2) were subjected to small random perturbations. These perturbations were generated using the *rocks* listed in Table 3.8. We used five randomly chosen values for the mixture percentages, ranging from 1% to 10%. [Note that Table 3.8 also lists minerals, soils, and vegetation, which were used as perturbing agents for testing set 2 (defined below).] Moreover, we used the following provision regarding our selection of the gain sizes in the mixing process. We perturbed the fine-grain rocks from the original training set with coarse rocks from Table 3.8 and we perturbed coarse-grain rocks from the original training data with fine-grain rocks using samples listed in Table 3.8. The rescaling procedure used in generating the extended training data, which was described in Section 3.5, was also used here. *We emphasize that the perturbing members that were used to create the testing data were different from those used for enlarging the original training data.* This was completed to enhance the robustness of our classification study.

Testing set 2: To create this set we enlarged testing set 1 by further including mixtures of the original training data with *soils*, *minerals and vegetation*, as listed in Table 3.8 (using the same mixing strategy as above). Again, the elements used to create this testing set were different from the ones we used to extend the original training set.

Table 3.8 Elements used to perturb the original training data for creation of testing data sets 1-2. The odd number columns (labelled in red color) contain the perturbation's identification number (ID), according to the database and the even number columns contain the sample's name.

MINERALS ID	***MINERALS***	***GREEN VEGETATION ID***	***VEGETATION*** *GREEN*	***BROWN VEGETATION ID***	***VEGETATION*** *BROWN*
22	Andranite	2	Deciduous	2	Cotton cellulose
28	Antigirite			8	Citrus pectin
95	Erionite			25	Sycamore-loer (yellow)
100	Fluorite			37	Ca buckwheat (brown)
252	Quartz			70	Sycamore (decayed leaf)
285	Spodumene				
WATER ID	***WATER***	***SOIL ID***	***SOIL***	***ROCK ID***	***ROCKS***
2	Sea foam	2	Grayish brown loam	2.1.10 Coarse	Basalt.H9
		3	Dark grayish brown silty loam	2.2.9 Fine	Basalt.H9
		7	Reddish brown fine sandy loam	2.6.13 Coarse	Pink marble
		19	Dark reddish brown fine sandy loam	2.7.16 Fine	Pink marble
				2.10.11 COARSE	BLACK SHALE
				2.11.9 FINE	BLACK SHALE

Testing set 3: To test the ability of the classifiers to generalize to new samples, we formed Testing set 3 from samples outside the training set. We imported additional spectra from the ASTER library and assigned them to classes according to their geological group names, as we described in Section 3.4. The new members are presented in Table 3.9. After we selected the samples, we further enlarged their number by perturbing them with five randomly chosen weighted values (from 1% to 10%) of fine and coarse grain rocks, minerals, water, and vegetation listed in Table 3.7. In contrast to testing sets 1 and 2, Testing set 3 uses the same mixing members as those used to enlarge the training data, but scales them with different random weights.. Because rock samples of the same class can exhibit wide variations in their spectral shapes, Testing set 3 provides a challenging test of each classifier's generalization ability.

Table 3.9. Samples outside of the original training set which are used to create testing set 3. The letter “f” denotes fine size rocks and letter “c” denotes coarse size rocks.

GROUP 1	GROUP 2	GROUP 3	GROUP 4	GROUP 5	GROUP 6	GROUP 7
Spotted Hornfel-c	Dolmitic marble-c	Green Shist-f	Chloritic Gneiss-f	Basalt-c-H1	Arenaceous Shale-c	Dolomitic Limestone-f
Banded Hornfel	Serpentine Marble-c	Green Schist-c	Chloritic Gneiss-c	Basalt-c-H2	Phosphatic Shale-c	Dolomitic Limestone-c
Spoted Hornfel-f	Dolmitic Marble-c	Mica Schist-f	Garnet Gneiss-f	Basalt-c-H5	Calcareous Shale-c	Oolitic Limestone-f
	Serpentine Marble-c	.Mica Schist-c	Garnet Gneiss-c	Basalt-c-H7	Illite-bearing Shale-c	Oolitic Limestone-c
	White Marble-c			Basalt-c-H9	Arenaceous Shale-	Dolomite 350
	Pink Marble-c			Basalt-f-H2	Phosphatic Shale-f	Dolomite 391
	.Dolomitic Marble-f			Basalt-f-H5	Calcareous Shale-f	
	Serpentine marble			Basalt-f-H7	Black Shale-f	
	Dolmitic Marble-f			Basalt-f-H9	Illite-bearing Shale-f	
	Serpentine Marble-f			Alcalic Granite-c	Carbonaceous shale-f	
	White Marble-f			Granite-H2-c	Limestone Siltstone-c	
	Pink Marble-f			Granite-H3-c	”Limestone” Siltstone-f	
	Green Quartzite-c			Alcalic Granite-f	Arcosic Sandstone-c	
	Purple Quartzite-c			Granite-H2-f	Glauconitic Sandstone-c	
	Gray Quartzite-c			Granite-H3-f	Micaceous Red Sandstone-c	
	Green Quartzite-f			Granite-H5-fn	Ferruginous Sandstone-c	
	Purple Quartzite-f				Arcosic Sandstone-f	
	Gray Quartzite				Glauconitic Sandstone-f	
	Green Quartzite-c				Micaceous Red Sandstone-f	
					Ferruginous Sandstone-f	
					Black Shale-c	
					Carbonaceous Shale-c	

3.6.3 Separability Study Outline

The separability study consisted of the following four studies:

1. We considered the initially enlarged training data named **training set 1** (see Section 3.5) as a training set for the classifier and observed the separability performance, by calculating the misclassification error for each of the seven groups and the average error probability of all groups.

2. We augmented training set 1 by testing set 1, creating a **training set 2 (training set 2 = training set 1 ∪ testing set 1)** and examined the separability performance of the classifier on this training data set.

3. We launched another study, were we augmented training set 1 with testing set 2, creating a new **training set 3 (training set 3 = training set 1 ∪ testing set 2)** and examined the separability performance of the classifier on this new training set.

We performed a fourth study, in which we augmented training set 1 with testing data 3, creating training set 4 (**training set 4 = training set 1 ∪ testing set 3**) and examined the separability performance of the resulting classifier on this fourth training set.

3.6.4 Classification Study Outline

The classification study consisted of the following three studies:

Case 1. **Training set 1 → testing set 1:** We applied the classifier trained by training set 1 to testing set 1 and observed classification performance by calculating the classification error for each group and the average classification error for all groups.

Case 2. **Training set 1 → testing set 2:** We applied the same classifier to testing set 2.

Case 3. **Training set 1 → testing set 3:** We repeated the same procedure with testing set 3 and compared the performance results for all three cases by comparing the average probability of error for each case.

The results of the above studies are discussed in the next section. We chose training set 1 as a designated training set for the classification study, because it performed best at our separability study. In addition, in Section 3.8, we extend the analysis using certain feature extraction techniques such as the principal-canonical transformation (linear feature selection) and the use of spectral indices (nonlinear feature extraction techniques).

3.7 Results Using Uncompressed Features

Our first goal is to investigate separability and classification accuracy of Bayesian classifier applied to all eleven features of the data, represented by MTI filer's response for bands A, B, D, E, G, I, O, J, K, M and N.

3.7.1 Separability According to Using Inter-Class Metrics

We begin by calculating the Euclidian, Bhattacharya, and Mahalanobis confusion matrices for training data set 1, 2, 3 and 4, as shown in Tables 3.10 through 3.15. For ease of comparison, each matrix entry is normalized by the maximal distances between groups, so that the maximum distance is always unity in each matrix. The best separability with respect to the Mahalanobis distance (see Table 3.11) is achieved between groups 1 (Horfelsic) and 4 (Semischistose). The worst cases are between groups 5 (Igneous) and 6 (Clastic Sedimentary), 5 (Igneous) and 7 (Chemical Sedimentary), and groups 4 (Semischistose) and 5 (Igneous). In comparison to the Euclidean-based confusion matrix, the use of the Mahalanobis distance only improves the separation between groups 1 (Horfelsic) and 4 (Semischistose). However, the application of

Bhattacharya distance leads to a substantial improvement in the accuracy as demonstrated in Tables 3.12, 3.13, 3.14 and 3.15. Unlike the Mahalanobis distance, *Bhattacharya distance takes into account the inter-class covariance even when the means are non-distinguishable*. The separation between groups 1 (Horfelsic) and 7 (Chemical Sedimentary) changes from being the worst case (with respect to the Euclidean distance, see Table 3.11) to being the best case with respect to Bhattacharya metric (see Table 3.12). We notice also that all the normalized Bhattacharya distances between any two groups have values that are above 0.6, indicating a good separability.

From the data presented in Tables 3.10 through 3.15 it is clear that the Bhattacharya distance allows for a maximal separability, namely, the inter-class distances become large almost uniformly in all inter-class incidents. Compared to the rest of between group distances, the distances between groups 2 (Granoblastic) and 5 (Igneous) and between groups 5 (Igneous) and 6 (Clastic Sedimentary) are shorter. *Thus, we deem these groups problematic*.

Table 3.10 Normalized Euclidian (relative to the maximal Euclidian distance) distances between members of any two groups when training set 1 is used as a training set for the classifier. The red color denotes the maximal value and the blue denotes the minimal value. The Euclidean distance measures only a relative distance from the mean point in the group. It does not take into account the distribution of the points in the group. The best separability, according to Euclidian distance, is achieved between groups 2 and 3 and between groups 2 and 7. The worst is between groups 1 and 7. Clearly, the Euclidean distance does not take into account the variability of the values in all dimensions and is, therefore, not an optimum discriminant analysis algorithm for this case.

	GROUP 2	**GROUP 3**	**GROUP 4**	**GROUP 5**	**GROUP 6**	**GROUP 7**
GROUP 1	0.9	0.4	0.7	0.25	0.5	**0.12**
GROUP 2		**1**	0.3	0.7	0.4	**~1**
GROUP 3			0.8	0.4	0.6	0.3
GROUP 4				0.5	0.2	0.8
GROUP 5					0.3	0.3
GROUP 6						0.6

Table 3.11 Normalized Mahalanobis (relative to the maximal Mahalanobis distance) distances between any two groups when training set 1 is used as a training set for the classifier. The red color denotes the maximal value and the blue color denotes the minimal values. Mahalanobis distances look at not only variations (variance) between the responses at the same wavelengths, but also at the inter-wavelength variations (co-variance). However, when the Mahalanobis distance is employed, only the separability between groups 1 and 4 is improved, compare to the case when Euclidian distance is used. The worst cases are between groups 5 and 6 and between groups 5 and 7.

	GROUP 2	**GROUP 3**	**GROUP 4**	**GROUP 5**	**GROUP 6**	**GROUP 7**
GROUP 1	0.9	0.4	0.7	0.25	0.5	**0.12**
GROUP 2		**1**	0.3	0.7	0.4	**~1**
GROUP 3			0.8	0.4	0.6	0.3
GROUP 4				0.5	0.2	0.8
GROUP 5					0.3	0.3
GROUP 6						0.6

Table 3.12 Normalized Bhattacharya (relative to the maximal Bhattacharya distance) distances between any two groups when training set 1 is used as training data for the classifier. The red colors denote the maximal value and the blue color denotes the minimal value. The best separability, according to Bhattacharya distance, was achieved between groups 1 and 4 and between groups 1 and 7. The worst are between groups 2 and 5 and between groups 5 and 6. We deem these groups to be *problematic*.

	GROUP 2	**GROUP 3**	**GROUP 4**	**GROUP 5**	**GROUP 6**	**GROUP 7**
GROUP 1	0.85	0.9	**~1**	0.8	0.8	**1**
GROUP 2		0.7	0.7	**0.6**	0.7	0.8
GROUP 3			0.8	0.7	0.7	0.8
GROUP 4				0.7	0.8	0.9
GROUP 5					**0.6**	0.7
GROUP 6						0.8

Table 3.13 **Normalized (relative to the maximal values) Euclidian, Mahalanobis and Bhattacharya distances between any two groups when training set 2 is used as training data for the classifier.**

	GROUP 2			GROUP 3			GROUP 4			GROPUP 5			GROUP 6			GROUP 7		
	ED	MD	BD	ED	MD	BD	ED	MD	BD	ED	MD	BD	ED	MD	BD	ED	MD	BD
GROUP 1	0.9	0.7	0.8	0.4	0.5	0.9	0.7	1	~1	0.3	0.1	0.8	0.5	0.1	0.8	0.1	0.2	1
GROUP 2				1	0.5	0.7	0.3	0.2	0.7	0.7	0.07	0.6	0.4	0.2	0.7	~1	0.5	0.8
GROUP 3							0.8	0.7	0.8	0.4	0.2	0.7	0.6	0.2	0.7	0.3	0.4	0.8
GROUP 4										0.5	0.1	0.7	0.2	0.3	0.8	0.8	0.8	0.9
GROUP 5													0.3	0.06	0.6	0.3	0.07	0.8
GROUP 6																0.6	0.1	0.8

Table 3.14 **Normalized (relative to the maximal values) Euclidian, Mahalanobis and Bhattacharya distances between any two groups when training set 3 is used as training data for the classifier.**

	GROUP 2			GROUP 3			GROUP 4			GROPUP 5			GROUP 6			GROUP 7		
	ED	MD	BD	ED	MD	BD	ED	MD	BD	ED	MD	BD	ED	MD	BD	ED	MD	BD
GROUP 1	0.9	0.7	0.8	0.4	0.4	0.9	0.7	1	~1	0.2	0.1	0.8	0.5	0.1	0.8	0.1	0.2	1
GROUP 2				1	0.4	0.7	0.3	0.1	0.7	0.7	0.07	0.6	0.4	0.2	0.7	~1	0.3	0.8
GROUP 3							0.8	0.5	0.8	0.4	0.1	0.7	0.6	0.2	0.7	0.3	0.3	0.9
GROUP 4										0.5	0.1	0.7	0.2	0.3	0.8	0.8	0.7	0.9
GROUP 5													0.3	0.05	0.7	0.3	0.07	0.8
GROUP 6																0.6	0.1	0.8

Table 3.15 **Normalized (relative to the maximal value) Euclidian, Mahalanobis and Bhattacharya distances between any two groups, when training set 4 is used as training data for the classifier.**

	GROUP 2			GROUP 3			GROUP 4			GROPUP 5			GROUP 6			GROUP 7		
	ED	MD	BD	ED	MD	BD	ED	MD	BD	ED	MD	BD	ED	MD	BD	ED	MD	BD
GROUP 1	0.8	0.3	0.8	0.2	0.2	0.9	0.5	0.9	1	0.1	0.2	0.9	0.2	0.1	0.9	0.2	0.3	~1
GROUP 2				1	0.3	0.7	0.4	0.2	0.8	0.9	0.2	0.7	0.7	0.2	0.7	0.9	0.2	0.8
GROUP 3							0.7	0.3	0.9	0.2	0.1	0.8	0.4	0.2	0.8	0.2	0.3	0.9
GROUP 4										0.6	0.1	0.8	0.3	0.2	0.8	0.6	1	0.9
GROUP 5													0.3	0.1	0.8	0.1	0.2	0.8
GROUP 6																0.3	0.1	0.8

3.7.2 Separability According to Average Classification Error

The average classification errors on the training data sets for the four cases (namely, training sets 1-4) described earlier are shown in Table 3.16. By inspecting the average errors, it is clear that applying a Bayesian discriminant function, assuming a Gaussian model with equal priors for each class we observe that we can almost perfectly discriminate between all seven geological groups. Moreover, the best separability is achieved for training set 1. As we increased the size of the training data by individually adding testing sets 1, then 2 then 3, small misclassification errors occur in some of the groups and the overall average error in classifying the relevant training data increases from 0.2% to 5%. Training set 4, which incorporates Test set 3, not only contains the largest number of samples, but also includes the largest number of rock samples from different origins for each class. Thus, it presents the greatest challenge to the Gaussian-model-based classifier.

Table 3.16 Separability performance of the Bayesian classifier, when uncompressed data (all eleven bands) are used. Training sets 2-4 are created by adding testing sets from 1 to 3 (described in Section 3.5) consecutively to the training set 1. For each case, the average separability error is calculated, according to Bayesian classifier. It is clear from the results, that best separability between all of the seven groups is achieved for training set 1. Separability error increases from 0.2% (training set 1) to 5% for the training data set 4, containing members outside of the original training data set (see Table 3.9).

	SIZE OF TRAINING SET 1	AVERAGE SEPAR. ERROR 0.002	SIZE OF TRAINING SET 2	AVERAGE SEPAR. ERROR 0.003	SIZE OF TRAINING SET3	AVERAGE SEPAR. ERROR 0.008	SIZE OF TRAINING SET 4	AVERAGE SEPAR. ERROR 0.05
GROUP 1	202	0	232	0	402	0.019	505	0.04
GROUP 2	505	0	580	0	1005	0	2424	0.04
GROUP 3	505	0	580	0	1005	0	909	0.035
GROUP 4	202	0	232	0	402	0.007	606	0.008
GROUP 5	1515	0	1740	0	3015	0	3131	0.1
GROUP 6	808	0.016	928	0.02	1608	0.02	3030	0.1
GROUP 7	404	0	464	0	804	0.005	1010	0.03

3.7.3 Classification of the Testing Data

The classification analysis shows very promising results. The classification errors on the testing data for the three sets described earlier (testing sets 1, 2, and 3) are shown in Table 3.17. For the testing set 1, the average misclassification error is 4%, for the second it is 7% and for the third test it is 70%. The large margin of error corresponding to the testing set 3 probably reflects the inherent difficulty in generalizing rock type classification. We suspect that the training data did not represent the testing data comprehensively. This problem is well known as an unrepresentative training samples problem (Shahshahani and Landgrebe [1994]). In remote sensing, the training data is usually selected from spatially adjacent regions and often, the spatial correlation among the neighboring samples is high. This fact introduces a problem when the training samples are used alone for estimating the class parameters because the parameters estimated in this way are representative of only the training field and their vicinity. As a result, outside the local vicinity, the data are not well represented. Thus, classification based on such a training field is not robust in the sense that, by changing the training field, the results may change significantly. This problem further aggravates the difficulties in analyzing remote sensing data (Shahshahani and Landgrebe [1994]). The next paragraph will shed further insight on this problem. Next, we will further investigate the high error probabilities associated with testing data 3.

Remark 1: Comments on the sources of misclassification:

We have observed that only group 5 performed perfectly well in *all* the tests presented so far. We believe that this excellent performance comes from the fact that group 5 has the largest training-data population and is, therefore, *better represented* compare to the rest of the groups. However, this fact affected adversely the remaining groups, especially those with the smallest initial training sets [e.g., groups 1 (Horfelsic) and 4 (Semischistose)]. As a result, most of the members of testing set 3 for groups 1 and 4 are classified as members of group 5. This observation was confirmed when we randomly reduced the size of the training data for group 5 by 50%, while keeping the training data for the rest of the groups unaltered. In this case, the classification error corresponding to testing data 3 was reduced to 64% (in comparison to 70% classification error with the original group 5). In addition to the average error reduction, the individual classification error for groups 2, 4 and 6 was also reduced. These results are tabulated in Table 3.18, which shows the classification errors when the classifier (based on the reduced group 5) is applied to testing sets 1, 2, and 3. Thus, by reducing the size of the training set for group 5 we can balance the group's representation in a way so that neither one of them overlaps the rest.

We also repeated the same experiment again, but this time instead of randomly choosing members of group five, we selected eight particular members to describe its geological properties (four fine-grain igneous rocks and the corresponding coarse-grain rocks). The members of the new, reduced-size group 5 are as follows: Mafic basalt (fine size), mafic basalt (coarse size), augite (fine and coarse size), mafic gabbro (coarse and fine size), and diorite (coarse and fine size). Then, the training set for group 5 was extended using only perturbations of these particular members. The original size for the tested sets (1, 2 and 3) for group 5 was kept the same. *Our goal here is to explore how reduction of the training set size by selecting specific set members affects classification performance for all seven groups, including the performance for the reduced group five*. The results of classification analysis are shown on Table 3.19. The separability error for training set 1 was reduced to 0. The average classification errors for each of the testing sets 1, 2, and 3 were reduced too. For example, for testing set 1, the random-reduction of size for group five gives a 3.4% classification error while the deterministic reduction gives a 1.4% average classification error. For testing set 2, deterministic reduction decreases the average classification error by 2%. For testing set 3, the change was from 64% for the random case to 62% for the deterministic case. In particular, the classification error for group 2 was reduced by 30% and for group 6 by 28% compare to the random case selection. However, in this case the error for group 5 increased from 0% to 44%. Most of the misclassified members were labeled as members of group 6, since groups 5 and 6 are very close to each other, according to Bhattacharya distance (see Table 3.12). As we can see, reducing the size of group 5 improves the overall separability and classification performance. However, the tradeoff is in the increased misclassification error for group 5.

Remark 2: The ability to distinguish between fine-grain rocks and coarse-grain rocks:

To address the problem associated with the size of the training and tested data, we extracted all the fine-size rocks from their groups and assigned them to a new, eighth group. We applied this segregation procedure to training sets 1 through 4 (Tables 3.1 and 3.2). The results of the separability analysis are shown in Table 3.20. Table 3.20 shows that the separability error increases from 0% to 0.8% as the training set varies from 1 to 4. The separability errors are significantly improved compared to those in Table 3.16, where the fine-grained rocks do not have their own group. This result suggests that fine-grained rocks should be classified separately.

Table 3.21 shows the ability to classify according to grain-size, where the classification error is shown when the classifier is applied to testing sets 1 through 3. Classification error increased from 2% to 9% as we moved from testing set 1 to testing set 2, and remained high (75%) for testing set 3. Notably, most of the members were misclassified as members of group 8, since it now contains all of the fine elements of the original training data and has a higher population compared to the rest of the groups. To further investigate the effect of grain size on the separability and classification performance, we selected only the first seven of all eight groups, containing the coarse-grain rocks only. The separability error is 0% for all the training sets, except for the training set 4, for which average separability error is 1% (see Table 3.22). These separability errors are lower than those in Table 3.16 and support the observation that fine-grained rocks should be classified separately. The average classification error also decreases. For testing set 1, the average error is 0%, for testing set 2 the average error is 6% (see Table 3.23). We received a higher error again for testing set 3 (70%). However, these results lead us to the conclusion that we can discriminate rocks not only according to their geological properties, but also according to their size.

Table 3.17 **Classification performance of the Bayesian classifier when uncompressed data (all eleven bands) are used. We applied the Bayesian classifier (trained with the training set 1) to testing sets 1-3 and compared the average classification error for each set. Comparing the results for testing set 1, 2 and 3, the average classification error increased from 4% to 70%. For the third test, the classifier is not able to correctly classify neither one of the members of tested data for groups 1 and 3. Similar is the situation with group 4 and 6 (only few members are correctly classified). The best performance is seen for group 5, without any misclassified members. However, most of the misclassified members for the rest of the groups were classified as members of group 5.**

	SIZE OF TRAINING DATA	AVERAGE SEPARAB. ERROR 0.002	SIZE OF TESTING SET 1	AVERAGE CLASSIF. ERROR 0.04	SIZE OF TESTING SET 2	AVERAGE CLASSIF. ERROR 0.07	SIZE OF TESTING SET 3	AVERAGE CLASSIFI. ERROR 0.7
GROUP 1	202	0	30	0.1	200	0.145	303	1
GROUP 2	505	0	75	0.026	500	0.046	1919	0.66
GROUP 3	505	0	75	0	500	0.016	404	1
GROUP 4	202	0	30	0.1	200	0.15	404	0.98
GROUP 5	1515	0	225	0	1500	0	1616	0
GROUP 6	808	0.016	120	0.05	800	0.067	2222	0.804
GROUP 7	404	0	60	0.03	400	0.062	606	0.67

Table 3.18 **Classification performance of the Bayesian classifier for tests 1-3, when the size of group 5 is reduced by random selection of eight members of the original fifteen bands. The individual classification errors for groups 2, 4 and 6 are reduced but still the members of testing set 3 for group 1 and group 3 are all incorrectly classified.**

	TRAINING DATA SIZE	AVERAGE SEPARABILITY ERROR 0.003	SIZE OF TESTING SET 1	AVERAGE CLASSIF. ERROR 0.034	SIZE OF TESTING SET 2	AVERAGE CLASSIF. ERROR 0.06	SIZE OF TESTING SET 3	AVERAGE CLASSIF. ERROR 0.64
GROUP 1	202	0	30	0.1	200	0.165	303	1
GROUP 2	505	0	75	0.04	500	0.036	1919	0.56
GROUP 3	505	0	75	0	500	0.006	404	1
GROUP 4	202	0	30	0.1	200	0.145	404	0.76
GROUP 5	316	0	225	0	500	0.009	241	0
GROUP 6	808	0.02	120	0.025	800	0.07	2222	0.5
GROUP 7	404	0	60	0	400	0.035	606	0.67

Table 3.19 **Classification performance of the Bayesian classifier for all tests 1-3, when the size of group five is reduced by "deterministic" selection of eight members of the original fifteen. The classification error for groups 2 and 6 is reduced compare to the case were the members are randomly selected. Still, the members of testing set 3 for group 1 and group 2 were entirely incorrectly classified. Note that a high misclassification error for group 5 appears. Most of the incorrect classified members are now confused as members of group 6, instead of group 5.**

	TRAINING DATA SIZE	**AVERAGE SEPARAB. ERROR 0**	**SIZE OF TESTING SET 1**	**AVERAGE CLASSIF. ERROR 0.014**	**SIZE OF TESTING SET 2**	**AVERAGE CLASSIF. ERROR 0.04**	**SIZE OF TESTING SET3**	**AVERAGE CLASSIF. ERROR 0.62**
GROUP 1	202	0	30	0.1	200	0.135	303	1
GROUP 2	505	0	75	0	500	0.006	1919	0.26
GROUP 3	505	0	75	0	500	0.002	404	1
GROUP 4	202	0	30	0	200	0.065	404	0.75
GROUP 5	808	0	120	0	800	0.001	1616	0.44
GROUP 6	808	0	120	0	800	0.02	2222	0.22
GROUP 7	404	0	60	0	400	0.04	606	0.7

Table 3.20 **Separability performance of the Bayesian classifier, when groups are created according to their geological properties and their grain size. The newly defined 8th group contains all fine elements of the original training data. With this data organization we achieve almost perfect separability.**

	TRAINING SET 1 SIZE	**AVERAGE SEPARAB. ERROR 0**	**TRAINING SET 2 SIZE**	**AVERAGE SEPARAB. ERROR ~0**	**TRAINING SET 3 SIZE**	**AVERAGE SEPARAB. ERROR 0.003**	**TRAINING SET 4 SIZE**	**AVERAGE SEPARAB. ERROR 0.008**
GROUP 1	101	0	116	0	201	0	202	0
GROUP 2	303	0	348	0	603	0.006	1212	0
GROUP 3	303	0	348	0	603	0	505	0
GROUP 4	101	0	116	0	201	0	303	0.003
GROUP 5	909	0	1044	0	2809	0.001	1717	0.06
GROUP 6	404	0	464	0	804	0.007	1515	0.002
GROUP 7	303	0	348	0.003	603	0.011	707	0.004
GROUP 8	1717	0	1972	0	3417	0	5454	0

Table 3.21 Classification performance of the Bayesian classifier at tests 1-3, applied over the eight groups. The higher error is again for testing set 3 and the performance is very close to the performance of the original data structure, where the rock's samplers were distributed among seven groups. Most of the misclassified members are confused with group 8, since it now has the highest population.

	TRAINING DATA SIZE	AVERAGE SEPARAB. ERROR 0	SIZE OF TESTING SET 1	AVERAGE CLASSIF. ERROR 0.019	SIZE OF TESTING SET 2	AVERAGE CLASSIF. ERROR 0.09	SIZE OF TESTING SET3	AVERAGE CLASSIF. ERROR 0.75
GROUP 1	101	0	15	0	100	0.18	101	1
GROUP 2	303	0	45	0.02	300	0.11	909	0.99
GROUP 3	303	0	45	0	300	0.05	202	1
GROUP 4	101	0	15	0.07	100	0.16	202	1
GROUP 5	909	0	135	0.02	900	0.009	808	0.5
GROUP 6	404	0	60	0	400	0.125	1111	1
GROUP 7	303	0	45	0.04	300	0.09	404	0.5
GROUP 8	1717	0	225	0	1700	0	3737	0

Table 3.22 Separability performance of the Bayesian classifier for training data sets 1-4, when the original seven groups contain only coarse size elements.

	SIZE OF TREINING SET 1	AVERAGE SEPARAB. ERROR 0	SIZE OF TRAINING SET 2	AVERAGE SEPARAB. ERROR 0	SIZE OF TRAINING SET 3	AVERAGE SEPARAB. ERROR ~0	SIZE OF TRAINING SET 4	AVERAGE SEPARAB. ERROR 0.01
GROUP 1	101	0	116	0	201	0	202	0
GROUP 2	303	0	348	0	603	0	1212	0
GROUP 3	303	0	348	0	603	0	505	0
GROUP 4	101	0	116	0	201	0	303	0
GROUP 5	909	0	1044	0	1809	0	1717	0.125
GROUP 6	404	0	464	0	804	0	1515	0.002
GROUP 7	303	0	348	0	603	0.003	707	0.001

Table 3.23 Classification performance of the Bayesian classifier for testing data sets 1-3, when the original seven groups contain only coarse size elements. Again, the classification performance for testing sets 1 and 2 is almost optimal, but the error for testing set 3 is still very high. Most of the misclassified members are confused as a members of group 5 and group 6.

	SIZE OF TRAINING SET 1	**AVERAGE SEPARAB. ERROR** **0**	**SIZE OF TESTING SET 1**	**AVERAGE CLASSIF. ERROR** **0**	**SIZE OF TESTING SET 2**	**AVERAGE CLASSIF. ERROR** **0.06**	**SIZE OF TESTING SET 3**	**AVERAGE CLASSIF. ERROR** **0.7**
GROUP 1	101	0	15	0	100	0.14	101	1
GROUP 2	303	0	45	0	300	0.04	909	0.7
GROUP 3	303	0	45	0	300	0.01	202	1
GROUP 4	101	0	15	0	100	0.11	202	1
GROUP 5	909	0	135	0	900	0	808	0.125
GROUP 6	404	0	60	0	400	0.05	1111	0.64
GROUP 7	303	0	45	0	300	0.043	404	0.5

3.8 Results Using Compressed Features

Our next goal is to investigate which are the important features and to what extent these features can represent our data without significant information loss. The feature extraction process is usually based on finding features that optimize a particular criterion. As we mentioned above, the individual bands of a multi-spectral image are highly correlated, i.e., they are visually and numerically similar. Analysis of all individual bands therefore can be extremely inefficient in terms of the amount of non-redundant data, present in the multi-spectral image. The desired goal is to eliminate the less informative features and thereby speed up the classification process. Moreover, certain feature extraction techniques, such as the spectral indices, will shed light on which bands are characteristic of different groups. We begin by employing a linear feature extraction that is designed to enhance separability. We will then use the method of spectral indices, which is a nonlinear feature extraction technique.

3.8.1 Feature Extraction Using Canonical Analysis

3.8.1.1 Theoretical Background

Principal and canonical component transformations are two pre-classification techniques for removing or reducing the spectral redundancy. They are similar in that they both form a new *n*-dimensional data set from a linear combination of the original *n* features (Schowengerdt [1983]). The transformed features are given (component-wise) by

$$x_i^{'} = \sum_{j=1}^{n} \omega_{ij} x_{j,} \qquad i, j = 1,\ldots,n, \tag{3.22}$$

were x_j and $x_i^{'}$ (primed variables) denote the feature components in the original and transformed data, respectively, and ω_{ij} are weights applied to the original training data x_j. This linear transformation can be written in vector notation as

$$X' = VX, \tag{3.23}$$

where **X** and **X'** are the original and transformed *n*-dimensional vectors and **V** is the *n* by *n* transformation matrix. The principal component analysis is a special case of the above equations, which is optimal in the sense that the matrix **V** is chosen to be the one that *diagonalizes* the covariance matrix of **X**. The principal component features are therefore uncorrelated. While the principal components transformation does not utilize any information about the class assignments, the canonical transformation maximizes the separability of the defined classes. Each class' mean vector and covariance matrix must be specified for the transformation; the *average within-class covariance matrix* is calculated from the individual class covariance matrices and the *between-class* covariance matrix is calculated from the class mean vectors. A transformation matrix is then determined, *simultaneously* diagonalizing the between-class covariance matrix and transforming the *average* within-class covariance matrix to the identity matrix (Schowengerdt [1983]). The goal is to maximize the separability between any two classes and minimize the variance within the classes.

To derive the transformation matrix **V**, we follow the procedure called "whitening," as described in (Tu, et al. [1998]). We give a brief explanation of this transformation:

Let **P** denote the average within-class covariance matrix and **Q** denote the between-class covariance matrix. Generally, these are *n* x *n* real symmetric matrices, where *n* is the features number.

Let $\mathbf{U} = (\phi_1, \phi_2, ...\phi_n)$ be an *n* by *n* matrix formed by adjoining the *n* normalized eigenvectors ϕ_i, *i*=1, ..., *n*, corresponding to the eigenvalues γ_i of the matrix **P**. The matrix **U** is unitary: it satisfies the property $\mathbf{U}^T\mathbf{U}=\mathbf{I}$ and $\mathbf{U}^{-1}=\mathbf{U}^T$. Because covariance matrices fall into a class of matrices called real symmetric, then according to (Tu, et al. [1998] (Theorem 5.4-4, p.256), **P** is similar to a diagonal matrix **M** in that

$$\mathbf{U}^T\mathbf{P}\mathbf{U} = diag(\gamma_1, ...\gamma_n) \equiv \mathbf{M}, \tag{3.24}$$

where $\gamma_1, ..., \gamma_n$ are the eigenvalues of **P**. To calculate the eigenvalues and the corresponding eigenvectors we used Matlab function eig, ([V, D] = eig(X) produces a diagonal matrix D of eigenvalues and a full matrix V whose columns are the corresponding eigenvectors so that XV = VD.)
Because **P** is positive definite (assuming that there is no class degeneracy), γ_i>0. Now define $\mathbf{Z} = diag(\gamma_1^{-1/2}, ...\gamma_n^{-1/2})$.

Now observe that $\mathbf{Z^T UPUZ} = \mathbf{Z^T MZ} = \mathbf{I}$. thus, by similarity transformation $(\mathbf{UZ})^{\mathbf{T}}\mathbf{P}(\mathbf{UZ})$, we not only diagonalize **P** but also reduce it to the identity matrix.

Next, we show that the similarity transformation $(\mathbf{UZ})^{\mathbf{T}}\mathbf{Q}(\mathbf{UZ})$ has produces a matrix that retains a real symmetric structure. Note that:

$$\left[\mathbf{Z^T U^T QUZ}\right]^{\mathbf{T}} = \mathbf{Z^T U^T QUZ},$$

so that

$$\mathbf{Z}^{\mathrm{T}}\mathbf{U}^{\mathrm{T}}\mathbf{QUZ} = \mathbf{A} \qquad (3.25)$$

is really symmetric.

Because **A** is really symmetric, there exists a unitary similarity transformation

$$\mathbf{W}^{T}\mathbf{AW} = diag(\lambda_1 ....\lambda_n) = \mathbf{\Lambda},$$

where $\mathbf{W}^{\mathrm{T}}\mathbf{W} = \mathbf{I}$, and $\square_1$, ..., $\square_{n.}$ ln are the eigenvectors of the matrix **A.**

Note that $(\mathbf{UZW})^{\mathrm{T}}\mathbf{Q}(\mathbf{UZW}) = \mathbf{W}^{\mathrm{T}}(\mathbf{UZ})^{\mathrm{T}}\mathbf{Q}(\mathbf{UZ})\mathbf{W} = \mathbf{W}^{\mathrm{T}}\mathbf{AW}$, which is a diagonal matrix.

Thus, the transformation **V=UZW** diagonalizes the matrix **Q**.

Now it is easy to check (using $(\mathbf{UZ})^{\mathrm{T}}\mathbf{P}(\mathbf{UZ}) = I$) that $\mathbf{V}^{\mathrm{T}}\mathbf{PV} = \mathbf{I}$. Indeed,

$$(\mathbf{UZW})^{\mathrm{T}}\mathbf{P}(\mathbf{UZW}) = \mathbf{W}^{\mathrm{T}}(\mathbf{UZ})^{\mathrm{T}}\mathbf{P}(\mathbf{UZ})\mathbf{W} = \mathbf{W}^{\mathrm{T}}\mathbf{IW} = \mathbf{I}.$$

In conclusion, **V** simultaneously diagonalizes **Q** and transforms **P** to an identity matrix and **V** is given by:

$$\mathbf{V}=\mathbf{UZW}. \qquad (3.26)$$

Because **Q'**, the covariance matrix of the transformed data, is diagonal, the canonical components (transformed features) are uncorrelated and, by convention, are ordered in decreasing variance. Thus, the "canonically" transformed feature 1 (denoted by $\mathrm{CT}_{1)}$ has the largest variance and the "canonically" transformed feature *n* (denoted by CT_n) has the smallest variance (Viterbi and Omura [1979], Schowengerdt [1997]). As a result, any correlation present in the original *n*-dimensional data is removed and, at the same time, simultaneous compression of most of the total image variance into fewer dimensions is achieved as follows: We select the *k* eigenvectors having the largest eigenvalues, while the remaining *n-k* dimensions generally contain noise. These eigenvectors can be obtained from the columns of the transformation matrix **V.**

$$\mathbf{CT} = \mathbf{VDN} \qquad (3.27)$$

where **CT** denotes the Canonical Transformation of the original data, **V** is transformation matrix, and **DN** is the matrix containing the original data in full dimension.

3.8.1.2 Discussion of Results

We compare performance of Canonical Component Analysis using five and seven features, respectively as shown in Tables 3.24 through 3.27, of which tables 3.24 and 3.25 show the separability results for the five-feature and seven-feature reductions, respectively, while tables 3.26 and 3.27 show the classification results for the five-feature and seven-feature reductions, respectively. All results indicate almost identical performance for the two cases of feature selection. For instance, Table 3.25 shows that classification error performed with five features for testing set 2 has an error rate of 9%. Using seven features on the same testing set reduced the classification error by only 1% to 8%, as seen in Table 3.27. Likewise, for testing set 3, using seven features instead of five reduced the classification error rate from 74% to 72%. We can conclude that, for the data studied in this report, five features can adequately capture the multi-spectral information needed to classify the data. Comparing these results with the case for which all eleven data dimensions were used, we observe a slight increase in classification errors. Figure 3.12 shows how the separability error decreases with an increasing number of the features selected. However, the significant reduction in dimensionality justifies this approach.

Figure 3.12 Average separability and classification errors for 2 to 11 features selected.

Table 3.24 Separability performance of the Bayesian classifier for the five selected features using the canonical transformation.

FIVE FEATURES	**SIZE OF TRAINING SET 1**	**AVERAGE SEPARAB. ERROR 0.07**	**SIZE OF TRAINING SET 2**	**AVERAGE SEPARAB. ERROR 0.07**	**SIZE OF TRAINING SET 3**	**AVERAGE SEPARAB. ERROR 0.08**	**SIZE OF TRAINING SET 4**	**AVERAGE CLASSIF ERROR 0.19**
GROUP 1	202	0.001	232	0.013	402	0.02	505	0.06
GROUP 2	505	0.03	580	0.03	1005	0.03	2424	0.11
GROUP 3	505	0.002	580	0.003	1005	0.06	909	0.21
GROUP 4	202	0.004	232	0.04	402	0.04	606	0.02
GROUP 5	1515	0.25	1740	0.25	3015	0.3	3131	0.46
GROUP 6	808	0.12	928	0.125	1608	0.117	3030	0.42
GROUP 7	404	0.042	464	0	804	0.04	1010	0.05

Table 3.25 Classification performance of the Bayesian classifier for tests 1-3 using the canonical transformation.

FIVE FEATURES	SIZE OF TRAINING SET 1	AVERAGE SEPARAB. ERROR **0.07**	SIZE OF TRAINING SET 2	AVERAGE SEPARAB. ERROR **0.055**	SIZE OF TRAINING SET 3	AVERAGE SEPARAB. ERROR **0.09**	SIZE OF TRAINING SET 4	AVERAGE CLASSIF ERROR **0.74**
GROUP 1	202	0.001	30	0	200	0.04	303	1
GROUP 2	505	0.03	75	0	500	0.05	1919	0.61
GROUP 3	505	0.002	75	0	500	0.04	404	1
GROUP 4	202	0.004	30	0	200	0.1	404	1
GROUP 5	1515	0.25	225	0.26	1500	0.257	1616	0.131
GROUP 6	808	0.12	120	0.125	800	0.13	2222	0.75
GROUP 7	404	0.042	60	0	400	0.06	606	0.67

Table 3.26 Separability performance of the Bayesian classifier for seven features using the canonical transformation. The average separability error for each one of the four training sets is lower compare to the case when five features were selected.

SEVEN FEATURES	SIZE OF TRAINING SET 1	AVERAGE SEPARAB. ERROR **0.027**	SIZE OF TRAINING SET 2	AVERAGE SEPARAB. ERROR **0.03**	SIZE OF TRAINING SET 3	AVERAGE SEPARAB. ERROR **0.025**	SIZE OF TRAINING SET 4	AVERAGE CLASSIF ERROR **0.157**
GROUP 1	202	0.005	232	0	402	0.03	505	0.05
GROUP 2	505	0.01	580	0.014	1005	0.011	2424	0.193
GROUP 3	505	0.006	580	0.01	1005	0.01	909	0.19
GROUP 4	202	0.02	232	0.02	402	0.042	606	0.01
GROUP 5	1515	0	1740	0	3015	0.002	3131	0.27
GROUP 6	808	0.13	928	0.13	1608	0.051	3030	0.34
GROUP 7	404	0.02	464	0.03	804	0.031	1010	0.04

Table 3.27 Classification performance of the Bayesian classifier at tests 1-3 using the canonical transformation. Compared to the case for which five features were selected, the average classification error for testing set 1 in this case decreases, but for testing sets 2 and 3, the performances are very close. Most of the misclassified members at test 3 are labelled as members of groups 2, 5 and 6.

SEVEN FEATURES	SIZE OF TRAINING SET 1	AVERAGE SEPARAB. ERROR **0.027**	SIZE OF TRAINING SET 2	AVERAGE SEPARAB. ERROR **0.03**	SIZE OF TRAINING SET 3	AVERAGE SEPARAB. ERROR **0.08**	SIZE OF TRAINING SET 4	AVERAGE CLASSIF ERROR **0.72**
GROUP 1	202	0.005	30	0	200	0.1	303	1
GROUP 2	505	0.01	75	0.04	500	0.06	1919	0.52
GROUP 3	505	0.006	75	0	500	0.024	404	1
GROUP 4	202	0.02	30	0	200	0.14	404	1
GROUP 5	1515	0	225	0	1500	0	1616	0.06
GROUP 6	808	0.13	120	0.15	800	0.15	2222	0.81
GROUP 7	404	0.02	60	0.03	400	0.065	606	0.67

3.8.2 The Use of Spectral Indices

To further investigate the important features of the data set we applied a second, nonlinear feature extraction algorithm to the data. The objective of this study was to identify *k* bands from the larger set of *n* bands, which would represent the essential information contained in the full set of bands. We define the band indices as the ratio between MTI filter's responses for any two bands as:

$$R = \frac{D_i}{D_j}, \tag{3.28}$$

where $D_{i,j}$ $(i,j = 1,\ldots, 13,\ i \neq j)$ are values related to the MTI bands.

This type of processing can (Schowengerdt [1997]):

- Remove temporally- or spatially-varying gain and bias factors. This is accomplished only if these factors are same in the bands used in the ratio.
- Suppress radiance variations arising from topographic slope and aspect.
- Enhance radiance difference between soils and vegetations.

We conducted an exhaustive search over the space of all possible combinations of two and three ratios. Because the number of combinations grows exponentially, we did not continue our search beyond triples of band indices. First, the Bhattacharya distance was used as a criterion for best separability. We computed this distance between all possible pairs of groups. Then, for each pair, we selected the *n*-tuple of band indices, $n = 2, 3$, that gave the maximal Bhattacharya distance. The results are presented in Tables 3.28a through 3.29b. This experiment allowed us to determine which bands play an important role in the separation of any two groups. As we expected, using only a pair of indices did not allow us to determine a common set that would provide maximum separability for all possible pairs of groups. Nevertheless, we observed that certain ratios re-occurred frequently in almost all cases, albeit, in combination with other ratios. These are the ratios labeled as 34, 35 and 43. Index 34 corresponds to the ratio between bands 4 (**D**) and 5 (**E**), index 35 is the ratio between bands 4 (**D**) and 6 (**G**), and index 43 is the ratio between bands 5 (**E**) and 6 (**G**). Note that, at the end of each table, we describe the correspondence between the ratios and their respective labels.

When the number of indices was increased to three, we observed that the same ratios formed triples that provided the best separability between *any* two groups. Our interpretation of this fact is that the three indices do capture most of the essential information needed to uniformly separate the groups. Using pairs of indices necessarily leads to underrepresentaion of features so that inclusion of an additional (third) index was critical. Moreover, using triplets of indices allows obtaining a unique solution for all seven groups.

Because our goal was to optimize simultaneous separability among all seven groups, we considered three optimization procedures for selecting the best ratios**.**

Table 3.28a **Pairs of ratios, corresponding to the maximum Bhattacharya distance between designated pairs of groups. Indices 34, 35 and 43 reoccurred in almost all pairs. Index 34 corresponds to the ratio between bands 4 (D) and 5 (E), index 35 is ratio between bands 4 (D) and 6 (G) and index 43 is ratio between bands 5 (E) and 6 (G).**

	GROUP 2	**GROUP 3**	**GROUP 4**	**GROUP 5**	**GROUP 6**	**GROUP 7**
GROUP 1	34,43	34,64	35,43	1,34	34,35	34,43
GROUP 2		34,76	35,43	1,34	35,43	35,43
GROUP 3			37,45	34,76	34,76	34,76
GROUP 4				35,43	35,43	35,43
GROUP 5					35,43	1,34
GROUP 6						34,35

Table 3.28b **Maximum Bhattacharya distance values for pairs of ratios listed in Table 3.28a. Red color denotes the maximum Bhattacharya distance value and blue color denotes the minimum Bhattacharya distance value. When combination of two ratios is chosen according to Bhattacharya distance, maximal separability is achieved between groups 1 and 4 and the worst separability is between groups 3 and 5.**

	GROUP 2	**GROUP 3**	**GROUP 4**	**GROUP 5**	**GROUP 6**	**GROUP 7**
GROUP 1	15	12	**19**	14	16	18
GROUP 2		13	15	12	14	15
GROUP 3			13	**11**	12	13
GROUP 4				13	16	18
GROUP 5					12	13
GROUP 6						15

Table 3.29a Triplet of ratios, corresponding to the maximum Bhattacharya distances between designated pairs of groups. A unique triplet yields the best separability between all pairs of groups. This triplet contains the three ratios that most frequently occur in the two-ratios case (see Table 3.28a). Index 34 corresponds to the ratio between bands 4 (D) and 5 (E), index 35 is the ratio between bands 4 (D) and 6 (G) and index 43 is the ratio between bands 5 (E) and 6 (G).

	GROUP 2	GROUP 3	GROUP 4	GROUP 5	GROUP 6	GROUP 7
GROUP 1	34,35,43	34,35,43	34,35,43	34,35,43	34,35,43	34,35,43
GROUP 2		34,35,43	34,35,43	34,35,43	34,35,43	34,35,43
GROUP 3			34,35,43	34,35,43	34,35,43	34,35,43
GROUP 4				34,35,43	34,35,43	34,35,43
GROUP 5					34,35,43	34,35,43
GROUP 6						34,35,43

Table 3.29b Maximum Bhattacharya distance values for triplets of ratios listed in Table 3.29a. Red color denotes the maximum Bhattacharya distance value and blue color denotes the minimum Bhattacharya distance value. The best separability is achieved between groups 1 and 4. The worst separability is also again between groups 3 and 5.

	GROUP 2	GROUP 3	GROUP 4	GROUP 5	GROUP 6	GROUP 7
GROUP 1	30	24	**35**	25	30	33
GROUP 2		22	30	22	28	29
GROUP 3			24	**18**	23	23
GROUP 4				25	31	34
GROUP 5					22	24
GROUP 6						30

3.8.2.1 The Intersection Optimization Strategy

The first approach was to increase the tolerance for the inter-group separability (measured by the Bhattacharya distance for each pair of groups). Recall that, when the maximal Bhattacharya distance criterion was used, only one pair of indices satisfied this criterion for any pair of groups. When we started to relax the criterion, we found, as expected, that more than one pair of indices satisfied the new criterion. Thus, by relaxing sufficiently the upper bound, we found non-empty intersections between all pairs of indices that satisfy the almost-maximum Bhattacharya distance criterion. In our case, the threshold value for the upper bound turned out to be equal to 86% of the original bound. *That is, there exits a vector of two of ratios for which the* Bhattacharya *distance is guaranteed — uniformly in all pairs of groups — to be within 14% of the maximum inter-group* Bhattacharya *distance.* Reducing the threshold further led to the occurrence of non-unique intersections (i.e., more than one vector resulting from the intersection). Recall that, when three ratios were used, a unique triplet of ratios already existed that achieved the maximum Bhattacharya distance between any two groups.

3.8.2.2 The Max-Min Optimization Strategy

The second approach we considered was a max–min strategy. For each vector of indices, we looked at the Bhattacharya-distance matrix (a matrix consisting of the Bhattacharya distance between each pair of groups) and selected the pair of groups that had the minimum Bhattacharya distance. This selection gives the worst-case scenario (with respect to all pairs of groups) for that vector of indices. Then, we varied the vector of indices and found the corresponding worst-case distance, and so on, going through all possible vectors of indices. Finally, among all the selected worst-case vectors of indices, we selected the one corresponding to the maximum Bhattacharya distance among all worst-case Bhattacharya distances. The winning vector, thus, is guaranteed to yield the best (maximum Bhattacharya distance) worst-case (minimum distance) scenario, and thus the name “max-min.”

3.8.2.3. Exhaustive Minimum-Average-Error Optimization Strategy

The third approach that we undertook was a minimal average error strategy. We conducted an exhaustive search over all possible combinations of two and three ratios to find the combination (i.e., a vector of indices) that gives the minimal average error. It became clear that this strategy would not provide the minimal misclassification error for each group. Instead, it optimized the overall performance of the classifier.

3.8.2.4. Indices Involving Ratio of Three Bands

Depending on the multi-spectral characteristics of different members of training set and tested data, simple ratios between MTI filters bands (using only two bands) may not always capture the changes in the shape of the multi-spectral signature curve. As we can see from Figure 3.13, when a two-band ratio (band *)*/(band *j*) is used, the same ratio value can represent several different multi-spectral signatures. As a result, different materials can not be distinguished by this method.

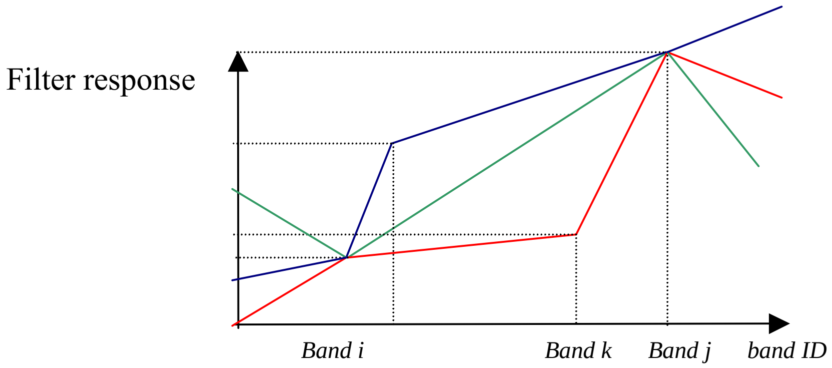

Figure 3.13 Multi-spectral signatures, representing three different rock types

Here, inspired by (Ninomiya [2002]) and conversation with Dr. Fogler, we used information from three bands to define a new type of ratio. The newly defined ratio will capture more typical multi-spectral characteristics of each geological group. The new ratio is defined as:

$$R1 = \frac{D_i + D_j}{D_k}, \tag{3.29}$$

where $i, j = (1,2,...,13), i \neq j$ and k takes any value between i and j. As a result, including between-band information in the ratios definition ensures more details in the compressed representation of the multi-spectral signature. To test potential advantages of using a 3-band ratio, we also formed an ad hoc combination of a 3-band ratio with two 2-band ratios. We combined the best pair of 2-band ratios selected according the minimum-average-error strategy with the best 3-band ratio selected according to the minimum-average-error strategy and compared the results against applying the optimization strategies to 2-band ratios only.

3.8.3 Discussion of Results

3.8.3.1. Combinations of Two Ratios:

We conducted some tests applying the three different optimization strategies to select combinations of two ratios. Our results in Tables 3.30 through 3.32 show that the intersection optimization strategy and max-min strategy performed very similarly. As expected, the minimal average error optimization performed best in the first two tests (corresponding to testing data 1 and 2). We recall that these two tests correspond to using perturbed versions of the original data. We also note that, for the third testing set, all three index optimization strategies performed approximately the same, as seen in Figure 3.14.

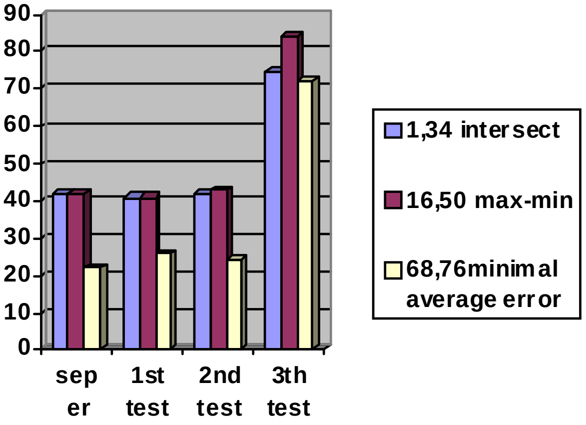

Label	Ratio
1	1/2
34	4/5
16	2/6
50	5/13
68	8/13
76	11/12

Figure 3.14 Comparison between the three optimization techniques, for selecting the best pair of indices.

3.8.3.2. Combinations of Three Ratios:

We conducted some tests applying the three different optimization strategies, as well as the ad hoc method of including a 3-band ratio, to select combinations of three ratios. Our results in Tables 3.33 through 3.36 again indicate that the minimal-average-error optimization strategy performed best for all of the tests. The error for test 3 is still high. The second best performer is the union of two-ratio combination selected according to the “minimal average error” strategy and the three-band ratio selected according to the same criterion. (As described earlier, the three-band ratio consists of a numerator that is the sum of any two bands divided by any band between the two bands.) Third place was the max-min optimization strategy with relatively close performance to the case for which three ratios are selecting according to the maximal Bhattacharya distance between any two groups. The results for all four cases are shown in Figure 3.15 below.

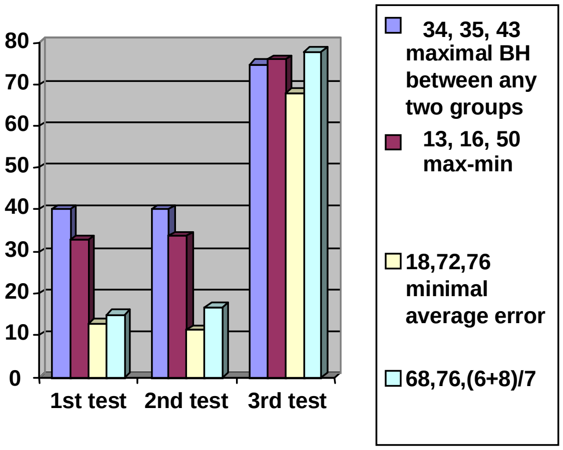

Label	Ratio
34	4/5
35	4/6
43	5/6
13	2/3
16	2/6
18	2/8
50	5/13
72	9/13
68	8/13

Figure 3.15 Comparison between the three optimization techniques for selecting the best triplet of indices

Table 3.30 **Bayesian classification performance for tests 1-3 when two ratios are selected according to intersection optimization strategy. Index 1 corresponds to the ratio between bands 1(A) and 2(B); index 34 corresponds to the ratio between bands 4(D) and 5(E).**

(1, 34) *1/2, 4/5*	TRAINING DATA SIZE	AVERAGE SEPARAB. ERROR 0.42	SIZE OF TESTING SET 1	AVERAGE CLASSIF. ERROR 0.41	SIZE OF TESTING SET 2	AVERAGE CLASSIF. ERROR 0.42	SIZE OF TESTING SET 3	AVERAGE CLASSIF. ERROR 0.75
GROUP 1	202	0.10	30	0.1	200	0.12	303	1
GROUP 2	505	0.78	75	0.75	500	0.78	1919	0.88
GROUP 3	505	0.12	75	0.17	500	0.1	404	1
GROUP 4	202	0.13	30	0.1	200	0.15	404	0.5
GROUP 5	1515	0.5	225	0.45	1500	0.48	1616	0.4
GROUP 6	808	0.8	120	0.8	800	0.8	2222	0.81
GROUP 7	404	0.5	60	0.5	400	0.5	606	0.67

Table 3.31 **Bayesian classification performance for tests 1-3, when two ratios are selected according to max-min optimization strategy. Index 16 corresponds to the ratio between bands 2(B) and 6(G) and index 50 corresponds to the ratio between bands 5(E) and 13(N).**

(16, 50) *2/6, 5/13*	TRAINING DATA SIZE	AVERAGE SEPARAB. ERROR 0.42	SIZE OF TESTING SET 1	AVERAGE CLASSIF. ERROR 0.41	SIZE OF TESTING SET 2	AVERAGE CLASSIF. ERROR 0.43	SIZE OF TESTING SET 3	AVERAGE CLASSIF. ERROR 0.84
GROUP 1	202	0.13	30	0	200	0.095	303	1
GROUP 2	505	0.6	75	0.6	500	0.61	1919	0.68
GROUP 3	505	0.03	75	0	500	0.008	404	1
GROUP 4	202	0.09	30	0.1	200	0.155	404	0.75
GROUP 5	1515	0.94	225	0.93	1500	0.93	1616	0.87
GROUP 6	808	0.46	120	0.56	800	0.52	2222	0.87
GROUP 7	404	0.67	60	0.68	400	0.66	606	0.69

Table 3.32 **Bayesian classification performance for testing sets 1-3 when two ratios are selected according to minimal average error optimization strategy. Index 68 corresponds to the ratios between bands 8 (O) and 13 (N) and index 76 corresponds to the ratio between bands 11 (L) and 12 (M).**

(68, 76) 8/13, 11/12	TRAINING DATA SIZE	AVERAGE SEPARAB. ERROR 0.22	SIZE OF TESTING SET 1	AVERAGE CLASSIF. ERROR 0.26	SIZE OF TESTING SET 2	AVERAGE CLASSIF. ERROR 0.242	SIZE OF TESTING SET 3	AVERAGE CLASSIF. ERROR 0.72
GROUP 1	202	0.04	30	0	200	0.04	303	1
GROUP 2	505	0.6	75	0.65	500	0.6	1919	0.92
GROUP 3	505	0.008	75	0.05	500	0.02	404	1
GROUP 4	202	0.09	30	0.1	200	0.13	404	0.64
GROUP 5	1515	0.35	225	0.35	1500	0.36	1616	0.7
GROUP 6	808	0.31	120	0.375	800	0.32	2222	0.43
GROUP 7	404	0.18	60	0.28	400	0.21	606	0.35

Table 3.33 **Bayesian classification performance for testing sets 1-3 when three ratios are selected according to the maximal Bhattacharya distance between any two groups. Index 34 corresponds to the ratio between bands 4 (D) and 5 (E), index 35 is the ratio between 4 (D) and 6 (G) and 43 is the ratio between bands 5 (E) and 6 (G).**

(34, 35, 43) 4/5, 4/6, 5/6	TRAINING DATA SIZE	AVERAGE SEPARAB. ERROR 0.4	SIZE OF TESTING SET 1	AVERAGE CLASSIF. ERROR 0.4	SIZE OF TESTING SET 2	AVERAGE CLASSIF. ERROR 0.4	SIZE OF TESTING SET 3	AVERAGE CLASSIF. ERROR 0.75
GROUP 1	202	0.09	30	0	200	0.09	303	0.77
GROUP 2	505	0.8	75	0.8	500	0.8	1919	1
GROUP 3	505	0.14	75	0.213	500	0.14	404	1
GROUP 4	202	0.08	30	0	200	0.03	404	0.73
GROUP 5	1515	0.7	225	0.7	1500	0.7	1616	0.47
GROUP 6	808	0.5	120	0.55	800	0.53	2222	0.83
GROUP 7	404	0.4	60	0.5	400	0.4	606	0.5

Table 3.34 **Bayesian classification performance for testing sets 1-3, when three ratios are selected according to max-min optimization strategy. Index 13 corresponds to the ratio between bands 2 (B) and 3 (C), index 16 is the ratio between bands 2 (B) and 6 (G) and index 50 is the ratio between bands 5 (E) and 13 (N).**

(13 ,16, 50) *2/3, 2/6,* *5/13*	TRAINING DATA SIZE	AVERAGE SEPARAB. ERROR 0.33	SIZE OF TESTING SET 1	AVERAGE CLASSIF. ERROR 0.33	SIZE OF TESTING SET 2	AVERAGE CLASSIF. ERROR 0.34	SIZE OF TESTING SET 3	AVERAGE CLASSIF. ERROR 0.76
GROUP 1	202	0.08	30	0.1	200	0.1	303	1
GROUP 2	505	0.41	75	0.4	500	0.43	1919	0.67
GROUP 3	505	0.17	75	0.2	500	0.198	404	1
GROUP 4	202	0.16	30	0.13	200	0.195	404	0.58
GROUP 5	1515	0.74	225	0.804	1500	0.77	1616	0.65
GROUP 6	808	0.42	120	0.4	800	0.44	2222	0.9
GROUP 7	404	0.3	60	0.25	400	0.26	606	0.5

Table 3.35 **Bayesian classification performance for testing sets 1-3 when two 2-band ratios are selected according to minimal average error optimization strategy and one 3-band ratio is selected again according to the minimal average error optimization strategy.. Index 68 corresponds to the ratio between bands 8 (O) and 13 (N). Index 76 corresponds to the ratio between bands 11 (L) and 12 (M).**

68,76,6+8/7) *8/13, 11/12,* *(6+8)/7*	TRAINING DATA SIZE	AVERAGE SEPARAB. ERROR 0.17	SIZE OF TESTING SET 1	AVERAGE CLASSIF. ERROR 0.148	SIZE OF TESTING SET 2	AVERAGE CLASSIF. ERROR 0.168	SIZE OF TESTING SET 3	AVERAGE CLASSIF. ERROR 0.78
GROUP 1	202	0.03	30	0	200	0.025	303	1
GROUP 2	505	0.36	75	0.3	500	0.4	1919	0.85
GROUP 3	505	0.003	75	0.04	500	0.008	404	1
GROUP 4	202	0.13	30	0.06	200	0.11	404	0.95
GROUP 5	1515	0.31	225	0.31	1500	0.31	1616	0.63
GROUP 6	808	0.3	120	0.3	800	0.3	2222	0.42
GROUP 7	404	0.05	60	0	400	0.04	606	0.61

Table 3.36 Bayesian classification performance for testing sets 1-3 when three ratios are selected according to the minimal average error optimization strategy. Index 18 corresponds to the ratio between bands 2 (B) and 8 (O), index 72 corresponds to the ratio between bands 9 (J) and 13 (N), and index 76 corresponds to the ratio between bands 11 (L) and 12 (M).

18, 72, 76 2/8, 9/13, 11/12	Training Data Size	Average Separability Error **0.077**	Size Of Testing Set 1	Average Classification Error **0.13**	Size Of Testing Set 2	Average Classification Error **0.114**	Size Of Testing Set 3	Average Classification Error **0.68**
GROUP 1	202	0.03	30	0.1	200	0.065	303	1
GROUP 2	505	0.15	75	0.2	500	0.2	1919	0.58
GROUP 3	505	0.002	75	0.04	500	0.014	404	1
GROUP 4	202	0.044	30	0.07	200	0.11	404	0.68
GROUP 5	1515	0.2	225	0.2	1500	0.2	1616	0.5
GROUP 6	808	0.08	120	0.1	800	0.12	2222	0.42
GROUP 7	404	0.04	60	0.15	400	0.07	606	0.58

3.9 Conclusions

To date, our study has shown that it is not the first-order variation but the second-order variation that bears the discriminant power among the classes. The large average classification errors produced by the minimum distance classifier clearly indicated that the Euclidian-distance alone can not provide good inter-class separability because the Euclidean distance does not account for the covariance differences among the classes. When the means are indistinguishable, the Euclidian metric fails to separate the classes.

To estimate second-order statistics, we first augmented the limited training data by adding small percentages of water, minerals, and vegetation and then heuristically selected spectral features to reduce the feature space dimensionality. We increased the size of the training data significantly (e.g., by a factor > 10) by introducing small perturbations of the original training data with vegetation, soil, water, and other valid minerals. We obtained reliable estimates of covariance matrices for Bayesian classification. Our experience shows that this approach can be successfully adopted in cases when initial training data sets are small and do not permit direct application of Bayesian classifiers.

These results suggest that the Bayesian classifier can discriminate between the rock classes when the test samples are subject to small variations from the training data. However, these experiments showed that the classifier failed to generalize novel rock samples because of its limited training set. In particular, the study showed that grain size can affect the classifiability of the rock samples. Thus, we recommend assigning rock classes according to both rock type and grain size and training the classifier to recognize both. We recommend extending the study to include larger and more comprehensively characterized training and test sets. This follow-on study would allow us to characterize the conditions under which the classifier can reliably generalize and discriminate novel rock samples.

By applying the canonical feature extraction technique to our data, we lowered the dimensionality of the multi-spectral data in an optimal way. Classification using five and seven of the canonically transformed features performs almost as well as classification using all of the eleven features. Moreover, the significant reduction in dimensionality justifies this approach. Our experience suggests that canonical transformation is a promising methodology for feature extraction.

The second systematic feature extraction strategy that we explored was based on data feature compression via ratios between bands (indices). We found that this strategy is capable of capturing the most relevant information from the data. First, we tried the traditional approach wherein the ratios were determined according to the maximal Bhattacharya distance between any two groups. As expected, combinations of two ratios did not provide us with unique pair of indices that maximized all possible distances. Fortunately, combinations of three ratios lead to a unique triplet that maximized the Bhattacharya distance between any two groups. Since our goal was to achieve good separability between all seven groups, we considered three optimization procedures for selecting pairs and triplets of ratios based on improving the simultaneous separability between all seven groups. Not surprisingly, classification accuracy improves with the number of indices employed. Unfortunately, the penalty for using this approach is in the need to perform an exhaustive search over the data, which becomes prohibitively expensive for more than three index combinations.

Our first approach was to increase the tolerance for the inter-group separability (measured by the Bhattacharya distance for each pair of groups)**.** By relaxing the upper bound sufficiently, we found a non-empty intersection between all pairs of indices that satisfied the almost-maximum Bhattacharya distance criterion. Our second approach was a max-min strategy. The max-min strategy does not provide for the best between class separability; however, it does provide a set of indices that ensure *uniform* separability in the best worst-case manner. Our third approach was a minimal average error strategy. We conducted an exhaustive search over all possible combinations of two and three ratios to find the combination that gave the minimal average error. It is clear that this strategy will not provide the minimal misclassification error for each group. Instead, it optimizes the overall performance of the classifier. Our results indicate that the combination of ratios selected according to the minimal average error optimization strategy performed best in all tests. Based on our experience, we would recommend considering a further optimization by merging a combination of two and three ratios, determined according to the above–mentioned optimization strategies.

Depending on the multi-spectral characteristics of different members of the training and test data, the ratio between only two bands may not always capture the changes in the shape of the multi-spectral signature curve. As a result, different materials cannot be distinguished in this manner. We used information from three bands to redefine the ratio, capturing more typical multi-spectral characteristics of each geological group. Inclusion of between-the-bands information in the formulation of more complex ratios generates more details in the compressed representation of the multi-spectral signature.

One ratio of all possible combinations was selected, according to the minimum average error strategy. It was appended to the two ratios already selected according to the same optimization strategy. The performance of this triplet was close to the performance of the three ratios selected according to the minimal average error strategy.

3.10 Future Work

We wish to continue working on all the problems mentioned to further optimize performance of the separation techniques that we considered. The prospective issues to be addressed include:

- Further explore the effect of the grain size on between-class separation.
- Form classes according to both rock type and grain size; train the classifier to recognize both.
- Extend the study to include larger and more comprehensively characterized training and test sets, which would allow us to characterize the conditions under which the classifier can reliably generalize and discriminate novel rock samples.
- Test separability taking into account spectral variability imposed by the atmosphere.
- Test separability on MTI data taken from geographically dissimilar places.
- Go beyond MTI: For a given number of multi spectral bands, find the set of filters that optimizes the performance of the Bayesian classifier for the seven rock groups. This problem is different from the hyperspectral problem because here we put a constraint on the number of bands (<14, say) and put a constraint on the spectral resolution of each band, which would be much coarser than the resolutions seen in hyperspectral images.

3.11 References

Chen, Xianfeng, 1998, “Topographic Normalization of TM Imagery for Rock Classification in Pershing County, Nevada,” Report, (http://www.geo.wvu.edu/geog455/spring98/12/intro.htm).

Duda, R.O., Hart, P.E., Strok, D.G., 2000, “Pattern Classification,” second edition, John Wiley and Son.

Fogler, R.J., “Multi- and Hyper-Spectral Sensing for Autonomous Ground Vehicle Navigation,” SAND2003-1980, Printed June 2003, Sandia National Laboratories, P.O. Box 5800.

Haertel, V., Langrebe, D., “On the Classification of Classes with Nearly Equal Spectral Response in the Remote Sensing Hyperspectral Image Data,” *IEEE Transaction on Geosciences and Remote Sensing*, Vol. 37, No. 5, Part 2, September 1999. http://dynamo.ecn.purdue.edu/~landgreb/publications.html).

Ientilucci, E., “Hyperspectral Image Classification Using Orthogonal Subspace Projection: Image Stimulation and Noise Analysis,” Center for Image Science, Rochester Institute of Technology, Technical Report, April 23, 2001. (http://www.cis.rit.edu./~ejipci/Report/osp_paper.pdf).

Jackson, Q. and Landgrebe, D.A., “An Adaptive Classifier Design for High-Dimensional Data Analysis with a Limited Training Data Set,” IEEE Transaction on Geosciences and Remote Sensing, Vol. 39, No. 12, December 2001. (http://dynamo.ecn.purdue.edu/~landgreb/publications.html).

Jimnez, L., Landgrebe, D., “Supervised Classification in High Dimensional Space: Geometrical, Statistical and Asymptotical Properties of Multivariate data,” *IEEE Transaction on Geosciences and Remote Sensing*, Vol. 37, No. 6, November 1999. (http://dynamo.ecn.purdue.edu/~landgreb/publications.html).

Ninomiya, Y., **“**Mapping Quartz, Carbonate Minerals, and Mafic-Ultramafic Rocks Using Remotely Sensed Multispectral Thermal Infrared ASTER data,” *Proc. SPIE*, Vol. 4710, p. 191–202, Thermosense XXIV, Xavier P. Maldague Andres E. Rozlosnik Eds., March 2002.

Patel, N., “Spectral Discrimination of Rrock Types in the Aravalli Mountain Ranges of Rajasthan, India, using Landsat Thematic Mapper Data.” (http://www.gisdevelopment.net/aars/acrs/2002/geo/060.pdf).

Schowengerdt, R.A., 1997, “Remote Sensing. Models and Methods for Image Processing,” second edition, Academic Press.

Schowengerdt, R.A., 1983, “Techniques for Image Processing and Classification in Remote Sensing,” Academic Press.

Shahshahani, B.M., and Landgrebe, D.A., “The Effect of Unlabeled Samples in Reducing the Small Sample Size Problem and Mitigating the Hughes Phenomenon,” *IEEE Transaction on Geosciences and Remote Sensing*, September 1994. (http://dynamo.ecn.purdue.edu/~landgreb/publications.html).

Stark, H., Woods, J., 2002, “Probability and Random Process with Applications to Signal Processing,” third edition, Prentice-Hall.

Tu, T.-M., Chen, C., Wu, J., Chang, Ch., “A Fast Two-Stage Classification Method for High-Dimensional remote Sensing Data,” *IEEE Transaction on Geosciences and Remote Sensing*, Vol. 36, No. 1, January 1998.

Viterbi, A.J., and Omura, J.K., 1997, “Principles of Digital Communication and Coding,” McGraw-Hill electrical engineering series.

4 Other Tools

The RemoteGeo team has identified ongoing work at SNL that provides techniques potentially useful to enhancing a geologist's interpretation of a remote site. This section describes three techniques relevant to geological characterization.

4.1 Spatial and Spectral Derivatives

The SNL MTI data exploitation team has implemented spatial and spectral derivative filtering on MTI images to enhance features within the images. They compute the spatial derivatives within each spectral band image and sum all band derivatives together. The spatial derivatives show local variations in texture and enhance scene details, such as trails, buried pipelines, hidden tarps, and underground facility vents. Extremely faint patterns and signals become noticeable. Figure 4.1(a) shows a true color image of a section of the Ivanpah Playa in Nevada. Figure 4.1(b) shows the results of combining bi-directional derivatives from the visible and NIR MTI bands. The derivative image highlights spatial details such as trails and pipelines.

Figure 4.1(a) MTI true-color image (Ivanpah, NV)

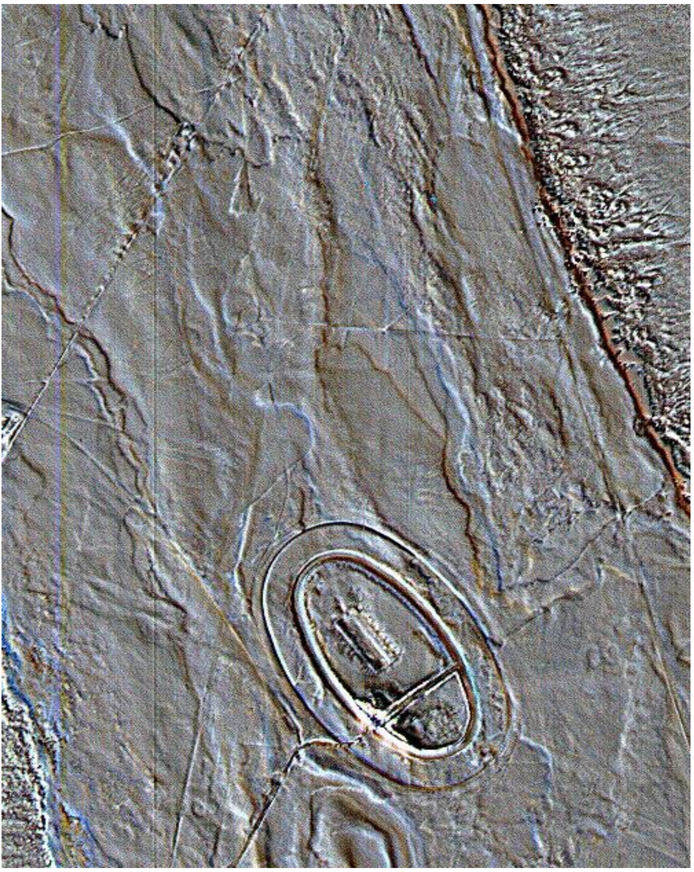

Figure 4.1(b) MTI VNIR Multi-spectral bi-directional derivative image

The spectral derivatives emphasize regions with steep spectral features. Figure 4.2a shows a color infrared image of a river in Delaware. Figure 4.2b shows spatial derivatives applied to the visible and NIR bands. It enhances small features such as buoys in the water. Figure 4.2c shows spatial derivatives applied to the LWIR bands. This derivative shows the lingering thermal wake of the boat. Figure 4.2d shows a spectral derivative applied to the visible and NIR bands. The spectral derivative highlights the spectral differences between the clear and sediment-filled sections of the river.

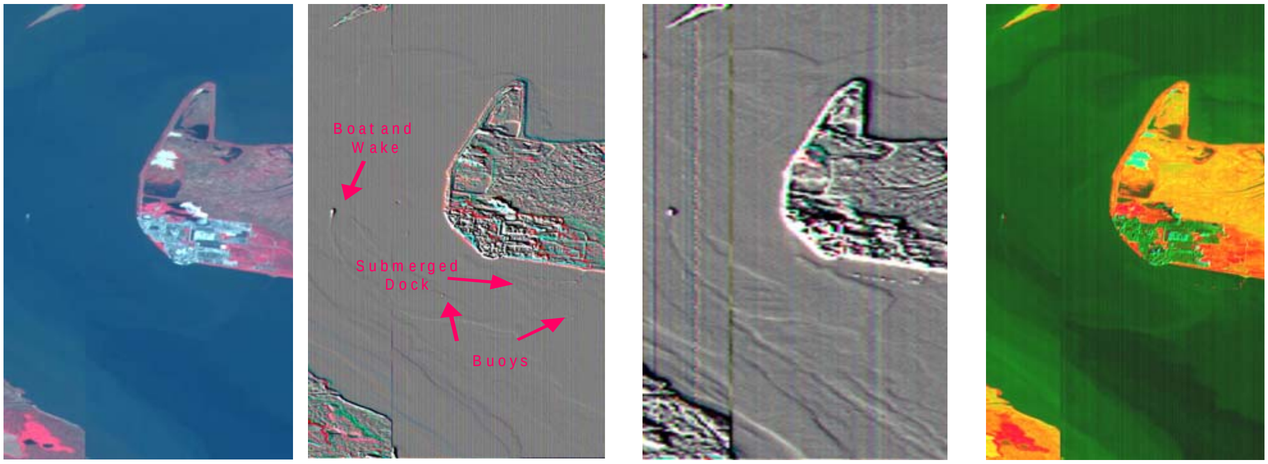

Figure 4.2 **(a) MTI color infrared image (Delaware); (b) Derivative filteredVNIR Image; (c) Thermal texture Filtered TIR Image; (d) Spectral DerivativeVNIR Image**

4.2 Supersampling

The SNL MTI data exploitation team has created a method of generating a synthetic high-resolution image from a collection of several low-resolution images. The method employs microscanning, which takes advantage of the MTI satellite's flexible pointing capability and its overdesigned optical system. The satellite moves the imager by slight, subpixel amounts to generate sub-Nyquist data sets, which are then processed to generate a supersampled image. The imager collects four samples of each pixel as sensor sweeps in the along-track direction. The detector's high responsivity reduces the required sample time and enables collection of multiple samples in the time allotted. The satellite rotates to allow supersampling in both directions. Figure 4.3 show a graphic representation of the satellite yaw and microscanning maneuvers to generate improved resolution in both spatial dimensions. Processing the supersampled image requires a premeasured estimate of the imager's point spread function (PSF). MTI developers compute the PSF from an image of known object. They then deconvolve the supersampled image with PSF to yield increase in spatial resolution by a factor of four in both dimensions: 1.25m effective GSD in VNIR bands and 5m effective GSD in SWIR/TIR bands. Figure 4.4a shows an example of an MTI LWIR supersampled image of New Orleans Pontchartrain Center with effective 5 meter GSD. The high-resolution thermal detail could provide important information about thermal surface features for geological characterization. For comparison, Figure 4.4b shows a panchromatic image with 3 meter GSD.

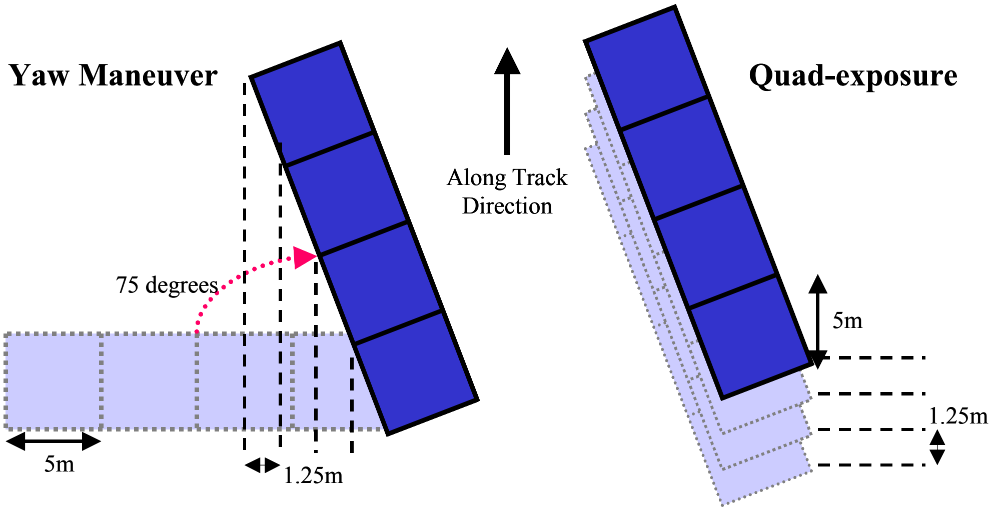

Figure 4.3 Microscanning and Yaw for Two-dimensional Supersampling

Figure 4.4(a) MTI thermal image of New Orleans Pontchartrain Center with 5 m effective GSD

Figure 4.4(b) Airborne panchromatic image of New Orleans Pontchartrain Center with 3 m GSD†

4.3 Segmentation Using VNIR/SWIR for Rock Classes

The purpose of a spectral segmentation algorithm is to identify spectrally similar regions, or segments, within a spectral image. Ideally, the segments would correspond to objects in the field of view comprised of similar materials. The segmentation algorithm should include spectra that have the same general shape characteristics in the same segment. It should ignore minor spectral variations that result from noise or insignificant deviations in the material's characteristics. However, traditional segmentation algorithms that are based on distance metrics produce brittle segments and rely heavily on operator adjustment of the threshold parameter. Large threshold values tend to produce segments that incorporate multiple objects and materials. Smaller threshold values tend to make discriminations based on minor insignificant spectral deviations and, thus, produce too many segments within single objects and materials. Thus, it becomes impossible to adjust the threshold value to produce segments that correspond to recognizable and physically significant objects and regions in the image. These segmentation algorithms fail to produce segments that are robust to changes in perspective view.

To avoid the difficulties associated with distance metric based segmentation, José Salazar has developed a new Robust Spectral Segmentation (RSS) algorithm designed to cluster spectra with the same overall shape characteristics and ignore minor spectral deviations. His approach produces segments that are robust to minor spectral variations. Furthermore, his approach requires no parameter selection; it determines the number of segments from the inherent properties of the data.

The RSS algorithm first applies a quantizing transformation to each pixel of the spectral image data. The quantizing transformation reduces sensitivity to multiplicative and additive scaling of the spectral data, such as the multiplicative scaling induced by changes in illumination angle. It also reduces sensitivity to pixel-to-pixel variabilities within a material. The quantized data inherently form local clusters. The RSS algorithm then applies a modified version of the Distribution Free Clustering algorithm (Comaniciu) to determine which clusters stand as separate segments and which groups of clusters should coalese to form single segments. José has tested the RSS algorithm with MTI data in the visible and near-infrared bands of the Primm Valley Golf Course near Ivanpah Playa, Nevada. Figure 4.5 shows color infrared imagery of six different perspective view of the golf course collected on six different occasions with the MTI sensor. Figure 4.6 shows the spectral segmentations produced by RSS for these golf course perspective views. The algorithm has correctly segmented the grass, water traps, and surrounding playa background for every perspective view. The RSS algorithm is currently undergoing further testing. Initial indications suggests that it can provide reliable segmentations to aid analysts and geologists in identifying regions of similar rock type, tailings piles, and changes, such as disturbed earth.

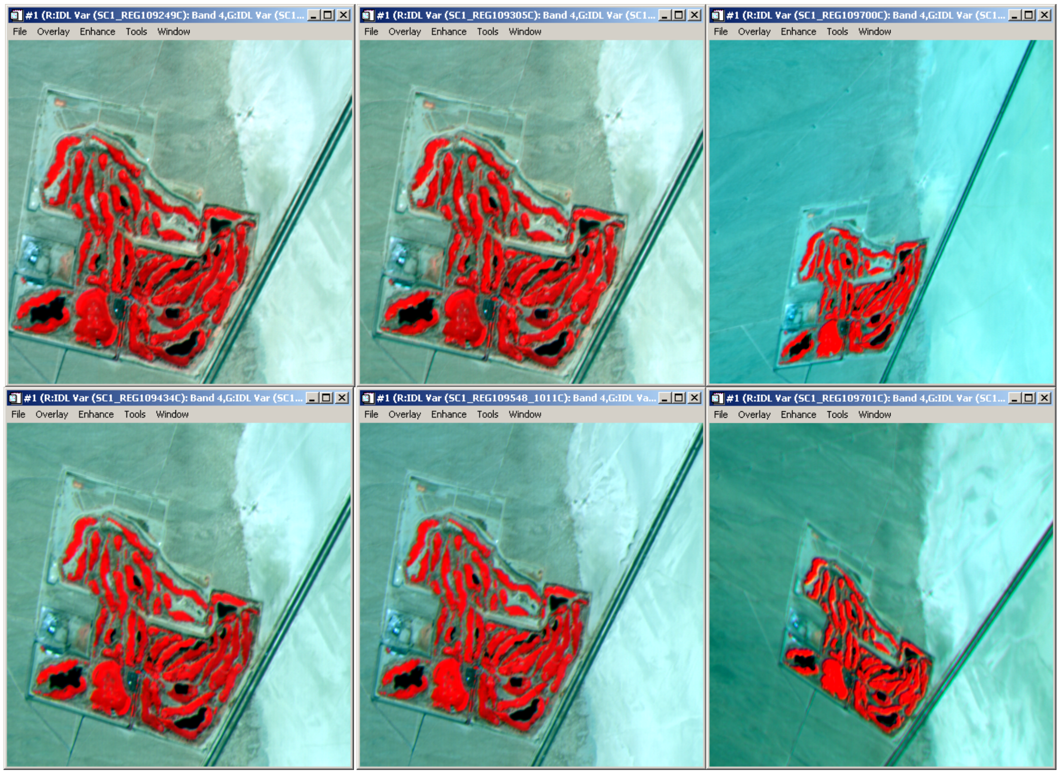

Figure 4.5 Color Infrared Composite Images of Primm Valley Golf Course taken from six perspective views of MTI Imagery

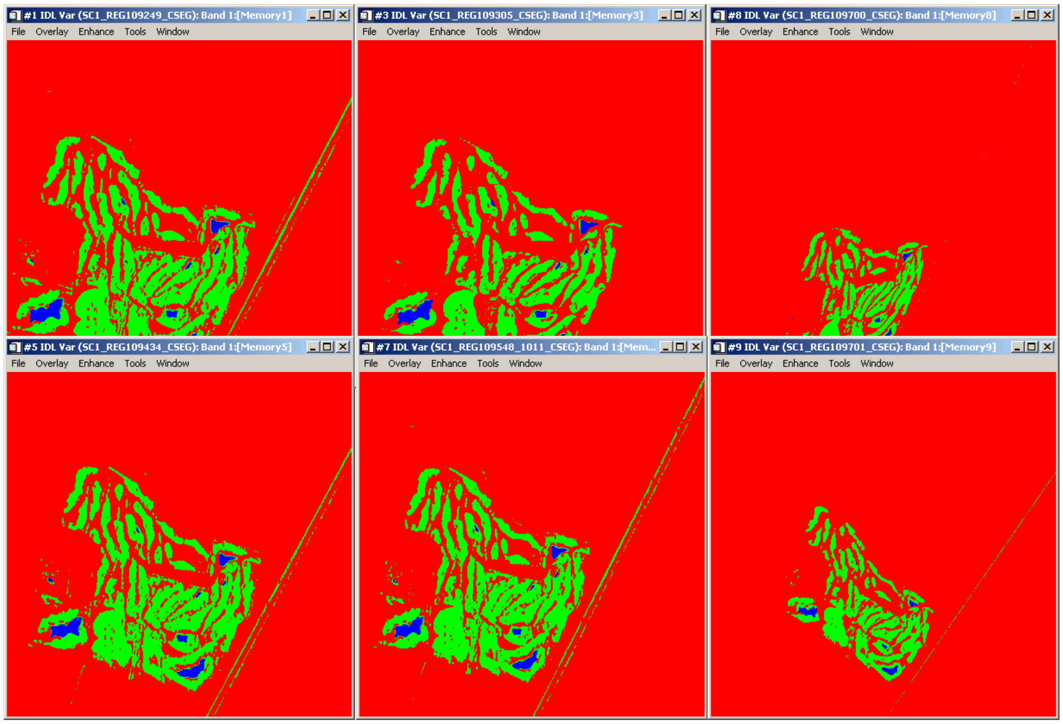

Figure 4.6 RSS-produced Segmentations from visible and near-infrared MTI bands of Primm Valley Golf Course

4.4 High-Resolution Interferometric SAR Imagery and Rivertools

The SNL Synthetic Aperture Radar (SAR) Dept. can generate interferometric SAR data to construct high resolution DEMs. DEMs with 3-meter post spacings are typical. Figure 4.7a shows a 3-meter DEM of Coyote Canyon, south of Albuquerque, NM. The elevation information provides valuable clues to geologists about the nature of drainage patterns in the area. To speed and enhance the ability of the geologist to interpret elevation data, Research Systems, Inc. has written a Rivertools software package that estimates the drainage patterns by computing local gradients from the elevation data. Combining the capabilities of Rivertools with the IFSAR DEMs could provide the geologist with enhanced ability to detect and understand large-scale fracture networks, faults, localized ground subsidence, drainage patterns, and other discontinuities.

Figure 4.7(a) SNL 3m IFSAR DEM of Coyote Canyon on Manzano Base, Albuquerque, NM

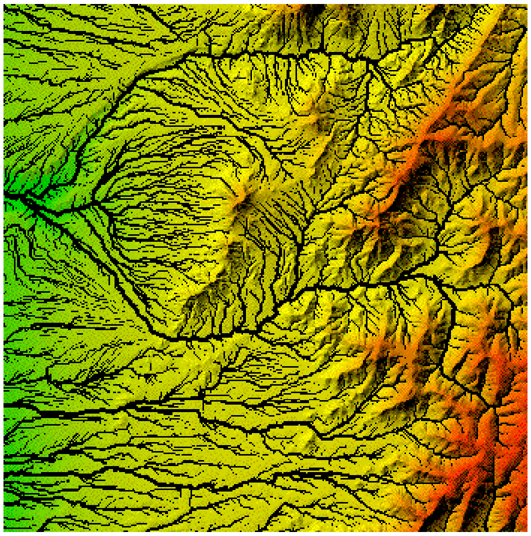

Figure 4.7(b) Rivertools Output Derived from USGS 10 m DEM Manzano Base, Albuquerque, NM

5 Summary and Recommendations

5.1 Summary and Conclusions

This study has developed some new and promising methods for extracting information from remotely sensed spectral data to aid an analyst in interpreting the geology and geotechnical characteristics of an underground facility.

We developed a method to estimate rock thermal properties from Multi-Spectral Thermal Imager (MTI) thermal measurements of rock surfaces subject to differential heating histories produced by terrain shading. The method takes advantage of high spatial resolution in the MTI thermal bands and MTI's flexible pointing capability. The method applies a least mean square optimization procedure to search for the rock parameters that minimize the differences between model-predicted radiances and measured radiances of the pixels in the vicinity of the shadow. We applied the Dykhuizen and Helmich numerical model to predict pixel radiances and DAKOTA code for optimization. (Dykhuizen and Helmich [1994], see reference listing at end of Chapter 2.)

Because predicting the surface heating history requires a digital elevation model (DEM) registered to the multi-spectral data, we developed a method for extracting elevation data directly from three or more MTI images taken from different perspective views. In this study, we developed fundamental pieces of the geometric model and developed and tested match point algorithms for parallax determination. Follow-on work under another project will complete the implementation and testing of the geometric model, identify and mitigate error sources, test the alternative point matching algorithms, investigate improvements to estimating spacecraft attitude, complete the exterior orientation model, and implement and test the DEM extraction. This method promises to eliminate tedious hand-registration of multi-spectral data to digital elevation data.

Simulations of the rock parameter estimation approach demonstrated its validity. A sensitivity analysis showed that the method produces useful rock parameter estimates even with radiance measurement errors. We applied the method to MTI thermal data collected at two desert sites: Coyote Canyon, located in the Manzano Mountains south of Albuquerque, NM, and Red Wing Mine, located at China Lake, CA. The initial application of the approach to these sites produced inaccurate rock parameter estimates probably because the model included insufficient atmospheric compensation and failed to account for moisture and vegetation in the region. We developed some analytical models to study sun-shade temperature difference phenomena and the effects of moisture and vegetation.

Our simple analytical models predict temperature differences between sunlit and shaded areas. The first analytical model includes no provisions for moisture and applies to dry, bare surface conditions, such as exposed faces of intact rock. The dry analytical model confirmed the trend predicted by the numerical model.

The second analytical model incorporates a simple model for near-surface soil moisture. Including the latent heat flux due to evaporation increases the apparent thermal inertia of the soil. The presence of soil moisture substantially affects the temperature difference between sunlit and shaded regions; more than one-half of the total incident energy is consumed by evaporation from a wet soil. The surface temperature difference decreases with increasing saturation.

The third analytical model incorporates a simple model for sparse vegetation. Vegetation significantly affects the near-surface energy balance by reducing the amount of incident solar radiation that reaches the ground surface. In addition, the remotely sensed surface temperature is a function of the amount of vegetation. Consequently, the utility of sun-shade temperature differences to deduce the thermal inertia of the ground decreases with increasing vegetation.

These analytical model results suggest the following conclusions. Identifying near-surface properties from sun-shade temperature differences appears feasible but becomes increasingly difficult if significant soil moisture and vegetation are present. Two factors complicate the analysis: 1) moisture and vegetation reduce the magnitude of the temperature difference between sunlit and shaded regions; and 2) because evaporation and transpiration are difficult processes to model robustly yet simply, approximate models incorporate additional uncertainties. The results suggest that the fractional vegetation coverage is a crucial input to any attempt to interpret temperature differences between sunlit and shaded areas. We have developed an approach to use vegetation index measurements from multiple perspective views of a site to predict the temperature of the bare ground beneath the vegetation.

We also conducted a number of field tests to study temperature measurement phenomena and validate the thermal models. We discovered that evaporation, even well less than the maximum amount, is significant enough to affect the surface temperatures and temperature differences that develop in the soil. Even soil that appears dry can evaporate water. Field test results suggest that the moisture status of the near-surface material can be more important than its thermal properties. Thus, for the goal of estimating near-surface thermal properties, it is imperative to have some information regarding moisture content.

Our field experience suggests caution in interpreting remotely sensed temperatures, which are integrated over large areas, in comparison to thermal responses of near-surface materials derived on a smaller scale. We also found that a measured temperature difference depends on both the average wind speed in the local area and the wind speed near the time of sensing.

These field measurements suggest the following conclusions. Measurable temperature differences, which are related to the thermal properties of the materials, develop in sunlit and shaded regions. The presence of moisture, vegetation, self-shaded regions on a scale smaller than the sensor resolution, and variable wind speeds complicate using temperature differences to infer material properties.

The field evaluation of the analytical models showed that the measured temperature differences were consistent with model-predicted temperature differences. This suggests that the models capture much of the important behavior and processes that control the development of temperature differences. However, the tests also reveal that the models are highly sensitive to surface moisture, wind speed, albedo, and roughness length and that, for surface materials, these unconstrained inputs complicate the prediction of precise thermal properties. This conclusion suggests that combining empirical and/or comparative data analysis methods with the analytical models may yield more accurate results.

We also investigated improved methods of estimating the atmospheric transmittance and emitted path radiance associated with MTI thermal band measurements. In-scene atmospheric correction approaches depend on the availability of water or dense vegetation in the scene, and, thus, are impractical for application to generic scenes, especially those located in the desert. Radiative transfer programs (such as MODTRAN) require vertical profiles of temperature and water vapor content from the time and location of image collection. For a denied site, interpolating low-resolution weather information from global databases could provide the required input to approximate the atmospheric components with the radiative transfer method. The split-window method requires two spectral bands within a single atmospheric window to estimate the water vapor content. MTI lacks the requisite two bands within the 10.5- to 12.5-μm window. The multi-angle method requires two looks through the atmosphere from two different perspective views. However, MTI lost its two-look capability with the failure of its gyro.

Thus, the radiative transfer method holds the most promise for improving atmospheric estimates provided that vertical profile information is as accurate as possible. Future sensors could benefit from two bands in the long-wave atmospheric transmission window and a flexible pointing capability.

The work from this study has demonstrated the initial feasibility of estimating rock thermal properties from remote thermal measurements and identified numerous potential error sources including atmosphere, moisture, vegetation, wind, small-scale shading, and surface texture. We have identified potential means of mitigating the error sources, but recommend further testing to determine whether they constrain the errors within a range that is useful to the geological and geotechnical interpretation.

The second major effort in the study developed an initial method for classifying rock types from simulated MTI spectral data, derived from laboratory spectra. The classifier provides discrimination based on covariance differences rather than mean differences between the classes. The study showed that the covariance-based classifier could discriminate rock samples subject to small spectral variations. It showed that grain size can significantly affect the classification results and that assigning samples with different grain sizes to different classes yields improved separation and classification. We recommend forming classes according to both rock type and grain size and training the classifier to recognize both. The experiments also showed that the classifier failed to classify novel rock samples correctly because of its limited training set. The study is limited by its reliance on a small number of laboratory spectra for each rock-type class. Thus, we recommend further study to develop classifiers for larger and more variable training and test sets. The follow-on study should build a well characterized database of remotely collected samples for each rock-type class to train a classifier and test its separability and classifiability subject to variations in perspective view, atmosphere, grain size, weathering, moisture content, and other factors, which would allow us to characterize the conditions under which a classifier can reliably generalize and discriminate novel rock samples.

The rock classification study also searched and found the combinations of MTI band ratios that produce best classification results. In fact, the study identified a number of band-ratio combinations that produced classification results similar to the full 11-band classifications. The band ratios identified yield insights about specific MTI bands that influence the separation of the rock-type classes. It is not clear whether such feature space reductions would provide similar generalization for more comprehensive training and test sets, but if they do, they could increase computational efficiency.

In the course of this study, we have also identified other methods being developed at SNL that could enhance the interpretation of multi-spectral imagery for geological characterization. The Robust Spectral Segmentation method identifies and groups together spectrally similar regions within an image. Initial indications suggest that it can provide reliable segmentations to aid analysts and geologists in identifying regions of similar rock type, tailings piles, and changes such as disturbed earth. Spectral and spatial derivatives can enhance small and low contrast features, as well as local variations in texture, such as pipelines, buried cables, hidden tarps, and underground facility vents. Supersampling generates a synthetic high-resolution image from a collection of several low-resolution images. Such high-resolution thermal detail could provide important information about surface features for geological characterization, such as the thermal contrast of a relatively narrow layer of high-density rock between two lower density layers. Interferometric SAR can produce high-resolution DEMs, which, when processed with Rivertools, can produce accurate predictions of drainage patterns to aid geologists' interpretation of a remote site.

5.2 Recommendations

While this study has provided an initial proof-of-concept for rock property estimation and rock-type classification, we recommend further study to analyze and mitigate potential sources of error identified herein. We recommend further studies with real MTI data from dry, unvegetated sites with better atmospheric estimation to validate the application of the method to real data. In addition, we make the following recommendations:

- Additional studies to test and validate the analytical models that include moisture and vegetation.
- Investigation of methods to estimate the moisture present in the scene.
- Testing our proposed method for predicting the temperature of bare ground located underneath sparse vegetation cover.
- Further study to understand other potential sources of error identified in this study, including moisture, vegetation, wind, albedo, and roughness.
- Statistical analysis of the error sources to quantify the reduction in uncertainty that they introduce. Because geologists lack so much information about a denied site, even information with 20% or 30% error can improve their understanding and interpretation, particularly when the uncertain data can be combined with information from other sources.

We also recommend a follow-on study for rock-type classification to search for the broadband spectral filters that best discriminate between the rock types of interest. Furthermore, we recommend collecting (using remote sensing) and building a database of rock-type samples to test separability, classifiability, and generalizability of the proposed classifiers. The database should include common sources of variability including perspective view, atmosphere, grain size, weathering, and moisture content.

For future multi-spectral sensors, we recommend the following capabilities to enhance their ability to address the problems specific to geological characterization identified in this report:

- High spatial resolution in the long-wave infrared (LWIR) to exploit the thermal information present in shaded areas and two bands within the 10.5 to 12.5 μm atmospheric window to facilitate estimation of atmospheric water content.
- Inclusion of more bands in the 2.0- to 2.5-μm short-wave infrared (SWIR) range for geologic discrimination, similar to Advanced Spaceborne Thermal Emission and Reflection Radiometer (ASTER). In addition, the follow-on rock-type classification study may identify additional bands important for rock-type discrimination.
- Flexible pointing enables a number of capabilities, including DEM generation, multi-angle atmospheric estimation, and supersampling. Supersampling also requires over designed optics and enhanced data collection.
- Also desirable is the capability to collect daytime and nighttime images of the same site separated by 12 hours.

In conclusion, this study has developed a method to estimate rock thermal properties from MTI thermal measurements and a preliminary method for classifying generic rock types from multi-spectral image data. The study demonstrated initial proofs-of-concept for both these methods and shows the potential benefit to augment geologic and geotechnical interpretation. We recommend further analysis and development of these methods to mitigate potential sources of error identified in this report. This recommended follow-on development should produce predictable methods for extracting information from remote multi-spectral imagery to aid an analyst in characterizing the geology and understanding the geotechnical characteristics of remote sites.

Appendix A

RELATIONSHIP OF IRRADIANCE AND TEMPERATURE ERRORS IN SENSITIVITY ANALYSIS

As outlined in the discussion of the approach to analyzing sensitivity of the rock parameters to deviations in the “truth” temperatures or irradiances, a temperature (or irradiance) standard deviation is specified in the noise case (in which each pixel is assigned a different deviation). This number is used to generate deviations for each pixel based on a zero-mean gaussian distribution with the given standard deviation. These deviations are added to the “true” values that are then used to calculate the rock parameters by minimizing the objective function (e.g. sum of square errors in temperature). The relationship between irradiance standard deviation and temperature standard deviation and their relation to the objective function sum of square error arises.

The theoretical irradiation, E , in (W/m^2) leaving a surface of temperature, T K, is given by $E = \sigma\varepsilon T^4$ where σ is Boltzmann’s constant (5.67 x 10^{-8} W/m^{2}K^4) and ε is the emissivity of the surface. For small deviations, we can calculate differentials as

$$dE = \sigma T^4 d\varepsilon + 4\sigma\varepsilon T^3 dT \tag{A.1}$$

or

$$dT = \frac{1}{4\sigma\varepsilon T^3} dE + \frac{T}{4\varepsilon} d\varepsilon \tag{A.2}$$

where we take absolute values of differentials. Relative deviations are given by

$$\frac{dT}{T} = \frac{1}{4}\left(\frac{dE}{E} + \frac{d\varepsilon}{\varepsilon}\right). \tag{A.3}$$

These relations are shown graphically in Figures A1 through A3.

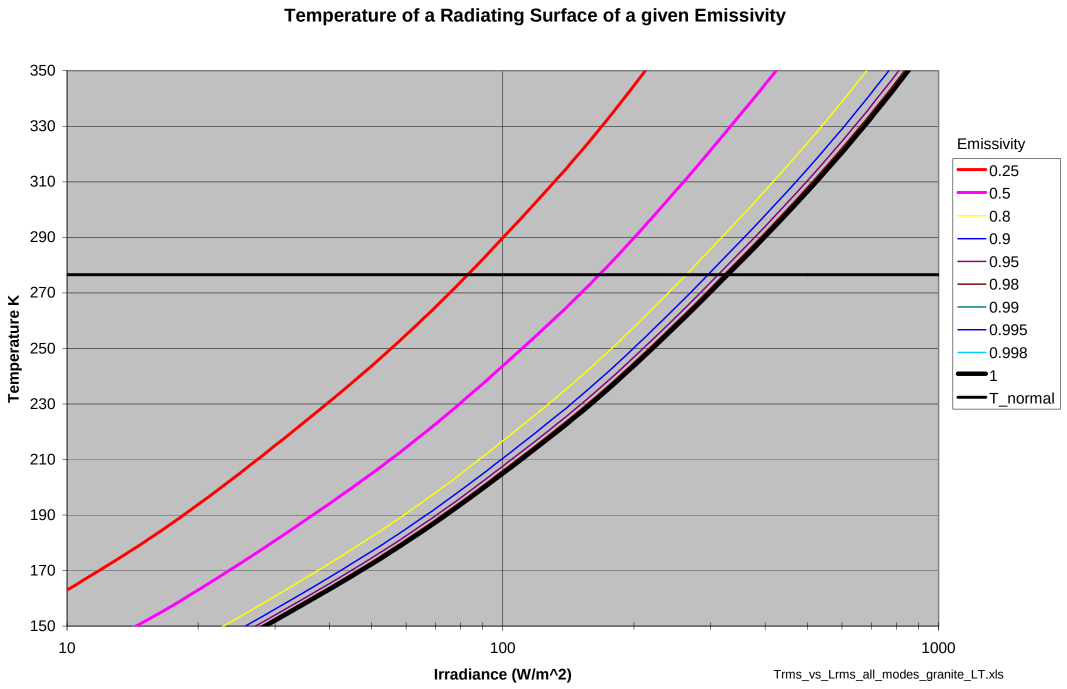

Figure A1 Temperature of radiating surface

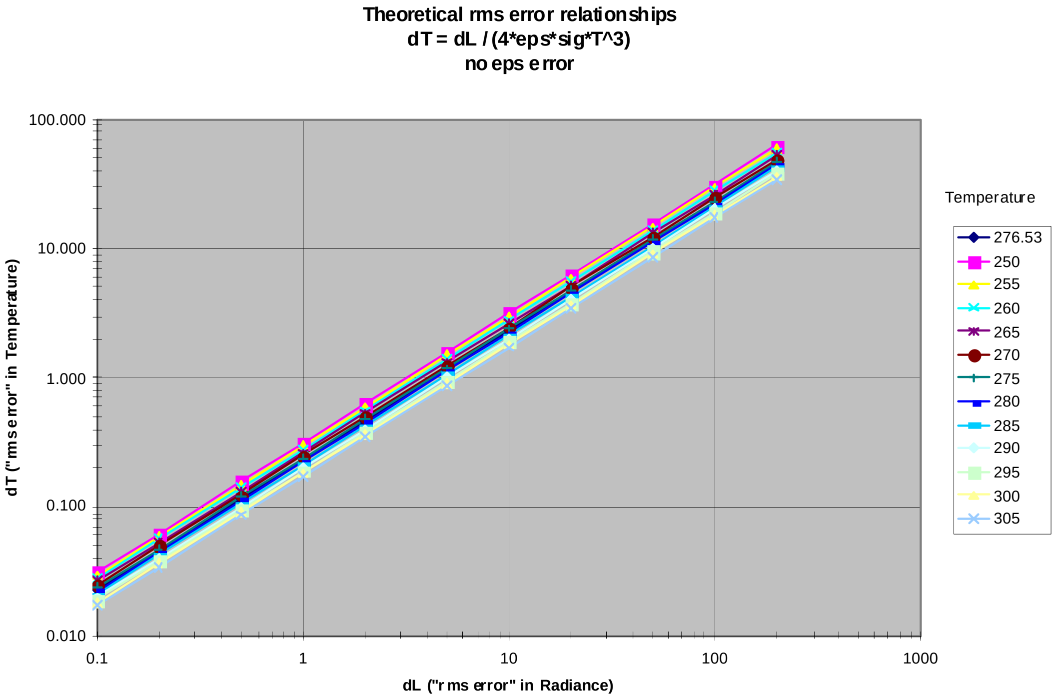

Figure A2 Theorectical error relation between Temperature and Irradiance with no emissivity error

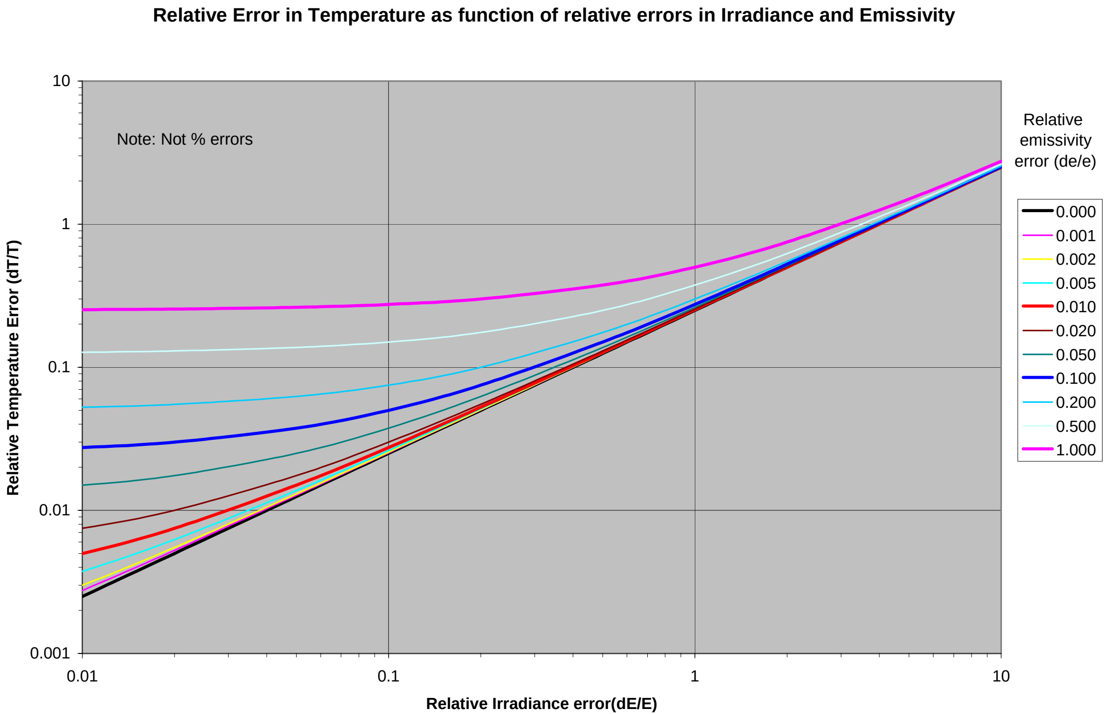

Trms_vs_Lrms_all_modes_granite_LT.xls

Figure A3 Relative errors Temperature as function of Irradiance and emissivity errors

Thus for small errors we can use these formulae to relate temperature and irradiance errors.

In order to verify the usefulness of these formula we can compare temperature and irradiance “errors” for two types of calculations. In the first, called Multi-Start runs, the convergence properties of the Dakota-IR_Dak program was investigated using “true” values of temperature and irradiance determined from the true rock properties of granite (granite17) and running optimizations using different initial initial (i.e. starting) rock parameter points. (The second case uses data from the sensitivity analysis. See below.) In general the convergence points (in terms of final optimization parameter values and objective function are not exactly the same for different initial conditions. In these cases both the Temperature square error and the Irradiance square error were output. The “square errors” were the Objective Functions used and are the “sum of square errors over all pixels”. In all cases, 16 pixels with differing solar irradiation histories were used. Thus we can readily compute root-mean-square (rms) values for these. The rms values are more readily compared to the input standard deviations for the noise cases and are easier to relate to physical properties.

After the optimization (in this case using Irradiance sum square error as the objective function) the relationship between Irradiance and Temperature errors are shown in Figure A4.

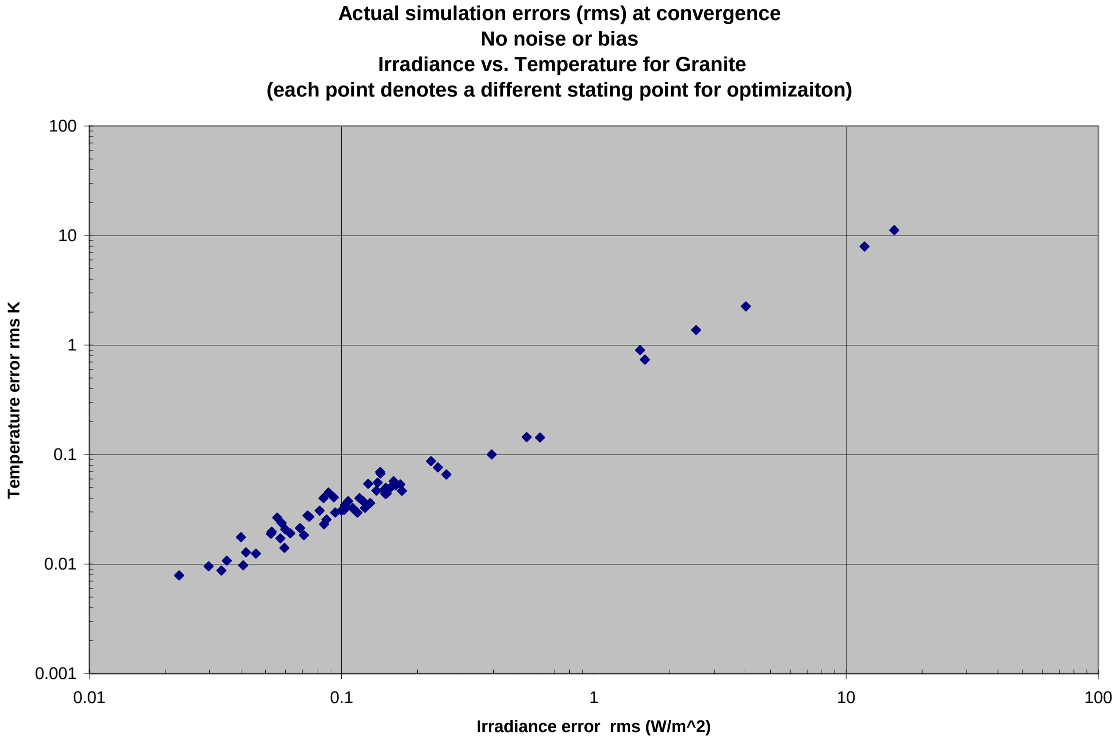

Figure A4 **Temperature and Irradiance errors from multiple start simulations (no noise or bias)**

In this case, the relationship between irradiance and temperature errors is obvious. In order to make comparisons that are more direct the temperature and irradiance values are in root-mean-square form:

$$E_{rms} = \sqrt{\frac{E_{err}}{N}}$$

or

$$E_{rms} = \sqrt{\frac{\sum_{1}^{N} (E_{meas} - E_{true})^2}{N}} \qquad \text{(A.5)}$$

where N is the number of pixels, and similarly for T_{rms}

This data can be compared with the theoretical values of dT, dE, and $d\varepsilon$ (from Equations A.1 through A.3) as shown in Figure A5.

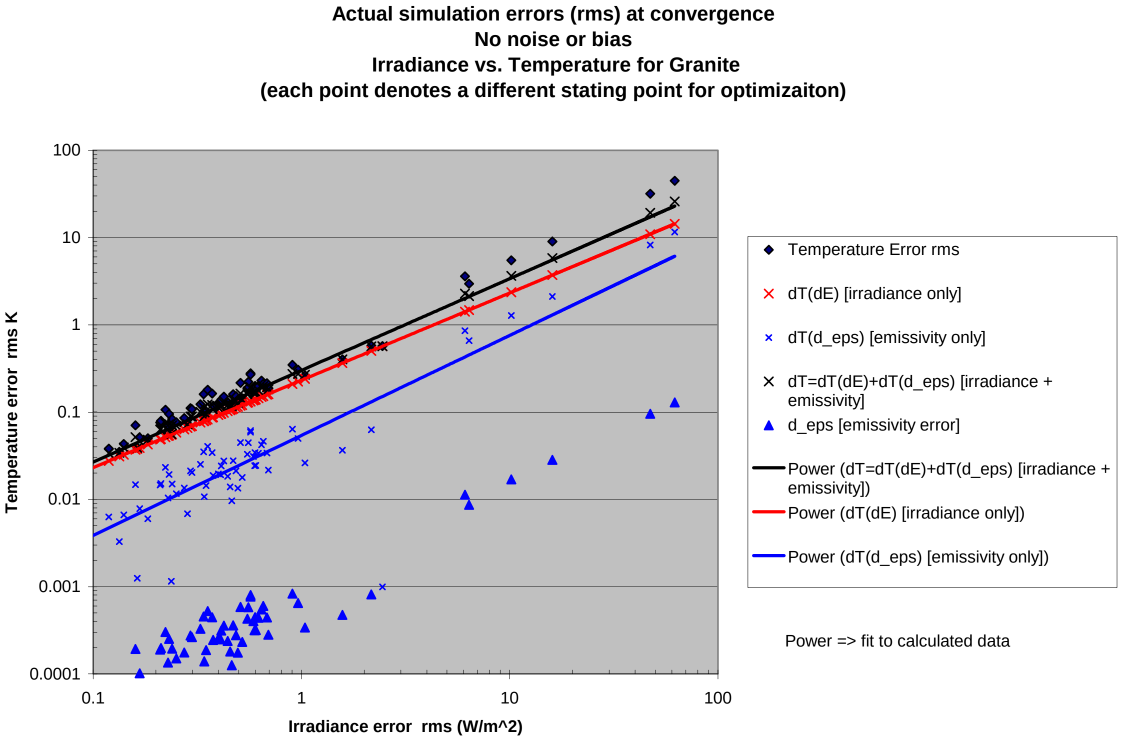

Figure A5 Sources of simulation errors

In this figure, we show all the data for the Multi-Start runs. In this figure we indicate "theorectical" temperature errors dT(dE) and dT(d_eps). The values of dT(dE) were calculated from Equation A.2 with the emissivity error $d\varepsilon = 0$. Similarly, dT(d_eps) is from Equation A.2 with $dE = 0$. The points for dT=dT(dE)+dT(d_eps) uses non-zero error values for both. The solid curves are power law fits for the indicated errors. In the formula for *dT,* we must pick a value of temperature about which the errors occur. The best match for $dT = dE/(4\sigma\varepsilon T^3)$ (i.e. with $d\varepsilon = 0$) to T_{rms} occurred at a value of $T = 273.52$K. This value is used in the figures. The reason for this particular value is unknown, however it is close to the average (274.25 K) of the "true" pixel temperatures used in the calculations as shown in Table A.1.

In Figure A5, we see that the match between theoretical and measured rms values is somewhat close but not exact. It should be noted that the values for ε and $d\varepsilon$ are known from the numerical experiment and are they are not shown explicitly in the figure. The values shown in Figure A5 contain a few large values of irradiance and temperature indicating that the optimization was not particularly good. If we omit the larger values (rms Temperature errors > 1K) we obtain a much better agreement as shown in Figure A6.

The match between the theoretical and measured values are very close in this case.

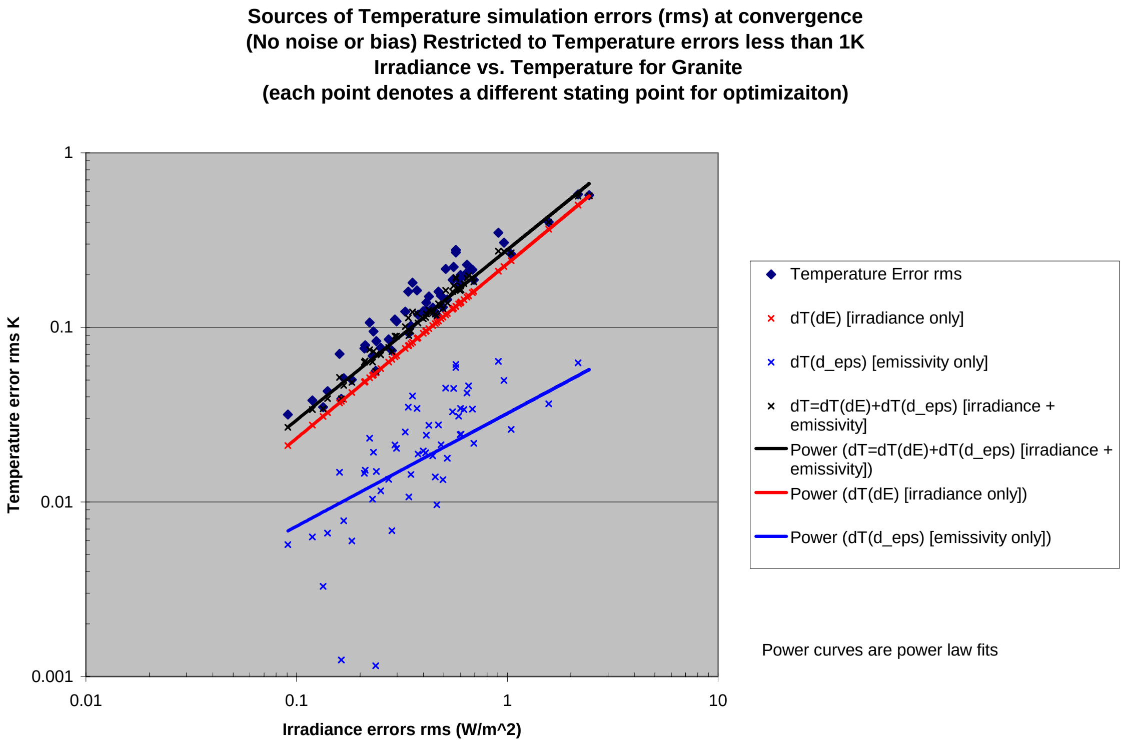

Figure A6 Sources of simulations error (Temperature vs. Irradiance) for small values of Temperature error

In addition to examining the relationship between temperature and irradiance errors using the multiple-start no noise case we also considered the data from the irradiance noise sensitivity study. The results of this analysis is shown in Figure A7. In this case the "theoretical" temperature errors are given again by Equation A.2. In this case the actual value of emissivity that was obtained at convergence was used to calculate dT(dErms,de) as well as the appropriate errors. As seen in Figure A7, the agreement between the "theoretical" and actual values of the temperature errors is not as good as in the noiseless case (Figures A5 and A6). It is interesting to note that for the noisy case the theoretical result provides an upper bound on the temperature errors as a function of the irradiance errors. This upper bound agrees well with the no noise case. Thus, even in the noisy case, when we state an equivalent temperature error given an irradiance error we overstate the amount.

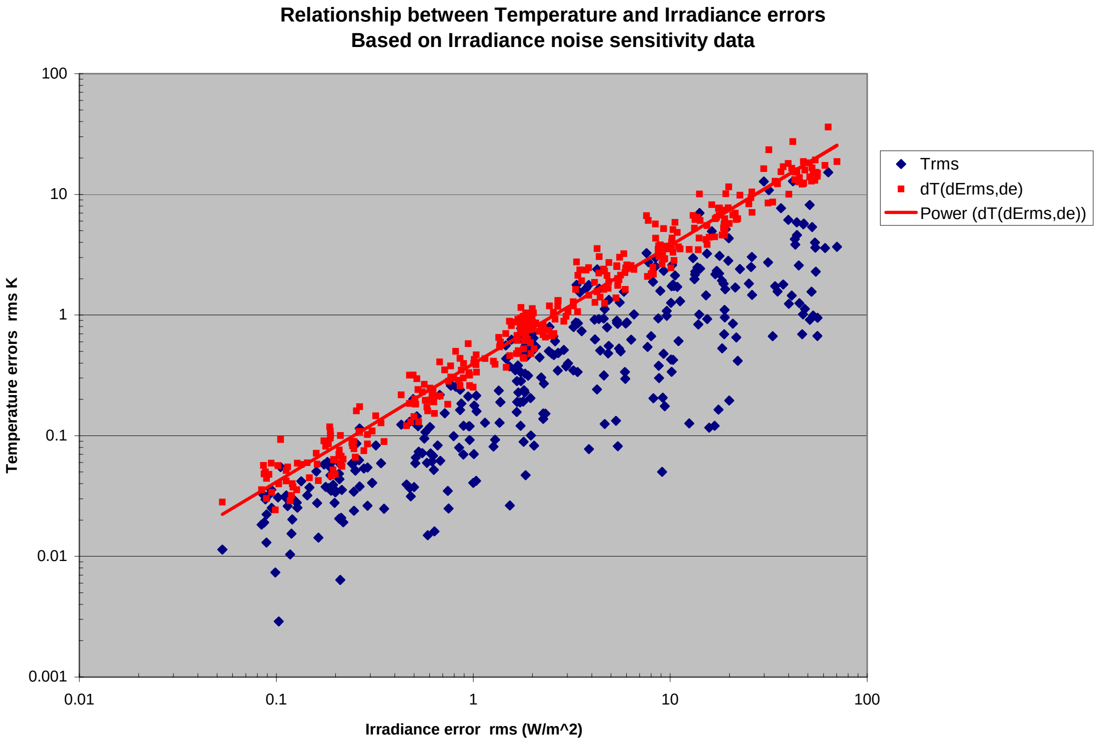

Figure A7 Temperature errors vs. Irradiance errors from Irradiance noise sensitivity data

As a result of these simulation measurements we can be confident that the relationships among the errors in temperature, irradiance, and emissivity are adequately given by Equation A.2.

Table A1 Pixel Properties for Granite

init_IR_s_granite17_jd356_3epa_LT

Pixel ID	Erad_meas	T_meas	Ridge Height	Pixel Offset	Ridge direction
1	256.73	266.32	3001	-100	EW
16	322.81	282.02	3001	100	EW
2	259.90	267.14	3001	-4040	EW
3	259.53	267.05	3001	-4050	EW
4	263.58	268.08	3001	-4060	EW
5	273.74	270.63	3001	-4070	EW
6	278.18	271.72	3001	-4080	EW
7	280.72	272.34	3001	-4090	EW
8	282.97	272.88	3001	-4100	EW
9	290.09	274.58	3001	-4150	EW
10	294.79	275.69	3001	-4200	EW
11	300.92	277.11	3001	-4300	EW
12	305.09	278.07	3001	-4400	EW
13	308.25	278.79	3001	-4500	EW
14	325.44	282.59	3001	-10000	EW
15	327.30	282.99	0	0	EW
Average	289.38	274.25			

DISTRIBUTION:

1	MS9018	Central Technical Files, 8945-1
2	MS0899	Technical Library, 9616
1	MS0323	LDRD Office, 1101
5	MS0751	Laurence S. Costin, 6117
1	MS0751	Allen Lappin, 6117
1	MS0859	Terry Stalker, 15351
2	MS0844	Mary M. Moya, 15352
1	MS0751	Charles L. Walker, 15352
1	MS0844	Wallace J. Bow, 15352
1	MS0844	R. Joe Folger, 15352
1	MS0844	José S. Salazar, 15352
1	MS0570	Jody L. Smith, 5712
1	MS0972	Bridget K. Ford, 5712
1	MS0570	Jeffrey A. Mercier, 5712
1	MS0570	Prabal Nandy, 5712
1	MS0972	C. Andy Boye, 5710
1	MS0570	Max L. Decker, 5743
1	MS0971	Anthony J. Medina, 5720

1 Colin Shellum
Springfield Research Facility (HTRAC)
6350 Walker Lane, 4th Floor
Alexandria, VA 22310-3226

1 David Bensley
NIMA West
3838 Vogel Road
Attn: PTRGC, D. Bensley, MS L-41
Arnold, MO 63010

1 Mel Podwysocki
United States Geological Survey
Mail Stop 926A
Reston, VA 20192

1 Edward Tremba
Defense Threat Reduction Agency
ATTN: TDTT Ed Tremba
Albuquerque Field Operations
1680 Texas ST SE
Kirtland AFB, NM 87117-5669

1 Robert Weber
Defense Intelligence Agency
Building 6000
Washington, DC 20340
Attn: DIAC/Robert Weber/UFAC